AFRL-RB-WP-TR-2010-3013

UNSTEADY LOW REYNOLDS NUMBER AERODYNAMICS FOR MICRO AIR VEHICLES (MAVs)

Michael V. OL

Low-Speed Aerodynamic Configuration Branch
Aeronautical Sciences Division

MAY 2010
Final Report

AIR FORCE RESEARCH LABORATORY
AIR VEHICLES DIRECTORATE
WRIGHT-PATTERSON AIR FORCE BASE, OH 45433-7542
AIR FORCE MATERIEL COMMAND
UNITED STATES AIR FORCE

NOTICE AND SIGNATURE PAGE

Using Government drawings, specifications, or other data included in this document for any purpose other than Government procurement does not in any way obligate the U.S. Government. The fact that the Government formulated or supplied the drawings, specifications, or other data does not license the holder or any other person or corporation; or convey any rights or permission to manufacture, use, or sell any patented invention that may relate to them.

This report was cleared for public release by the USAF 88th Air Base Wing (88 ABW) Public Affairs Office (PAO) and is available to the general public, including foreign nationals. Copies may be obtained from the Defense Technical Information Center (DTIC) (http://www.dtic.mil).

AFRL-RB-WP-TR-2010-3013 HAS BEEN REVIEWED AND IS APPROVED FOR PUBLICATION IN ACCORDANCE WITH THE ASSIGNED DISTRIBUTION STATEMENT.

*//signature//

MICHAEL V. OL
Project Engineer
Low-Speed Aerodynamic Configuration Branch
Aeronautical Sciences Division

//signature//

CHRISTOPHER P. GREEK
Chief
Low-Speed Aerodynamic Configuration Branch
Aeronautical Sciences Division

//signature//

DIETER MULTHOPP
Technical Advisor
Low-Speed Aerodynamic Configuration Branch
Aeronautical Sciences Division

This report is published in the interest of scientific and technical information exchange and its publication does not constitute the Government's approval or disapproval of its ideas or findings.

*Disseminated copies will show "//signature//" stamped or typed above the signature blocks.

REPORT DOCUMENTATION PAGE

Form Approved
OMB No. 0704-0188

1. REPORT DATE *(DD-MM-YY)*	2. REPORT TYPE	3. DATES COVERED *(From - To)*
May 2010	Final	01 June 2002 – 01 December 2009

4. TITLE AND SUBTITLE
UNSTEADY LOW REYNOLDS NUMBER AERODYNAMICS FOR MICRO AIR VEHICLES (MAVs)

5a. CONTRACT NUMBER
IN HOUSE

5b. GRANT NUMBER

5c. PROGRAM ELEMENT NUMBER
0602201

6. AUTHOR(S)
Michael V. OL

5d. PROJECT NUMBER
A07C

5e. TASK NUMBER

5f. WORK UNIT NUMBER
A07C0B

7. PERFORMING ORGANIZATION NAME(S) AND ADDRESS(ES)
Low-Speed Aerodynamic Configuration Branch (AFRL/RBAA)
Aeronautical Sciences Division
Air Vehicles Directorate, Air Force Research Laboratory
Wright-Patterson Air Force Base, OH 45433-7542
Air Force Materiel Command, United States Air Force

8. PERFORMING ORGANIZATION REPORT NUMBER
AFRL-RB-WP-TR-2010-3013

9. SPONSORING/MONITORING AGENCY NAME(S) AND ADDRESS(ES)
Air Force Research Laboratory
Air Vehicles Directorate
Wright-Patterson Air Force Base, OH 45433-7542
Air Force Materiel Command
United States Air Force

10. SPONSORING/MONITORING AGENCY ACRONYM(S)
AFRL/RBAA

11. SPONSORING/MONITORING AGENCY REPORT NUMBER(S)
AFRL-RB-WP-TR-2010-3013

12. DISTRIBUTION/AVAILABILITY STATEMENT
Approved for public release; distribution unlimited.

13. SUPPLEMENTARY NOTES
PAO Case Number: 88ABW 2010-0446, cleared 02 February 2010. Report contains color.

14. ABSTRACT
This work introduces the Micro Air Vehicle (MAV) problem from the viewpoint of aerodynamics. Water tunnels are assessed as tools for MAV aerodynamics. The design, construction and instrumentation of RB's "Horizontal Free-surface Water Tunnel" is documented. Experiments in steady aerodynamics at low Reynolds number for airfoils, plates and wings of various planforms are mentioned, with focus on laminar to turbulent transition and documentation of how Reynolds number, flowfield conditions and model geometry interplay to affect laminar separation and possible turbulent reattachment, and how planform effects impact lift generation. Passing to the unsteady aerodynamics problem, the HFWT's "High-Intensity Pitch-Plunge Oscillator" Rig is described. Then, the bulk of the report focuses on experiments in unsteady aerodynamics. A broad range of periodic and transient problems is covered, anchored in traditional problems of airfoil dynamic stall, and expanding to MAV applications of perching and flapping. New knowledge includes elucidation of the surprisingly broad limits of linear superposition in markedly nonlinear problems, and notes on the relative importance of laminar to turbulent transition in a broad range of unsteady problems.

15. SUBJECT TERMS
Unsteady Aerodynamics, Micro Air Vehicle, Vortex Dynamics, Dynamic Stall

16. SECURITY CLASSIFICATION OF:			17. LIMITATION OF ABSTRACT:	18. NUMBER OF PAGES	19a. NAME OF RESPONSIBLE PERSON (Monitor)
a. REPORT	b. ABSTRACT	c. THIS PAGE			Michael V. OL
Unclassified	Unclassified	Unclassified	SAR	150	19b. TELEPHONE NUMBER *(Include Area Code)* N/A

Standard Form 298 (Rev. 8-98)
Prescribed by ANSI Std. Z39-18

Table of Contents

List of Figures

List of Tables

Acknowledgements

While the present report has only one author, it would be ludicrously pompous and unfair to fail to mention the contributions of a long list of students and visiting associates who conducted experiments in the HFWT and/or materially contributed to development of test articles, who wrote software and developed algorithms, and so forth. These include:

- Mr. Robert Downs, for conducting hot-wire and freestream PIV measurements to characterize HFWT flow quality, for conclusively reporting on hot wire limitations in the present setup, and for running a detailed parameter study of airfoil wake momentum losses using PIV.
- Lt. (at the time) Deepak Peter, for conducting a different series of hot-wire measurements.
- Lt. (at the time) Sergey Kaplan, for running PIV experiments on the AR=2 tip-vortex static aerodynamics.
- Prof. Aaron Altman, for calibration and experiments with the Rolling Hills Research Corporation force balance, for a long series of mutual research consultations, and for supporting a steady stream of graduate students from the University of Dayton to participate in HFWT research.
- Prof. Luis Bernal, for developing the Fiber Bragg Grating force balance, for designing the various iterations of the balance, and for developing the balance initial calibration procedure.
- Mr. Jonathan Rausch and Mr. Dan Stanley, for running a series of PIV and dye injection experiments on plunging flat plate (not reported here, but materially influencing concepts of vorticity transport cited in related projects).
- Dr. Craig Cox, for writing essentially all of the motion control routines for the HIPPO rig, for developing the electrical installation of the 3rd HIPPO linear motor, for improving the calibration process of the FBG balance, and for general automation of data reduction in the HFWT.
- Mr. Doug Szczublewski, for running a long series of dye injection experiments in the HFWT, developing several data reduction routines, and general assistance in lab operation.
- Lt. (at the time) Daniel Fredberg, for running airfoil plunge PIV experiments.
- Ms. Meredith Almoney and Ms. Jeanette Aukerman, for developing a hydrogen bubble flow visualization capability in the HFWT (not reported here) and for initial debugging of the 2-motor version of the HIPPO rig.
- Dr. Sergey Fonov and Dr. Jim Crafton, for introducing the Surface Shear Stress Sensitive film technique in the HFWT, and for providing a steady stream of advice on optics and electronics equipment.
- Dr. Ernest Hanff, for suggesting the idea of a two vertical motor, two plunge-rod concept for pitch/plunge actuation, and for extensive exchange of ideas in the aerodynamics of separated flows.
- Profs. Rolf Radespiel, Cam Tropea, Holger Babinsky, Jeff Eldredge, David Williams, Haibo Dong, Don Rockwell, Ashok Gopalarathnam, Mark Reeder, Haibo Dong, Yongsheng Lian, and Wei Shyy, for the many insightful discussions, collaborations, and general exchange of ideas.

The author apologizes to all those who have been involved with HFWT experiments and collaborations, but who for whatever reason have not been included here, or whose contributions are inadequately noted. One can only remember such things in wistful reminiscing – not in the fury of clerical hustle required to finish a long technical report!

1. Summary

Work under the present project, and therefore this report, can be somewhat artificially but nevertheless usefully segmented into the following:

1. Introducing the Micro Air Vehicle (MAV) problem, and the relevance of low Reynolds number aerodynamics – especially unsteady low Reynolds number aerodynamics – to performance, stability and control, and the overall problem of flight of MAVs.
2. Assessment of water tunnels as tools in aerodynamic research, for MAVs and for incompressible configuration aerodynamics in general. We document the design, relocation from its original installation, reconstruction and shakedown of A FRL/RB's "Horizontal Free-surface Water Tunnel" (HFWT), to include instrumentation for flowfield measurements and force measurements.
3. Experiments in steady aerodynamics at low Reynolds number: airfoils, and wings of various planforms. Here the focus is on laminar to turbulent transition and documentation of how Reynolds number, flowfield conditions and model geometry interplay to affect laminar separation and possible turbulent reattachment, and how planform effects impact lift generation.
4. Passing to the unsteady aerodynamics problem, we recite the requirements definition, design, installation and shakedown of the HFWT's "High-Intensity Pitch-Plunge Oscillator" Rig, or HIPPO, which in its first configuration performs a broad range of two-degree-of-freedom longitudinal oscillations, and a subsequent upgrade added a third degree of freedom.
5. Experiments in Unsteady Aerodynamics using the HIPPO rig, first in two degrees of freedom of motion, and then in three – to include airfoils, flat-plates and wings. We cover a broad range of periodic and transient problems, anchored in traditional problems of airfoil dynamic stall, and expanding to MAV applications of perching and flapping. New knowledge, or what passes for knew knowledge in a mature field, includes elucidation of the surprisingly broad limits of linear superposition in markedly nonlinear problems, and notes on the relative importance of laminar to turbulent transition in a broad range of unsteady problems.

The experiments detailed here parallel numerous related computational and experimental investigations. For example, "canonical problems" in pitch and plunge of airfoils were identified by the PI and studied by several research groups to compare methodology and hierarchy of methods. However, generally the results reported herein are limited to those obtained in the Principal Investigator's lab.

2. Introduction: Philosophy, Scope, and Approach

This report covers in-house experimental work on aerodynamics with applications primarily, but not exclusively, directed towards the so-called Micro Air Vehicles, or MAVs. The period 2002 through 2009 is covered.

2.1. General Musings on MAVs

Writing in 2010, it seems fair to remark that principal problems in aerodynamics remaining at the research-level are at the extremes of very fast and very slow. Very fast problems – hypersonics and the like – involve problems of compressibility and heat transfer. In contrast, very slow problems – low speeds and small scales – are incompressible and non-thermodynamic, but rife with complications from the effects of viscosity and consequent flow separation. In the opinion of the PI, these are the most celebrated and most intriguing problems at the juncture between fluid mechanics and flight vehicle engineering. And they form the subject of this report.

But what are the applications? Here we consider MAVs. MAVs are not only a topical application in modern times, but are also an intriguing problem of fundamental interest to the fluid mechanicist, the aeronautical designer and the biologist, as the relation between flight of natural creatures and MAVs is not merely a metaphorical motivation, but is quite literally true. The definition of MAVs is somewhat amorphous, depending on the biases of the definer. Loosely following McMichael and Francis[1], Pines and Bohorquez[2], Shyy et al.[3], and Mueller[4], we can "define" MAVs for present purposes as flyers in the Reynolds number range of 10^4 to 10^5 based on the relevant length scale (typically wing chord) and velocity scale (typically flight speed), which translates into vehicle maximal dimensions on the order of 10-30 cm, or possibly somewhat less. Truly insect-scale vehicles are not excluded, but the concomitant Reynolds number range is not studied in the following work, which has a lower bound of $Re \sim 5000$, stemming from the operating limits of the available experimental facility.

Most MAV-relevant flows are fundamentally unsteady. Even in approximately steady-level flight, the vehicle is subject to ambient gusts and other disturbances, such as passage through the wakes of buildings. Low flight speed and small moments of inertia imply that even nominally quiescent atmospheric conditions introduce palpable disturbances. Maneuvering flight, such as in making turns and altitude changes, course changes to avoid obstacles, landing approaches and the like, are an obvious source unsteadiness, where angle of attack variations are large in amplitude and relatively fast in terms of convective time. This is an essential difference between MAV flight and the flight of larger aircraft. Yet another difference, coupling into the first, is low-Reynolds number effects, where boundary layers are generally laminar and thus strongly susceptible to flow separation. The amount of flow separation depends on Reynolds number (and in turn on flight speed) and other factors. Flow separation directly affects flight mechanics, and vice versa. So we find a tightly coupled problem between fluid dynamics and flight mechanics, fed by both low Reynolds number and small vehicle mass/inertia/speed. The result is massive unsteadiness – and this is before we even consider the important problem of structural flexibility and fluid-structure interaction for MAVs[5]. And for flapping-wing MAV configurations, which attempt to follow examples of bird flight[6,7] or insect flight[8,9], unsteady aerodynamics and time-varying flow separation are obviously dispostive factors.

But how unsteady is the aerodynamic force time history for even obviously unsteady flow fields? The question is not trite or rhetorical. The simplest flows – the ones most amenable to closed-form analysis – are potential flows. Lift curve slope is 2π, stall does not occur, and streamlines can negotiate curved paths with arbitrarily large adverse pressure gradients without separating, except for possibly at discrete points of infinite curvature. The latter describes the trailing-edge Kutta condition, which fixes separation and together with the no-through-flow boundary condition also fixes the circulation. This "bound" circulation, together with the so-called noncirculatory lift or apparent-mass effects, determines the lift and pitch time history for a broad class of flows where separation is limited to the trailing edge region. In the work presently described, we study various geometric and kinematic abstractions of

unsteady aerodynamics, with at least the preliminary assessment that quasi-steady models may be suited to MAV conceptual design for even massively separated and unsteady flows.

Recent reviews on the subject of MAV flight are given by Shyy et al.[10] and Mueller[4], among many others. Here we will not dwell on the conceptualization of MAVs, beyond making some philosophical observations about the now-fashionable subject of flapping flight, and how flapping – besides other MAV aerodynamics problems – maps to the more abstract problems in unsteady aerodynamics, reminiscent of the classical problems of dynamic stall and impulsive start. These are among the threads justifying the present work.

2.1.1. Opinions on Benefits and Drawbacks of Flapping Wings

It is perhaps appropriate here to journalize some musings on the attractive and bewildering field of flapping-wing MAVs, and the aerodynamics challenges that these vehicles pose. Why should any manmade vehicles use flapping wings? We have spent over a century on spectacularly successful development of fixed-wing aircraft, where propulsion and lift are explicitly separated, and the better part of a century developing rotary-wing aircraft, where lift/propulsion/control are combined. Flapping-flight failed in the early 20th century in essence because the mass/power/area/speed relationships for flapping fliers scale poorly to craft large enough to carry humans or human-sized cargo. And we know this from observing birds. Larger birds fly more like fixed-wing aircraft, while smaller birds flap more vigorously in frequency and amplitude relative to their wingspan. Does this mean that at extremely small scales, say that of insects, flappers are more efficient than fixed-wing or rotary-wing craft? Is this statement further strengthened if to the simple geometric scaling we add low-Reynolds number effects?

So far one can not say. There are many ways to flap in nature, with seemingly very disparate solutions to broadly similar flight problems, such as the hovering of insects vs. hummingbirds[11]. If there is no one preferred solution, then how do engineers pursue bio-inspiration for designing an "optimal" flapper? But from the scientific viewpoint, as opposed to that of practical engineering, what makes flapping so interesting is that it combines the nonlinearities of aerodynamics, structures and controls. It speaks to some of the most celebrated problems in continuum dynamics, in a way that only now is becoming amenable to our computational methods and our experimental tools. And it rests on intriguing parallels between performance objectives in nature (perching, hovering, precision maneuver, predator evasion, prey capture, and on and on) and desired performance for urban-type military flight vehicles. We do not, however, have any definitive evidence that a flapping vehicle is somehow superior to a rotary vehicle.

But we can offer some speculations about the possible superiority of flapping in problems in maneuverability. Two examples are flight near rigid walls (obstacle avoidance) and gust tolerance. Both are crucial for MAV applications.

All schemes of generating lift and propulsion by fluid mechanics involve momentum transfer. This is true for rotorcraft, flapping craft, or rockets, or fixed-wing aircraft. Flapping flight is not incomparably different from rotary flight, but there are potential advantages. In hover, there is a net high momentum jet underneath the aircraft, and to some extent this will result in wall suck-in. We speculate that for flapping craft this may be less deleterious than for rotorcraft, for at least two reasons: weaker tip vortices for flappers (and possible further inboard of the wing tip), and flappers' greater capacity to articulate and therefore to roll away from the wall.

Gust tolerance is governed by wing loading, moments of inertia and other quantities ineluctably related to physical scale; but also by lift curve slope (lower is better!) and in particular by the distinction between separated and attached flow. Attached incompressible flow responds quickly. Bound vorticity changes instantaneously, and shed vorticity decays according to well-known theoretical descriptions - in most cases also quickly. But separated flows, we speculate, respond more slowly to abrupt inputs. Obviously separated flows are less efficient than attached flows, but attraction of operating in separation

is potentially smoother gust response. This is not a proven fact, but is sufficiently compelling to justify the requisite research and flight test of flappers.

Flappers operating in mostly attached flow are quite similar to rotorcraft, especially if the dynamics of flipping the wing at the stroke endpoints are fast, and the wings are relatively rigid. The main differences are in actuation, structural dynamics and aeroelaticity - not in aerodynamics or thrust production. In both cases there is an effective airspeed at each blade section, which forms a dynamic pressure; there is the sectional chord, the kinematic angle of incidence, and thus the sectional lift and drag, resolving in to thrust and rotational resistance (power absorbed by the wings/blades).

The aerodynamic difference between flapping and rotorcraft comes from management of separated flow. At scales above MAVs, dynamic-stall literature attests that rotorcraft operating in regimes of large flow separation suffer an almost completely unmitigated penalty. Leading edge vortex production is parasitic, not beneficial. Classical aerodynamic intuition suggests that a rotor operating at large effective angle of attack is a horrible idea, because massive disorganized separation will lead to both high drag and low lift. But some recent experiments on revolving wings at MAV Reynolds numbers and large incidence suggest retention of the LEV and therefore a lift benefit, though possibly at the cost of poor L/D. Other experiments give contradictory results for revolving wings[41]. In any case, no rotorcraft, to our knowledge, has been developed to explicitly use managed separated flow at high blade effective angle of attack.

For flappers, however, LEV retention and large lift coefficients in separated flow are well documented[8]. As with rotorcraft, flappers operating in separated flow would suffer an efficiency penalty. But unlike rotorcraft, we speculate, the management of flow separation, by attached LEVs or otherwise, offers both high lift coefficients and a "slow" response to mitigate gusts. Rigorous substantiation of these conjectures is a huge fundamental research task, but the attraction of a viable flapping-wing flight article is that it motivates such research by anchoring in practical demonstration.

In summary, insect-type flapping at large effective angles of attack is perhaps not an efficient way to fly, but it may be a maneuverable and gust-tolerant way to fly. The question now is, to what extent is the time history of aerodynamic forces quasi-steady (with a possible phase lag or lead) with the effective angle of attack, and/or other kinematic parameters of the motion? That is, we seek a closed-form solution such as $C_L = f(\alpha, \dot{\alpha}, \ddot{\alpha}, ...)$, where the reduced frequency, amplitude and so forth are parameters subsumed in the proper choice of independent variables. Does such a solution exist, for low Reynolds numbers, for high rates, for aggressive motions, in closed-form? Clearly such a solution is possible for small-amplitude motions[87] in 2D. In attempting to bridge from this to the full problem of flapping, we consider a hierarchy of abstractions.

2.1.2. Unsteady Aerodynamics in Two Dimensions

2D problems are the natural starting point for more complex investigations. Here, by "2D" we mean not only airfoil-type problems, but problems of 3D wing planforms where the motion is limited to the rectilinear case – that is, pitch, plunge and fore-aft motion (surge).

Despite the geometric and kinematic complexity of flapping wings in nature or even in manmade vehicles, unsteady aerodynamics in two dimensions remains a critical area for Micro Air Vehicle flight, with applications including perching, gust response, maneuvering flight and flapping wings. The central question concerns the relation between time history of relative motion kinematics and aerodynamic loads production. The maneuver of perching is related to the classical-pitch up problem, where the angle of attack varies fairly quickly over a large amplitude[12]. For all of its complexity, the fully-articulated flapping-wing flight of bats, involving various geometric rotations, translations and planform changes, shows evidence that inviscid and "wake-only" methods can still approximate fairly-well the lift coefficient time-history[13]. The possibility of usefulness of quasi-steady sectional aerodynamic models and strip-theory-type of 3D generalizations for maneuvering insect flight[14] and potential applications to bio-inspired flight vehicles[15] implies a need to validate and to generalize the constituent assumptions

using a progress of well-defined abstractions, from simple classical problems to more geometrically-rich cases closer to MAV applications. For geometrically simple problems such as sinusoidally oscillating airfoils, where there is always an acceleration, indications are that at high reduced frequency, noncirculatory effects dominate[16,105], thus simplifying the force modeling. This contrasts with the complexity of the dynamic stall problem at more moderate rates[17]. In sum, it would be advantageous in applied problems if full resolution of vortex shedding and the resulting flowfield evolution were not strictly necessary to obtain reasonable accuracy of aerodynamic loads time history.

The problem can be divided into periodic and nonperiodic motions. Periodic motions – typically sinusoidal – are more thoroughly studied[18], but are more applicable to cruise-type of MAV applications, where one is primarily interested in flapping-wing propulsion. Nonperiodic motions are arguably the richer problem, as there is no forcing function to give a repeatable bulk flowfield response, and because such motions are closer analogues of maneuver and gust interaction. Pitch-ramps of airfoils are perhaps the most oft-studied nonperiodic motion. This was, evidently, a subject of intense interest in the mid 1980's to mid 1990's, for applications to maneuvering fixed-wing manned aircraft. Typically the airfoil was the NACA0012 or 0015, but the Re range was 10^4 to 10^5 – that is, not far removed from MAVs. A brief survey includes the experiments of Graham et al.[19,20,21], Chandrasekhara et al.[22,23], Walker et al.[24,25], Daley and Jumper[26], Ramaprian et al.[27,28], Acharya et al.[29,30], Koochesfahani and Vanco[31], and Schreck et al[32]. Typical measurement techniques were flow visualization, such as by dye injection in water; surface pressure measurements and force-balance measurements. For instance, Graham and Yeow[19] visualized the linear pitch-ramp LEV structure in water, at higher angle of attack excursions but lower rates than those presently considered. Shih et al.[33] and Crisler et al[34]. applied particle image velocimetry to the airfoil pitch-ramp problem. Computational examples include Ghosh Choudhuri and Knight[35], Okongo'o and Knight[36], and Visbal et al.[37,38,39]. Visbal and Shang[37], for example, computed in 2D the linear pitch-up of a NACA0015 airfoil at $Re = 10^4$, finding that lags between evolution of leading-edge flow separation and the airfoil motion kinematics should increase with increasing reduced frequency.

2.1.3. Rectilinear vs. Nonrectilinear Motions

The experimental facilities pursued in the subject research accommodate primarily "rectilinear" motions – oscillations in the longitudinal plane, consisting of pitch or rotation, plunge or heave, and surge or fore-aft motions. Non-rectilinear motions, such a rotation in the sense of a mapleseed or most insect wings[40], are excluded – with one except at the very end of this report. How important is the distinction between rectilinear and nonrectilinear motions? If the latter can be analyzed in a strip-theory approach as a collection of 2D sections linked by spanwise location and local dynamic pressure, then evidently the distinction should be small. Here there is considerable controversy. For example, Dickinson and his various colleagues (see for example Lentink and Dickinson[40] for a recent summary), find evidence that rotation stabilizes the leading edge vortex forming at high angle of attack as the wings moves about each half-stroke. This LEV is important in regularizing the separated flow, maintaining high lift coefficient and therefore producing sufficient lift/thrust for aggressive maneuver – which, ultimately, is asserted to be the whole point of flapping. On the other hand, Babinsky and Jones[41] found very little difference in either lift coefficient history or flowfield evolution for impulsive-start problems in rectilinear motion (translation at a fixed angle of incidence) or non-rectilinear motion (wing impulsively revolving from rest, at a fixed angle of incidence). Further, Babinsky and Jones found qualitatively similar lift histories to those of Dickinson et al.[9]. So we have to ask…

1. Do rectilinear and nonrectilinear motions, at the same nominal Re, reduced frequency, acceleration profile and so forth, produce fundamentally different flowfields, in particular regarding LEV formation, retention and shedding?
2. Do nonrectilinear motions produce similar flowfields along the span, except possible near the root and tip?
3. Do nonrectilinear and rectilinear motions produce similar lift coefficient time histories?

4. Can lift coefficient histories be similar, despite large differences in the flowfield?
5. Is the role of noncirculatory force the same in rectilinear and nonrectilinear motions?
6. Do large accelerations at motion onset effectively make "all flows look alike"?

So there are many questions. The nonrectilinear problem is especially difficult because it is kinematically complex, and so unlike the classical dynamic stall problems that naturally emanate from steady airfoil aerodynamics. Here we therefore concentrate on the latter. Of particular interest is the establishment of common problems, abstracted and phrased to be of general interest, to benchmark the various methods and to suggest points of departure for parameter studies. If we are going to build motion rigs, what kinematic properties should they possess? The question is informed by pursuit of canonical problems.

2.2. Canonical Problems

A large portion of the subject work in the past 7 years, often led by the PI, has been the suggestion, delineation and promulgation of "canonical problems" in steady and unsteady aerodynamics at low speed. By "canonical problems" one means abstracted test cases of general appeal, with clear parameter definitions, which are to be studied by several computational and experimental efforts, by different research groups working towards a common reporting goal. Objectives include: (1) cross-validation of the various methods, (2) baselining the state of the art, (3) engendering interest in the subject amongst researchers with affinity towards this area but otherwise lack of connection to the specific subject, (4) establishment of a known test case for archival reference, and (5) providing a point of departure for individual researchers to run parameter studies. The idea is that once a common baseline is achieved, the subsequent parameter studies have better contextual motivation and are on firmer ground because the "correct" answer was found for the canonical case. Examples of such canonical problems in the past 7 years have been:

- Airfoil laminar separation bubbles (LSBs) under NATO RTO Task Group AVT-101
- Various unsteady aerodynamics problems under NATO RTO Task Group AVT-149
- Pitch ramp-hold-return maneuvers proposed in the AIAA Fluid Dynamics Technical Committee's "Low Reynolds Number Aerodynamics Discussion Group"
- High-frequency low-amplitude airfoil pitch and plunge sinusoidal periodic motions, studied by the PI and a range of academic collaborators.

These are each documented throughout the report. The evolving theme is pursuit of experimental-computational agreement as basis of commencing future parameter studies. Therefore, the present focus is less on exposition of physical trends, than one establishment of the assertion that our various tools are adequate for quantitative study of such trends.

3. The Water Tunnel as a Research Tool in Low-Speed Aerodynamics

Aeronautical engineering, or at least external aerodynamics, is concerned with the flow of gasses, not liquids. Some motivation for the use of experimentation in water is therefore incumbent. Here we describe the philosophical underpinnings of water tunnel experiments for low-speed aerodynamics, and then describe Air Force Research Lab, Air Vehicles Directorate (AFRL/RB) water tunnel.

3.1. The Case for Water Tunnels for Low-Speed Aerodynamic Research

3.1.1. Introductory Remarks

In all of experimental science there is a tension between small/cheap/simple/readily-accessible experimental apparatus on the one hand, and elaborate/detailed/complex/expensive apparatus on the other hand. It is specious to claim that the one is better than the other, as each enjoys its proper place in the spectrum from exploratory investigation of fundamentals to detailed engineering design. But it is possible to devise a metric of return on effort, or value for money. By such metric one can find very favorable result from water tunnels.

Water tunnels definitely belong to the first category in experimental aerodynamics, as almost universally they are of scale and scheme commensurate with what one finds in university labs, rather than showpieces of government or industry installations. They can generally be operated and maintained by 1-2 engineers with no special proficiency in machine operation, electronics and the like, beyond general familiarity with fluid mechanics measurements. Environmental impact and electrical power requirements are small (power use is rarely > 50 KW), safety concerns are minimal (and generally overwhelmed by concerns for constituent equipment, such as lasers, rather than the facility itself), and facility availability is essentially continuous. There are complications in dealing with water – corrosion, leaks, requirements for water filtering and so forth; but these remain in-scope for small facilities in general. In some situations water tunnels compare favorably with similarly-sized wind tunnels. In others, chiefly where Reynolds number scaling is important, water tunnels compare unfavorably.

Water tunnels, like any facility, are not a panacea for low-cost solutions to complex engineering problems. Their key strengths in recent years have been twofold:

- The explosive growth in laser-based distributed flowfield-diagnostic methods provides a ready and powerful means of comparison with the equally fast-growing power of computational fluid dynamics. Most such methods are easier to apply in water than in air.
- The high density and low dynamic viscosity of water can potentially greatly simplify measurements in unsteady aerodynamics and in dynamic testing of aeronautical configurations and abstracted shapes such as airfoils.

But water tunnel testing is subject to severe limitations, principally due to unavoidably low Reynolds numbers and strictly incompressible flow. The true promise of water tunnels can best be fulfilled when water tunnel users work together with the CFD community and the large-wind-tunnel community, for example in the areas of CFD validation and development of test matrices for large Test and Evaluation wind tunnels.

3.1.2. Reynolds Number Effects

The first impediment in usefulness of water tunnels for aerodynamic applications is from Reynolds number scaling. Chord-based Reynolds numbers for airfoils, wings and aircraft models are typically limited in water tunnels to an upper-bound of 100,000. For whole-airplane configurations, Re based on mean aerodynamic chord can be limited to 10,000 for the smaller water tunnels. For airfoil performance, and therefore airplane performance measurements even at the conceptual-design level, this

is a devastating and likely unacceptable flaw, since below Re = 100,000 most airfoils evince large laminar separations wholly unrepresentative of flight conditions or even large wind tunnel conditions, and at Re ~ 10,000 all airfoils operate in separated flow at all angles of attack. For Re ~ 50,000 – 250,000, Reynolds numbers will be subcritical, and laminar separation bubbles will either be very large or will be "open", resulting in the airfoil be having something like a bluff body. This to some extent depends on the smoothness of the airfoil surface; "rough" airfoils are less Re-sensitive; refer to the classic airfoil performance cartoon by Horten[4] (Figure 1), which compares airfoil maximum lift to drag ratio across the Re range, down to the range for insects. Drastic fall of maximum L/D is concurrent with large, open separations.

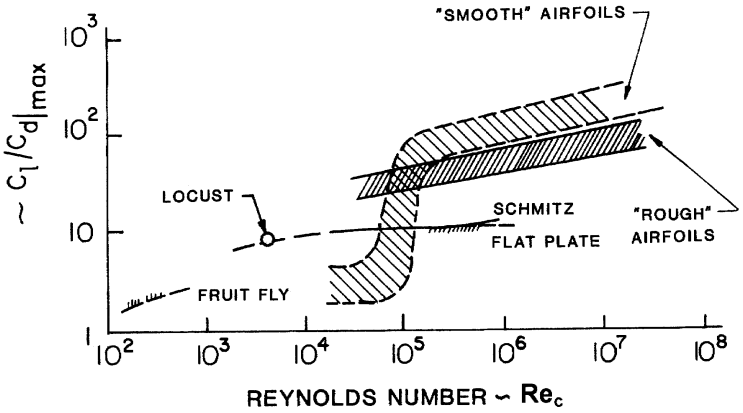

Figure 1. Notional estimate of airfoil performance vs. Re. From Horten, as reported by Mueller.[4]

A more quantitative rendition of prototypical decline in airfoil performance is given in Figure 2, which shows what happens to airfoil drag polars in going from Re = 500K down to 60K. While C_{Do} doubles in going from Re = 200K to 500K, and certainly this is a problem for performance-type of aerodynamic testing, the far greater problem is the explosive growth in drag in going below Re = 200K.

Thus we have a qualitative, and not just a quantitative disparity between water tunnel test condition and flight (or large wind tunnel). There are other problems besides decline of airfoil performance at low-Re. Control surface performance will be anomalous, so for example for a classical airplane configuration the Cm_delta_e will be wrong. The stall dynamics will also be quite different. Wind tunnels of similar size (say, test section diameter of order 0.5m) have an advantage of ~5X increase in airfoil sectional Re, which is enough to exceed the critical Re and therefore to at least qualitatively match the flight-like scenario, at least for angles of attack below stall. Referring to Figure 2, the small wind tunnel will still give a palpably overestimated CDo, but should at least qualitatively capture the "correct" gross flowfield – whereas the water tunnel may not. Of course, for laminar-flow airfoils all of these conclusions must be attenuated, and the better approach for performance testing would be to avoid small tunnels entirely, be they wind or water.

The second disadvantage of water tunnels is the conductivity and corrosive property of water. This makes strain gauge force balance design quite troublesome, as gauges need to be waterproofed. The waterproofing courts the possibility of balance fouling, and in any case is never robust. Optical methods, such as fiber-Bragg load cells, are a promising alternative to conventional strain gauge balances, albeit immature at this stage. Corrosion, meanwhile, implies that models must be made from stainless steel or water-resistant plastics. The latter shows good potential from the viewpoint of rapid prototyping and 3D printing – of which more below.

Thirdly, because at all practical test speeds water is incompressible, those aeronautical applications where compressibility is important, such as shock-boundary layer interactions, will fail in water tunnel testing. But this point is generally obvious and is unlikely to cause error in practice.

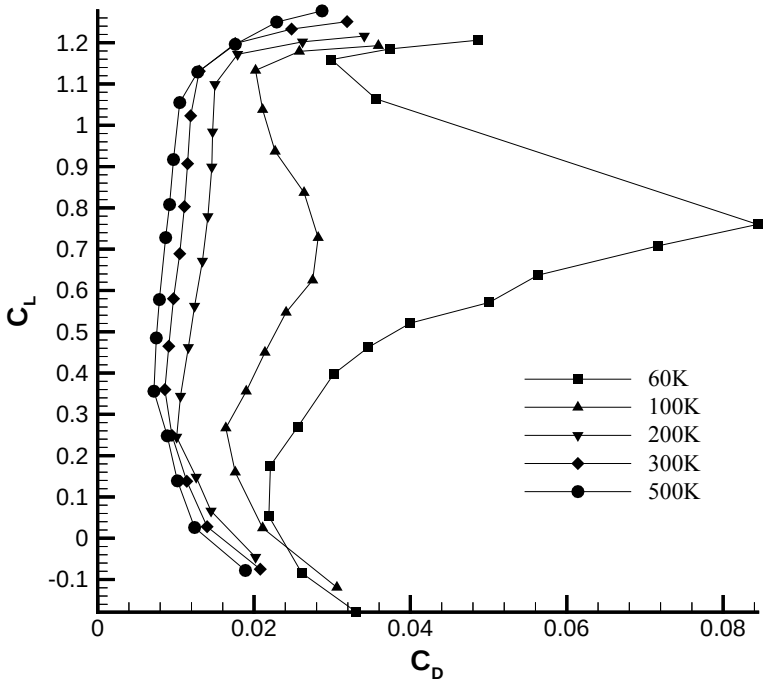

Figure 2. Eppler E387 airfoil drag polar, Re = 60K to 500K, collected from wind tunnel data at the University of Illinois, Urbana-Champaign.[71]

It would therefore be foolish to employ a water tunnel for airplane performance testing, for data such as lift curve slope, stall angle, elevator control power, trim angle of attack range, CDo, and so forth, even at the conceptual design level. Instead, given the modern state of things, one should do potential-flow computations with viscous corrections (such as XFOIL), and if necessary run RANS computations for C Do a nd s tall b ehavior. One w ould appeal t o e xperiment in water tunnels either u pon f inding anomalies o r am biguities in t he c omputations, o r i n doing f undamental r esearch pr ior t o i nvestigating applications to airplanes. And water tunnels could be used as "pilot" facilities to guide test planning in larger wind tunnels, later in the design cycle.

Broadly, water tunnels are a powerful tool for basic discoveries in fluid mechanics; problems of bluff bodies, jets/wakes/shear layers, cavities, oscillating bodies and plates, boundary layers and so forth. Where R eynolds num ber is m atched be tween w ind t unnel a nd w ater tunnel, w ater t unnels pe rform admirably; an example is laminar separation bubble and boundary layer transition experiments on a Selig SD7003 airfoil, where water tunnel, wind tunnel and tow tank produced similar results[42]. Water tunnels do have particular strengths in some practical aeronautical engineering applications even at the detailed-design level. These are principally those cases where the full-scale Reynolds number is itself low or is otherwise unimportant. For the former, two examples are some cases in turbine blades, and the emerging area o f Mi cro A ir Vehicles. F or the l atter, s harp-edged sw ept w ings a re p erhaps the m ost ce lebrated example, though not without controversy. Dynamic stall is another example.

A simple but convincing steady-aerodynamics example is water tunnel testing of an aspect ratio = 2 t hin rectangular flat p late[43], w hich i s de scribed in further de tail in i ts ow n section o f t his R eport. Between the low aspect ratio and the "sharp" leading edge, Re-effects are attenuated to the point where the measured lift coefficient comports very well with classical *inviscid* theory. Further, lift coefficient from direct m easurement via a f orce balance compares well with lift derived f rom Kutta-Joukowski treatment of the tip-vortex circulation in the Trefftz plane, obtained from particle image velocimetry. The three-way comparison with theory holds well, up to stall. This implies that the term "Reynolds number insensitive" is neither a t rite platitude nor a r are exception in flows of interest in applied aerodynamics. But certainly one must use caution!

It should also be noted that in any small-scale facility, water or air, the small size of models will result in inferior manufacturing tolerances and inability to capture configuration features in detail. For detail-sensitive flowfields, such as separation from some aircraft and missile forebodies, the loss of geometric fidelity incurred with small models may have profound impact on the resulting flowfield, possibly leading to erroneous conclusions. It is therefore crucial to approach water tunnel methods in consultation between tunnel practitioners and the airplane design community, and not to schedule the water test campaign as an ancillary process to be fitted-in ad hoc.

3.1.3. Laser-Based Distributed Flowfield-Diagnostic Methods

For all of water tunnels' disadvantages vs. wind tunnels for aerodynamic testing, water tunnels merit vociferous vindication whenever the research objective is obtaining flowfield data, rather than integrated force/moment on the model. Particle Image velocimetry, or PIV, is today's principle experimental technique for obtaining time-resolved, distributed flowfield velocity data[44]. PIV is considerably easier in water (and in liquids in general) than in air. Water's large density makes distribution and suspension of PIV tracer particles much easier than in air, whereby seeding density is improved, and concomitantly PIV data quality. Particles in water are much more likely to follow the local flow trajectory, especially in high-gradient locales such as vortex cores, than would be the case in wind tunnels. Thus, one occasionally finds PIV wind tunnel data with voids of no-data inside vortex cores, whereas such is demonstrably not the case for water tunnels. Thus one has to carefully weigh the disadvantages of Re-scaling in water tunnels vs. the advantages in PIV.

3.1.4. Rapid Prototyping of Water Tunnel Models

The cost and time savings of water tunnels can only be realized if every test component is inexpensive, including the model. Wood or aluminum models are common in small wind tunnels, but create problems in water due to absorption of water, oxidation, and deterioration of surface finish, which result in flaws in outer mold lines and therefore unreliable aerodynamic results. Sometimes these are no great problem for short tests (< 1 day of total immersion time), but the culture of small water tunnel testing generally implies that a model is installed and the researcher revisits the experiment sporadically, at his/her leisure, rather than undertaking a time-constrained concerted test campaign of short duration, as is generally necessary in large facilities. Thus, durable models are imperative. The alternative – stainless steel – is expensive to machine. A better alternative is rapid prototyping of plastic models. As of this writing (2008), for $200K USD one can obtain a "3D printer" capable of 0.0006" build-layer (0.15mm), in a build volume of 12" cubed. Assuming a good 3D input file, the cost per model is <<$1000 USD, and involving perhaps one man-day of setup and post-finishing. And a "good" 3D input file is identical to the input file for a viscous-CFD 3D mesh. Thus, one obtains the former for free, upon building the latter. Of course, the same sort of model is suitable for a small wind tunnel as well as a small water tunnel, provided that the dynamic pressures are not too high.

3.1.5. Dynamic Testing

"Dynamic testing" is a broad and amorphous term, connoting motion of the test article with respect to the lab-frame of reference. A detailed list of dynamic-testing subtopics may be:

1. Standard measurement of dynamic stability derivatives for relatively conventional airplanes in assumed linear conditions. These are typically the roll, pitch and yaw damping derivatives, measured by forced sinusoidal oscillation about a trim point. The application would be building the flight dynamic model and control laws.
2. Spin-tests and other forced or free oscillations, where the objective is to assess departure-characteristics of the airplane, presumably in conditions peripheral to the normal performance envelope, but important for safety certification.
3. High-alpha/high-rate tests, where one is interested in helicopter blade dynamic stall, or maneuvers for aerobatic/combat aircraft. Large flow separations and concomitant nonlinearities

are expected. Here one is interested in both the 6DOF aerodynamic loads and flowfield measurements to elucidate the causes behind those loads. This area also includes (a) leading edge vortices of sharp-edged highly-swept configurations, and (b) the vortical structures emanating from missiles, forebodies and after-bodies at high angle of attack.

4. Aeroelastic tests, where an intentionally flexible model undergoes measurable time-dependent deflections, and may be tested to destruction, to ascertain flutter limits and other fluid-structure interaction problems. Problems include safeguarding the tunnel from damage by model debris, and time-resolved measurements of structure and flowfield.
5. Micro Air Vehicles (MAVs) and related small UAVs, which are capable of violent maneuvers and are expected to encounter strong wind gusts, relative to their flight speed. This includes flapping-wing MAVs, which always operate in an unsteady flowfield. For this application there is little distinction between basic research and engineering testing.
6. Store-separation tests, such as with a captive-trajectory system, involving relative motion of two or more bodies. Typical problems are at high flight speeds, involving compressibility.
7. Wind-engineering tests, including fixed ground structures, ground-vehicles, aircraft in landing scenarios, etc., where a high-turbulence environment is simulated together with ground-effect.
8. Gust tests, where the tunnel is shuttered or otherwise the free-stream is modified from steady, to assess aircraft response to transient flowfield conditions.
9. Free-flight tests, where the aircraft is tethered or completely free, and is "flown" in the tunnel test section, thus combining testing of aerodynamics and flight dynamics.

The advantage of water tunnels in dynamic testing is that for a given reduced frequency of motion (scaled by model length scale and tunnel free-stream velocity) the physical rate of motion is much smaller in water than in air. This makes data acquisition much easier. Dynamic tares to remove the model inertial forces, are either very easy or sometimes completely unnecessary, in contradistinction to wind tunnel testing, where dynamic tares are difficult and the inertial load dominates the total measured load[48]. Flow visualization is made easier by the slower physical rates of motion. Mechanism design and model construction are much easier, since models can be heavier and internal loads in the forced-oscillation rig will be much lower.

However, some dynamic tests are either impossible or very difficult in water. (6) Is beyond to scope of water tunnels whenever compressibility is important, such as in cavity acoustics. (9) Is not amenable to water tunnels because of the tunnels' small size, and because of the difficulty of propelling a "flight" article in water (the exception is flapping-wing MAVs). Froude scaling, necessary for free-flight tests, becomes problematic because of the density of water. (2) Is in principle possible, but again is awkward because of water tunnels' small size and Froude scaling. This is best done in an open-jet wind tunnel.

(4) Aeroelastic scaling is both problematic and promising in water tunnels. It is problematic because it is impossible to match the density ratio between the model material and water. Any test requiring high model surface fidelity is unlikely to be successful, for the same reasons as for static problems. And the aforementioned problems with force balances also hold for dynamic tests, though again the low motion rates in water offer much advantage. However, the mechanics of aeroelastic testing in water are easier because broken models are easily contained before parts go downstream to potential damage the pump – a huge concern in wind tunnel testing. And the slow rates make recording of model vibration easier.

(7) Is usually reserved for large wind tunnels, owing to a need for proper separation of lengths scales of the desired ambient turbulence environment, and the need for relatively large models with fine structure. The chief obstacle in running such tests in water tunnels is difficulty in obtaining the "right" turbulence environment. This raises the larger question, of how does one characterize water tunnel test section flow quality. It is not a trivial topic, since hot wires and Pitot tubes perform marginally in water, requiring alternative or at least improved techniques.

(8) Shuttering a wind tunnel is a convenient means of producing well-defined gusts[45], for gust-response testing, and for producing disturbances in general, for system identification tests. Shuttering a water tunnel is difficult because of the density of water, the resulting pressures (waterhammer), and risk of spillage. However, for the same reason that high-rate testing in water tunnels is straightforward, impulsive-start testing, such as to validate classical models such as Wagner's, is readily possible in water tunnels, but very difficult in wind tunnels. One example is use of a piston-driven water tunnel, producing very rapid acceleration of the free-stream, for studying impulsive-start problems for airfoils at high angle of attack[46]. Such an experiment is impossible wind tunnels. For water tunnels with a long test section, such as the US AFRL water tunnel, it is possible to run the tunnel as a tow tank, with the model carriage translated on rails in the free-stream direction, modeling a "gust" by moving the model, or modeling impulsive-start by violent acceleration. It should in principle be possible to run close approximations to indicial motions, thus explicitly constructing the indicial response integral[47], opening new vistas in massively-unsteady aerodynamics. But this is a niche area, of interest at present primarily to just MAVs.

(1) Is the main-line dynamic test in aeronautical engineering. Its outlook for swept-wing configurations in water tunnels is discussed by Kramer[48], who points out remarkable similarity in dynamic-derivative data between water tunnels, wind tunnels and flight test, but also notes the ease of obtaining such data in water tunnels. It remains however to systematically assess the outlook for low-sweep configurations lacking sharp leading edges, such as transport aircraft. Again the crux of the problem is Re-scaling. The authors would like to refrain from definitive recommendations, pending a systematic comparison between wind tunnel and water tunnel tests on a common configuration.

Water tunnels perform brilliantly for items (3) and (5): for high-rate testing, especially for MAVs, where it is essentially impossible to produce the requisite motion dynamics in air, but straightforward to do so in water. This is the overarching justification for our research.

3.1.6. Example: Forced Airfoil Oscillation in Pure Plunge

The test case is sinusoidal pure-plunge of a Selig SD7003 airfoil, and Reynolds number 40,000 based on airfoil chord and free-stream flow speed (~26 cm/s). The reduced frequency is the very high value of 3.93, but the physical frequency is only 0.54 Hz! The reduced amplitude of plunge oscillation is 0.05. Because the motion is periodic, we are interested in phase-averages of the flowfield response. In Figure 3, the top row of vorticity contours is taken at the phase of motion corresponding to the top of the plunge stroke; the second row is at halfway down the plunge stroke, where motion-induced angle of attack is maximum positive; the third row is at the bottom of the plunge stroke; and the four and final row is at halfway back up the plunge stroke, where motion-induced angle of attack is maximum negative. Experiment (particle image velocimetry) is compared with two different computations. Apart from dissipative effects in the computation, the mutual comparison is striking. This sort of experiment is crucial for flapping-wing micro air vehicles – and essentially impossible in wind tunnels, where the required high physical frequency of motion would likely destroy the motion rig, or at least make the data acquisition very problematic.

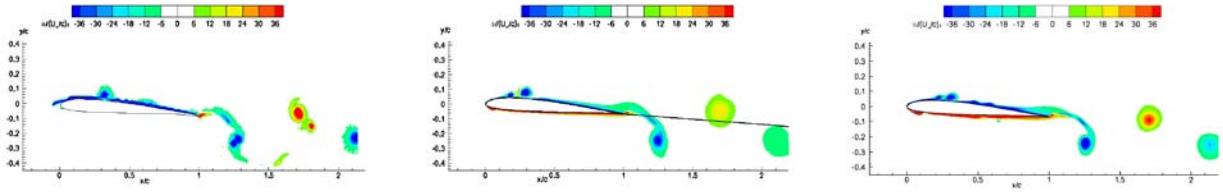

Exp, φ=0 CFL3D, φ=0 IB, φ=0

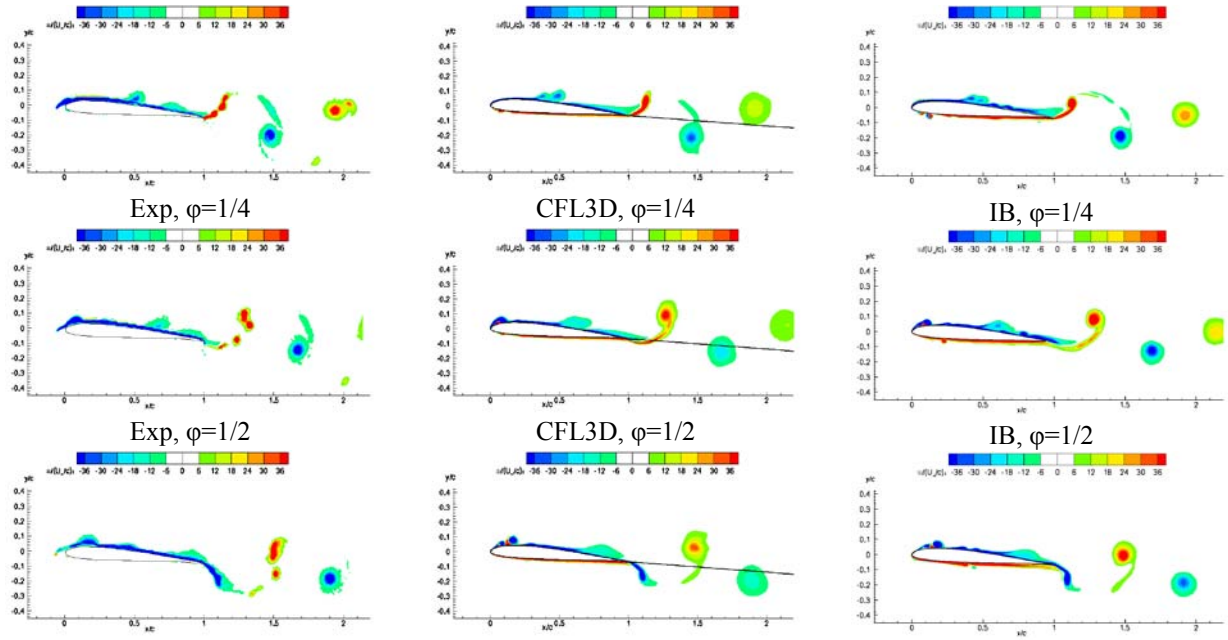

Figure 3. Comparison of out-of-plane vorticity contours from experiment in the water tunnel (left column), 2D computation using the commercial code CFL3D, and 2D immersed boundary-method computation, at various phases of motion; Re=40,000, SD7003 airfoil pure-plunge.

As Micro Air Vehicle applications emerge from a niche area into more regular aeronautical engineering practice, the relevance and importance of water tunnels promises to increase. The one word of caution is regarding aeroelastic scaling; most MAV configurations are structurally flexible, and structural scaling in water can be problematic. Rigid abstract shapes – airfoils, plates and the like, undergoing high-rate motions – are easiest to test in water tunnels. Full configurations are harder – which is precisely the same scenario as for static testing.

3.1.7. Example: Particle Image Velocimetry for a UCAV Configuration

Here the motivation was to conduct flowfield velocimetry to understand the fluid mechanics behind force/moment/surface-pressure results obtained in a high-quality test entry in a large industrial-type wind tunnel[49]. PIV was not possible for this test, because of complexity of seeding, of laser power required for such large scales, required alternations to model surface finish (to minimize laser reflection), and of the intractable burdens of equipment setup and data reduction. Pressure-tap data just aft of the wing leading edge on the suction side showed loss of LE-suction at outboard stations of the wing, at angles of attack commensurate with the so-called "pitch break". Was this due to tip stall, or to formation of LEVs at the model apex or wing/body "juncture"? The hypothesis is that the wingtips stall, losing loading, resulting in a nose-up pitching moment due to sweepback. To verify or to refute this, we need knowledge on whether the wingtips indeed stall at the pitch-break angle of attack, while further inboard the flow remains attached. This requires flowfield information, and was pursued in a water tunnel experiment on a 12"-span 3D-printed model of the 1303 UCAV configuration in a water tunnel (Figure 4)[50]. The model leading edge was "sharp", as far as possible given the manufacturing process.

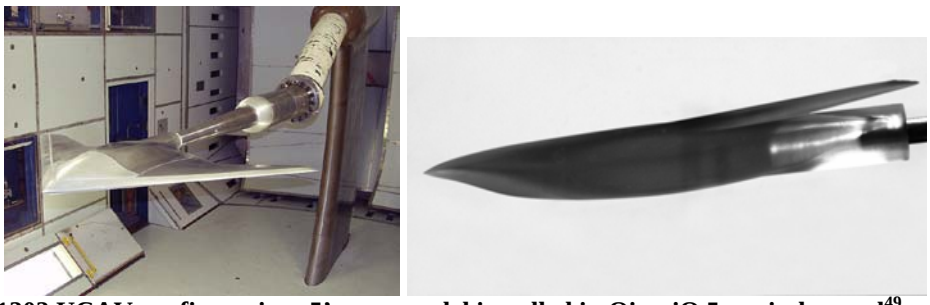

Figure 4. The 1303 UCAV configuration: 5'-span model installed in QinetiQ 5m wind tunnel[49], and 3D-printed (plastic) installed in water tunnel test section[50].

Sectional Re of the 1303 configuration varied from ~10,000 to 32,000, depending on spanwise station. This is clearly in the regime of large flow separations. If fully attached flow is not possible at any angle of attack, then how could one possibly reach conclusion on presence or absence of tip stall, and regarding stall at the tips vs. further inboard? The answer lies in making reasoned qualitative distinction between a large but *closed* separation, and an *open* separation. This is seen from comparison of Reynolds Stress contours, u'v'. For a closed separation, even where the closure occurs in the near-wake, the u'v' distribution will be a characteristic "lobe" pattern just downstream of the trailing edge, with lobes of opposite sign. This is what one sees at the 30% semispan spanwise station at the pitch-break angle of attack, $\alpha = 6^{\circ}$. In fact here the u'v' contour is characteristic of a usual airfoil laminar separation bubble, terminating with free shear-layer transition and reattachment just ahead of the trailing edge. At the 90% semispan spanwise station, at $\alpha = 6^{\circ}$ the flow is in contrast seen to be fully separated, with an open separation. But at $\alpha = 4^{\circ}$ at the same location, one sees a closed separation, evinced by the u'v' double-lobes. This is convincing evidence that the wingtips undergo stall between $\alpha = 4^{\circ}$ and $\alpha = 6^{\circ}$, while further inboard the flow remains attached. Similar results (not shown here) suggest the absence of a discernable LEV structure, whence we conclude that the pitch-break is due to loss of lift outboard on this highly-tapered cranked-wing configuration, and that a vortex-related process is not a primary cause. Thus, despite the huge disparity in Reynolds number between wind tunnel and water tunnel, the latter gives good qualitative explanation for flowfield phenomena speculated but not measured in the former.

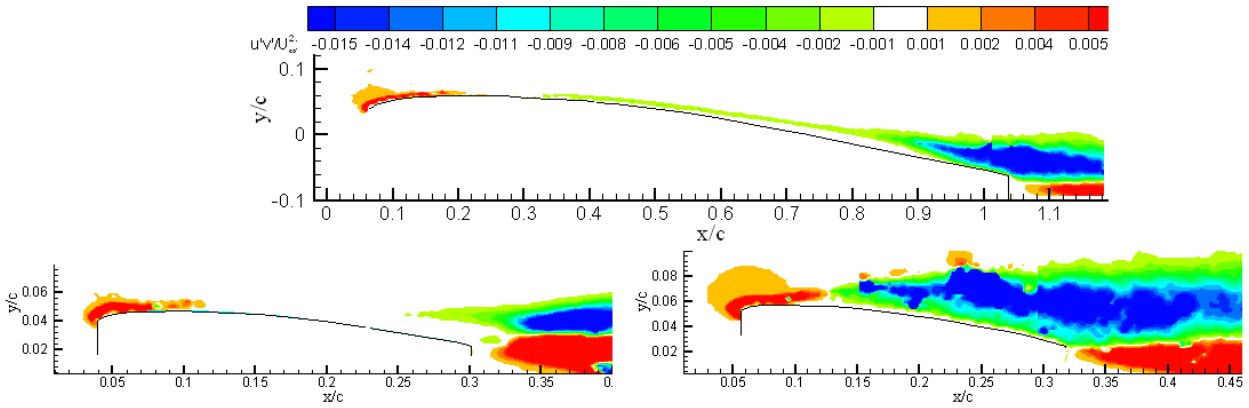

Figure 5. 1303 UCAV water tunnel PIV, contours of Reynolds stress u'v': 30% semispan, $\alpha = 6^{\circ}$ (top); 30% semispan, $\alpha = 4^{\circ}$ (bottom-left); and 30% semispan, $\alpha = 6^{\circ}$ (bottom-right).

3.1.8. Summarizing the Case for Water Tunnels

Water tunnels will not obviate large-scale, high-precision industrial-type testing, and are at most marginally useful for producing reliable results in configuration aerodynamics, even in the conceptual design stage. For conventional aircraft configuration testing, such as drag polar measurement, they

compare unfavorably to similar-sized wind tunnels, because the latter produce much larger operating Reynolds numbers at the same model scale. Water tunnels are more of a fundamental research tool than an applied aerodynamics tool. However, they are eminently useful as part of a larger solution space, by focusing the test matrix in large wind tunnels and providing validation for CFD. This is especially true when equipped with modern optical flowfield velocimetry techniques, such as PIV, which is much easier to implement in water tunnels than in wind tunnels.

In problems insensitive to Reynolds number, or where Reynolds number between the application and the water tunnel test article are closely matched, water tunnels should be regarded as the principal tool of experimental aerodynamics. Examples include Micro Air Vehicles, very high-rate dynamic testing, and high-sweep sharp-edge configurations.

Dynamic testing has been suggested as an application particularly amenable to water tunnel testing, because of the favorable scaling of physical motion frequencies in liquid flows. While this is broadly true, the conclusion must be qualified by the kind of dynamic testing that one has in mind. For high-rate and/or high angle of attack problems, the utility of water tunnels is demonstrably obvious. But for conventional dynamic-derivative measurements for airplane configurations, we recommend withholding judgment until a definitive test is conducted. This would be a common experiment in a water tunnel and a large wind tunnel, running the same configuration at the same rates and the same motion kinematics.

The focus of the subject work is Micro Air Vehicles, whence the advantages of water tunnels are palpably evident. This has been the motivation for AFRL/RB's Horizontal Free-surface Water Tunnel, built in 2002 and described in the following section.

3.2. AFRL/RB's "Horizontal Free-surface Water Tunnel" (HFWT)

Here we outline the evolution of the principal facilities in which the subject research was conducted. This includes construction of the water tunnel and synopsis of its operations, and resume of diagnostics tools available in the HFWT.

3.2.1. The HFWT's Origin and Installation History

The HFWT was originally based on the "Student Water Channel" at the California Institute of Technology (Caltech). The tunnel was rebuilt in 1997 at Caltech by the PI, as part of his Ph.D. research. The 1997-2001 installation is shown in Figure 6. This entailed removing the test section from the Student Water Channel, and mating it with new semi-custom fiberglass intake and exit plena. The exit plenum is essentially a rectangular box that accept outflow from the test section, turns it with vertical and horizontal vanes, and dumps it into a holding vessel, which connects to a 8"-diameter schedule-40 PVC return pipe. The intake plenum is rather akin to a wind tunnel contraction. The contraction ratio is about 4:1 (small for wind tunnels, but typical for water tunnels). The entry to the intake plenum is a vertical perforated 8"-diameter PVC pipe, designed to ensure vertical uniformity of inflow speed. The uneven and turbulent jet efflux then goes through a series of perforated plates, followed by two screen-honeycomb combinations and a final screen, before entering the contraction section. Driving the whole circuit is a 12" single-stage axial-flow impeller. The design and shakedown of the tunnel are covered in detail by Ol[51].

In 2001-2002, the tunnel was moved to AFRL and rebuilt in Building 24C, in the AFRL/RB facilities complex. Installation and shakedown of the HFWT were the first portion of the presently-reported research.

In the AFRL rebuild, the HFWT's recirculation circuit was revised, and the drive pump was switched from vertical to horizontal installation. Otherwise the setup was largely a reproduction of that at Caltech. A schematic of the rebuild is given in Figure 7, while a chronology of the installation of the HFWT in Building 24C, from site preparation to tunnel operational condition, is given in Figure 8.

Figure 6. The HFWT installed at Caltech, as originally built by the PI (1997).

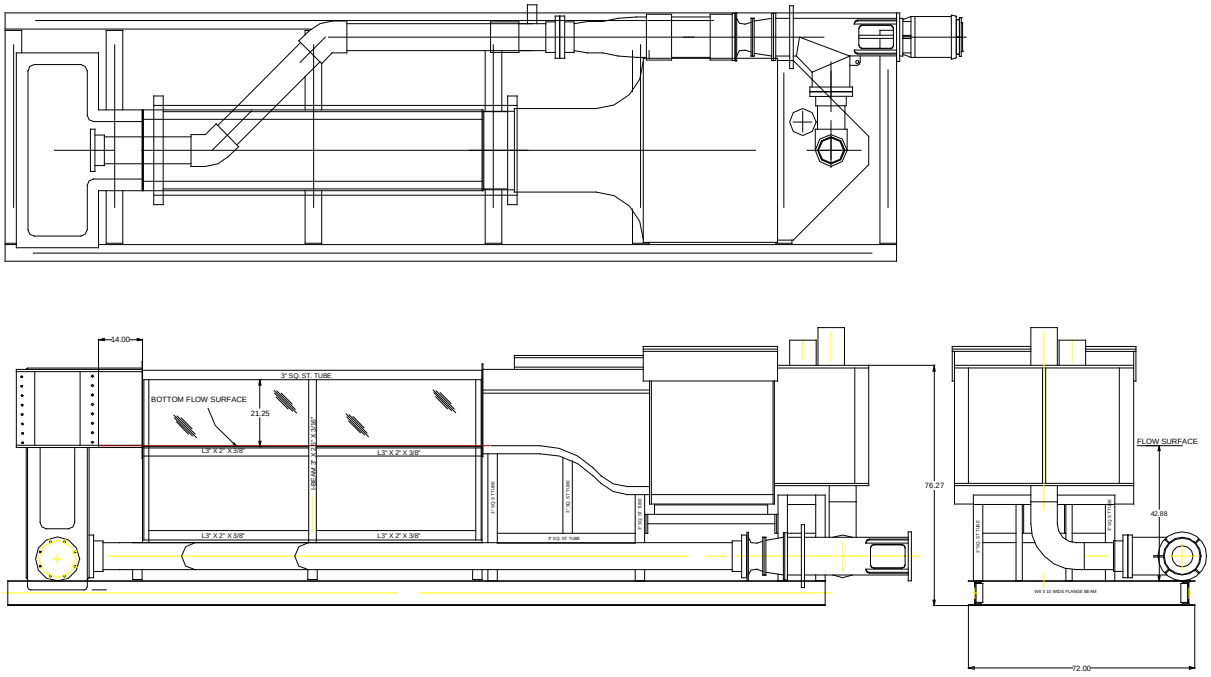

Figure 7. Schematic of the HFWT as installed in Building 24C, Wright-Patterson.

A key feature of the present installation is the placement of the entire tunnel on a steel I-beam frame, which can be elevated and placed on rollers for moving. This feature was deemed useful in 2001, when it was surmised that Building 24C would undergo comprehensive renovation. While this has not happened, the steel frame has arguably been useful for vibration isolation.

Figure 8. HFWT installation history: site preparation, including excavation for sewer drain (top left); mockup of main components on support frame, without connecting plumbing and test section glass walls (top right), and tunnel operational (above).

3.2.2. Flow Quality Measurements and Instrumentation Suite of the HFWT

The essential property of any aerodynamics ground test facility is flow quality. One seeks a uniform, low-turbulence flow that is representative of free-flight conditions. Detailed flow characterization is beyond the scope of the present report, but a rendition of instruments and their main results is given herewith.

3.2.2.1. Pitot-Manometer Measurements

The simplest experiment for a new facility is to calibrate bulk flow speed in the test section, with settings for the tunnel controller. Any of a number of flow velocimetry schemes is possible, including of course particle image velocimetry (PIV). But partly out of cultural deference, and before PIV was available in the HFWT, an experiment was run with a conventional inclined manometer and Pitot-static tube, with the dynamic and static lines of the Pitot tube connected to opposite ends of the manometer. For manometers in a water tunnel, one of course can not use water as the manometer working fluid. Instead, a special oil immiscible with water, with specific gravity 1.7, was used. At the low head differences in HFWT operational speeds, care is required to measure manometer variations, whence signal to noise ratio is not high. Further, care is required to purge the manometer of bubbles, lest the readings in head difference be grossly inaccurate. The final results were cross-checked by an even cruder method: injection of a clump of dye into the test section, and timing its convection over a known run length, say 2

meters. A summary of results for flow speed vs. controller setting (from a low of around 3.5 to a high of 60; controller setting times 30 = pump RPM) is given in Figure 9.

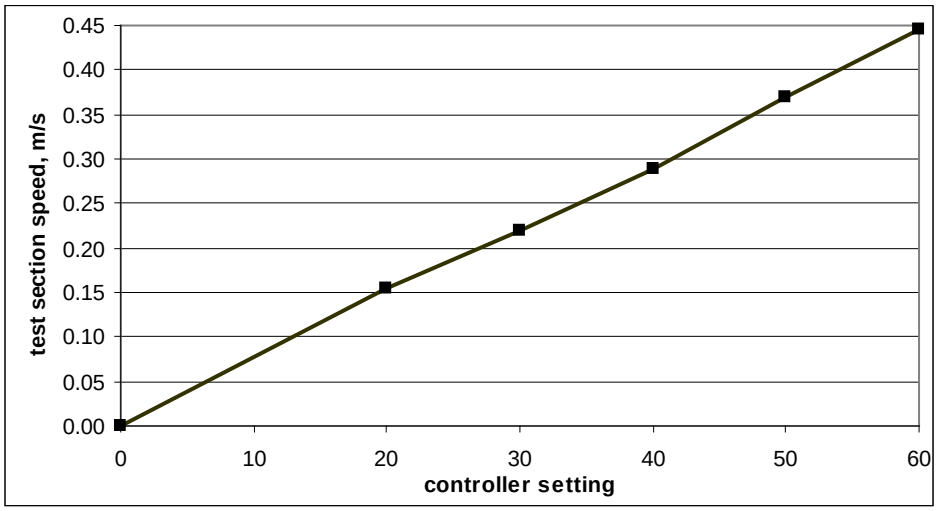

Figure 9. Pitot-manometer-derived HFWT calibration curve; test section free-stream speed vs. pump controller setting.

3.2.2.2. Hot Film Measurements

Knowing the bulk free-stream flow speed in the test section, the next measurement of interest is flow quality: spatial flow uniformity (quality of mean velocity profile), angularity (presence of parasitic vertical and lateral velocity components), slow temporal variation (sloshing, thermal gradients), medium-speed temporal and spatial variations (secondary flow due to the contraction section and corners of the test section) and fast temporal variation ("turbulence"). By way of context, specifications for a competing water tunnel design of 24"x36" test section, from Rolling Hills Research Corporation[52], the principal provider of research-grade water tunnels today, are listed as: <0.1% RMS turbulence intensity, < ±2% velocity uniformity, and < ±1° mean flow angularity. The HFWT aims to exceed these standards. In practice, one is often only concerned with velocity profile uniformity and the free-stream component of temporal variations, or "turbulence intensity". Both quantities can be measured by a hot wire or hot film, at least in principle. Figure 10 shows a single-component hot film setup in the HFWT test section[53], mounted to an older rig rendered obsolete by the pitch-plunge rig described elsewhere in this report.

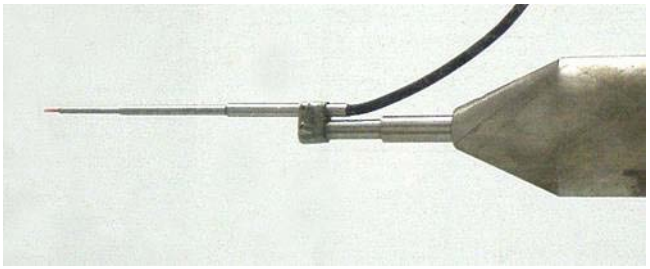

Figure 10. 1-component hot film probe installed in HFWT test section.

We define, in the usual sense, the fluctuating streamwise velocity component as subtraction of the mean from the time-varying signal:

$$u_i^{'} = U(t_i) - \frac{1}{n}\sum_{i=1}^{n} U(t_i)$$

And then the root mean square streamwise velocity component is

$$u'_{rms} = \frac{1}{\sqrt{n}}\left(\sum_{i=1}^{n}(u'_i)^2\right)^{1/2}$$

The turbulence intensity is then the ratio of the RMS streamwise component to the mean.

Unfortunately hot-film experiments were plagued by (1) formation of bubbles at the probe, and (2) drift of the sensor reading in steady conditions[54]. Bubble formation is related but not necessarily caused buy local boiling. It is somewhat improved by using "old" water – that is, not draining/refilling the water for months. Drift, on the other hand, has no solution. It comes from the hot wire operating more like a thermometer than a velocimeter. The reason is the low overheat ratio when operating in water. Roughly, a 3°C temperature difference is comparable to 100% velocity error at typical HFWT operating speeds. Since some fraction of °C variation happens often, not only as a function of time but from place to place in the test section, the resulting drift – even if no bubbles form on the instrument – is unacceptable for spatial surveys with a traverse. The hot wire was however used for a few single-point streamwise-component turbulence measurements, by subtracting the "mean" drifting velocity from the time-trace, instead of the mean-proper. That is, one uses a moving-average with a window much larger than the temporal variations associated with turbulence. Typical results are shown in Figure 11, for nominal tunnel speed of 15 cm/s. The resulting fluctuations equate to a RMS speed of 0.0867 cm/s, or a turbulence intensity of 0.58%.

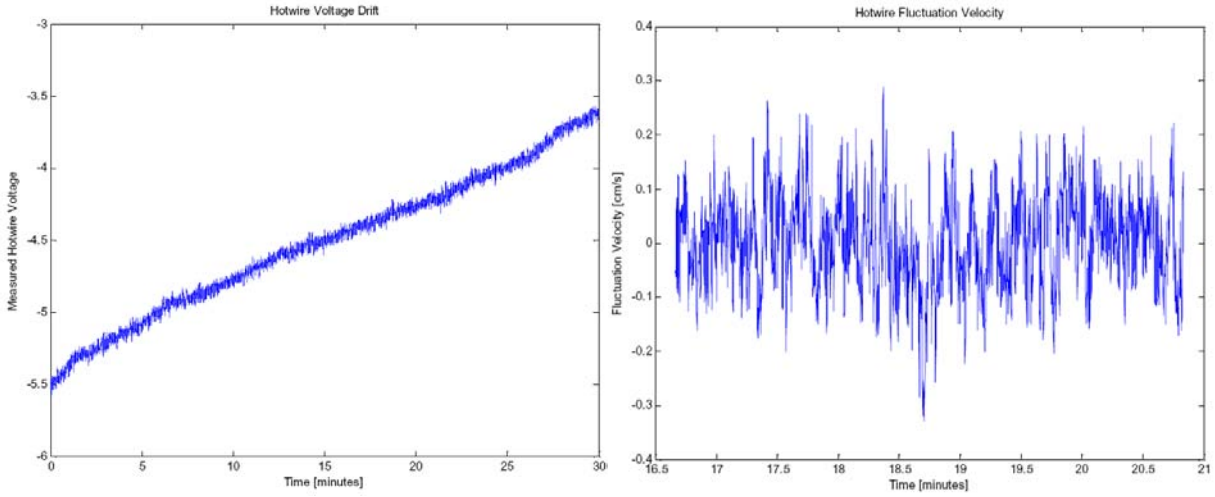

Figure 11. Typical hot wire time-traces, constant mean streamwise velocity of ~15 cm/s; voltage drift with time (left) and fluctuating velocity vs. time, after subtracting moving-average of mean signal.

We briefly note in passing that besides hot film/hot wires, laser Doppler velocimetry is another obvious single-point technique. The HFWT does not have an LDV permanent capability, but a backscatter portable system from Measurement Science Enterprises, Inc[55] was demonstrated, finding a turbulence intensity of 0.4% at flow speeds from 15 through 40 cm/s. But the LDV almost assuredly samples at a lower temporal resolution than the hot wire – and thus the apparently lower turbulence intensity.

3.2.2.3. Free-Stream Flow Quality Measurements by PIV

Particle image velocimetry does not give sufficient temporal resolution for studying temporal statistics of turbulence with the present equipment, where the sampling rate is 15 image pairs per second. But the "ergodic hypothesis" – that turbulence spatially is akin to turbulence temporally – allows use of spatial statistics from PIV to study not only spatial uniformity, but to quote turbulence intensity proper. A given PIV interrogation window is selected, and the velocity values for each shot stored as a string, much

akin to the approach for hot wire velocimetry, but with a much lower temporal frequency content. This gives an RMS velocity and thus a turbulence intensity. One can also plot the spatial variation of turbulence intensity, as it were. But this "turbulence" intensity is limited to the PIV sampling frequency – or more properly, to half of the sampling frequency. The alternative is to step window-by-window across one PIV image, gathering the individual velocity vectors into a string, as if they were temporal records. This is the ergodic hypothesis. Unfortunately one must subtract the spatial variation from the image, in the sense of how the bulk flow, not associated with turbulence proper, varies across the test section. This amounts to a smoothing or low-pass filtering of the PIV image, and subtraction of the result from the original. Care, or artful enterprise, is required in determining how to filter, lest one artificially drive the reported turbulence intensity too low, but subtracting spatial variation (the filtered data) from spatial variation (the unfiltered) and arrive at, well, low spatial variation. Therefore here we revert to the earlier-mentioned approach and merely report the ensemble-variation for one selected PIV window in a sequence of images. Figure 13 plots a time trace for a nominal speed setting of 15 cm/s, where the mean is subtracted from each data point to produce a fluctuating value. This qualitatively recalls the hot wire signal in Figure 11. Calling this a turbulence intensity results in Tu ~ 0.35% - close to the aforementioned LDV-derived value. This is slightly lower than the LDV-derived value, as befits the lower temporal resolution of the PIV. So we are gratified by 3-way consistency between hot wire, LDV and PIV.

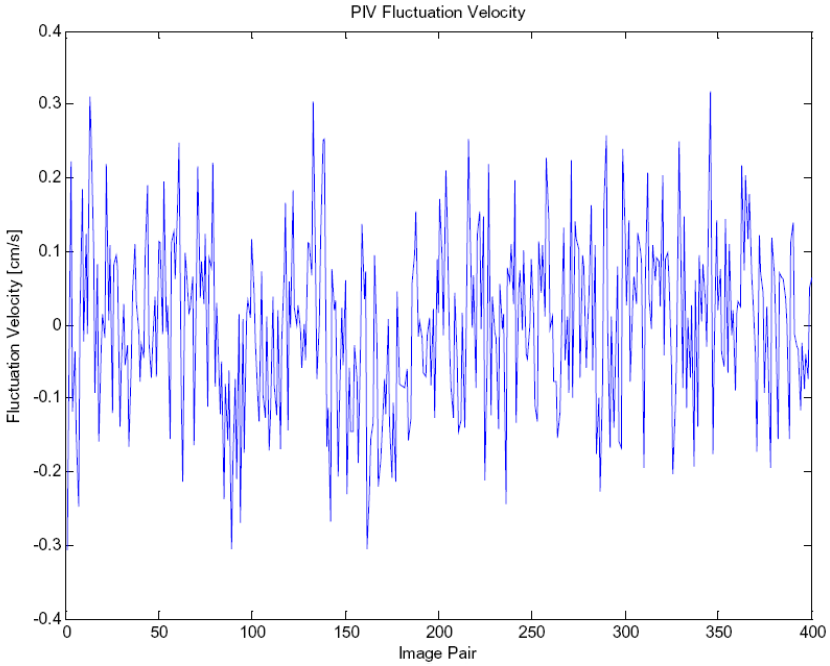

Figure 12. Fluctuating u-component of velocity vs. PIV ensemble point, cm/s; mean is 15 cm/s.

Of course, there is no artifice in using PIV to study spatial variation of mean velocity; a sample result, at nominal setting of 15 cm/s (normalized by this number), is shown in Figure 13, for the u-component.

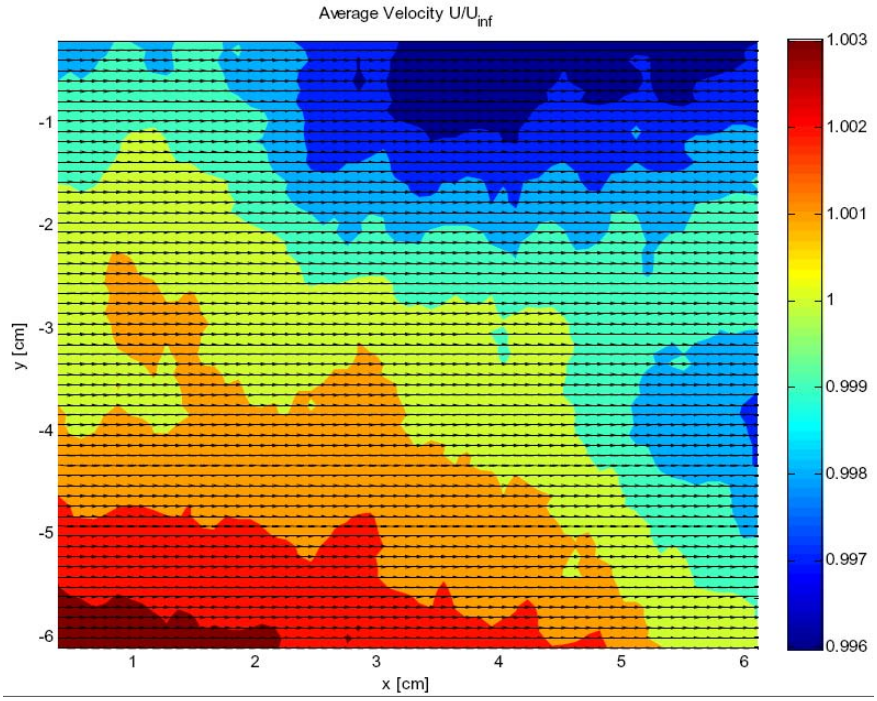

Figure 13. Contour plot of streamwise velocity distribution in the HFWT, over 400 (nominally) shots, using PIV; nominal speed is 15 cm/s, and the PIV light sheet is at the test section centerplane.

3.2.2.4. Surface Skin Friction Measurements

Besides flowfield data (velocity and vorticity) it is desirable to characterize on-surface properties, namely the pressure and skin friction field. This is all the more desirable if one has field data, instead of merely discrete-point data. The pressure field can be integrated to calculate lift, while the skin friction field, not directly useful for performance calculations at low-Re because so much of the drag is pressure-drag, nevertheless gives invaluable insights into time-dependent flow separation. Skin friction and pressure are hard to measure for the usual signal-to-noise reasons; at low speeds, stresses are low, while model supports are generally flimsy, whence vibrations can easily overwhelm the desired measurements, if a displacement-based measurement technique is used.

The proposed approach was a "shear stress sensitive film", or S3F. The details of S3F chemistry, principles of operation, data reduction and limitations are covered by Fonov et al.[56] In brief, a polymer doped with a fluorescent filler is applied to the area of interest, and its surface is sprinkled with tracer particles. Typically the polymer is 0.1mm-1mm thickness, with very large range of possible shear and bulk modulus, depending on the expected range of aerodynamic loads. As the polymer is nearly incompressible, it does not respond to pressure distribution directly, but it does respond to pressure gradient through local changes in thickness. It also responds to shear stress by locally deforming in shear, with a linear distribution of deformation, from zero at the wall to full-range at the outer surface. The thickness change is interrogated as a change in fluorescence, while the shear deflection is interrogated by what amounts to PIV, taking the statistically most likely displacement of a window of surface particles. Thus one compares wind-off and wind-on polymer deformation states, to obtain both pressure and skin friction. There is the issue of crosstalk: a pressure gradient will cause outward shear-like displacement of the polymer away from the point of maximum pressure, while a shear will cause a thickness change too, because the polymer is incompressible. Fonov et al.[56] describe mathematical methods for crosstalk attenuation; essentially, this is a calibration matrix. The result of the shear stress measurements is lines of skin friction, akin to streamlines from PIV.

The challenge of using S3F is to arrive at polymer properties where sensitivity is high, but the flow does not cause waves or other undulations in the polymer. Thickness should be kept as small as possible, in the spirit of non-intrusive diagnostics. Failing that, an indentation can be milled in the body, and filled with the S3F polymer. This produces erroneous readings at the periphery of the indentation, and may materially affect the overall skin friction field, but is the simplest proof-of-concept approach. A candidate flow suited to S3F preliminary measurements is the sharp-edged delta wing, with its concentrated LEVs and resulting well-known skin friction and pressure signatures on the suction side. Accordingly, a delta wing with 50-degree leading edge sweep (reminiscent of the PI's Ph.D. thesis) was instrumented with a S3F patch inside a milled indentation, and the mean skin friction field was measured (Figure 14). The LEV contribution to skin friction is quite clear.

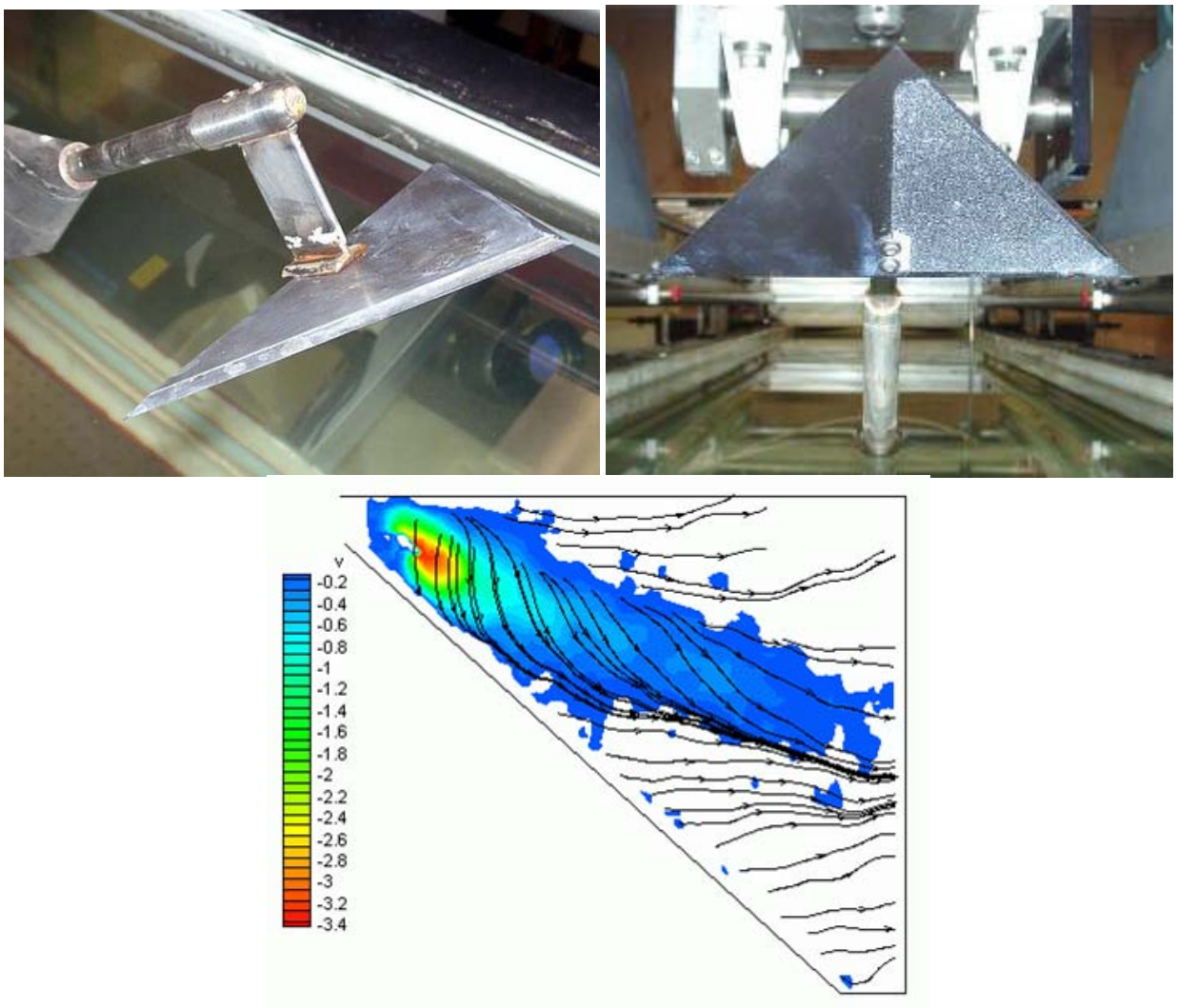

Figure 14. 50°-sweep delta wing with port-panel of leeward side instrumented with S3Ffilm, in collaboration with ISSI, to measure skin friction field: model about to be lowered into the HFWT test section (top left), view of metric side of model (top right), and typical result of skin friction intensity (bottom).

Many obstacles remain. One is the temporal response of the S3F. Another is balancing sensitivity (needs to be down to 0.1 Pa) with robustness. The experiments on which Figure 14 is based were taken at a time when S3F chemistry was still in its infancy, and progress was curtailed by the aforementioned obstacles. S3F proved to be very successful in water at dynamic pressures much higher than those normally obtained in the HFWT, but these are not of interest for MAV applications. In future

work, we intend to revisit S3F in the HFWT, taking advantage of the developments in chemistry in recent years, and perhaps using stereo PIV-type of techniques to infer both pressure and skin friction from the surface particle displacement, instead of pressure separately from ratioing fluorescence intensity.

3.2.3. Dye Injection

The quintessential distinction of fluid mechanics, from all other engineering disciplines, is that things move large distances relative to each other, in complex and intriguing ways. Perhaps no other field of study is so visual and so infused with the importance of visually perceiving where things move and how they evolve over time. While applied aerodynamics is more concerned with measuring total forces on bodies (lift, drag and so forth), and the actual flowfield is of secondary interest unless there are anomalies in the force measurements, flow visualization is the foundation of experimental fluid mechanics. By far the most accessible scheme of flow visualization is qualitative methods of tagging the flow and observing the tags. These can be rendered quantitative by simple means (time-stamping the position of traces, such as by pulsing hydrogen bubbles or dye clumps) or elaborate means (particle image velocimetry). Here we consider the simplest means. And as mentioned above, water tunnels are ideally suited to such means.

We assume that the passive scalar of dye concentration is an adequate surrogate for the out-of-plane component of vorticity, at least for qualitative assessment of attached vs. separated flow. A 1k x 1k-pix digital camera (UniqVision UP-1830) at 30 frames/second was used in most experiments for imaging, operating unshuttered. In some cases this is sufficiently fast to "freeze" the motion of the model, while in others it causes blurring. For k = 0.25 reduced-frequency oscillation of an airfoil model of 152.4mm chord (typical) at Re = 60K, one motion period corresponds approximately to 158 frames at 30 frames/second, giving temporal resolution of ~2.3 degrees of motion phase per video frame.

A wand with 0.5mm internal diameter, injecting concentrated blue food coloring, is typically used. For models with sufficient internal volume, such as airfoils, the dye wand can be fitted inside the model and exits flush with the outer mold lines, firing approximately wall-normal. An example is the SD7003 airfoil model in Figure 15.

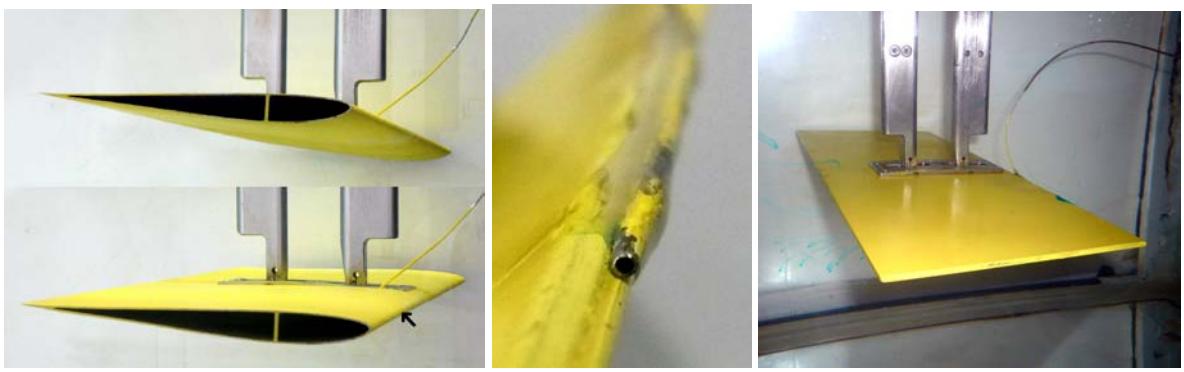

Figure 15. SD7003 airfoil installed inside test section, showing smooth suction-side of airfoil (top left) and plunge rod coupling on pressure-side of airfoil (bottom left). Black arrow in bottom image points to dye injection exit port location. Middle: injector tube attached to flat-plate model leading edge, firing spanwise outboard. Right: flat plate model with no internal dye passages, showing position of externally-fed dye at the leading edge.

The dye exit location is not visible in Figure 15, but is marked by the black arrowhead in the bottom-right-hand portion of Figure 15. Dye is entrained towards the suction side at those phases of airfoil injected by a "New Era" NE-1000 syringe pump[57], with infusion volumetric flow rate programmed to attain desired flow speed. For wall-normal firing this is typically ~$0.25U_\infty$ at the probe exit. Dye flow streaklines tend to be independent of dye exit rate for rates less than ~$0.5U_\infty$, and the value of $0.25U_\infty$ was selected to attain reasonable flow visualization image contrast while further reducing likelihood of

flowfield disturbance. For thin models, such as flat plates, the dye wand is epoxied to the model outer mold lines. A typical location is a downstream-firing wand on the model pressure-side, or a wand running along the leading edge, firing spanwise outboard. For the former, typically the dye exit velocity is matched to free-stream velocity.

3.2.4. Force Balances

3.2.4.1. Rolling Hills Research Corporation 5-Component Force Balance

The first force balance considered under the present study was an off-the-shelf model built by Rolling Hills Research Corporation (RHRC). This is a 5-component balance – missing only a drag link – consisting of 5 single-channel stages ganged in series, with a common waterproofing and interfacing with a conventional aft-mount sting. A photo of the installation for a wall-to-wall airfoil model is shown in Figure 16.

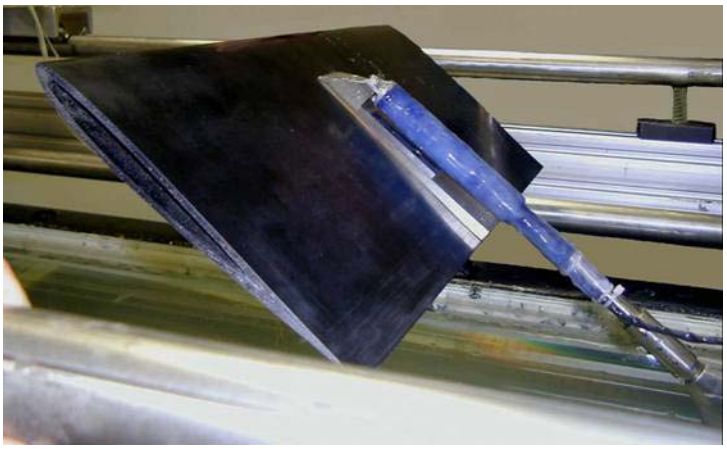

Figure 16. SD7003 airfoil mounted upside-down, below Rolling Hills Research Corporation 5-component waterproof force balance; lifted from the test section for model installation.

The RHRC balance was used for static force measurements on the SD7003 airfoil[58] and a series of aspect ratio = 2 flat plate planforms[43]. As this device suffered mechanical failure and gauge delamination in two successive iterations, and is no longer in use, we will limit ourselves to reporting a summary of the measurement results. Details of balance calibration, software development, and operating procedure are given by Altman[58].

3.2.4.2. Fiber-Bragg Grating Custom Balance

The RHRC force balance, even if operating robustly, can not be directly integrated into the pitch-plunge rig used in the unsteady experiments, as detailed in sections below. This requires a custom geometry of balance, though not necessarily an unconventional design. However, to circumvent difficulties associated with electrical strain gauges in water – waterproofing, routing of wires, drift, gauge delamination and so forth – an optical approach, using fibre-Bragg gratings (FBGs)[59], was used. This is not strictly speaking a novelty, as FBGs are used widely for example in civil engineering; but to this author, the present instance is the first use of FBGs in aerodynamic applications.

Coherent light is sent through the fibre and through gratings written onto the fibre. Each grating reflects light of very narrow bandwidth. If the segment of the fibre containing a grating is strained, the reflected light wavelength shifts proportionately. Strain of the fibre could be due to mechanical strain of the underlying substrate (the flexure joint in the force balance) and to thermal effects, which must be removed though appropriate compensation. In the present application, a single fibre with 4 grating elements was integrated into a two-flexure-joint airfoil mount, thus serving as an integrated force balance

(Figure 17). The balance can resolve axial force, normal force and pitching moment, though only the lift is reported here.

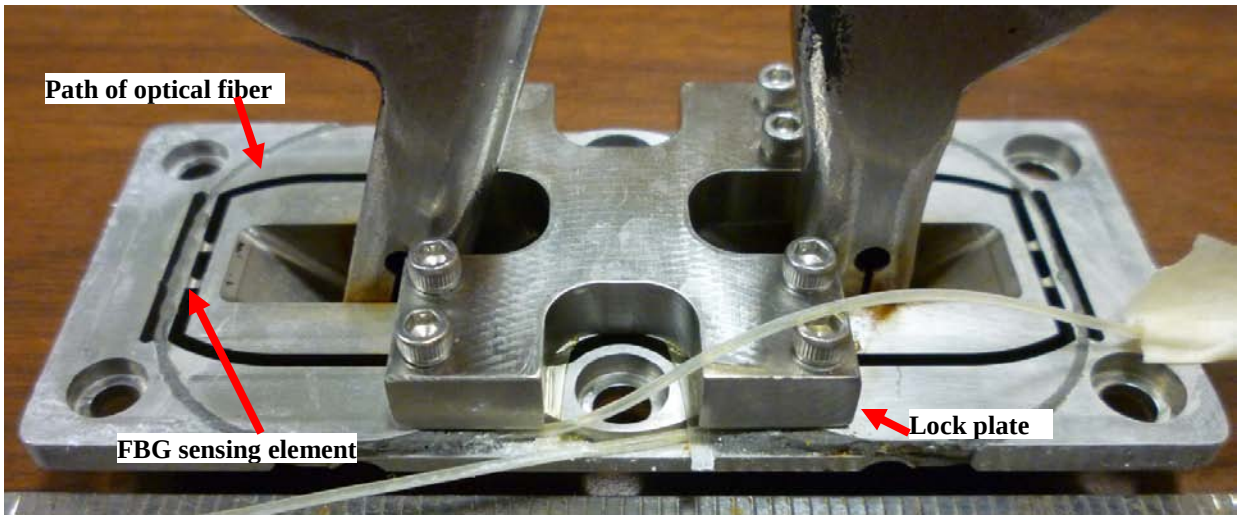

Figure 17. 3-component force balance based on Fibre Bragg grating (FBG) sensors, integrated with airfoil mount; photo shows the HIPPO plunge rods bushed into the inner frame of the balance, and a lock plate bridging the inner and outer frames, to lock the two safely during model installation.

Like hot wires, the FBGs are sensitive to temperature as well as the desired measurement quality (mechanical strain). To circumvent thermal crosstalk, a later iteration of the balance had a 5th, unstrained FBG element, whose signal assisted in the calibration to remove temperature response of the whole unit.

To further reduce thermal response, the balance was calibrated in-situ, mounted on the HIPPO plunge rods with the test section filled. Weights were hung from several points along the balance length, at 0° and ±45°, and angles in between. These data were used to compute the load cell calibration matrix. The standard error of the calibration matrix for the lift force is 0.16N, which corresponds to a lift coefficient standard error of 0.03.

The FBG signal was interrogated via a Micron Optics sm130 instrument[60], with sampling ranging from 250Hz to the instrument's maximum rate of 1Khz, typically over 100 periods of oscillation for periodic motions. Data were ensemble-averaged and further smoothed with a moving average, and the first 5 periods removed from the sample. Inertial tares were conducted by draining the water tunnel and repeating the airfoil motion. More details on the theory and implementation of the balance are given in Appendix 1. An example of lift measurements for an airfoil heavily featured in this report is given in Figure 18, where comparison is also made with results of Selig[71] and with the classical $2\pi\alpha$. The favourable comparison implies both that the balance is working acceptably well, and that the static behaviour of the airfoil is nearly commensurate with 2D; alternatively, it could imply a perfect cancellation of errors, but we discount this possibility because at heart we are optimists.

The main drawback of the FBG balance is that loads sensed by the flexures include not only the directly measured normal force, axial force and pitching moment, but also loads imparted to the outer frame of the balance, from torquing the bolts connecting the balance to the model. These loads result in a DC offset from zero. If this offset remains constant on time intervals comparable to a typical dynamic test sequence, then the offset can be removed through a tare procedure. And if the offset begins to vary significantly, that is indication that the FBGs are beginning to delaminate from the flexures, and it is time to renew the balance. This has happened at least twice in the period that an FBG balance has been in operation in the HFWT (2008-2010).

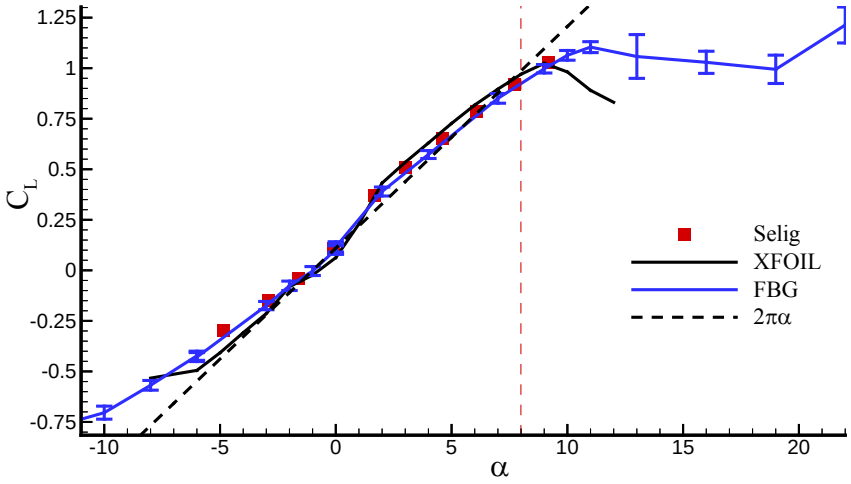

Figure 18. SD7003 airfoil static lift coefficient vs. angle of attack, Re = 60K: XFOIL results at amplification factor N = 9 (black line), wind tunnel data of Selig et al.[71], and water tunnel data (blue line), with error bars at 95% confidence intervals. Mean angle of attack for oscillatory motions discussed in a later chapter of this report, 8°, labeled by the dashed red line.

3.2.4.3. ATI Nano Balance

The second balance currently (as of January 2010) in operation in the HFWT is an off-the-shelf 6-component internal, integrated with the HIPPO plunger rod non-metric coupler, and designed to be mounted as a conventional aft sting. As results using that balance are still in the development stage, details will be limited to the cursory observation that where both the ATI and FBG balances have full functionality, they return comparable lift time traces.

3.2.5. Summarizing the HFWT

Looking ahead to other sections of this Report, it is perhaps fitting here to summarize the operating conditions and capabilities of the HFWT and of its concomitant instrumentation suite:

- Main parameters of the Horizontal Free-surface Water Tunnel (HFWT)
  - Tu ~ 0.4%, 18" wide x 24" high x 108" long test section, 3 cm/s – 45 cm/s flow speed.
  - Supports range of experiments in abstracted-configuration and vehicle external aerodynamics, fundamental flows such as bluff bodies and plates, unsteady aerodynamics and vortical flows.
  - Free-surface terminated by splitter plate damps sloshing while allowing user interaction with the test article during the test.
- High-Intensity Pitch-Plunge Oscillator (HIPPO Rig)
  - 3DOF sinusoidal and nonsinusoidal oscillation capability (8" vertical stroke, max 48-deg pitch, 48" streamwise stroke).
  - Can support perching experiments where the model changes angle of attack and comes to relative rest (with respect to free stream) upon maneuver completion.
  - Can support flapping experiments with prescribed or free-to-pivot motions, taking advantage of favorable temporal and dynamic scaling in water vs. air.
- Particle Image Velocimetry system

    - Pair of PCO 11 Mpix CCD cameras and 120mJ/pulse laser allows for LES-type resolution (for validation) near boundary layers and beyond-DNS resolution in bulk flow
    - Synchronized to HIPPO at user-selectable phase, for phase-averaged data, first order and second order flowfield statistics, and instantaneous PIV.
    - Complements dye injection system for rapid visualization of flow separation and qualitative tagging of vorticity transport.
- Fiber-Bragg Grating force balance
    - 3-component balance supports instantaneous and phase-averaged data for lift, pitch and drag/thrust.
- ATI 3/6-component internal balance
    - Integrated with aft-sting arrangement for 3D models in rectilinear motions

We now turn to a selection of results in static aerodynamics at low Reynolds number, before describing the HIPPO rig, and then moving to the unsteady aerodynamics results, which are the core of this report.

4. Experiments in Steady Aerodynamics at Low Reynolds Number

While the principal objective of the underlying research is in unsteady aerodynamics, one must first approach the steady problem, to assess the state of the art and to ascertain opportunities where unsteady problems are most pressing. Here we consider three core areas:

- Laminar separation bubbles of conventional airfoils at low Reynolds number: flow physics, flowfield properties, force measurements, and implication for flight vehicle performance in this Reynolds number range.
- Lift production by low aspect ratio wings of various planforms. Since MAV configurations tend to be low aspect ratio, the natural point of departure is the steady problem, where we compare classical theories to several different measurements.

4.1. Laminar Separation Bubbles for the SD7003 Airfoil

The formation, presence and burst of laminar separation bubbles (LSBs) has long been known as a detriment to the performance of airfoils at low Reynolds number, directly affecting not only MAV endurance – an issue conceivably ameliorated by improvements in system components such as batteries and multifunctional materials – but, more importantly, degrading vehicle handling and stability, due to the time-dependency of separated structures sensitive to disturbances encountered in flight[4]. Better understanding and ultimately management of LSBs is therefore useful for improving the flight mechanics of MAVs. The LSB is a classical topic in laminar to turbulent transition, having been extensively examined both from the viewpoint of fundamental fluid mechanics (see for example Tani[61], Watmuff[62], Bao and Dallmann[63]) and in the context of aerodynamics of airfoils and wings (Arena and Mueller[64] Roberts[65]; Bastedo and Mueller[66], Gopalarathnam et al.[67]; Biber et al.[68], and McAuliffe and Yaras[69]).

The present study seeks to track the development of the LSB over a range of angles of attack, from low angles where the bubble is stable and well-defined, to higher angles, where burst eventually occurs. Of primary interest is to produce a data set suitable for validation of computations. Therefore, emphasis is on resolving the velocity field and its statistics, rather than obtaining integrated forces and moments. The near-wall velocity distribution can be compared with the results of commonly-used airfoil analysis codes, for example XFOIL[70], by looking at the predicted vs. the measured shape of the LSB for a given critical amplification factor. The code is expected to be reliable for those conditions where the bubble is stable and closes well upstream of the airfoil trailing edge. The secondary objective of this study is to benchmark and compare three recently constructed experimental facilities of very different type; a water tow tank, a wind tunnel and a water tunnel, by testing a common geometry at nominally identical experimental conditions: matching the model, the Reynolds number and the angle of attack.

The SD7003 airfoil[71] was chosen because of the long, stable LSB that it exhibits over a broad range of angle of attack, at Reynolds numbers below 100,000. Here the Reynolds number of interest is 60,000.

The work pursued here was paralleled in two other facilities: at water towing tank at the Canadian Institute for Aerospace Research, National Research Council, Ottawa, Canada; and the Technical University of Braunschweig, Institute of Fluid Mechanics, Braunschweig, Germany. Snapshots of LSB results for all three facilities are compared, but details are only reported for the AFRL experiments.

PIV measurements were taken at α=4°, where the LSB is long, thin and well-behaved; at α=8°, where the LSB is short or possibly absent, and in any case is close to the airfoil leading edge; and at α=11°, near stall, where there is a small LSB near the leading edge underneath a largely open separation. At α=4°, recirculating projected time-averaged "streamlines" are well-resolved inside the LSB, but at α=8°, they are no longer resolved. Evidently, this is due to comparative lack of resolution, either due to the thinness of the bubble and hence the decrease of PIV velocity vector density in the wall-normal

direction, relative to the bubble thickness; or greater flow unsteadiness, requiring more PIV image pairs for the flow statistics to be adequately converged; or both. The problem of insufficient convergence of flow statistics becomes progressively worse at α=11°, where mismatch in both mean velocity and Reynolds stress contours, in going from PIV interrogation field to field, is quite clear.

To obtain reasonable resolution, the airfoil was imaged piecewise, in six overlapping fields of view, skipping the aft ~30% of the chord (Figure 19). The averaged velocity data were based on 840 images (420 velocity fields) in the two upstream fields, and 1176 images (588 velocity fields) in the four downstream fields, with 28.9mm x 28.9mm field size. The PIV algorithm was two-pass, (locally adapted window translation in the second pass, but no window resizing) with 32x32 pixel windows and 50% overlap. The large window size was chosen to minimize the number of PIV outliers, at the potential expense of reduced spatial resolution. Mean velocity contours for α=4° are shown in Figure 20. Contours of Reynolds stress are shown in Figure 21. Normalization is with respect to free-stream velocity and chord length, so that a speed of "1" equals free-stream. Similarly, mean velocity and Reynolds stress are plotted for α=8° in Figure 22 and Figure 23, respectively. This is continued for mean velocity and Reynolds stress for α=11° in Figure 24 and Figure 25, respectively.

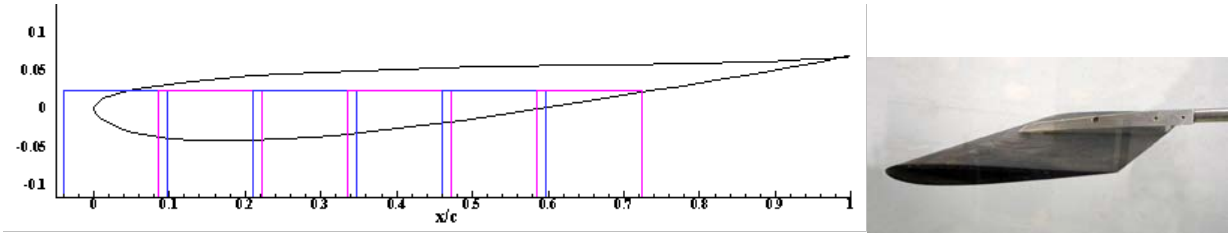

Figure 19. Schematic of PIV interrogation window tessellation on SD7003 airfoil (left), and photo of airfoil mounted in the water tunnel test section (right).

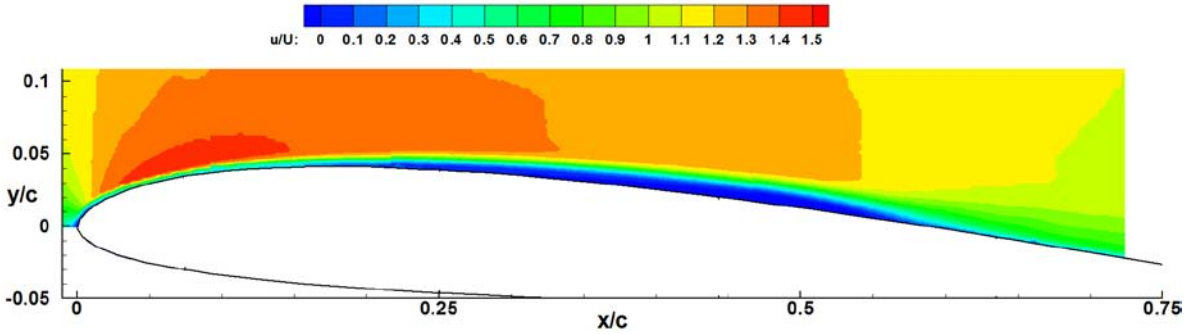

Figure 20. Contours of SD7003 LSB mean streamwise velocity component, α=4°.

The cross-prime Reynolds stress, u'v', in Figure 21 and subsequent related figures is normalized by free-stream speed squared. The value of -0.001 is taken as the "cutoff" value beyond which transition to turbulence is posited to occur.

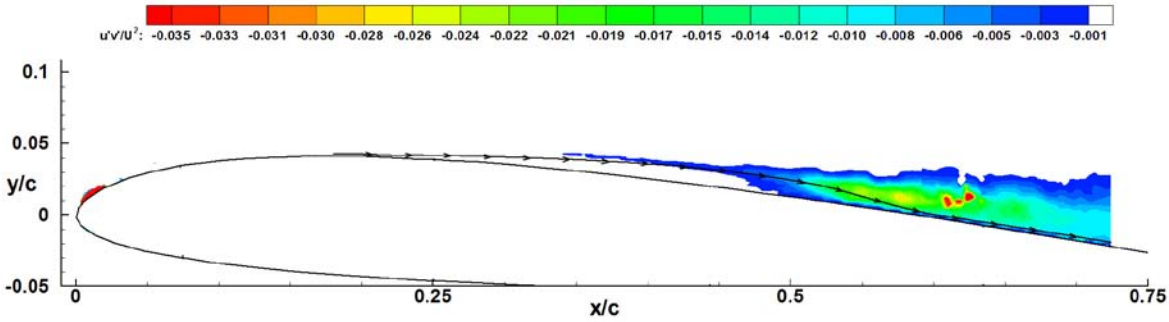

Figure 21. Contours of SD7003 LSB normalized Reynolds stress, α=4°, together with LSB dividing streamline.

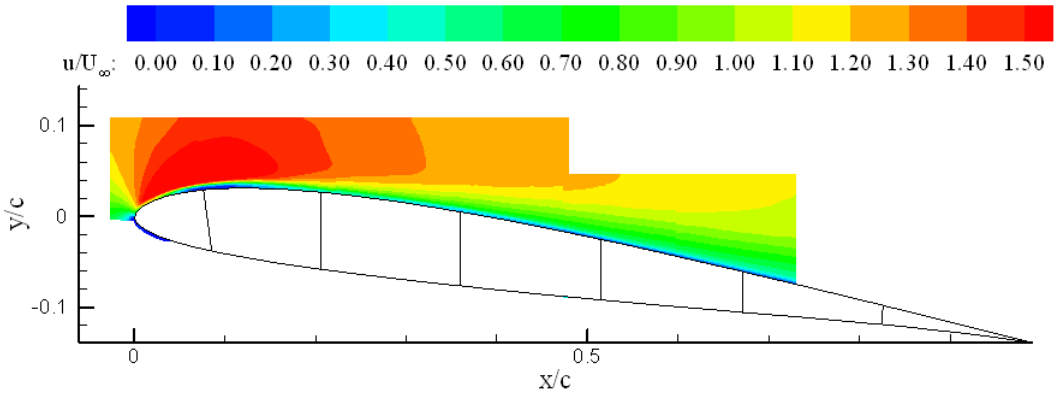

Figure 22. Contours of SD7003 LSB mean streamwise velocity component, α=8°.

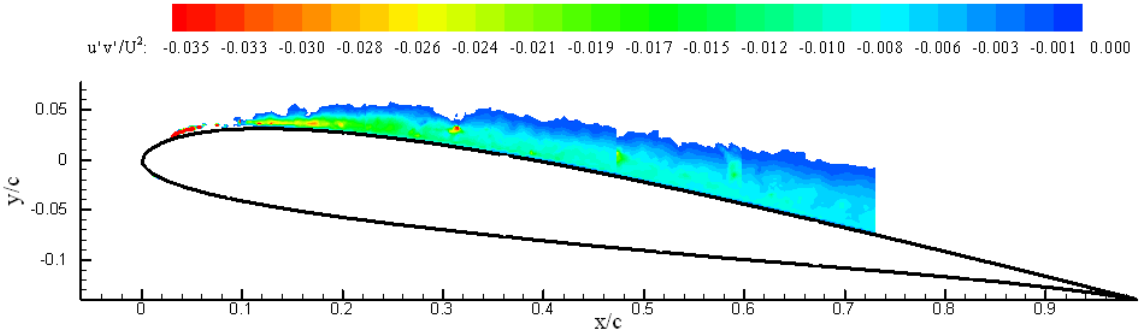

Figure 23. Contours of SD7003 LSB normalized Reynolds stress, α=8°.

For α=11° the Reynolds stress levels are much higher than for the lower angles of attack, evidently because large-scale separation is accompanied by turbulent mixing. That is, unlike the mostly attached-flow case, it is not the case that there is a large run of laminar separation followed by transition in a free shear layer and turbulent reattachment. Stall, perhaps trivially, is turbulent in this Reynolds number range.

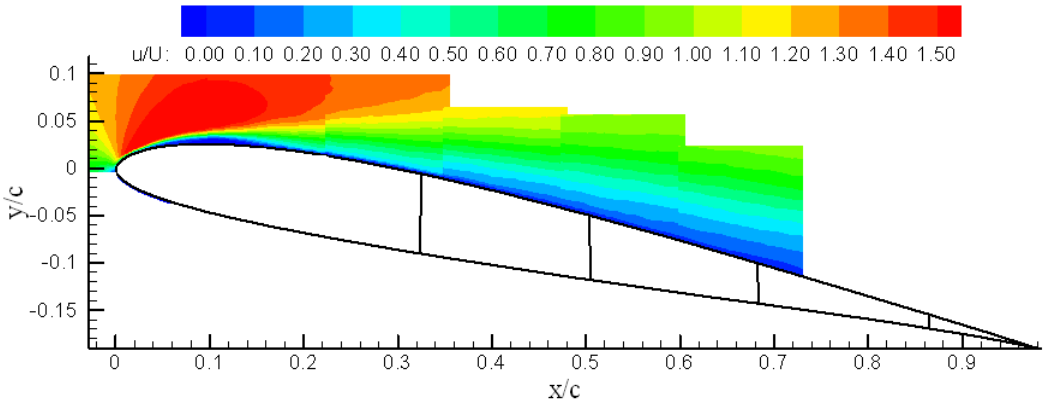

Figure 24. Contours of SD7003 LSB mean streamwise velocity component, α=11°.

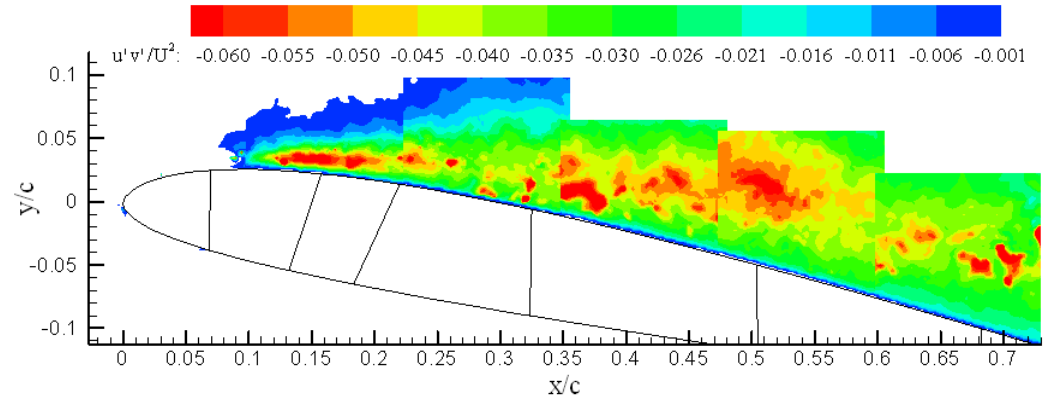

Figure 25. Contours of SD7003 LSB normalized Reynolds stress, α=11°; not the higher magnitude of Reynolds stresses in the contour levels.

The locations of LSB separation, transition onset, time-averaged reattachment, and maximum bubble height for the three sets of results are listed in Table 1, along with the estimated facility turbulence intensity. Respective locations predicted by XFOIL for the disturbance amplification factor N=9 are also given, with separation and reattachment inferred from streamwise coordinates where the skin friction coefficient first reaches zero declining from positive (separation) and returning back to positive (reattachment). IAR and TU-BS data on the LSB separation, reattachment and transition points agree quite well. In the AFRL data set, the bubble forms considerably further upstream and reattaches further upstream, though its length is somewhat longer than in the IAR and TU-BS results (~40%c compared to ~30%c). Transition is dominated by the Kelvin-Helmholtz instability mechanism which leads to the roll-up, pairing, and subsequent shedding of large-scale vortices[69], as opposed to turbulent spot-based transition in which bursting of small-scale turbulence occurs directly within the separated shear layer (as observed by Roberts and Yaras[72], for example). Therefore the locations of transition onset listed in Table 1 are reliable measurements and are probably not affected by spatial resolution errors.

Table 1. Measured and computed SD7003 LSB Properties, *Re*=60,000, α=4°

Data Set	Freestream Turbulence, Tu [%]	Separation, x_S/c	Transition, x_{TR}/c	Reattachment, x_R/c	Max Bubble Height*, h_b/c
IAR	0*	0.33	0.57	0.63	0.027
TU-BS	0.1	0.30	0.53	0.62	0.028
AFRL	~0.1	0.18	0.47	0.58	0.029
XFOIL	0.070 (N = 9)	0.21	0.57	0.59	

*thickness of entire boundary layer at maximum bubble thickness

We can therefore conclude that modern, yet conventional off-the-shelf 2D particle image velocimetry is capable of resolving averaged velocity fields in an airfoil laminar separation bubble at a Reynolds number of 60,000. Comparison of nominally identical experiments in three very different facilities – a water tow tank, a wind tunnel and a water tunnel – shows encouraging qualitative similarity in the bubble shape and velocity fields, as well as Reynolds stress distributions. However, discrepancies in the measured location and flow structure of the bubble remain. The former is perhaps due to minor variations in angle of attack or ambient turbulence intensity; the latter being a result of inadequate spatial (magnification too low) or temporal (insufficient number of PIV samples) resolution. Results from the present study form a promising database for validation of low Reynolds number airfoil numerical solutions. At even lower Reynolds numbers, separation bubbles are larger and the interplay between LSB physics and global aerodynamic properties such as the drag polar would become more significant. Research continues. A thorough computational study, motivated by the present work, was recently conducted by Galbraith and Visbal[73], generally confirming the experimental findings.

4.2. Aspect Ratio = 2 Flat Plates of Various Planform

Here we shelve the problem of 2D airfoil aerodynamics and transition, and instead consider thin flat-plate sections, where presumably transition is "forced" by the square leading edge. Evidence for such a claim includes for example Gursul et al.[74], who found Re-insensitivity for various low aspect ratio planforms with sharp-edges sections, at least for Reynolds numbers above approximately 20,000. This can be counterintuitive in the context of conventional aerodynamics. Normally, sharp leading edges produce a small pocket of separation that closes by turbulent reattachment – not really a LSB, but a flow structure that can be thought of as such. As compared with rounded-edge airfoils, in moderate and high Re applications the peak L/D is attenuated. But for low-Re applications one might find the reverse; for instance, Spedding et al[75] report that at Re = 12,000 and AR=6, flat-plate airfoils produced higher lift to drag ratio and more gentle stall than some low-Re optimized airfoil sections. Use of such thin flat-plate "airfoils" allows for the isolation of planform effects, rather than airfoil sectional effects. Our focus is therefore on planform effects on lift curve slope, and how well direct lift measurements correlate with inferences from the vorticity convected into the wake.

Laitone[76] studied rectangular planform wings at Reynolds numbers near 20,000, taking force balance lift and drag measurements for flat and cambered plates in a wind tunnel. His results for a rectangular flat plate wing of aspect ratio of 2.18 were used to validate results in the present study. Other examples in the recent literature are Cosyn and Vierendeels[77], who conducted fully-turbulent computations on rectangular wings at Re = 100,000, finding close agreement with lift predicted by lifting surface theory with Polhamus's leading-edge suction analogy[78]. In looking at numerous planform shapes in an aspect ratio range from 0.5 to 2, at Reynolds numbers from 70,000 to 140,000, Torres and Mueller[79] showed increasing nonlinearity in the lift curve slope and an increase in stall angle of attack as the aspect ratio decreased. Zuhal and Gharib[80] studied tip vortex meandering for a NACA 0012 AR~4.6 wing in a wind tunnel at Reynolds numbers close to 9,000, with stereoscopic PIV; this is useful for identifying vortex core location for wake-based inferences of lift coefficient.

The present study focuses on the connection between the coefficients of lift, experimentally obtained from studying trailing vortex structure (and circulation) at Re 8,000 - 24,000, experimentally obtained through force measurement, and theoretical inviscid predictions. Trailing vortex roll-up and formation is also observed with the help of flow visualization. Lift is calculated from the Kutta-Joukowski theorem, $L = \rho_\infty V_\infty \Gamma b'$, using peak circulation from area integrations of the vorticity field in the cross-flow plane as measured with digital particle image velocimetry. b' is taken as the effective span – namely, twice the distance between the observable core of the trailing vortex and the wing centerplane.

For slender wings, the inviscid approximation $C_L = \frac{1}{2}\pi AR\alpha$ (e.g., Thwaites[81]) happens to coincide with lifting-line theory, $C_L = \alpha\left[\frac{2\pi}{1+2/AR}\right]$ for AR=2. So AR=2 is a convenient prototypical low aspect ratio for general study, especially because it also fits well in the water tunnel at Re ~ 10,000 with minimal blockage. Effects of leading-edge sweep can be modeled with the approximation[81] $C_L = \frac{1}{2}\pi AR\alpha\left[\frac{4}{2+AR\tan(\varphi_{1/2c})}\right]$, or with Lamar's[82] extension of Polhamus' leading-edge suction analogy, $C_L = K_P \sin(\alpha)\cos^2(\alpha) + K_V \sin^2(\alpha)\cos(\alpha)$, where K_P, accounting for attached flow, is approximately 2.5 at AR = 2, while K_V, accounting for the vortical contribution is very close to π[82].

Models used in the experiment are shown schematically in Figure 26, the test matrix is given in Table 2. The uncertainty in the measurements of the velocity vectors and the calculation of the coefficient of lift is within 5%, which results from averaging 90 sets of individual velocity vector fields for each test in Table 2. The inaccuracy in the calculation of vortex position relative to the wing tip is on the order of 2 pixels, resulting in an uncertainty of ~ 2% based on the mean aerodynamic chord.

Table 2. PIV test conditions (left) and flow visualization test conditions (right).

	U_∞ = 0.09 m/s (Re: 8028)			U_∞ = 0.27 m/s (Re: 24083)		
	X/C = 1/10	X/C = 1	X/C = 2	X/C = 1/10	X/C = 1	X/C = 2
	AoA (deg)	AoA (deg)	AoA (deg)	AoA (deg)	AoA (deg)	AoA (deg)
Semi-ellipse	10	10	10	10	10	10
	15	15	---	15	15	---
Rectangle	5	5	5	5	5	5
	10	10	10	10	10	10
	15	15	---	15	15	---
Delta	10	10	---	10	10	---
	15	15	---	15	15	---

	U_∞ = 9 cm/s (Re = 8,028)			
	Angle of Attack			
Semi-ellipse	5	10		
Rectangle	5	10	15	20
Delta		10	15	

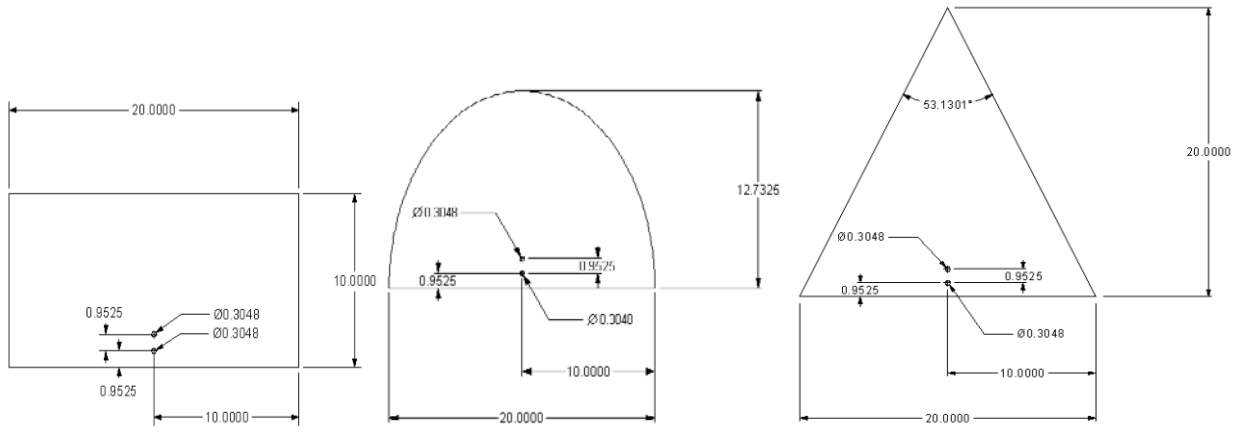

Figure 26. AR=2 planforms: rectangle (left), semicircle (middle) and delta wing (right).

Typical velocity and vorticity contour levels are given in Figure 27, and an example of downstream variations of vorticity is given in Figure 28. Variations with downstream location and Reynolds number were slight to negligible; full details are given in Kaplan et al.[43].

Circulation is calculated by integrating vorticity about a circular area centered at the vortex core. The vortex core location is obtained from dye injection, and confirmed by comparison with the vorticity peak in the contour plots. Results of circulation magnitude vs. circular contour radius are given in Figure

29 for all of the examined cases. There is a peak circulation, achieved at that radius from the vortex core, such that at subsequently larger radii vorticity of opposite sign is captured. This peak circulation is then used in the modified Kutta-Joukouski theorem to calculate lift.

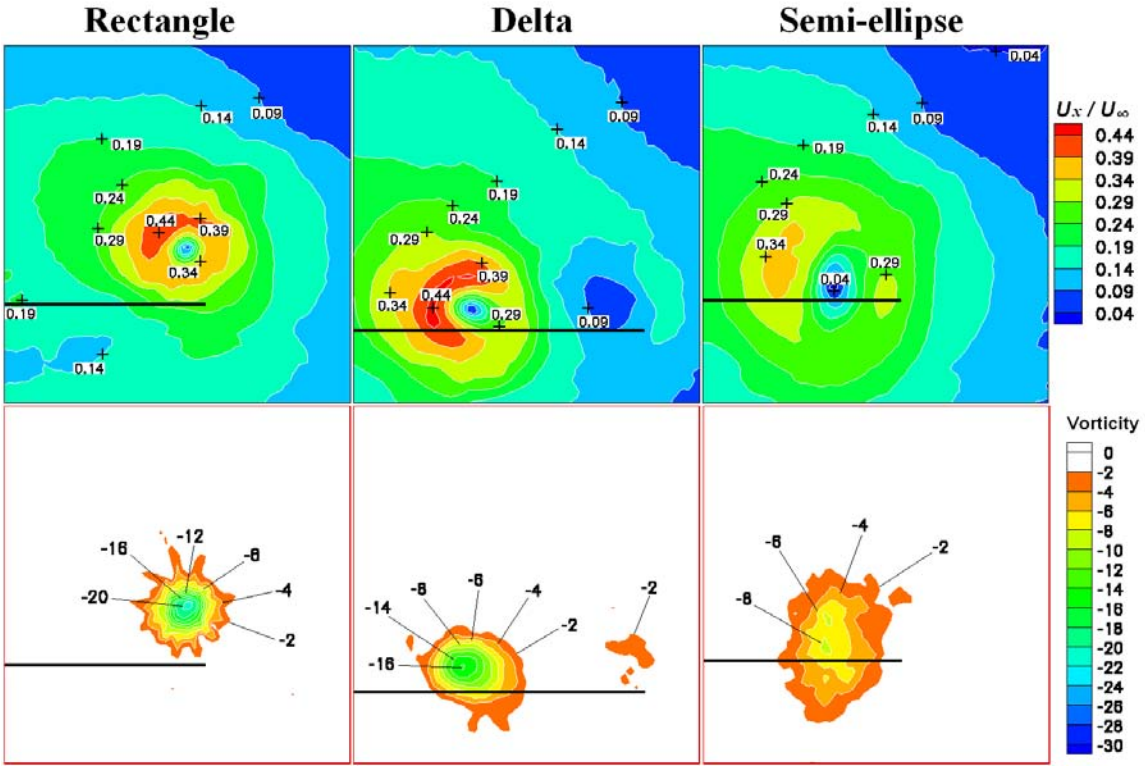

Figure 27. In-plane velocity magnitude and out-of-plane vorticity; α= 10°; downstream X/C = 1; U_∞ = 9 cm/s; Re = 8,000.

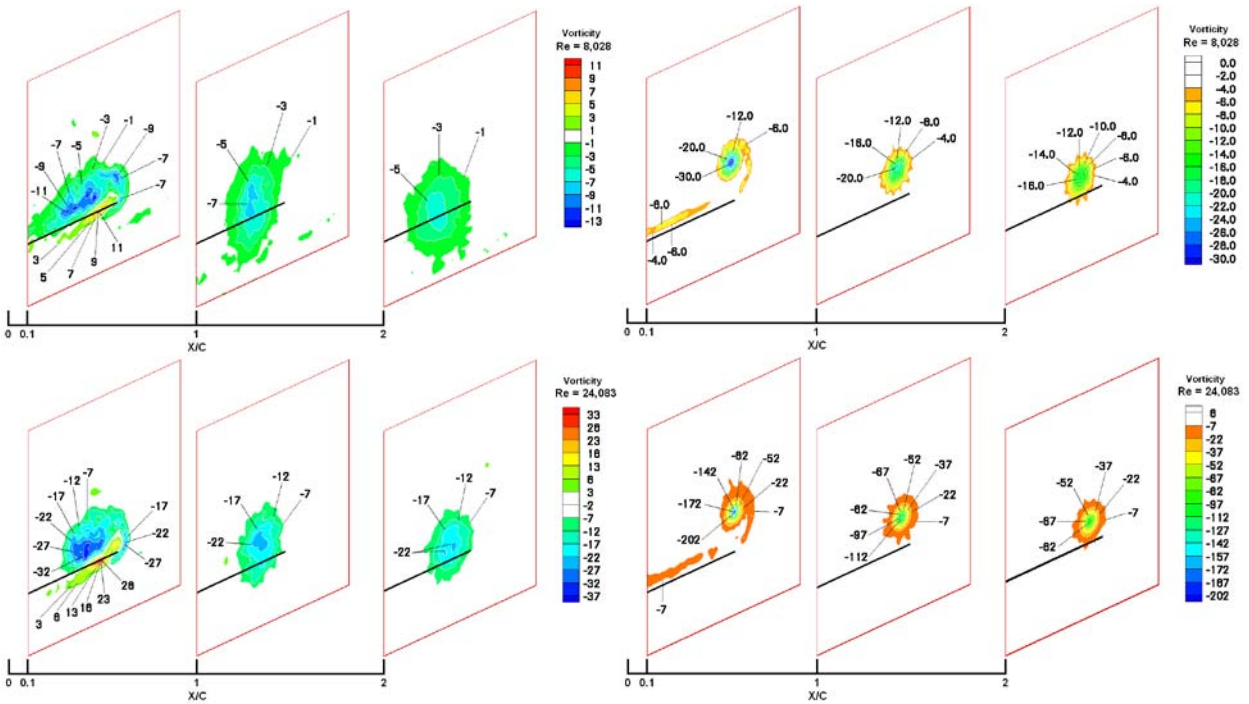

Figure 28. Vorticity evolution vs. distance downstream from trailing edge, α=10°; semi-ellipse (left) and rectangle (right); note difference in vorticity contour levels.

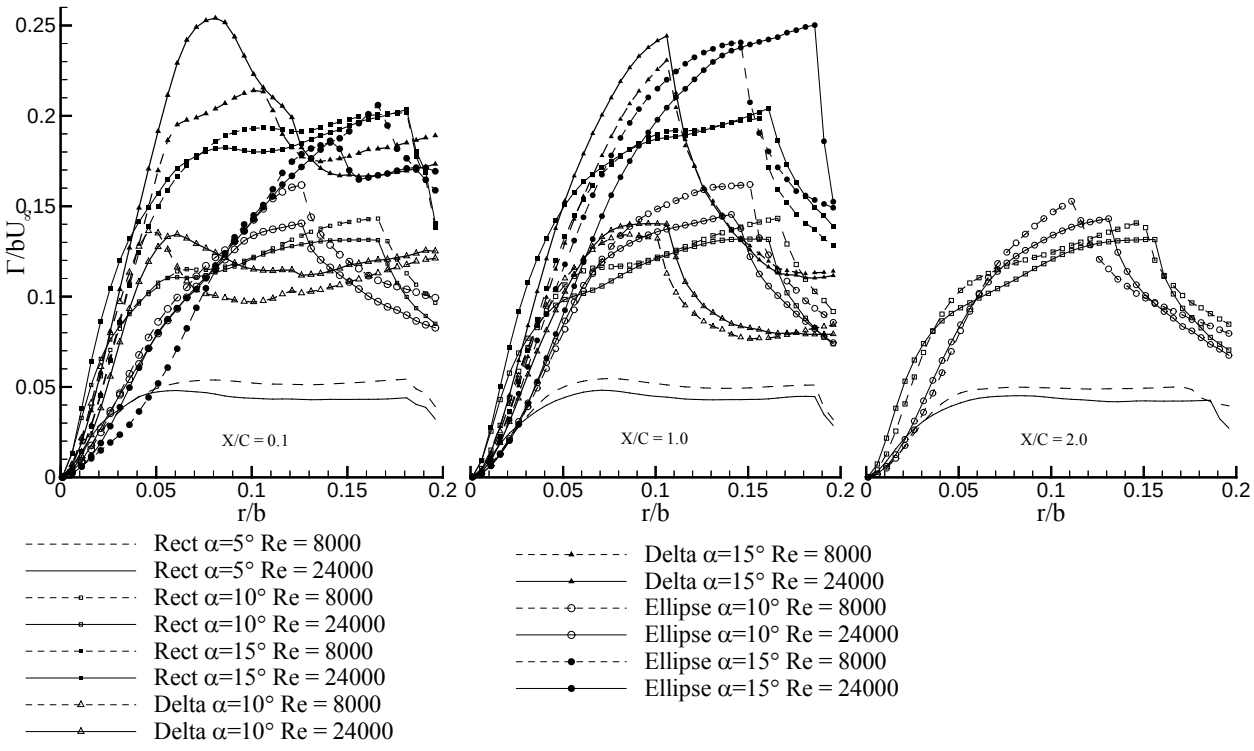

Figure 29. Normalized circulation vs. contour radius; X/C = 0.1 (left), X/C = 1.0 (center) and X/C = 2.0 (right).

An example of lift calculation using the Kutta-Joukouski relation and the effective vortex span is given in Figure 30, which shows that in all cases except for the near-stall case of the semi-ellipse, there is very little variation in predicted lift coefficient with respect to wake streamwise sampling station.

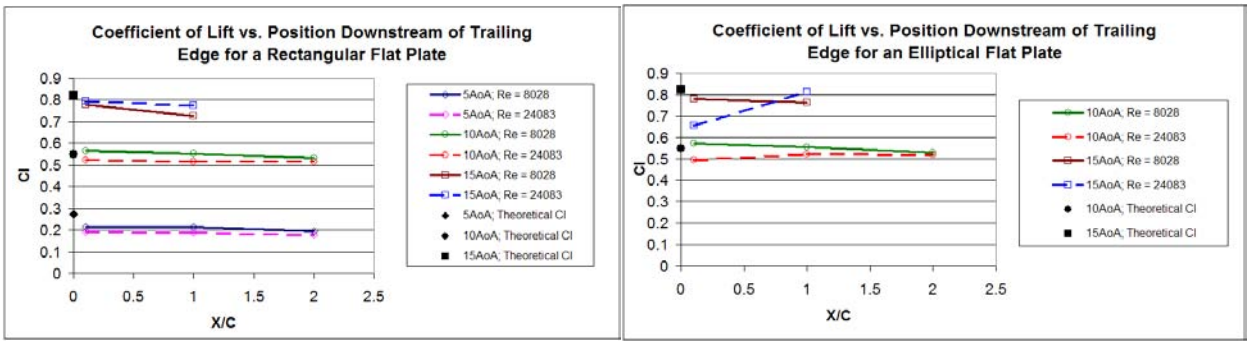

Figure 30. C_L vs. X/C Comparison for rectangle (left) and semi-ellipse (right).

Finally, the PIV-derived lift, the force balance measurement, and the various theoretical predictions of lift are compared for the rectangle, delta wing and semi-ellipse, together with comparison with Laitone's data for the rectangle[76] (rescaled using slender-body theory from the original aspect ratio of 2.18 to the present case of 2.0), in Figure 31. Mutual agreement is generally good, which is surprising given that the theories are developed for inviscid flow, and the PIV-derived circulation is likely plagued with errors due to dissipation and discretization. The only significant outlying cases are for the delta wing and low angles of attack, where LEVs and tip vortices may interact to cancel some of the wake-vortex circulation, thus underpredicting the lift.

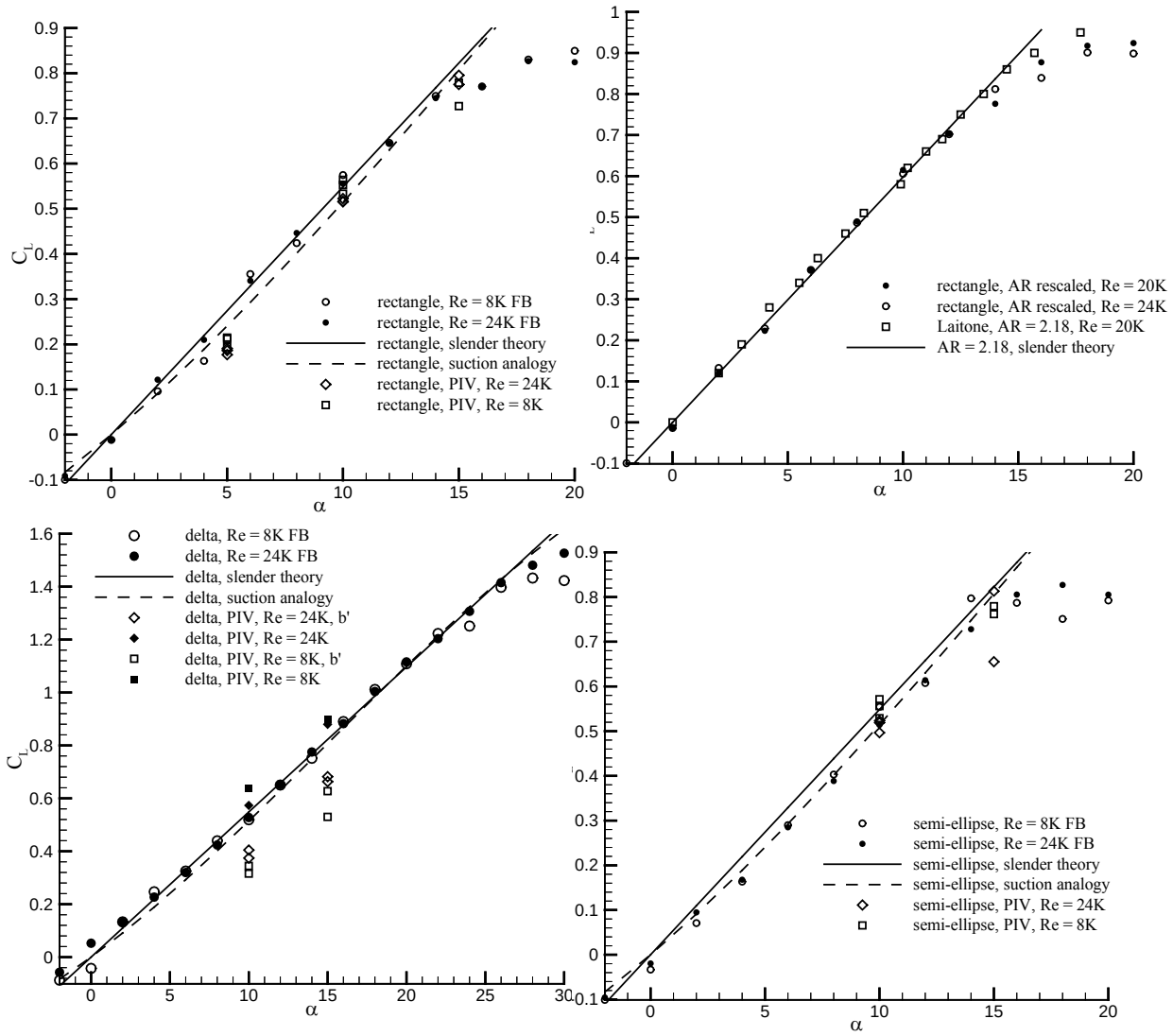

Figure 31. C_L vs. α; rectangle (top left), comparison of rectangle data with aspect-ratio scaled results of Laitone[76] (top right), delta wing (bottom left) and semi-ellipse (bottom right).

We conclude this section with the simple observation that viscous effects – that is low Reynolds number effects – are not necessarily present at low Reynolds number, at least for problems focusing on lift coefficient. The reason is a combination of low aspect ratio and sharp leading edges, which together produce a sort of forcing, that overwhelms viscous effects.

A different sort of forcing occurs in the unsteady case, which is the subject of the remainder of this report.

5. Establishing a Capability for Unsteady Aerodynamics Experiments

Having examined a range of nominally steady low Reynolds number aerodynamics problems, we now turn to the much broader question of unsteady flows. In this chapter, we document the design and construction of a mechanism for accurately producing high-speed, high displacement motions – first in two degrees of freedom, and then in three.

5.1. A Scheme for Pitch and Plunge Motions

We are interested as a baseline in the classical motions of unsteady aerodynamics, which are vertical translation (normal to the free stream) of an airfoil, and pitch about a fixed axis somewhere along the airfoil chord. This is a two degree of motion (2DOF) motion. Several schemes are possible for achieving this, and a few selected examples are briefly reviewed. Designs include (Figure 32) include those of Paquet[83] (top mount, two-component actuation at model end, with wing piercing free-surface), Parker, Soria and von Ellenrieder[84](top mount with pitch and plunge on separate carriages), Anderson et al.[85] (end-mounts, model horizontal with pitch and plunge on separate stages), Hanff[83] (center mount, pair of hydraulic actuators, similar to the present design), and Kurtulus et al.[86] (end-mount, separate pitch and plunge carriages).

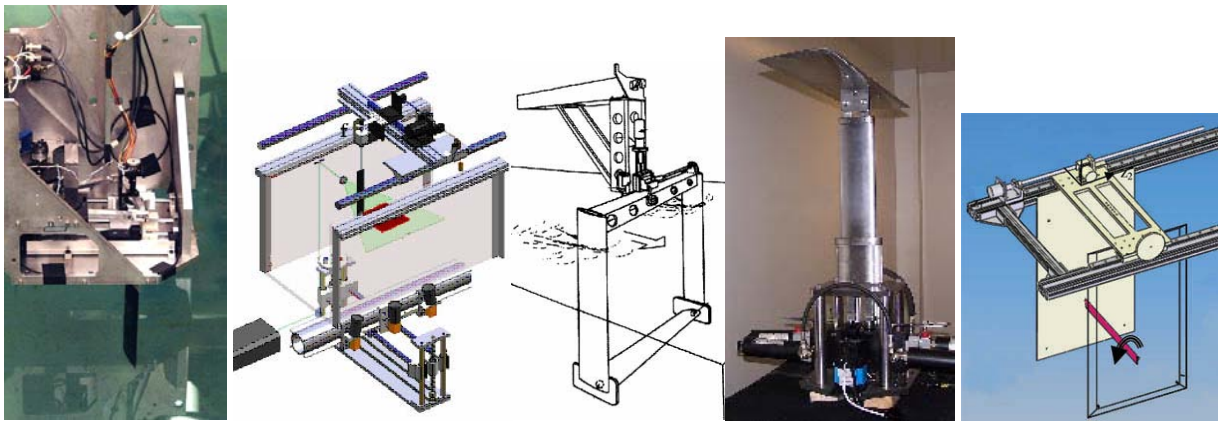

(a) (b) (c) (d) (e)

Figure 32. Examples of 2-degree-of-freedom rigs in water tow-tanks and water tunnels: (a) Paquet[83], Parker et al.[84], Anderson et al.[85], Hanff[83], Kurtulus et al.[86]

One 2DOF airfoil oscillation system design trade is supporting a vertically-hanging model from one tip, with the other free or abutting the test section floor; or, connecting to both tips, with the model horizontal; or, a center-mount system with struts connecting to the centerline of a horizontal model. The first has advantages of placing the force balance above the water line and thus solving the balance waterproofing issues, and has the least interference between the rig struts and the model flowfield. However, it makes free-surface effects largely unavoidable. The model mass (physical mass and motion-induced apparent mass) produces an unbalanced load on the model supports, which is especially troublesome for large models oscillating at high speeds in liquids. The second is limited to rigid airfoil models spanning the tunnel test section. The third keeps model loads balanced and allows for both wall-to-wall models and wings of various planform, but has large disadvantages of rig strut interference with the flowfield. This, however, is to some extent of secondary importance if particle image velocimetry data are taken in planar slices well-away from the model centerline. Assuming that this assertion is true, a center-mounted arrangement was selected.

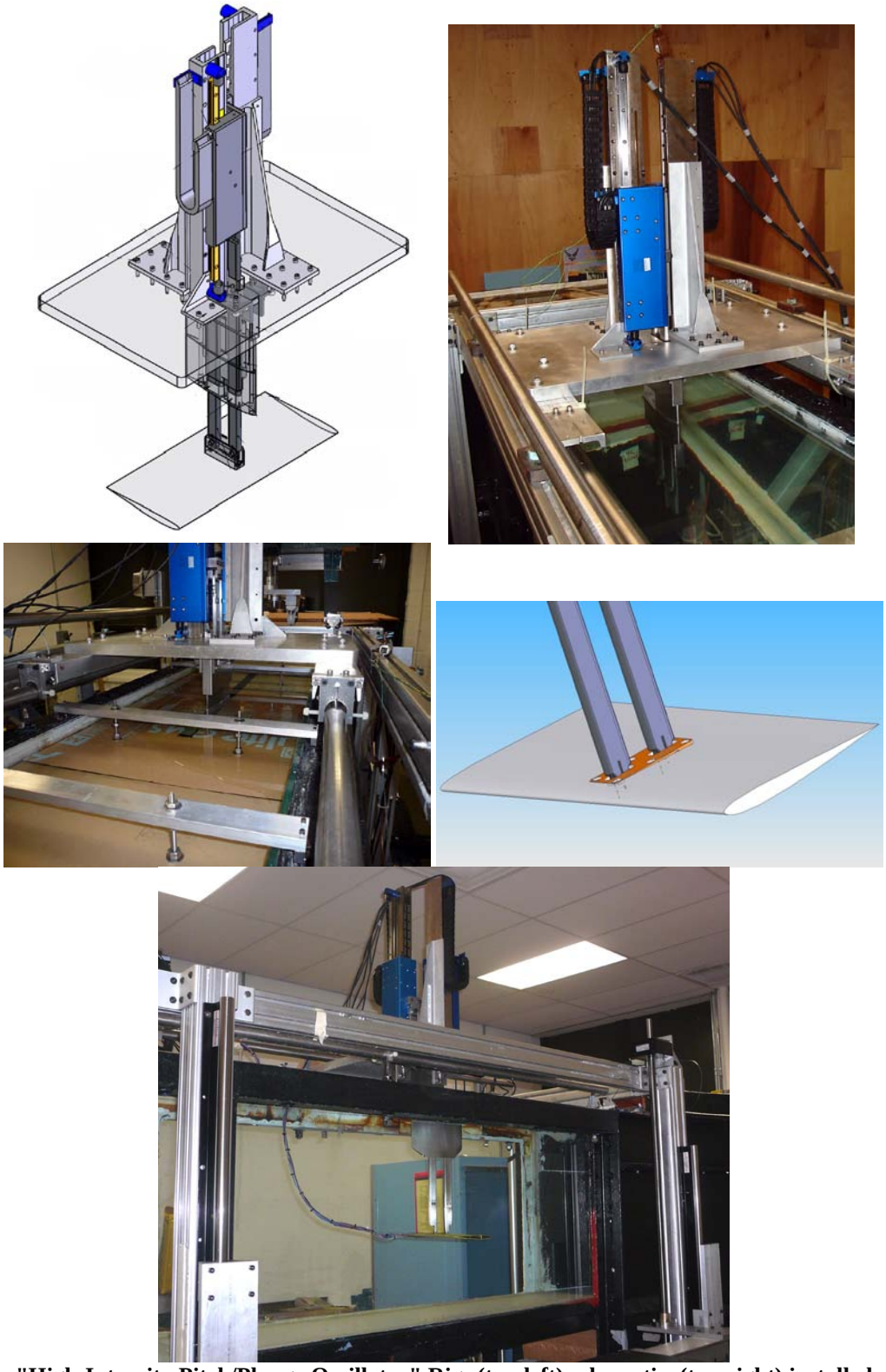

Figure 33. "High-Intensity Pitch/Plunge Oscillator" Rig: (top left) schematic, (top right) installed atop water tunnel test section, (middle left) with plates to damp free-surface oscillations caused by model motion, (middle right) schematic of SD7003 airfoil mount and plunge rods, with rod endpoints interior to the model; and (bottom) side view of test section with rig and airfoil model installed.

Actuation options include rotary servo (or stepper) motors, linear servomotors and hydraulics. Rotary motors are the most common choice and could provide large motion angles, but have the disadvantage of linkage backlash in motions with aggressive starts and stops. Also, the model pivot point would not be adjustable purely in software. This favors direct linear actuation. Electric linear motors were selected in favor of hydraulics, on account of the small rig scale and the savings in required support equipment. Linear motors mounted vertically have the disadvantage that unless current is flowing, model weight is unsupported, and the apparatus falls to its lower bump-stops. The start of every experiment thus requires a homing sequence. Also, the mass of the linear motors' moving-stages becomes part of the load that the motors need to support.

Aerodynamic loads that the motion rig must support can be estimated for example by Theodorsen's method[87], or just the simple $2\pi\alpha(t)$, where the effective angle of attack is the combination of pitch and plunge. As already mentioned above, for water tunnels it is not the case the inertial loads dominate aerodynamic loads; in fact, quite the opposite. However, for mechanism design purposes one can estimate the various masses involved, and the desired accelerations, to calculate overall loads. This can be important for abrupt motions with large transient accelerations, such as ramps and steps.

The present mechanism was design with large, heavy "plunge rods" – not only for improved stiffness, but also so that changing models would not greatly affect the total mass of the mechanism, whence the same controller coefficients (PID constants) could be used for all models.

The first iteration of the "High Intensity Pitch-Plunge Oscillator" Rig, affectionately dubbed with the acronym "HIPPO", consists of a pair of electric linear motors mounted vertically on a plate above the tunnel test section. Each motor actuates a vertical "plunge rod", which connects via a bushing to the airfoil at a fixed pivot point on the airfoil chord, in the test section vertical plane of symmetry. The upstream plunge rod is constrained to move purely vertically, whereas the downstream plunge rod is allowed to pivot in the test section vertical plane of symmetry. Motion trajectory of each rod is programmed independently, such that the desired angle of attack and vertical position time history of the airfoil are converted to position commands for each linear motor. This allows for single degree-of-freedom motions such as pure-pitch about a prescribed fixed pivot point, or pure-plunge. Pitch and plunge can be combined, and the pitch pivot point can be varied by suitable choice of phase and amplitude difference in trajectory of front or rear plunge rod. For all cases where the pitch pivot point is not coincident with the bushed end of the front plunge rod, there will be a small parasitic streamwise displacement of the model, which would be unavoidable unless the front plunge rod were to be allowed to pivot similarly to the downstream one. The first functional configuration of HIPPO is depicted in Figure 33.

5.1.1. Rig Performance

We will refer to the time-history of the difference between commanded (ideal) position of the two linear motors, and the attained position, as dynamic following error. Of course, error in positioning of the model depends also on structural behavior of the model and the connection between model and plunge rods, but upon ignoring those two factors, the dynamic following error implies directly the error in angle of attack, acceleration and so forth. The commanded motion of the two motors is translated in software from the desired pitch and plunge history, while the attained motion is sampled from an optical encoder on each motor track. Dynamic following error is shown for the representative case of sinusoidal pure-plunge with $h = 0.05$, $k = 3.93$, in Figure 34. For all pure-plunge cases that follow the motion is a cosine wave, so that velocity is continuous from rest. In the example in Figure 34 the motion is a cosine wave, showing the smoothing transient on startup. One half of a period after startup, dynamic following error is seen to be $< 0.5\%$ of the motion amplitude. Error peaks at phase locations of maximal acceleration in the sine wave; the frequency content of the error signal shows a peak at the actuation frequency, followed by harmonics. Two sets of data are given – for the forward plunge rod (green) and the aft (black). The position time histories of the two differ because the mean angle of attack of the model is 4°; with the

model mounted upside down (pressure-side of the airfoil towards the test section free-surface), the inclination of the model causes relative elevation of aft plunge rod.

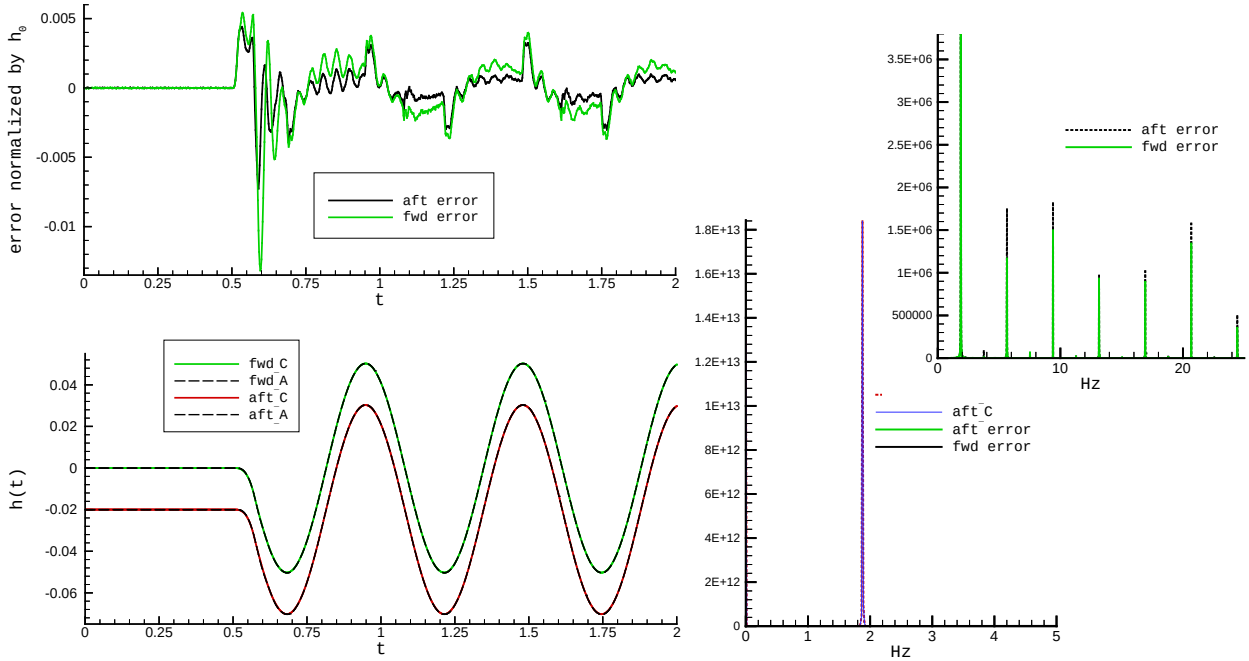

Figure 34. Time-traces and FFTs of plunge-rod commanded position, attained position and relative difference (error).

As an example of a classical, low-frequency, low angle of attack oscillation at the upper extreme of what is accessible in wind tunnels, we consider a k = 0.80 pure –plunge of the SD7003 airfoil at Re = 60,000 (Figure 35), where contours of streamwise velocity and out-of-plane vorticity are shown. This can be compared with the static results for the SD7003 in the previous chapter.

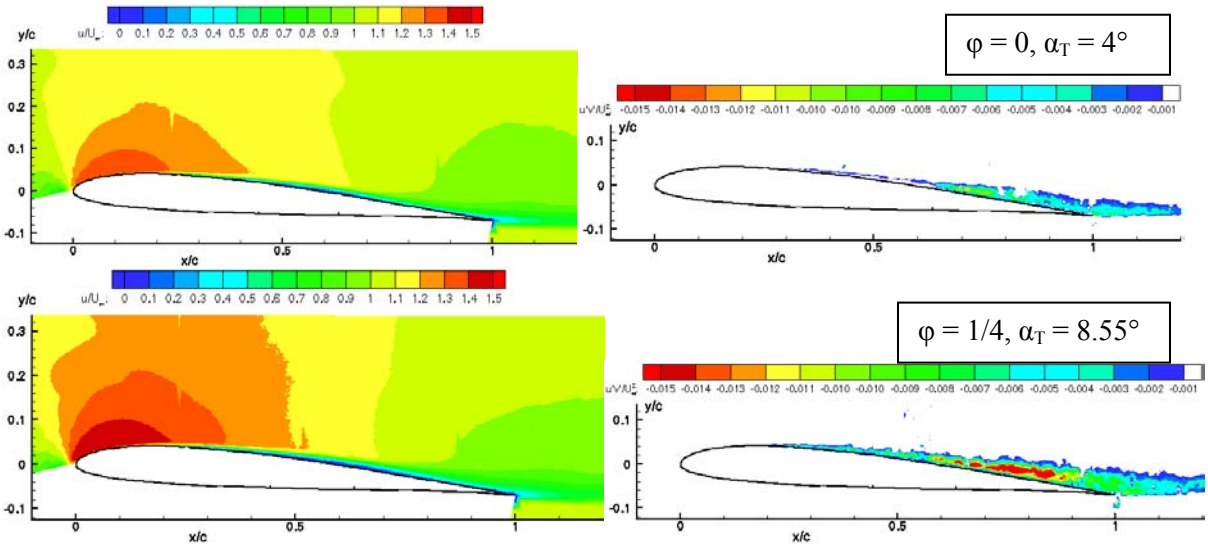

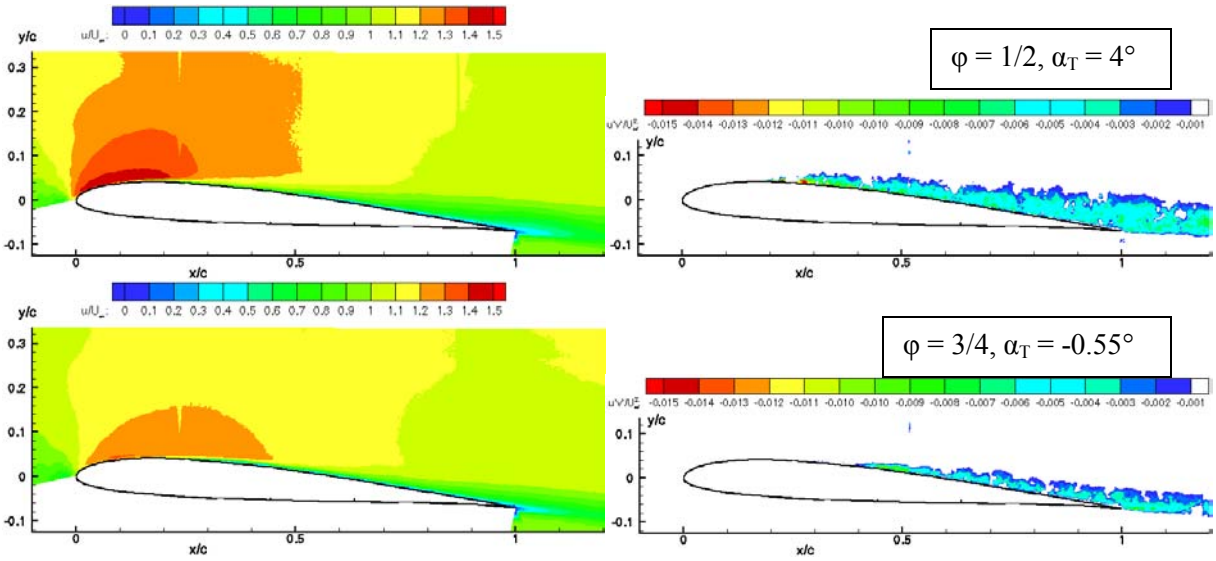

Figure 35. k = 0.80 pure-plunge, contours of phase-averaged (230 realizations) normalized streamwise component of velocity (left) and Reynolds shear stress (right), after periodic conditions established; φ = 0, 1/4, 1/2 and 3/4.

5.2. Extension of HIPPO to 3-DOF

Recognizing that longitudinal motions are spanned by three degrees of freedom (fore-aft, up-down, and rotation), a third linear motor was added to HIPPO in 2009. Since it was impractical to modify the existing pair of motors and the carriage on which they rest, it was necessary to size the third motor to be large enough to move the entire two-motor carriage as a single unit. This was accomplished with a 220V linear motor of 48" stroke, also from H2W. Taking advantage of the unusually long test section of the HFWT, the new motor sits on an aluminum plate over the downstream half of the test section and the exit plenum. Photographs of the three linear motors are given in Figure 36. It the latest iteration, all three motors were rewired with a Galil DMC-4040 Ethernet-based controller, with which a laptop can be plugged into an Ethernet junction box to issue commands and to receive encoder signals. This obviates the need for a dedicated lab computer – a large advantage for modularity.

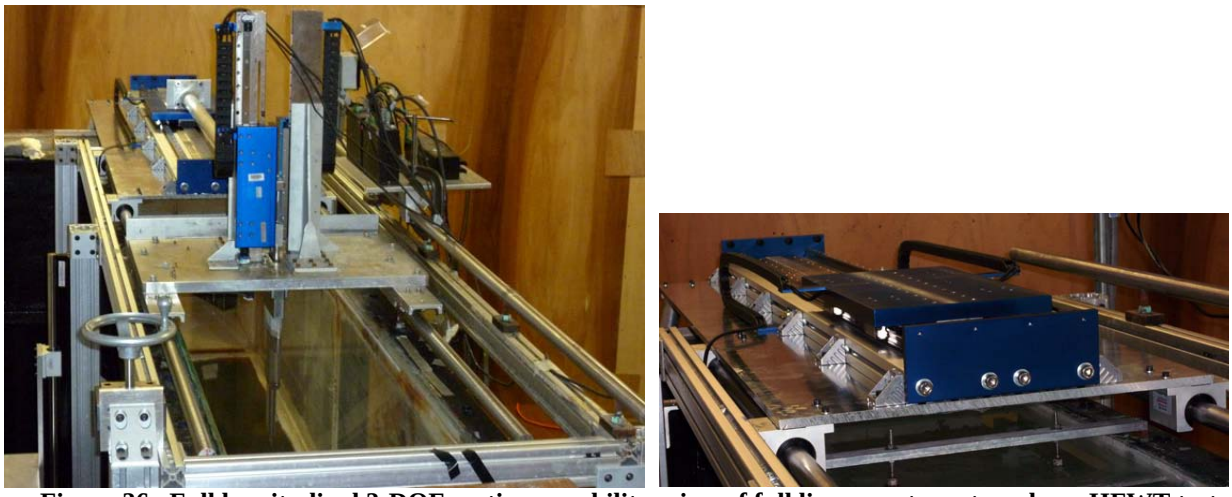

Figure 36. Full longitudinal 3-DOF motion capability; view of full linear motor setup above HFWT test section (left), and detail of linear motor enabling streamwise-direction motion (right).

6. Experiments in Unsteady Aerodynamics using the HIPPO rig

As a resume of research conducted in the past 7 years using the HFWT and HIPPO, we consider the following cases:

1. high-frequency pure-plunge
2. high-frequency pitch: sinusoidal and non-sinusoidal; and pitch-plunge comparison
3. further observations of relaxation from startup for high-frequency pitch
4. airfoil low-frequency pure-plunge and the role of transition for deep stall problems
5. airfoil low-frequency pitch-plunge and the role of transition for shallow stall problems
6. configurational effects in low-frequency motions; repeat of (4) and (5) for a flat plate
7. mixed-frequency problems, where pitch and plunge frequency differ
8. the nonperiodic problem of pitch ramp-hold-return
9. perching, or a generalized form or linear pitch ramp, with varying free-stream speed
10. flapping, here akin to the so-called "normal hover", but with the pitching angle free

Many of the below-mentioned experiments use the SD7003[71] airfoil. The first variant of HFWT model of the SD7003 had 8" or nominally 200mm chord, and was constructed from fiberglass. The second variant had 152.4mm chord and was constructed from 0.030"-thick stainless steel. The latter model consisted of 5 butt-welded segments each burned by wire-EDM from a block of 316 stainless steel. Both models were nominally 457mm span, leaving approximately 1mm (or less) gap from tip to tunnel test section sidewall, and were thus deemed "2D" or wall-to-wall". In most cases the mean angle of incidence was 4°. The airfoil and schematic of geometry are shown in Figure 37, for a typical Reynolds number of 10,000, and nominal values of pitch and plunge amplitude.

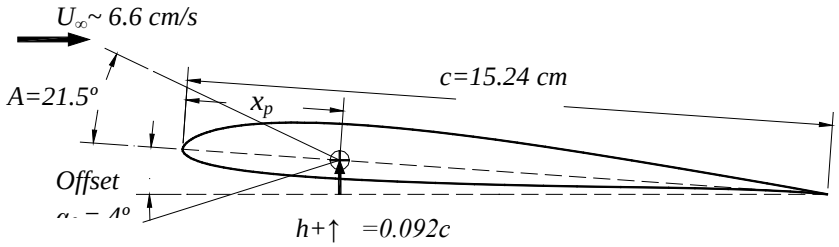

Figure 37. Schematic of airfoil pitch and plunge oscillation.

6.1. High-Frequency Pure-Plunge

6.1.1. Introduction

Plunging airfoils are useful and common abstractions in unsteady aerodynamics for a wide range of applications in low-speed flight, such as helicopter rotors[87]. MAV-related motivations of all three types – fixed-wing, rotary-wing, and flapping-wing – to some extent require departure from classical unsteady airfoil theory[88] and classical dynamic stall[89], in nontrivial and qualitatively important ways. The small size and low flight speed of MAVs necessarily leads to high dimensionless rates of motion, either intentional (aggressive maneuver, wing rotation for "perching", wing flapping in hover and loiter) or unavoidable (response to gusts of high amplitude relative to the vehicle flight speed). The desired underlying knowledge set is how the flowfield and integrated aerodynamic coefficients – lift, drag/thrust, and pitch – vary with angle of attack time history. Periodic, and in particular sinusoidal angle of attack variation is the most attainable and most commonly studied realization in practical laboratory settings.

One can ask how the flowfield relaxes to periodicity upon onset of the forced oscillation[90], and how the flowfield varies from period-to-period once nominal periodicity is attained. Even in the case of strong periodicity, the question is how aerodynamic response lags motion kinematics – that is, to what extent does this response depart from quasi-steady. Matters are further complicated by laminar separations at low Reynolds number, where even in steady airfoil aerodynamic one finds unusual behavior in $C_L = f(\alpha)$[91].

The MAV application, where $C_L>0$ is important, suggests a cambered airfoil with good on-design performance at MAV-relevant Reynolds numbers; the Selig SD7003 airfoil was chosen because of prior work on the static case[42]. Pure-plunge of the SD7003 airfoil[71] at Re = 60,000 at reduced frequency $k \leq 0.80$ was studied by Radespiel et al.[92], to compare the suction-side boundary layer transition and laminar separation bubble between weakly-unsteady and static cases. An extensive study of high-frequency NACA 0012 plunge cases was conducted by Lai and Platzer[93] and Jones et al.[94], where the focus was on thrust-production and wake structure for various combinations of reduced frequency and reduced amplitude.

Plunging motion is defined as $h(t) = h_o cos(2\pi ft)$ with resulting angle of attack time history $\alpha(t) = \alpha_o + arctan\left[2\pi fch(t-\frac{\pi}{2})/U_\infty\right] = \alpha_o + arctan\left[2kh(t-\frac{\pi}{2})\right]$ and maximal extent of angle of attack of $\alpha_T = \alpha_o \pm arctan[2kh_o]$. Following a plunge-case studied by Lai and Platzer[93], we take k = 3.93 (note the factor of 2 difference in definition of *k* between the present definition and that of ref.[93]) and h = 0.05.

6.1.2. Frequency and Reynolds Number Effects

We first consider a qualitative attempt to connect the low-frequency plunge studied by Radespiel et al., with the high-frequency cases considered by Platzer et al. Questions include how the near-wake passes from planar, in the quasi-steady case, to nonplanar and reverse-Karman vortex street[93]; what is the role of leading-edge vortex shedding and its coupling into the wake topology; and how the various flow separations depend on Reynolds number.

Figure 38 shows development of the near-wake for k = 0.80 through k = 2.62, for cosine-wave plunge with h = 0.05. Figure 40 extends the reduced-frequency range to k = 3.93. In both figures, snapshots are at the top and bottom of the plunge stroke. Figure 40 includes both the near-wake and the flowfield over the suction side of the airfoil. Figure 38 is at Re = 60,000, and Figure 40 is at 10,000. In all cases the mean angle of attack is $\alpha_0 = 4^o$, and snapshots were taken at least 5 periods after motion onset, to give good confidence that startup transients have relaxed. Substantiation of this assertion is given further below.

k = 0.80, bottom of plunge

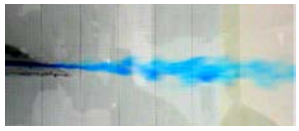

k = 0.80, top of plunge

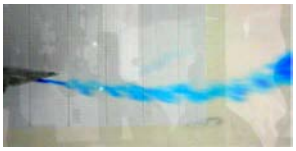

k = 1.31, bottom of plunge

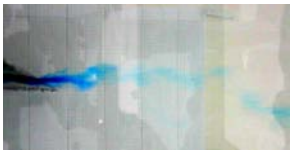

k = 1.31, top of plunge

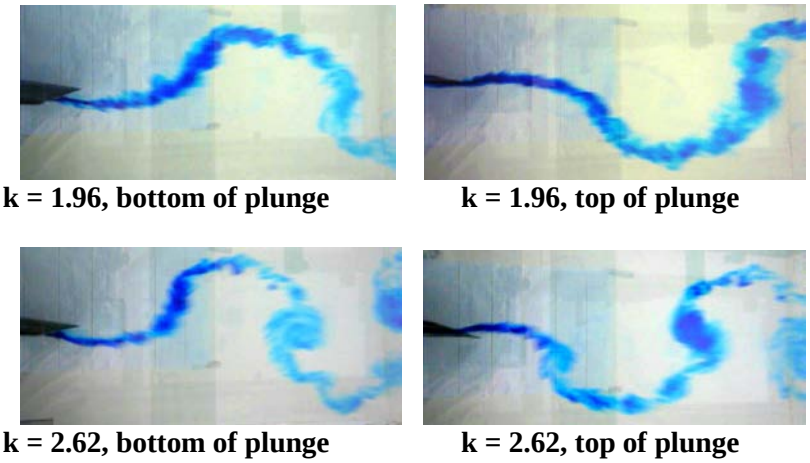

Figure 38. Dye Visualization, Re = 60,000, mean α = 4°, h = 0.05: k = 0.080, 1.31, 1.96 and 2.62, at the top (right-hand-side of page; φ = whole number) and bottom (left-hand-side; φ = n/2).

In Figure 39 the near-wake is rolling up into a reverse-Karman vortex street, much akin to that reported in Ref. 93 and [95], despite the large difference in Reynolds number and airfoil shape, and the nonzero mean angle of attack. Visualization of the flow over the suction-side of the airfoil is by injection just downstream of the leading edge. On the pressure side, visualization of the near-wake is by injection at the trailing edge, also on the pressure side. While for the latter the dye stream is thinner and more coherent, qualitatively the near-wake as resolved by the two injection methods looks similar. We observe, therefore, that the dye injection is not intrusive, despite the obvious presence of the injection probe.

On the suction side of the airfoil, the formation of a small dynamic-stall vortex[96] is discernable, shortly before the bottom of the plunge stroke. This vortex is not shed into the bulk flow, but convects along the airfoil surface essentially at the free-stream velocity. The same vortex from the previous period of oscillation is visible further downstream just ahead of the trailing edge. It does not, however, appear to strongly interact with vorticity shed from the trailing edge, in the form of a merged trailing-edge – leading-edge vortex pair.

Returning to Figure 38, at k = 2.62, the wake is akin to a reverse Karman street, but does not yet evince strong vortex rollup. At k = 1.96 there is still strong wake curvature, but no discernable rollup at all. By k =0.80, the near-wake appears almost planar, although at approximately 10 chord lengths downstream of the trailing edge, a sinusoidal dye streak (not shown) is visible. Interestingly, at low reduced frequency there is no regular Karman vortex street, akin to a bluff body. This is evidently because of the comparatively high Reynolds number (60,000), which is near the on-design condition of this airfoil. In contrast, a NACA 0012 will have clearly discernable Karman-type shedding at conditions where bluff-body-type behavior overwhelms the motion-induced shedding.[97]

It appears, then, to be broadly the case that as reduced frequency increases – while reduced amplitude is held constant – that "Reynolds number effects" become more benign. Indeed, comparing Re = 10,000 – 20,000 – 40,000 – 60,000 for k = 3.93, h = 0.05 at the bottom of the plunge stroke (Figure 41), the near-wake is essentially indistinguishable over this Reynolds number range. Of course, at the higher Re there will be more mass-diffusion, whence the dye streaks will be of lower contrast. There may also be viscous-effects in regions of high shear, such as interior to vortex cores and in the feeding-sheets connecting shed vortices.

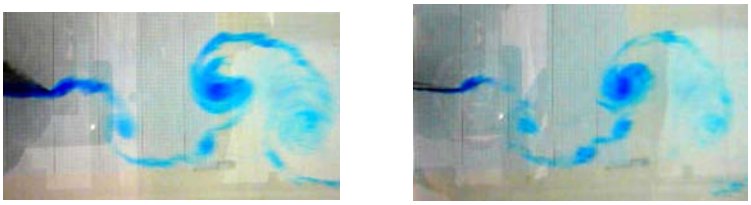

Re = 60,000 **Re = 40,000**

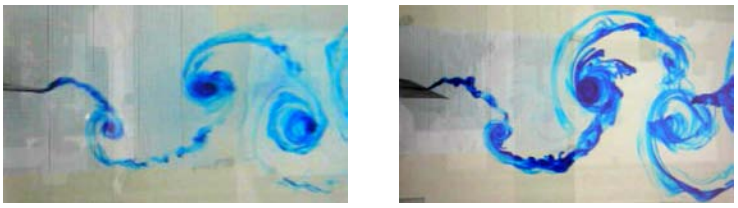

Re = 20,000 **Re = 10,000**

Figure 39. Re = 10,000 to 60,000, mean α = 4°, h = 0.05: k = 3.93, established flow, top of the plunge stroke.

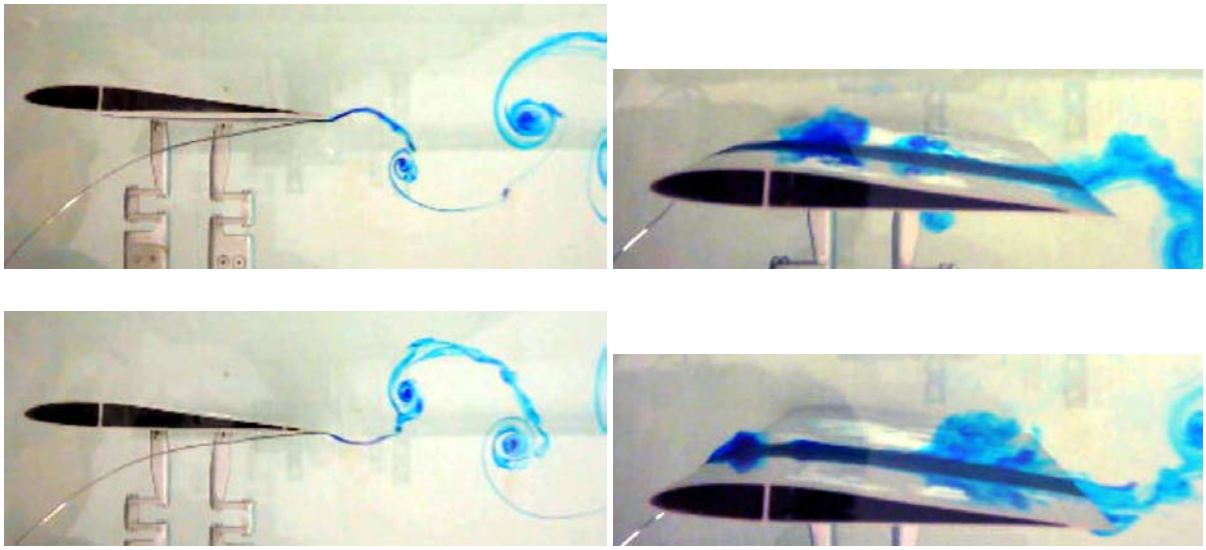

Figure 40. k =3.93, Re = 10,000: near-wake (left) and over the airfoil suction-side (right); top of stroke (upper two images) and bottom of stroke (lower two images).

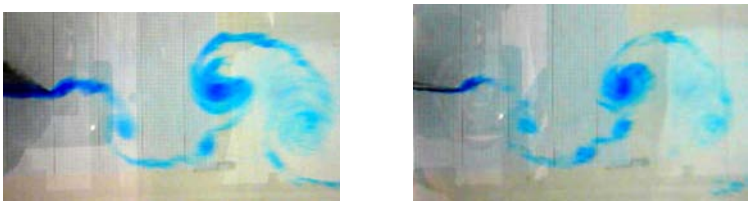

Re = 60,000 **Re = 40,000**

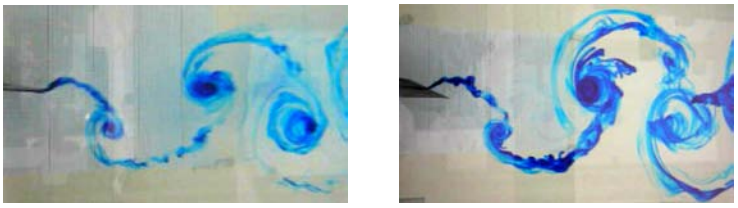

Re = 20,000 **Re = 10,000**

Figure 41. Re = 10,000 to 60,000, mean α = 4°, h = 0.05: k = 3.93, established flow, top of the plunge stroke.

6.1.3. Plunge at k = 3.93, Re=40,000 and Re = 60,000

We now consider PIV velocity and vorticity results, for the representative high-frequency case of k = 3.93, h = 0.05. Results are reported for four phases of motion: top of the plunge stroke ($\varphi=0$), halfway on the downstroke ($\varphi=1/4$), bottom of the plunge stroke ($\varphi=1/2$), and halfway on the upstroke ($\varphi=3/4$). At the two halfway phases, the effective angle of attack is just the mean angle of attack – again, $\alpha_T = \alpha_0 = 4°$. At $\varphi=0$, $\alpha_T = \alpha_0 + \text{atan}(\dot{h}/U_\infty) = 21.5°$, while at $\varphi=1/2$, $\alpha_T = \alpha_0 + \text{atan}(\dot{h}/U_\infty) = -17.5°$. Static stall for this airfoil, meanwhile, occurs at approximately $\alpha = 11°$[107] at Re = 60,000.

Figure 42 compares instantaneous PIV vorticity contour plots with phase-averages, based on 120 image pairs for each, at Re = 40,000. Vorticity was normalized by airfoil chord and freestream velocity, with the near-zero levels blanked off for clarity, and limits set somewhat arbitrarily at ± 36. The region below the pressure-side of the airfoil is also blanked, as it is in the shadow of the PIV light sheet.

While spurious vorticity ("noise") is apparent in the instantaneous images and absent in the phase averages, rendition of concentrated vorticity – over the airfoil suction-side and in the near-wake – is very close between instantaneous and phase-averaged, suggesting strong periodicity. This holds even for the discretization of vorticity concentrations in feeding sheets, especially at $\varphi=1/2$.

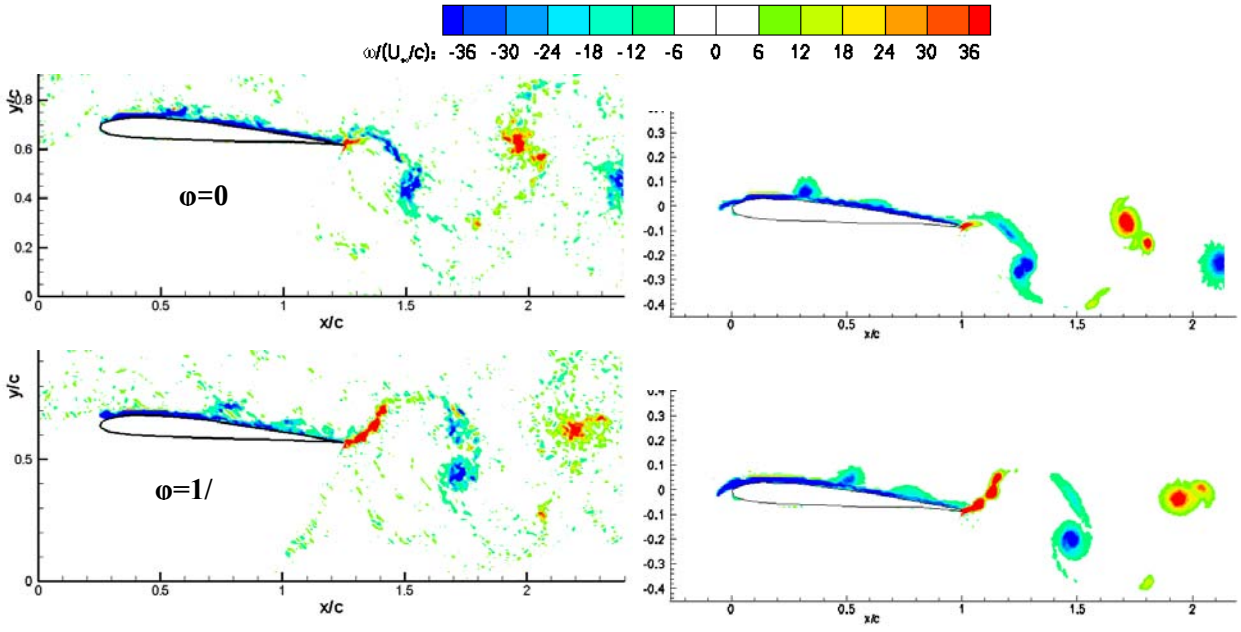

φ=1/

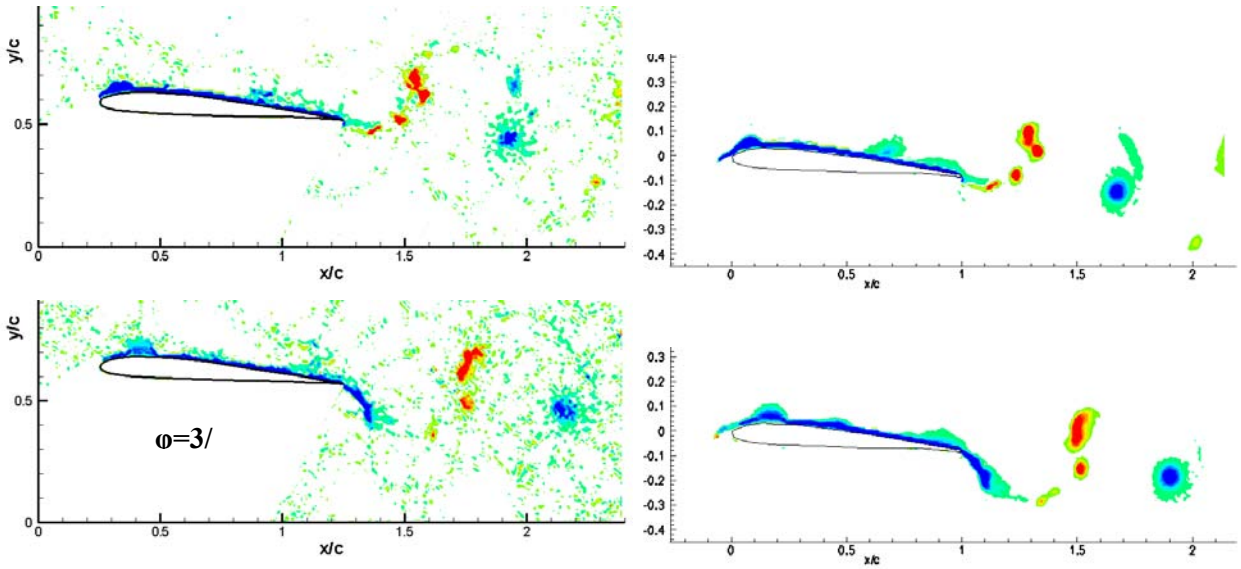

Figure 42. Vorticity contours based on single image pairs for four phases within the cycle. k= 3.93, Re = 40,000.

6.1.4. Strouhal Number and Reduced Amplitude

Lai and Platzer[93] point out for a NACA0012 airfoil in plunge that the production of net wake-like or jet-like momentum after the trailing edge varies with the product kh (proportional to Strouhal number), and not k or h individually. However, h individually seems to govern the size of shed vortices in the near-wake. The conclusion is broadly the same for the SD7003 with mean $\alpha = 4°$, investigated here. Figure 43 and Figure 44 cover three realizations of (k, h) each; the former for $kh = 0.196$ (St = 0.125) and the latter for $kh = 0.591$ (St = 0.376). In Figure 43 the starting-flow looks different for the different values of k, while qualitatively the established flow – as instantiated at the top and at the bottom of the plunge stroke – looks broadly invariant; the difference is linear scaling of vortex size, vertical and horizontal separation, which is essentially linear with h. In Figure 44 even the starting-flows for different k look qualitatively alike, with the same linear scaling of feature size with respect to h. In Figure 44 there is evidence of nonzero mean angle of the wake trajectory, akin to observations made by Jones et al.[94] for the NACA0012 at zero mean angle of attack. While a cambered airfoil at nonzero angle of attack intuitively suggests a nonzero wake trajectory angle, this happens only for sufficiently high St. Evidently, the wake follows the Strouhal number criteria identified by Jones et al. below a St threshold (~0.3, in the present notation) the wake will be symmetric, and vice versa.

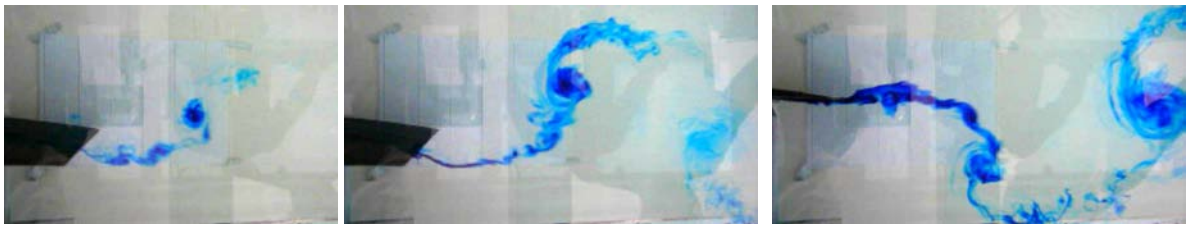

k = 1.96, h = 0.1, φ = 0.5 **k =1.96, h = 0.1, φ = n*0.5** **k = 1.96, h = 0.1, φ = n**

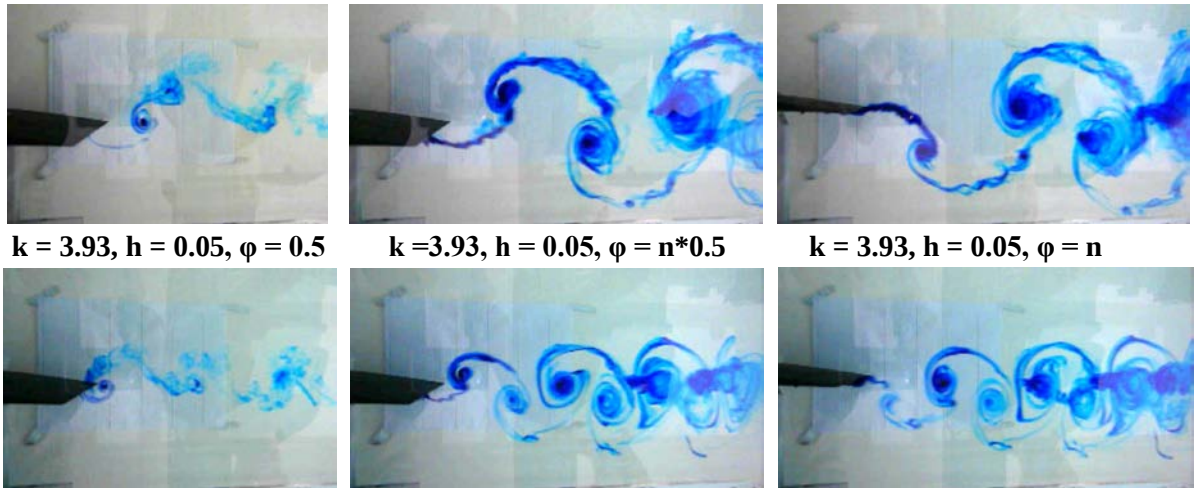

k = 3.93, h = 0.05, φ = 0.5 **k =3.93, h = 0.05, φ = n*0.5** **k = 3.93, h = 0.05, φ = n**

k = 7.85, h = 0.025, φ = 0.5 **k =7.85, h = 0.025, φ = n*0.5** **k = 7.85, h = 0.025, φ = n**

Figure 43. Pure-plunge, Re = 20,000, mean α = 4°; three cases of kh = 0.196, and three motion phases: φ = 0.5 after start-up (bottom of stroke), bottom of stroke in established flow, top of stroke in established flow.

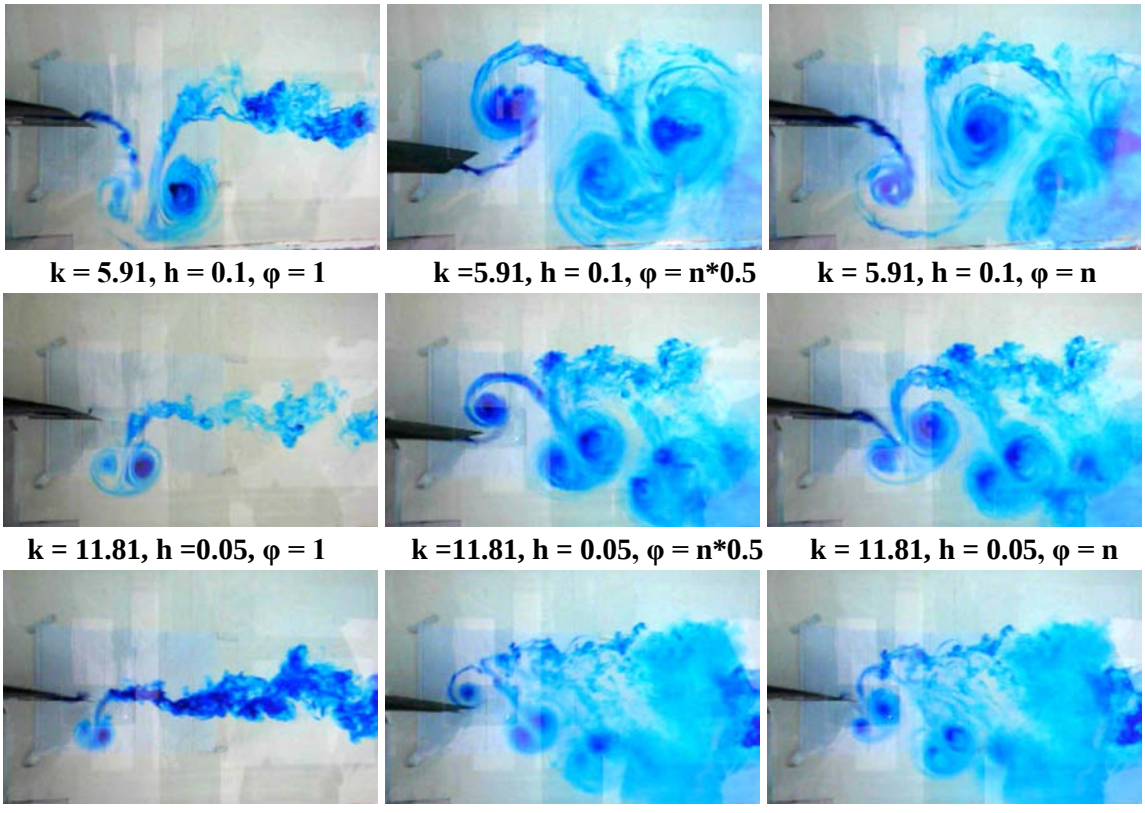

k = 5.91, h = 0.1, φ = 1 **k =5.91, h = 0.1, φ = n*0.5** **k = 5.91, h = 0.1, φ = n**

k = 11.81, h =0.05, φ = 1 **k =11.81, h = 0.05, φ = n*0.5** **k = 11.81, h = 0.05, φ = n**

k = 23.62, h = 0.025, φ = 1 **k =23.62, h = 0.025, φ = n*0.5** **k = 23.62, h = 0.025, φ = n**

Figure 44. Pure-plunge, Re = 20,000, mean α = 4°; three cases of kh = 0.591, and three motion phases: φ =1 after start-up (top of stroke), bottom of stroke in established flow, top of stroke in established flow.

6.1.5. Start-up and Relaxation to Periodicity

While favorable comparison between phase-averages and instantaneous PIV suggests reliable relaxation to periodicity at some time after motion onset, it remains to track how long this relaxation process takes. Figure 45 shows the evolution of the near-wake from motion onset through 10 periods of oscillation, again for k = 3.93, h = 0.05, Re = 60,000. The starting vortex is clearly visible at φ = ½. It convects downstream away from the trailing edge at approximately the free-stream velocity; at φ = 1 after motion onset, its core is ~0.8c downstream of the trailing edge. The starting transient dissipates (the flow relaxes to periodic) by φ ~ 2. This is evidenced by the similarity of the wake at φ = 2 and φ =10. Comparing φ = 3/2 and φ = 3/2, the first vortex pair upstream of the starting vortex – that is, φ = 3/2 – is very similar to its companion pair at φ = 3/2. Evidently, all vortex shedding subsequent to the starting vortex is essentially periodic. This contrasts with the much longer relaxation to periodicity for higher-amplitude motions at the same reduced frequency, implying a Strouhal number dependency as well as a reduced-frequency dependency.

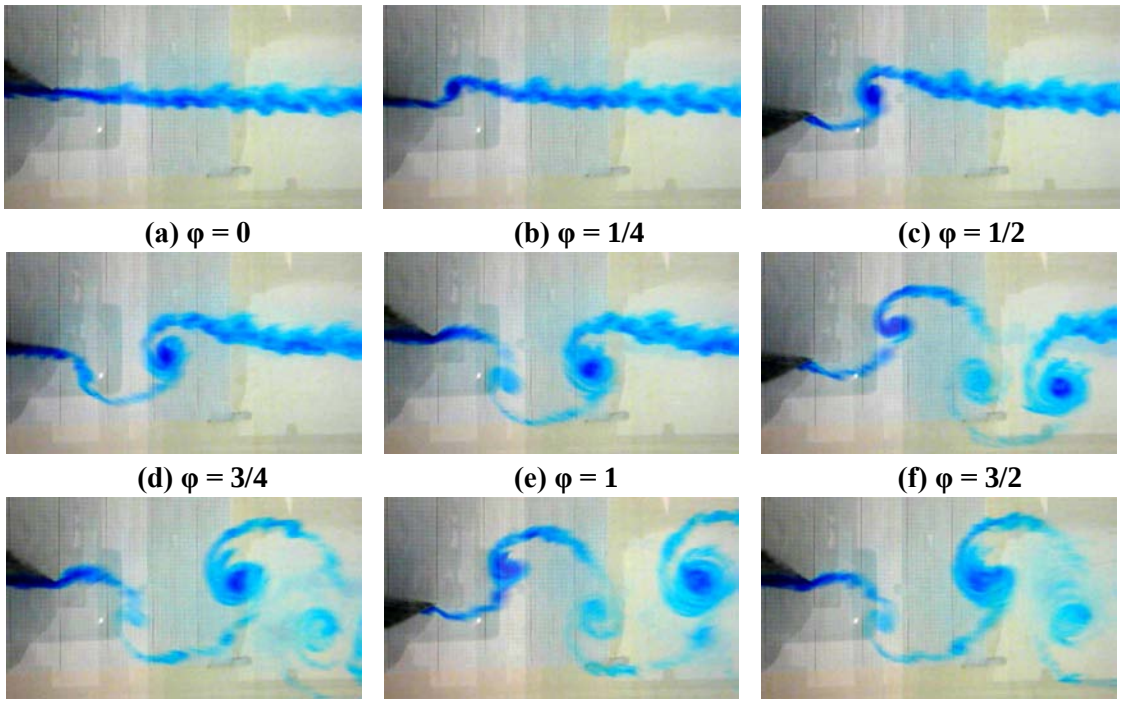

(a) φ = 0 **(b) φ = 1/4** **(c) φ = 1/2**

(d) φ = 3/4 **(e) φ = 1** **(f) φ = 3/2**

(g) φ = 2 **(h) φ = 5/2** **(i) φ = 10**

Figure 45. Dye streaklines for near-wake, *h* = 0.05 *k* = 3.93 plunge; evolution of starting-flow across 10 periods of motion. Re = 60,000.

6.1.6. Nonzero Mean Angle of Attack

The present study was in part an outgrowth of work on steady-state airfoil laminar separation bubbles, focusing on a cruise-type angle of attack of α = 4° [42]. Most pitching/plunging studies have been for mean α = 0° and for symmetric airfoils (NACA0012 is justifiably popular). The principal pure-plunge case, *k* = 3.93 and *h* = 0.05, is revisited at Re = 20,000 for mean α = 0°, 4° and 21.5° (Figure 46) – the latter being the increment of induced- α from the plunge itself, at the point of maximal vertical velocity. The α = 0° and 4° cases are similar, with the exception that dye streaks are rather finer for α = 0°. The α = 21.5° case shows strong interaction between the vortex shedding and the viscous wake of the airfoil, in the bluff-body sense.

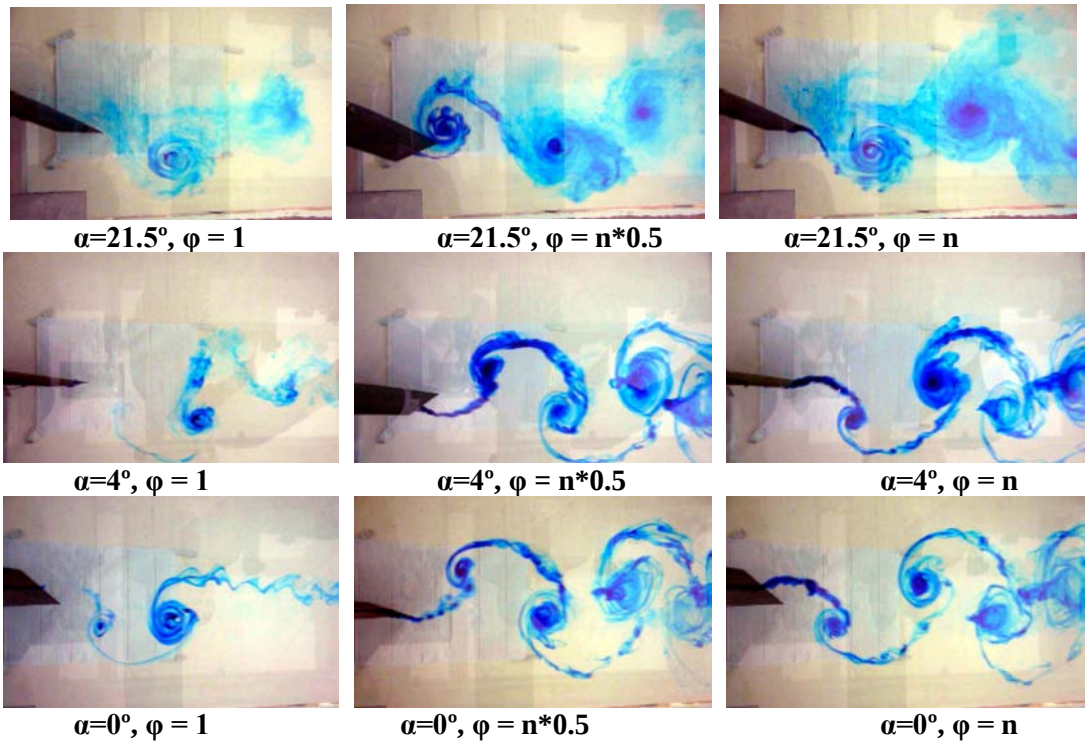

Figure 46. Pure-plunge, Re = 20,000, mean α = 21° (top row), 4° (middle row) and 0° (bottom row); h = 0.05, k = 3.93; left column: φ =1 after start-up (top of stroke); middle column: bottom of stroke in established flow; right column: top of stroke in established flow.

6.1.7. Summary

The presently-reported results for a SD7003 airfoil are in good accord with results given in the literature for the venerable NACA 0012. This gives reason to believe that the effects of a relatively intrusive model mounting, where the support rods bisect the pressure-side of the airfoil, does not greatly detract from a flow state commensurate with 2D expectations. Small nonzero mean angle of attack and airfoil nonzero camber do not cause significant departure from established results for NACA0012 plunge at k = 3.93, h = 0.05. However, for the Reynolds numbers studied here, no Karman vortex street was seen at low reduced frequencies, where viscous shedding dominates motion-induced shedding. Once the flowfield response has relaxed to periodicity, there is little difference in either the near-wake or in the flow over the airfoil suction side, between instantaneous PIV and phase-averages. Relaxation to periodicity for k = 3.93 and h = 0.05 is quite fast, taking less than two periods of oscillation.

This fundamental study leads to important and useful conclusions for MAV designers. First, this combined experimental and computational study serves as a step toward the ultimate goal of accurately predicting unsteady flow fields, and hence unsteady forces and moments, for an aircraft with flapping wings. Verification using relatively simple test cases is necessary in order to build confidence in new computational methods and, verification in this instance, applies specifically to an airfoil operated in pure plunge within the regime where the wake is symmetric. The asymmetric wake at large kh, which is also consistent with the literature, suggests a flow pattern which is quite complex, even when the airfoil motion is quite simple. Second, the results clearly illustrate that the flow field for an airfoil undergoing pure plunge, the vortex dynamics are not significantly altered by Reynolds number, within the range of Re = 10,000 to 60,000. As in most traditional applications, the establishment of Reynolds number independence in trends related to the flow field, and hence the pressure distribution on the aircraft, is important because the scale of a test article and fluid media may be different from that of the actual flight vehicle operating in air. In the case of MAVs, there may be instances where a larger model might perhaps

be simpler to build and more convenient to use in experiments. These results show that valuable testing might be conducted for a scaled-up, rather than scaled-down, model as long as the reduced frequency is taken into account.

6.2. Sinusoidal, Trapezoidal and Triangular Pitch; and Pitch-Plunge Comparison

6.2.1. Introduction and Problem Statement

Flapping in nature tends to be nonsinusoidal, and in any case, purely sinusoidal motions have limited frequency content. A more general study of pitch and plunge in two dimensions begs consideration of nonsinusoidal motions, and fortunately this is easy to achieve with the HIPPO apparatus. One example of nonsinusoidal motions is skewed sinusoidal time trace of pitch angle of attack, studied by Koochesfahani[97].; this produced various interesting wake vortex pairings not seen for sinusoidal motions. An alternative approach, pursued here, is to consider an amalgamation between ramp-type motions and sinusoidal periodic motions, where the motion has sharp corners and linear segments of velocity, but remains periodic. The idea is that discontinuities in acceleration – or at least, practically realizable approximations thereto – may result in significant departures from sinusoidal motions with identical reduced frequency and extremes of angle of attack, but where position time history in finitely differentiable. As a secondary objective we consider similarities in leading edge vortex shedding between pure-pitch and pure-plunge oscillations. Such comparisons are not new to the dynamic-stall literature (for example, Fukushima and Dadone[98]), but the subject can be extended to Micro Air Vehicle applications with more detailed information on shed vorticity, enabled by ease of flow visualization in water at high reduced frequencies.

We present a sequence of experiments at the same reduced frequency and angle of attack amplitude, but differing in kinematics:

1. Sinusoidal pitch, pivoting about $x_p = 0.25$, $\alpha(t) = \alpha_0 + A\cos(2\pi ft + \varphi)$.
2. Trapezoidal pitch, $x_p = 0.25$.
3. Linear-ramp or triangular pitch, $x_p = 0.25$.
4. Sinusoidal plunge, $h(t) = h_0 \cos(2\pi ft)$, $h_0 = 0.092$, with offset angle $\alpha_0 = 4°$.

All pitch motions commence with the airfoil at its maximum angle of incidence (=25.5º), for continuity of pitch speed from rest. Thus the first half of the first period of motion can be considered in isolation as a return-from-stall ramp motion.

Idealized time-traces of the pitch angle of attack for sinusoidal, trapezoidal and linear-ramp motions are shown in Figure 47, including the phases of motion at which PIV and/or dye-injection data are presented; values of geometric incidence for pitch are with respect to the left-side vertical axis. The choice of phases at which to take data is motivated by the trapezoidal pitch, where phases "a", "c", "e" and "g" are at the vertices of the trapezoid, while "b" and "f" are halfway on the downgoing and upgoing strokes, respectively.

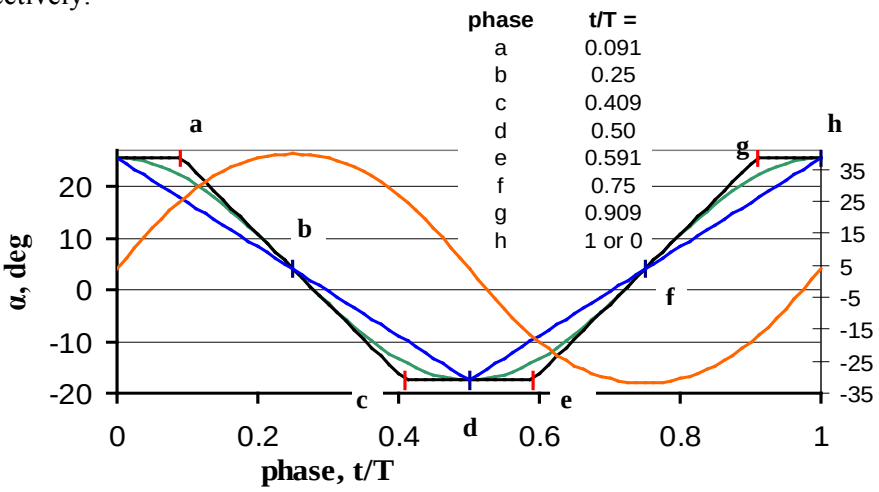

Figure 47. Sinusoidal (green), trapezoidal (black) and triangular (blue) time traces of pitch angle; and sinusoidal plunge-induce angle of attack (orange). "a" – "h" mark phases where data were taken.

For the sinusoidal plunge, the quasi-steady motion-induced angle of attack is shown as the orange curve in Figure 47, denoted with respect to the right-hand vertical axis. The quasi-steady motion-induced angle of attack amplitude with h_0 =0.092 is $\alpha_e = -\arctan(\dot{h}/U_\infty) = 36.0^o$; vs. 21.5º pitch geometric incidence amplitude. h_0=0.092 is equal to the airfoil leading edge peak displacement with 21.5º pitch and $x_p = 0.25$. It is 90º out of phase with the pitch motions, as the plunge motion begins with the airfoil at rest at the top of the stroke; the angles of attack are with respect to the right-side vertical axis. The phase difference between pitch and plunge has a significant effect on the startup conditions and relaxation to time-periodicity, but not on the time-periodic flow. Also, we note that the time trace of angle of attack for plunge with sinusoidal variation of elevation is itself not strictly sinusoidal.

The triangular motion or linear ramp simply connects peak positive and negative pitch angles in the sinusoid, while the trapezoidal motion matches the maximum positive and negative pitch rates of the sinusoid. The motivation of the trapezoidal motion is that by matching the sinusoid's angle of attack limits and peak rates, the principal terms of the circulatory lift in quasi-steady airfoil theory look identical – suggesting that flowfield velocity and vorticity history should look similar, if linear concepts remain valid. The triangular pitch, on the other hand, has a lower pitch rate of nominally constant magnitude, with an "instantaneous" switch of direction at upper and lower extremes of angle of attack.

6.2.2. Flowfield History from Startup: Dye Injection Results

We first consider dye injection for the four classes of motion, showing evolution from startup for 8 periods of motion for the pitch cases, and 5 periods of motion for the plunge. Trapezoidal pitch is shown in Figure 48 and continued in Figure 49; sinusoidal pitch is shown in Figure 50 and continued in Figure 51; and triangular pitch is shown in Figure 52 and continued in Figure 53.

In an effort to minimize the number of pictures while adequately resolving salient features, formatting of these figures is as follows: the trapezoidal and sinusoidal pitch cases are shown in phases "a", "b", "c", "e", "f", and "g". Phase "d" is similar to "c" and "h" is similar to "g", especially for the trapezoidal case, where theoretically there is no motion between those respective phases. The triangular pitch case is shown in phases "a", "b", "d", "e", "f" and "h", retaining the extremes of motion at "d" and "h". For all of the pitch cases, commencement of oscillation from a deep-stall incidence angle requires 4-5 periods to reach time-periodicity; that is, where snapshots of the n+ 1st cycle are not substantively distinguishable from the nth. The physical period of oscillation is 1.846s, or 0.8 convective times. Thus, relaxation to periodicity takes as many as 4 convective times. But as will be discussed in the subsequent section, large-amplitude large-frequency pitch ramps have a subtle relationship of flowfield evolution with starting conditions, which is ultimately related to Strouhal number.

Dye injection results for 5 periods after startup for the plunge case are given in Figure 54 for phases "a", "b" and "d", and continued in Figure 55 for phases "e", "f" and "h". Not surprisingly, because the motion commences from α_0 =4º and not from deep-stall, the relaxation to time-periodicity takes fewer periods of oscillation than reported for the pitch cases above; by the fourth period, if not sooner, the flow has reached periodicity.

The two motions with discontinuity in angle of attack rate – trapezoid and triangle – evince a concentrated vortex shedding just downstream of the trailing edge, in phase a and especially phase f. This is most pronounced for the triangle, which has the largest alpha rate discontinuity. The sinusoid has a more ambiguous TE vortex formation, and a strong vortex is not evident until phases b and f, where pitch rate is maximum. The principal distinction between the trapezoidal pitch the other two cases is the former's double-formation of shed vortices twice per stroke. This is clear in the dye injection images in phase "f" (circled in red in period-8, phase-f of Figure 49), and to a lesser extent in phase "b" (circled in red in period-8, phase-b of Figure 48. The greater clarity of vortex-doubling in phase f vs. b is ascribed to

the camber of the airfoil and positive offset, $\alpha_0 = 4^o$. Vortex-doubling is apparent as early as the second period, at least for phase f.

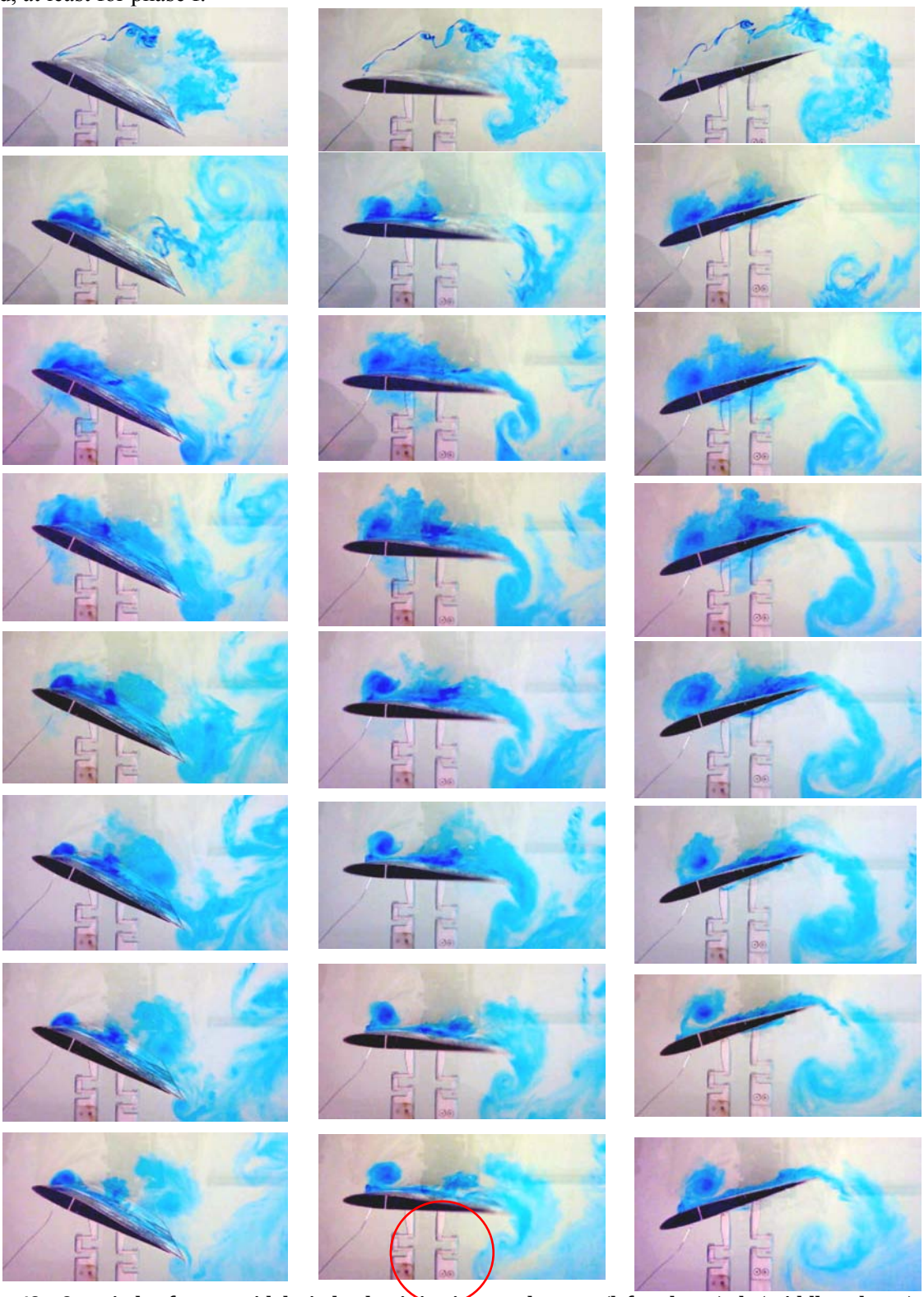

Figure 48. 8 periods of trapezoidal pitch: dye injection at phases a (left column), b (middle column) and c (right column); time from motion onset is from top to bottom. Top row is first period, second row is second period, and so forth, down to the 8th period. Double trailing vortex system is circled.

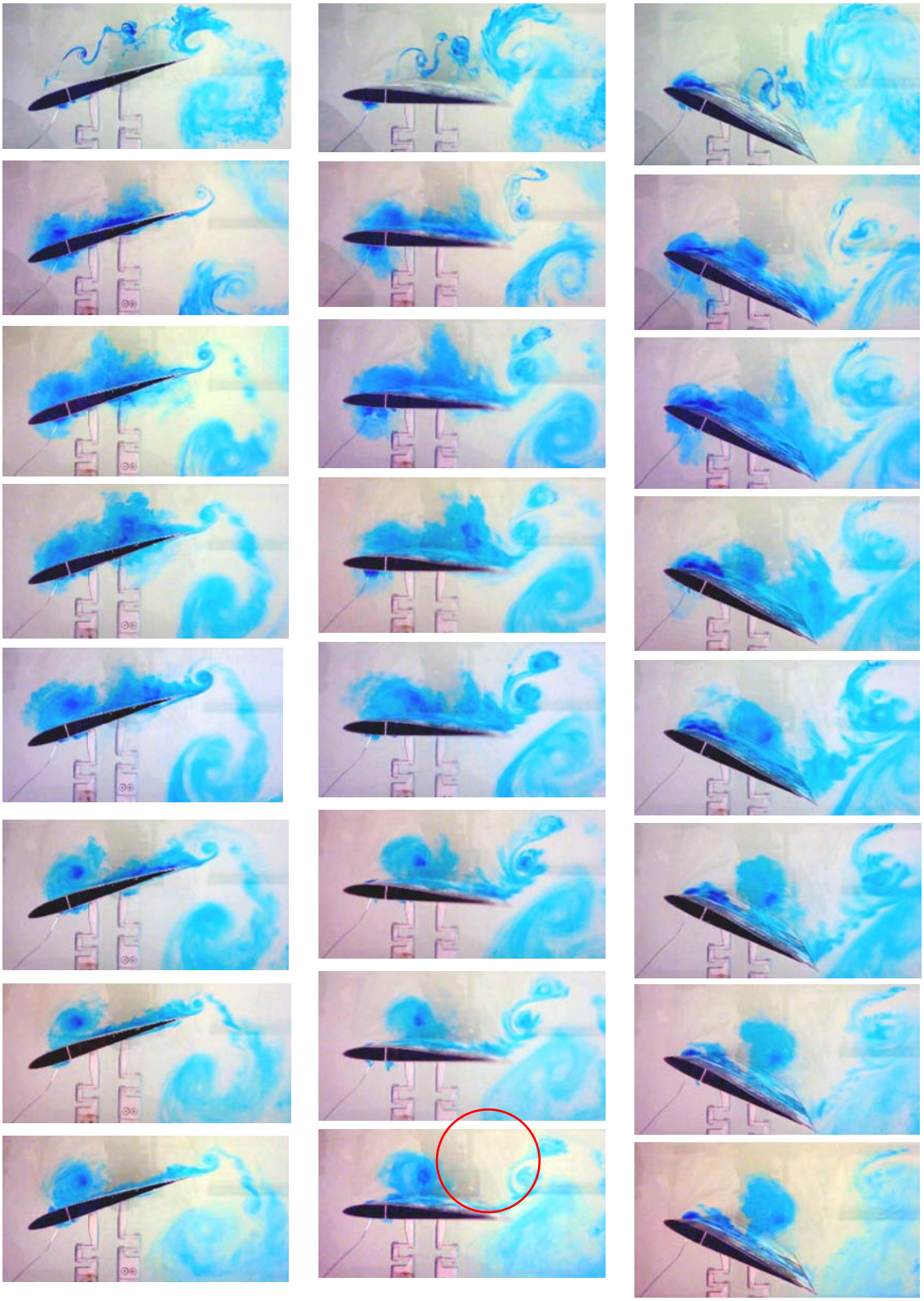

Figure 49. 8 periods of trapezoidal pitch, continued: sampling at phases e, f and g.

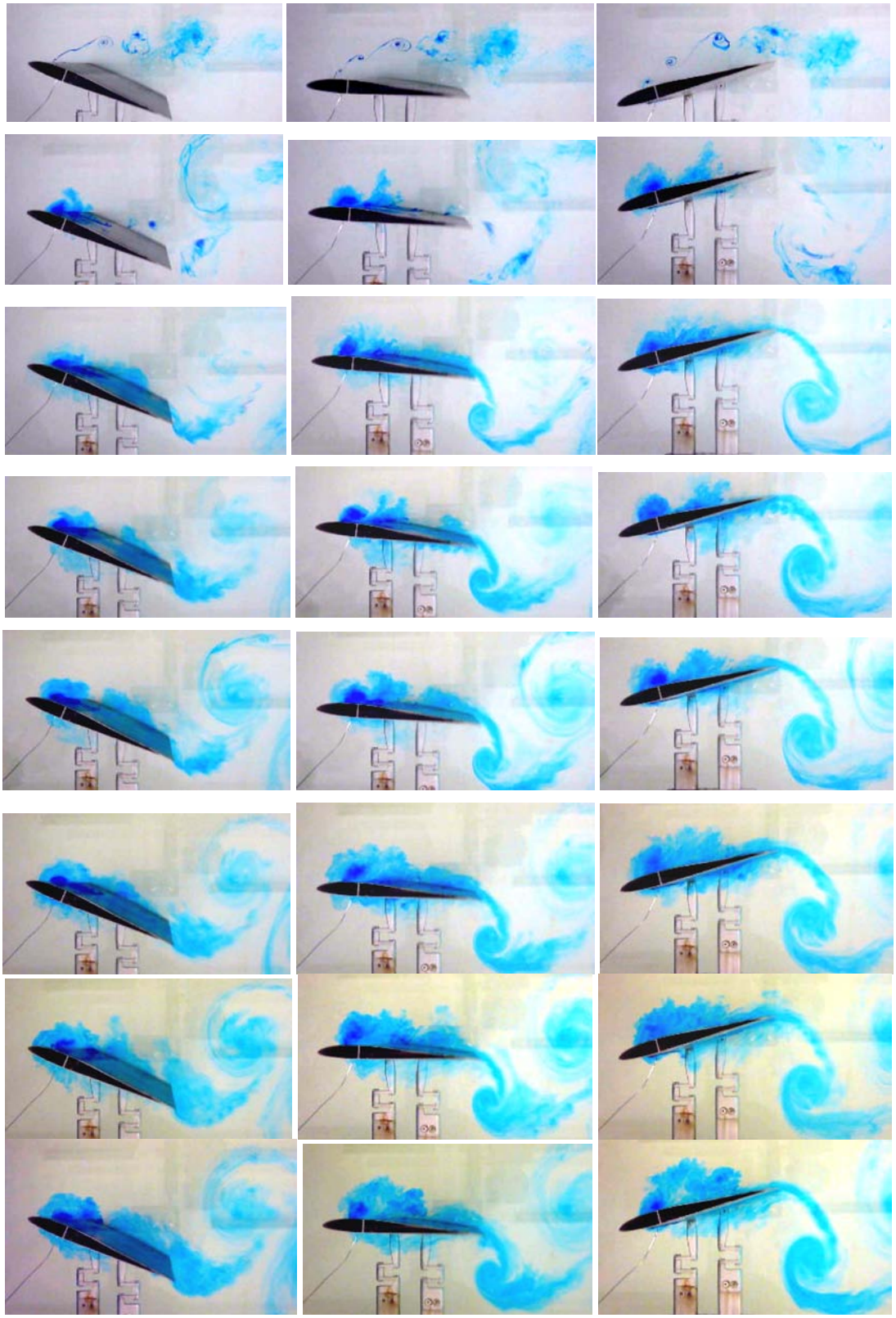

Figure 50. Sinusoidal pitch dye injection: phases a (left column), b (middle column) and c (right column). Top row is 1st period, 2nd row is 2nd period,…, bottom row is 8th period.

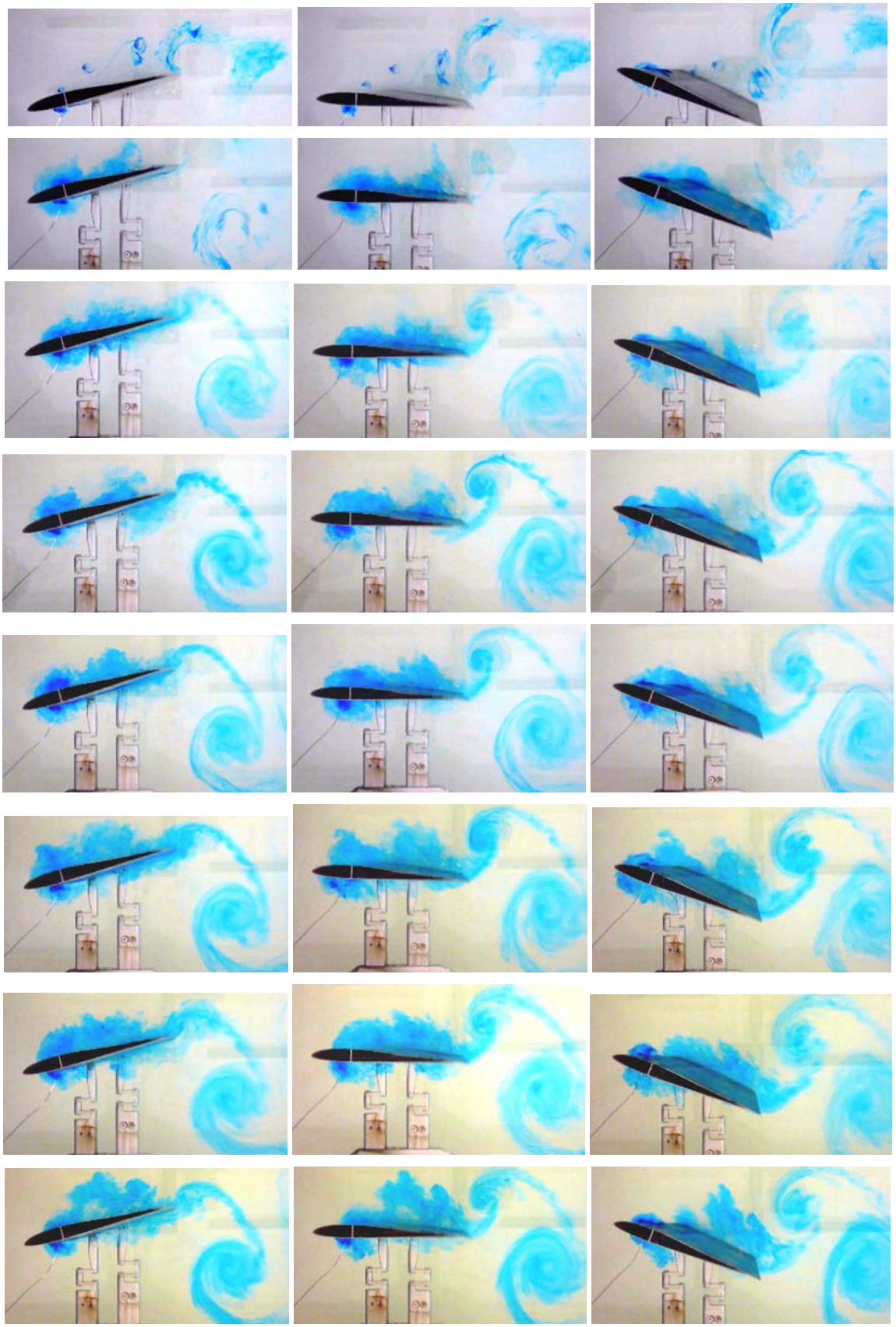

Figure 51. Sinusoidal pitch dye injection, continued: phases e, f and g.

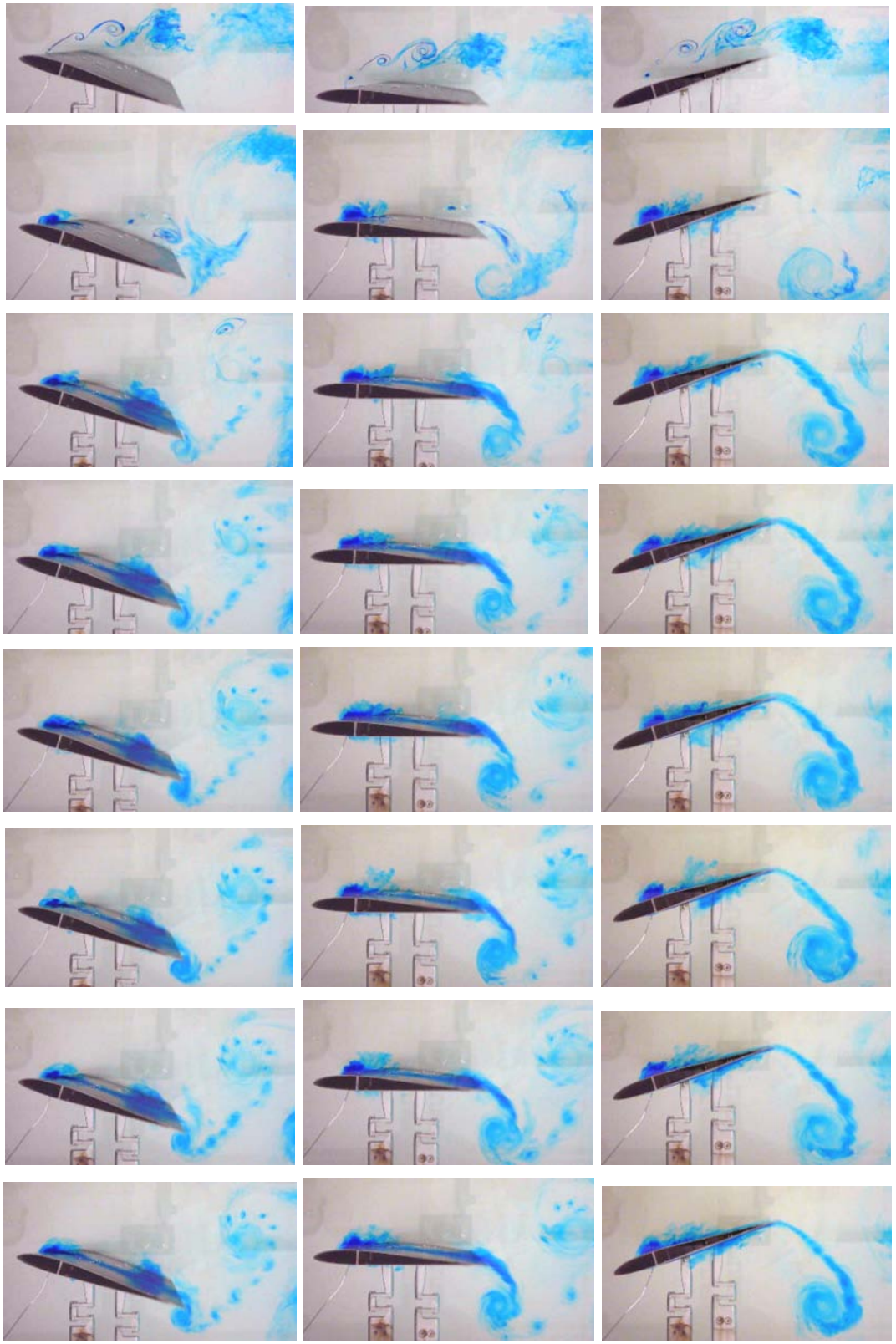

Figure 52. Triangular (linear ramp) pitch dye injection: phases a, b and d.

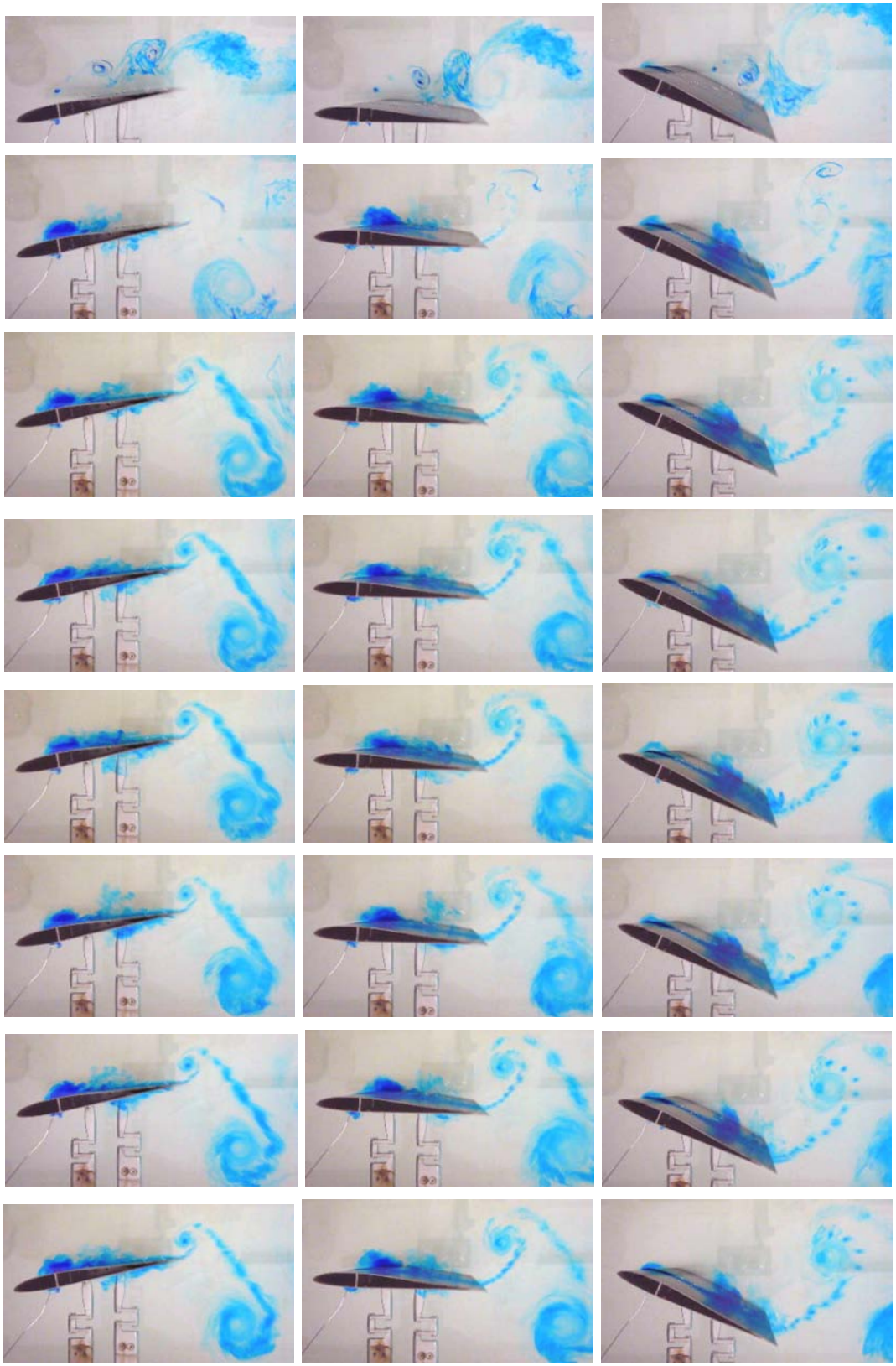

Figure 53. Triangular (linear ramp) pitch dye injection, continued: phases e, f and h.

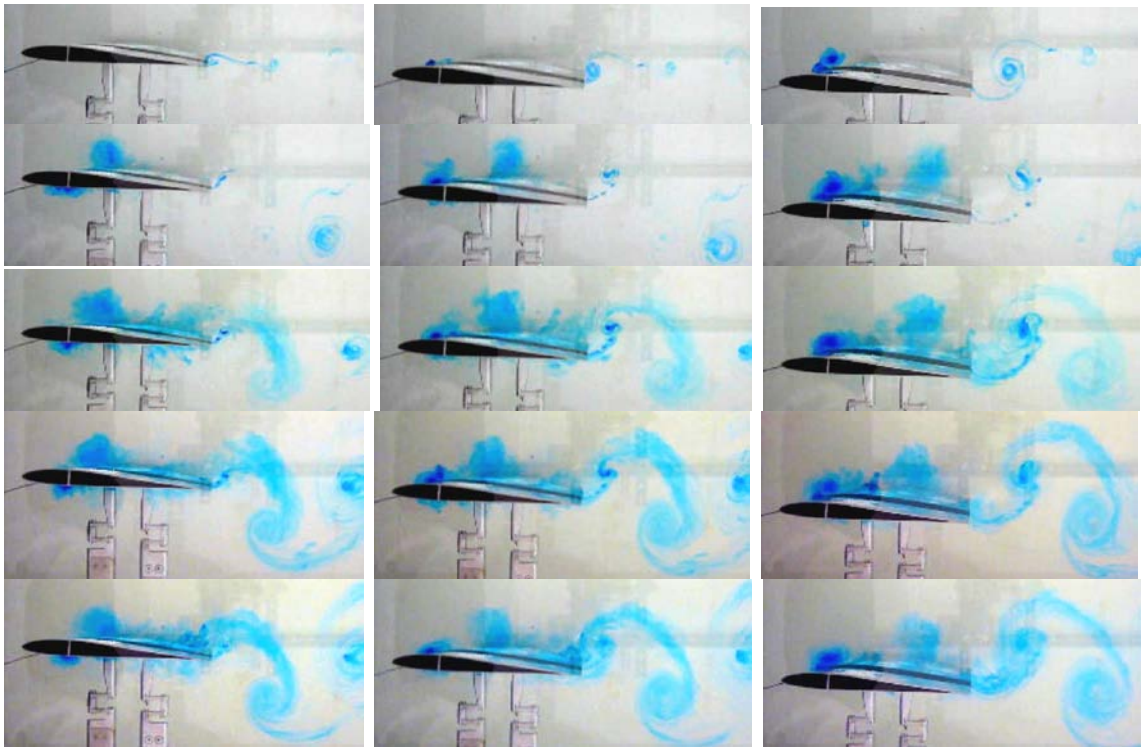

Figure 54. Sinusoidal plunge dye injection, 5 periods of motion, phases a, b and d.

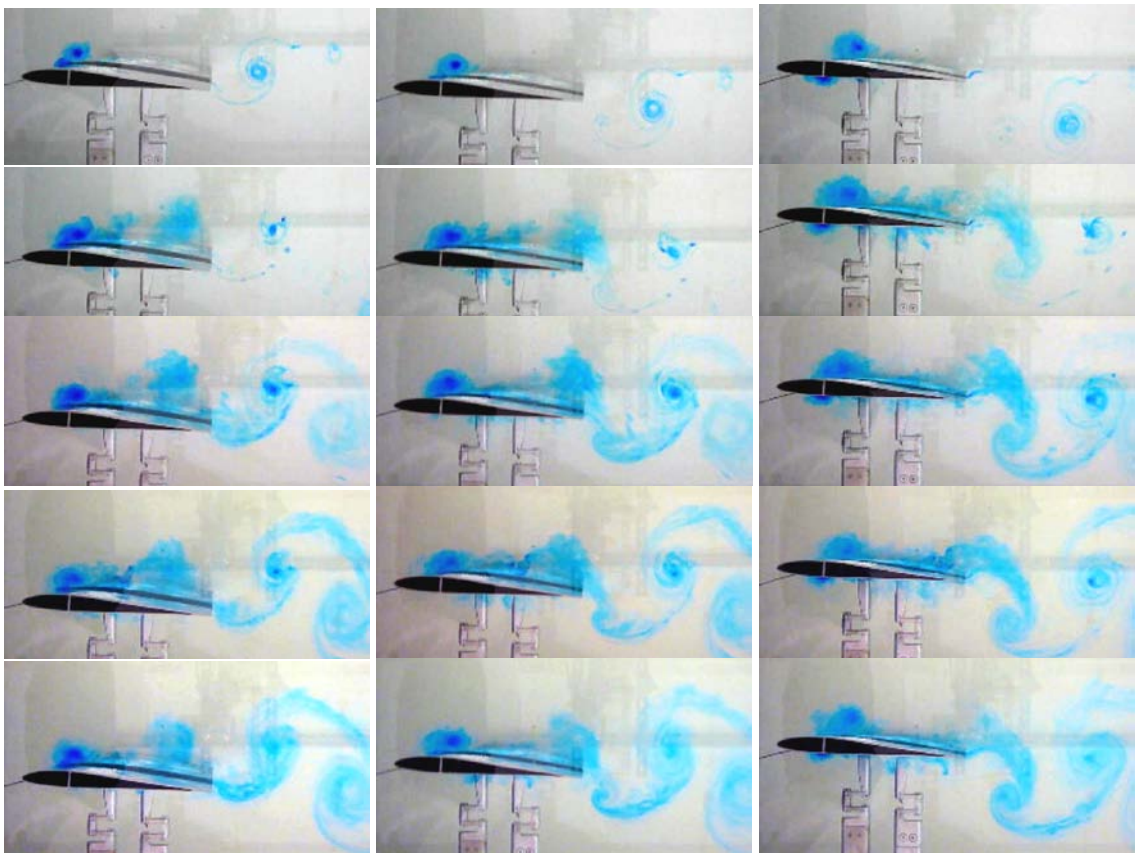

Figure 55. Sinusoidal plunge dye injection continued, phases e, f and h.

6.2.3. Established Flowfields: PIV Measurements

We next consider the sinusoidal and trapezoidal pitch cases after the flowfield response has relaxed to time-periodicity. PIV data were taken in sequences of 120 image pairs per motion phase ("a" through "h" for trapezoidal, "b", "d", "f" and "h" for sinusoidal), with the first 5 pairs disregarded and the remaining 115 ensemble-averaged for each phase (Figure 56). The aforementioned vortex doubling for the trapezoidal pitch is also clear from the phase-averages in the respective phases in the PIV, suggesting that the phenomenon is strongly periodic. Evidently, the two "shoulders" at the angle of attack extremes of the trapezoid are responsible for a shedding akin to that of a starting-vortex in impulse start. All of the pitch cases evince a LEV forming at or near the top of the pitch stroke. From the dye injection results, the strength of this LEV is somewhat greater in the trapezoidal than the sinusoidal, and in turn appreciably greater than for the triangular pitch. The triangular pitch's weaker LEV is intuitively attributable to a lower peak pitch rate. More properly, for the trapezoidal pitch one should speak of a LEV pair rather than a single vortex, albeit the positive-signed concentration of vorticity is much weaker than the negative. It is reasonable to surmise that for the trapezoid and sinusoid the LEV remains sufficiently coherent to interact with the trailing vortex system by the time that it arrives at the trailing edge. The triangular pitch's LEV, being weaker, does not have such an obvious relationship with the TE vortex system.

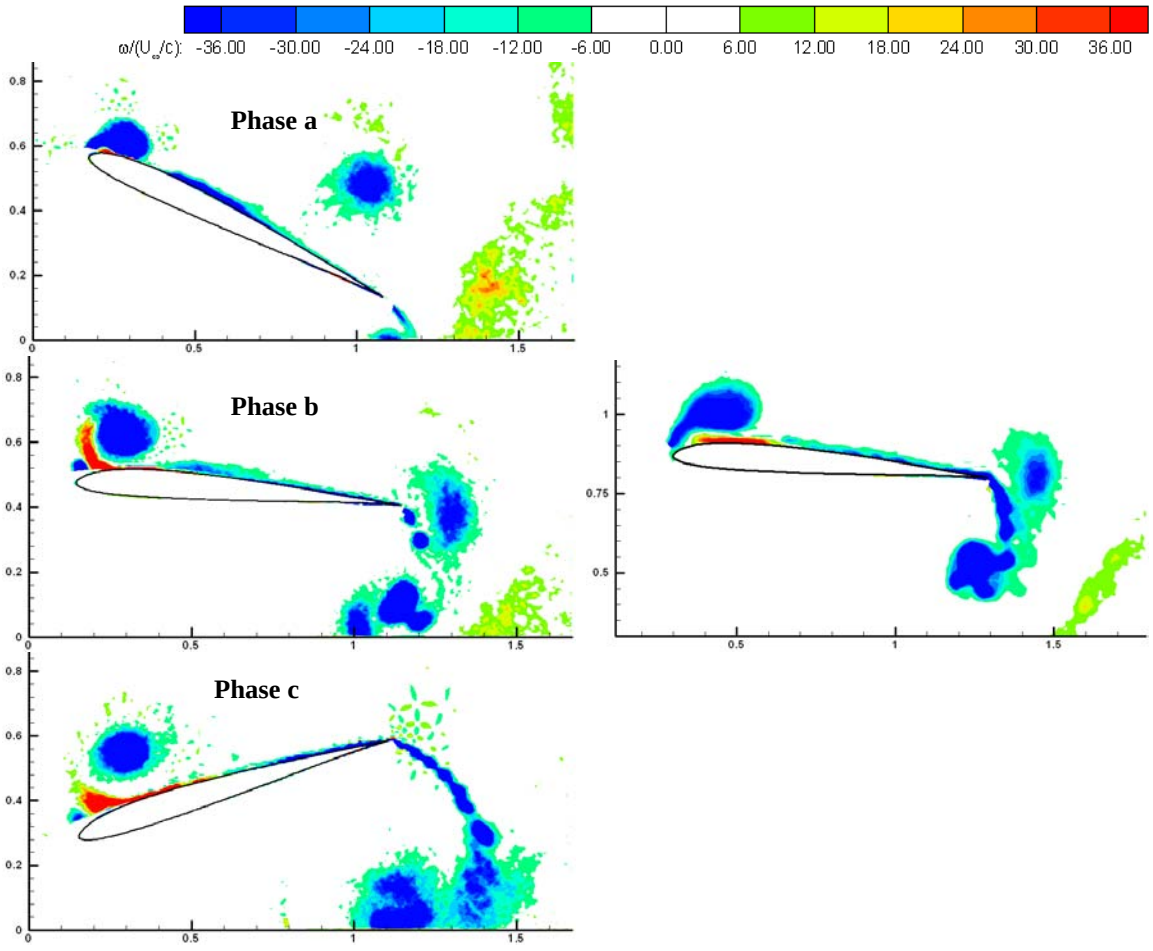

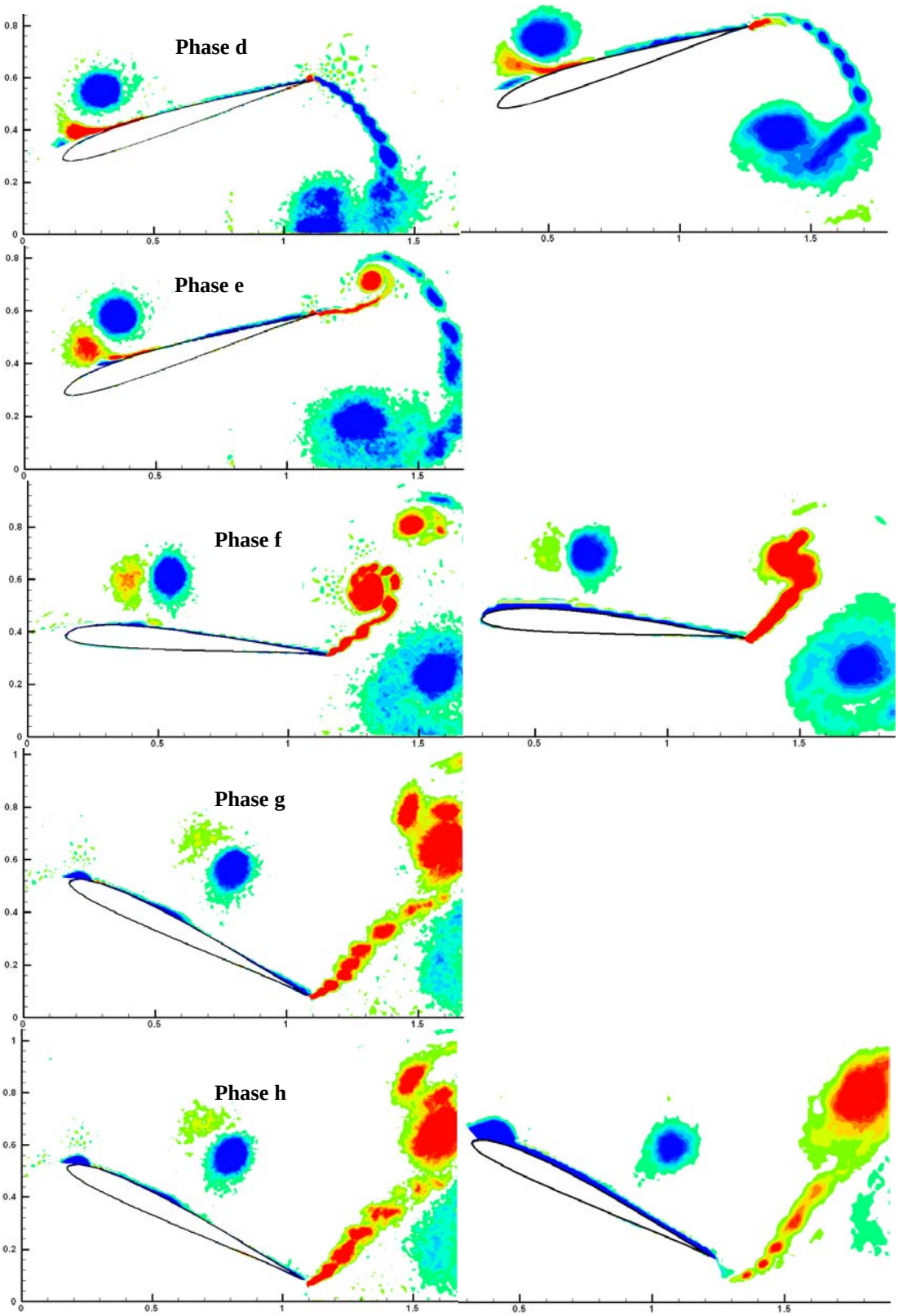

Figure 56. PIV phase-averaged vorticity contours for trapezoidal (left) and sinusoidal (right) pitch, Re = 10,000; 8 phases of motion (trapezoidal) and 4 phases (sinusoidal).

6.2.4. Discussion: Pitch-Plunge Comparison and Other Observations

Next, we turn to comparison of sinusoidal pitch and sinusoidal plunge. Pitch-plunge comparison is useful in the context of extending quasi-steady concepts. Perhaps through deeper understanding of pitch and plunge as canonical motions, it will be possible to "explain" all 2DOF airfoil oscillations, in the sense of pitch and plunge spanning the space of all possible 2D OF oscillations. While it remains premature to justify such lofty ambition, a preliminary extension relevant to massively-separated cases is assessment of what plunge amplitude is required to produce LEV strength similar to that observed in pitch. Matching plunge-induced and pitch-geometric angle of attack was shown to fail to give matching leading edge separation[105], but matching displacement of the airfoil leading edge between the pitch and plunge oscillations shows promise. As noted in Figure 47, the resulting induced angle of attack in plunge is far larger than the geometric angle of attack in pitch, nor does sinusoidal variation of plunge position produce truly sinusoidal angle of attack variation at these high motion rates.

Comparing phase "d" of the plunge, which corresponds loosely to phase "b" of the pitch cases (referring to the angle of attack time traces in Figure 47), it is evident that the LEV is very similar to that of the sinusoidal pitch, as shown in Figure 50. This holds for all phases where the LEV has not convected far from the leading edge, and breaks down as the LEV progresses further downstream. The wakes are in fact entirely different between the plunge and any of the pitch cases. For the plunge, the wake is a reverse-Karman street[95] with positive and negative concentrations of vorticity. The idea of LEV downstream convection and interaction with the TE vortex system resembles the "shear layer vortex" of McAlister and Carr[96], and Walker et al[99]. However, the shear layer vortex and LEV (or more properly, dynamic stall vortex) form essentially simultaneously, whereas in the present work we find that the vorticity concentration on the airfoil suction side just upstream of the TE is the leading edge vortex from a prior cycle of oscillation.

We conclude with a brief mention of lift coefficient comparability between the four cases. Because HFWT force balance results were not available for these cases, the discussion would be limited to the parallel computational results, as reported in Ol et al.[106] But this is not shown for brevity and for purposes of limiting this report to in-house experiments only, wherever possible. We mention in passing that (1) the sinusoidal-trapezoidal-triangular pitch motions evince differences in lift coefficient mostly limited to spikes associated with noncirculatory force; these are discussed in detail in a subsequent section on nonperiodic motion. Also, (2) the sinusoidal pitch and sinusoidal plunge show roughly comparable lift coefficient time histories, suggesting – but not proving! – that similarity of LEV development has correlation with similarity of lift coefficient time history.

We next turn to a kinematically similar set of motions, but at much lower reduced frequency, where noncirculatory forces are negligible, quasi-steady approximations are tantalizingly attractive, and both wind tunnels and water tunnels can accommodate the subject motions.

6.3. Further Observations of High-Frequency Sinusoidal Pitch

In the previous section, sinusoidal pitch oscillation was studied in onset from motion startup, through relaxation to periodicity. Roughly 8 periods (or less) were necessary to relax to periodicity. Does this always happen, and how does the startup transient vary with the starting position of the airfoil? Largely by accident, we discovered that the starting phase makes no difference in the eventual geometry of the wake, but it does make a large difference in how long it takes to reach that wake form, and how the evolution from startup to final periodicity unfolds. We first document this with dye injection, and then with PIV.

6.3.1. Dye Injection Results

Flowfield development from startup is seen from the systematic dye injection in Figure 57, for four different phases of motion (0 degrees, 90 degrees, 180 degrees and 270 degrees of phase). For the third column in Figure 57, the skewed up-going wake with trailing edge vortex pairing is evident as early as the 10^{th} period of oscillation, if not sooner. For the second column, such a wake is not attained until the 15^{th} or 20^{th} period. For the first column, the skewed wake becomes evident at around the 25^{th} period. Finally, for the fourth column, the skewed wake is not evinced until the 55^{th} period. Until then, there is an intermediate form of wake – a fairly symmetric reverse Karman vortex street, with no clear upwash or downwash. That is, there is a starting transient that takes about 2 periods to relax to periodicity, which is the reverse Karman wake. Thereafter there is a second time scale, on the order of 50 periods, before the skewed wake is manifested.

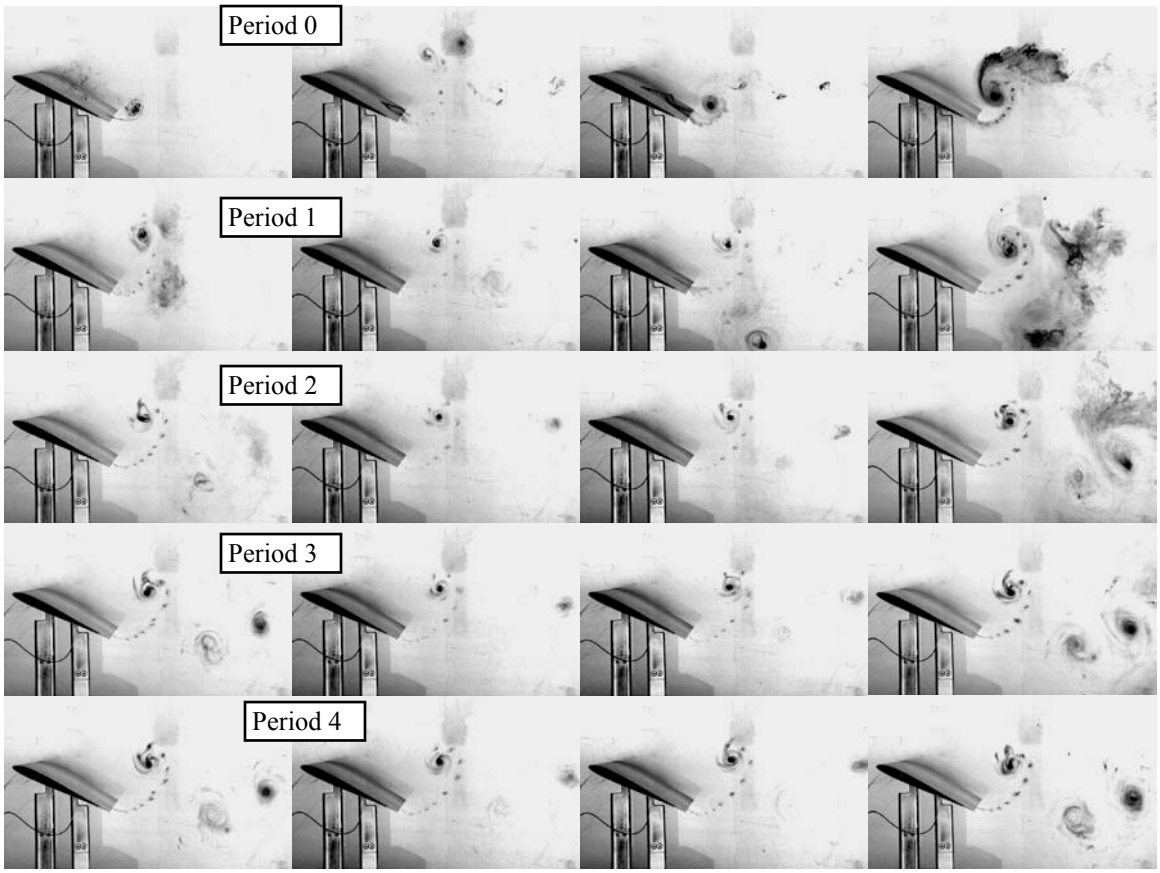

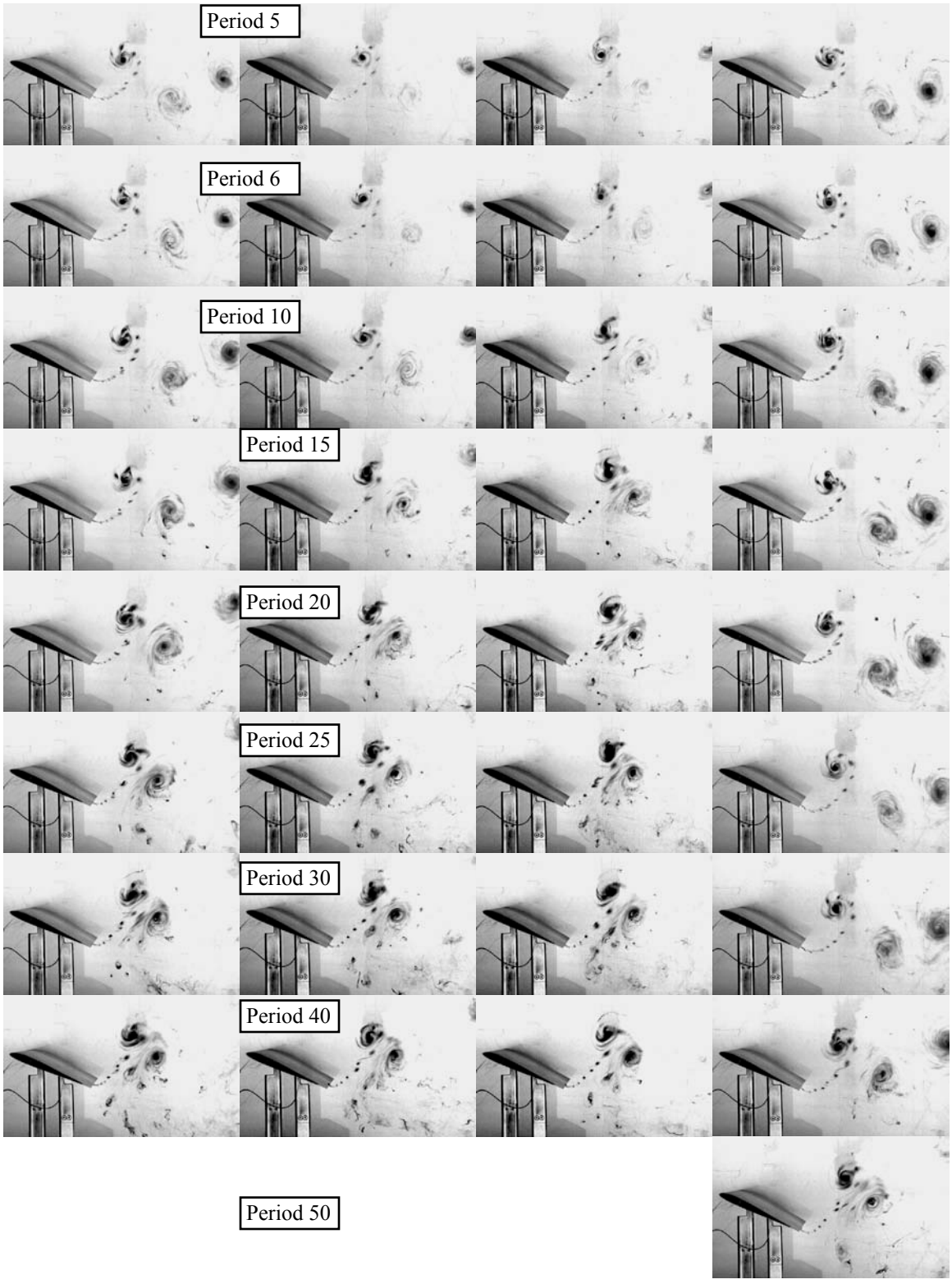
Period 5
Period 6
Period 10
Period 15
Period 20
Period 25
Period 30
Period 40
Period 50

Figure 57. Dye injection for 4 different starting phases of pure-pitch motion; k = 3.93, pivot about x/c = 0.25, Re = 10K, dye injected at trailing edge; periods of oscillation as marked, from start of motion.

6.3.2. PIV Results

Particle image velocimetry confirms the above assertions. Figure 58 shows instantaneous PIV vorticity contours (level is -36 to +36) – that is, with no ensemble- or phase-averaging – for one starting condition, but sampled at four phases per period. Each row of Figure 58 is one period; 1st period, 2nd period, and so forth, down to the 100th period. In the first period, one sees the evolution of the staring vortex, the first vortex of the stroke reversal, and so forth. At this point an LEV is forming (rightmost column) but is not convecting downstream. This situation changes by the 20th or 30th period, where there is a definite LEV-type of vortical structure on the airfoil suction side. It is also by around the 30th period that the reverse Karman vortex street has finally given way to the upswept paired-vortex wake.

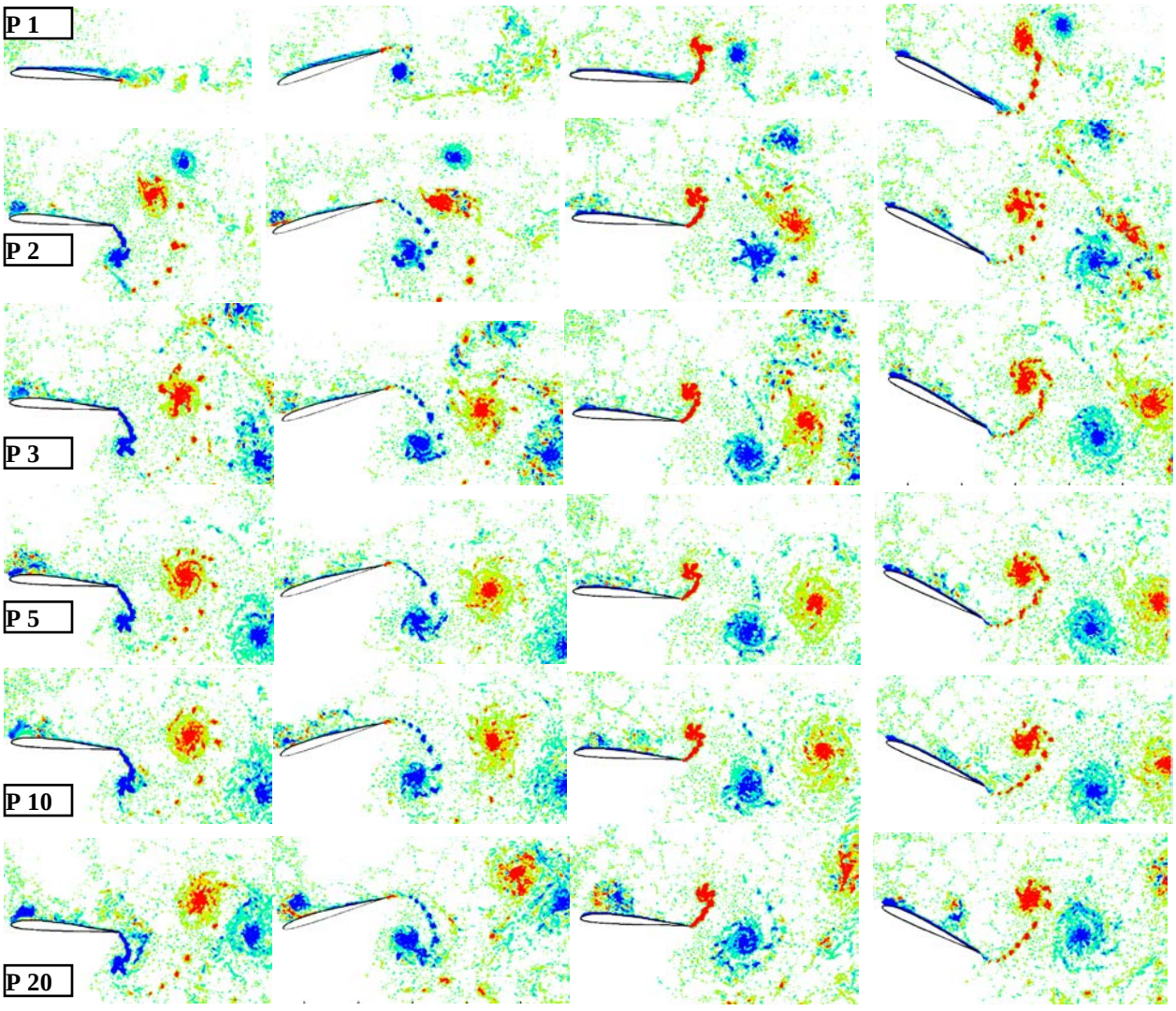

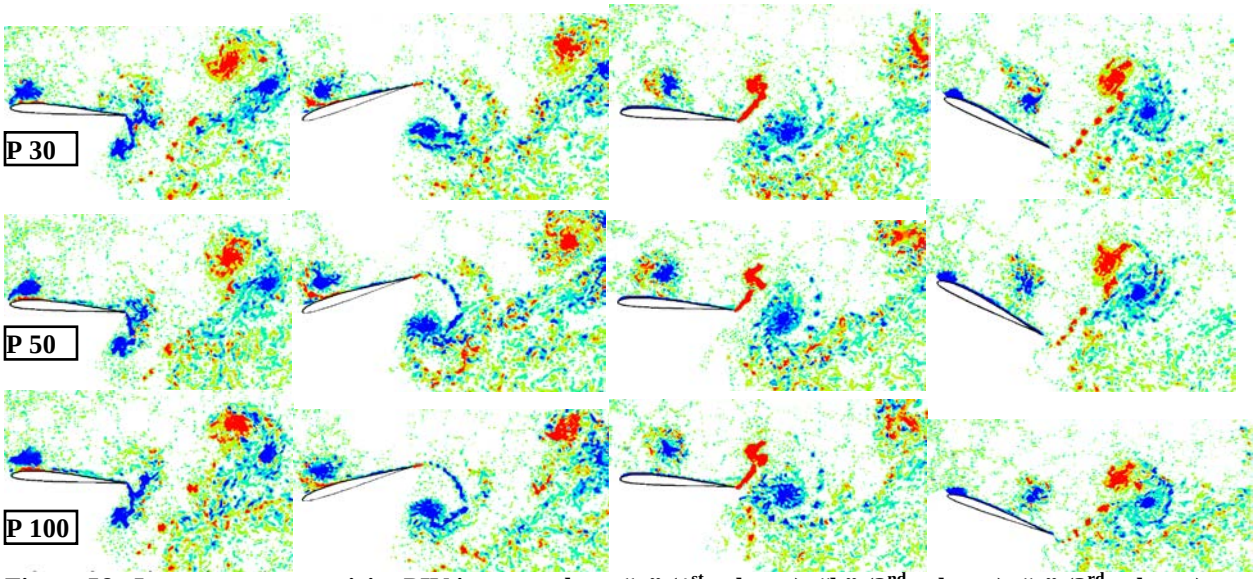

Figure 58. Instantaneous vorticity PIV images; phase "a" (1st column), "b" (2nd column), "c" (3rd column) and "d" (4th column); periods, in rows from top to bottom, are: 1, 2, 3, 5, 10, 20, 30, 50 and 100.

What causes the switching from reverse Karman vortex street to skewed paired vortex wake, and how is the starting phase (see previous subsection) responsible for the number of periods required before this wake switching? And why would the wake be upswept, when the airfoil is cambered and has a mean positive angle of attack, implying positive mean lift and therefore a necessary downwash in the wake? At present these questions have not been answered. We also know (not reported here) that for a flat plate, the eventual flowfield history *does* depend on the starting phase of motion, in the sense that the wake may become downswept or upswept. But the pairing of TE vortices does seem to be universal regardless of the airfoil sectional shape. A reverse-Karman vortex street at high Strouhal number is but a transitory phenomenon.

Arguably, these are academic questions. MAVs do not flap at such high frequency, and high-frequency flappers have a much more complicated stroke kinematics, which is probably nonsinusoidal, and which probably extends to much larger angles of attack. Aeroelastic problems, which can be at this reduced frequency or higher, are likely of much smaller amplitude. We therefore now turn to lower frequencies and higher amplitudes in our study of periodic sinusoidal oscillations.

6.4. Low-Frequency Pure-Plunge and the Role of Transition for Deep Stall Problems

We leave for now the high-frequency problems that can really only be studied in liquid flows, and turn to lower-frequencies, where both wind tunnels and water tunnels can contribute. The objective is cross-facility comparison by means of canonical problems; of course, this also includes comparison between experiment and computation; we are interested in seeing how standard off-the-shelf codes might cope with the role of transition, less so in modeling boundary layer physics itself, than in seeing how transition prediction affects the overall flow separation prediction. The numerical results, and results from other experiments, are not presented in this report, as we focus only on the HFWT. However, the different iterations of the same experiment in the HFWT give insight into the role of transition. Full coverage of experimental-computational comparison for these problems is reported by Ol et al[100].

6.4.1. Introduction and Problem Definition

We consider the following general kinematics for combined pitch and plunge:

plunge: $h(t) = h_0 c\cos(2\pi ft) = 0.5c\cos(0.5U_\infty t/c)$

pitch: $\alpha(t) = \alpha_0 + A\cos(2\pi(ft+\varphi)) = 8° + 8.42°\cos(0.5U_\infty t/c + \pi/2)$

The time traces of effective angle of attack for combined pitch-plunge and for pure plunge are given in Figure 59, which is the output of the HIPPO motor encoder tape – not theoretical prescription of motion. Our choice of reduced frequency, $k = 0.25 = \omega c/2U_\infty = \pi fc/U_\infty$, was motivated in part by cruise-type conditions for flapping flight of birds. Although the Strouhal number, $St = 0.08$, is below the range for maximum propulsive efficiency for most flyers in nature[101], the present flow conditions are on the upper-end of the dynamic-stall literature for helicopter blade applications[102], for which the traditional analytical or phenomenological models in aeronautics tend to focus. As is often taken in applications motivated by propulsive efficiency of pitch-plunge[85], pitch leads plunge by one quarter of phase (φ = 0.25) and thus the airfoil "feathers", with the geometric pitch angle partially cancelling the plunge-induced angle of attack, $\arctan(\dot{h}/U_\infty)$. The amplitude of pitch, A = 8.42º, was chosen from the expression $\lambda \equiv \dfrac{A}{\arctan(\dot{h}_{\max}/U_\infty)}$. λ is the ratio of pitch angle amplitude to the peak angle of attack induced by the plunge motion; we chose λ= 0.6,which as will be shown below, leads to shallow dynamic stall. λ =0, on the other hand, is a pure plunge, which produces a strong leading edge vortex, and is more akin to deep dynamic stall.. Variation of λ is an option for parameter studies (not pursued here) for search for lift and thrust efficiency, while keeping Strouhal number constant. Alternatively, Strouhal number can be varied (by changing reduced frequency or reduced amplitude) and λ varied such that the effective angle of attack history, when disregarding pitch rate effects, is kept constant.

Figure 59 shows the plunge trajectory (green curve), total effective angle of attack in pure-plunge (black curve), pitch geometric angle of attack (purple curve) and total effective total angle of attack for combined pitch-plunge (blue curves). For pitch-plunge, the total effective angle of attack time-trace, α_e, straddles the static stall value of ~ 11 º; this is just the sum of the pitch and plunge cosines with appropriate phase shift. But α_e, can be taken to include the effect of pitch rate, which depends on the pitch pivot point location, by summing all of the components inside the brackets in the third term of Equation 1; this is the dashed blue curve in Figure 59. The difference, vs. disregarding the effect of pitch pivot point location (solid blue curve) is a phase shift of ~0.05t/T. With inclusion of the pivot effect, the limits on α_e become $2.03º < \alpha_e < 14.03º$, whereas for pure-plunge they are $-6.0º < \alpha_e < 22.0º$.

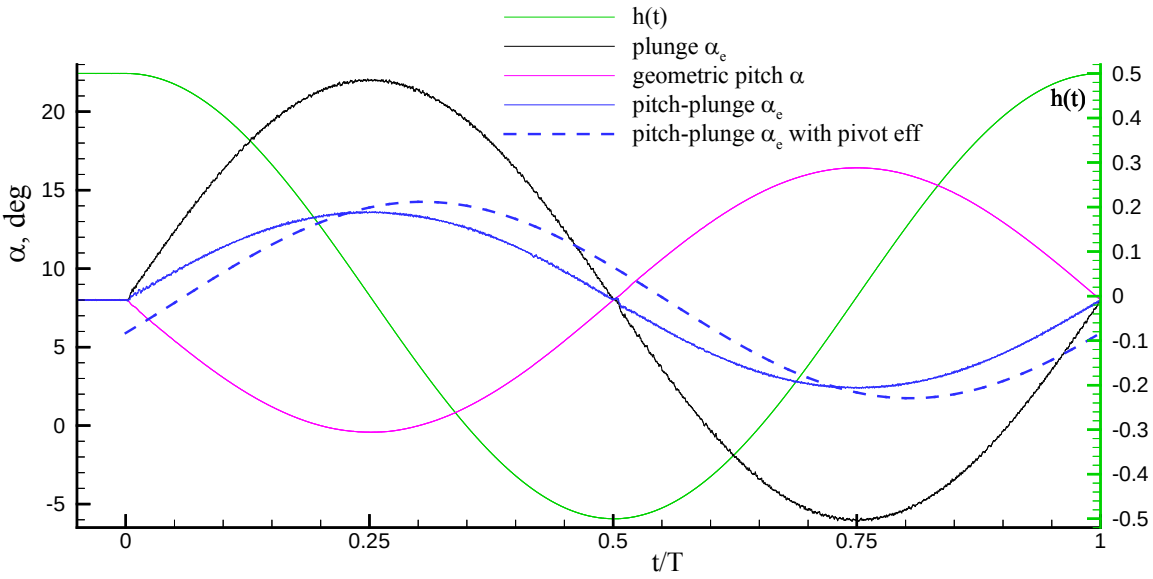

Figure 59. Motion kinematics and effective angle of attack time history for pure-plunge and combined pitch-plunge.

6.4.2. Re = 60,000 Results

Velocity and vorticity contour plots from PIV in the HFWT are shown in Figure 60 and Figure 61. Figure 60 is an older data set, and Figure 61 is an update. For velocity, we use the normalized streamwise component, u/U, as the metric of choice. Vorticity is limited to the out-of-plane component, and normalization is by free-stream velocity, U, and airfoil chord, c. For velocity the contour levels are 0 to 1.5, while for vorticity they are -36 to +36.

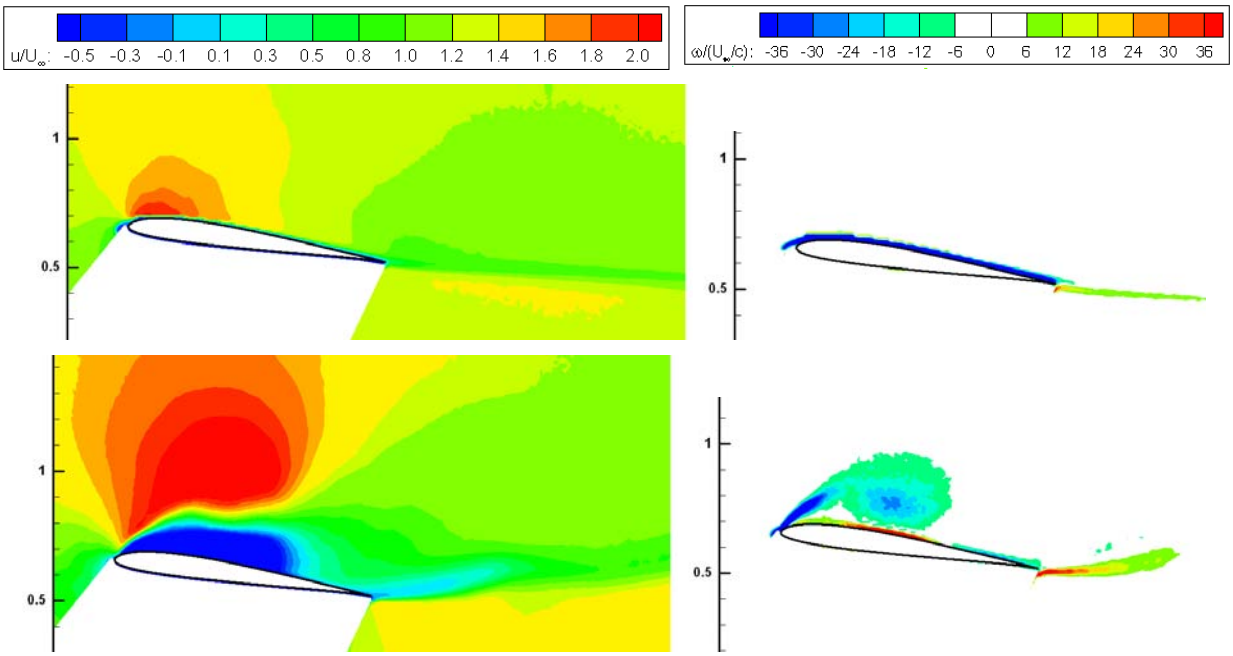

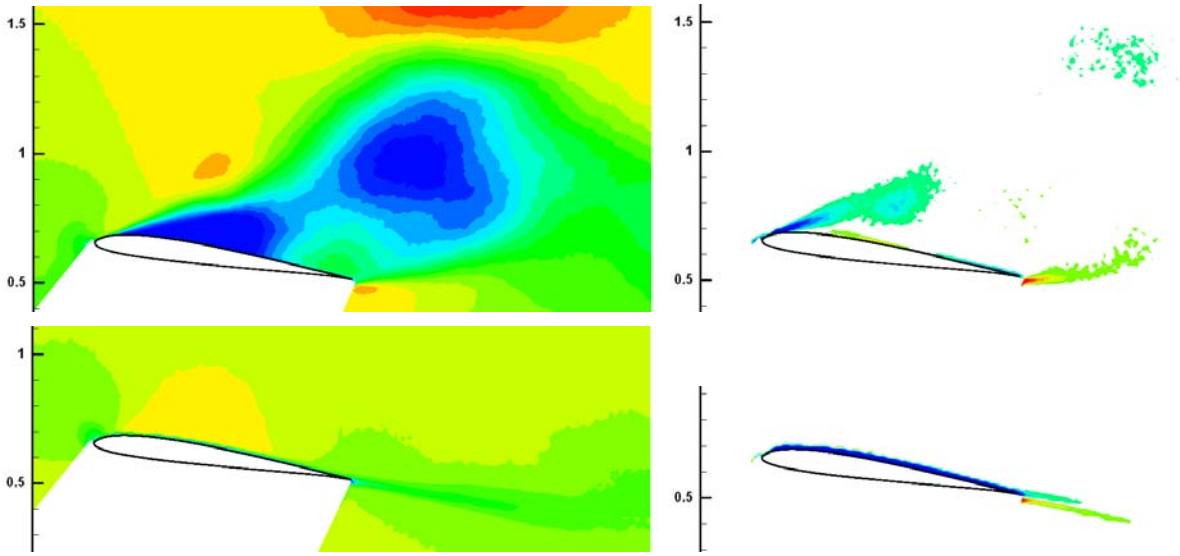

Figure 60. PIV entry #1; phases phi = 0, 90, 180 and 270.

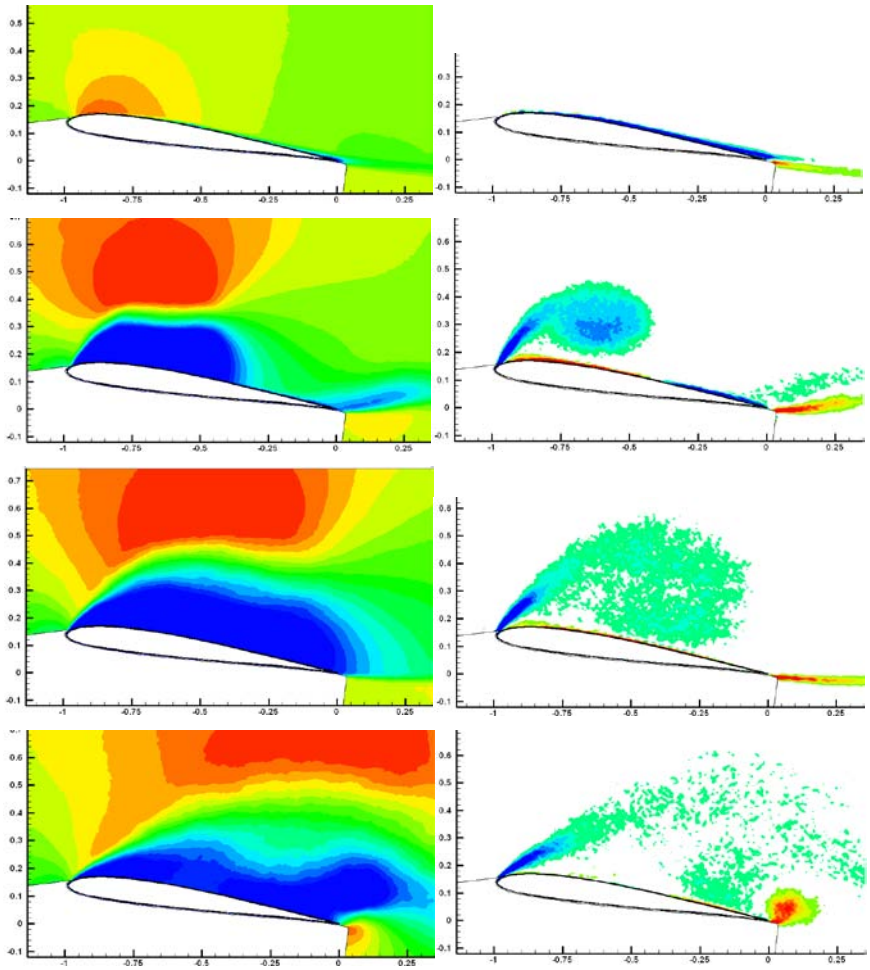

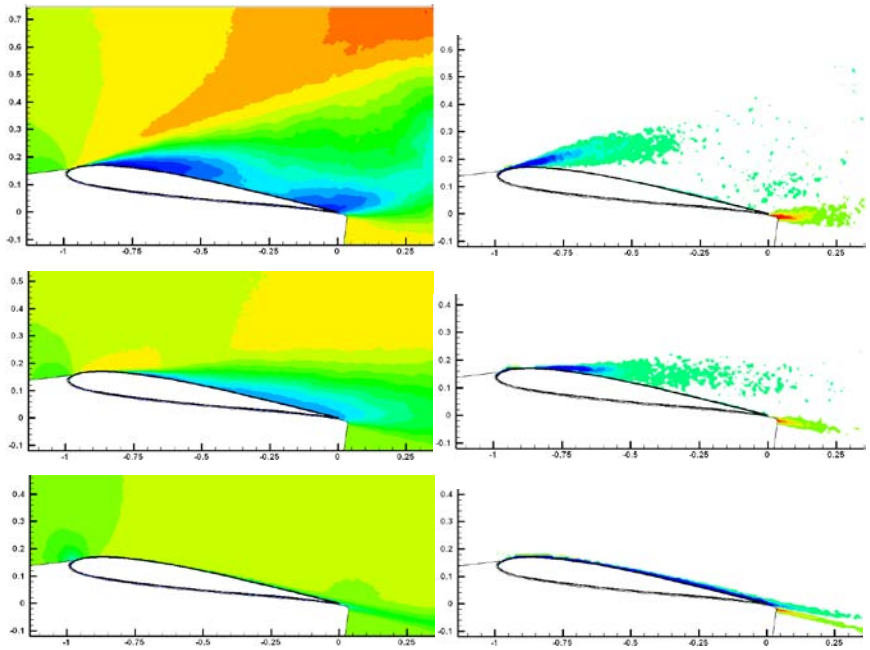

Figure 61. entry #2; phases phi = 0, 90, 120, 150, 180, 210, and 270.

The reason for having two data sets is the implications of other experiments and computations run by partners studying the same canonical problem, under the NATO RTO Task Group AVT-149, "Unsteady Aerodynamics for MAVs". The various experiments all largely agreed in how and when the LEV forms on the downstoke, but disagreed in subsequent flowfield evolution. Indeed, this is exactly the observation for the above two data sets. The later data set shows suction-side separation washing away earlier in the plunge stroke, while the older data set shows a large low-speed region lingering longer. Why? Both data sets have the PIV light sheet nominally at the ¾ span location, to be equidistant from two sources of disturbances: the HIPPO plunge rods, and the test section sidewalls. However, the position of the light sheet may have been somewhat different between the two, and that small difference, deemed insignificant at the time, could have been responsible for the aforementioned flowfield differences. Other experiments, whose results are not shown in the this report, show even more separation at the downstroke bottom; but in all of these cases the PIV light sheet was at the model centerplane, not the ¾ span location. We conclude, at least tentatively, that the HIPPO plunge rods are not the culprit, but that there is a spanwise variation in flow separation even for wall-to-wall models. That is, large flow separations are never truly 2D. This is further illustrated by the spanwise-view dye injection in Figure 62. At the top of the plunge stroke, phase t/T = 0, the dye streak is thin and of minimal spanwise extent, but spanwise eruption accompanies formation of the LEV at t/T = 0.25, broadening further as the LEV loses coherence and convects downstream. LEV formation, let alone shedding and downstream convection, is seen to be a 3D process. By t/T ~ 0.5 the spanwise extent of the dye streak is larger than one chord-length. This is not, in itself, proof that minor spanwise relocation of the interrogation plane accounts for large changes in the evinced flow at t/T = 0.5 between one PIV data set and another, but it does illustrate the strongly 3D nature of the flow. Reattachment at the leading edge brings return to nominal two-dimensionality upon commencement of the upstroke. By t/T = 0.75, the dye-tagged flowfield region over the suction side is again nominally 2D.

We mention here without proof (see Ol et al.[100]) that boundary layer transition plays at most a minor role in this flow. Much akin to classical dynamic stall, there is a strong LEV formed halfway down the plunge stroke. But since classical dynamic stall research is motivated by much higher Reynolds number applications, before considering lift time histories – which of course matter more for applications than do niceties of flowfield details – we consider, at least in a limited sense, Reynolds number effects.

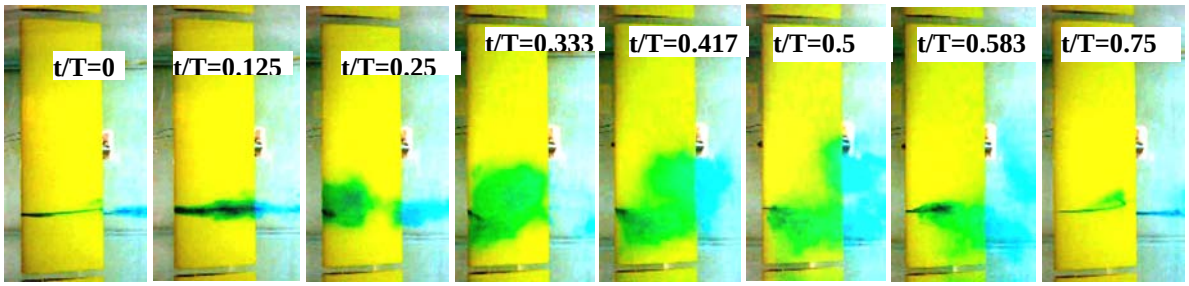

Figure 62. Planform view of dye streaks, over one period of motion; dye injected at ¾ span location, near nominal spanwise position of PIV light sheet. Re = 60K

6.4.3. Reynolds Number Effects

Figure 63 compares Re = 20K, 30K and 60K dye injection. To lower the operating Re, the tunnel is run more slowly, and the rig and the dye discharge rate are proportionately slower.

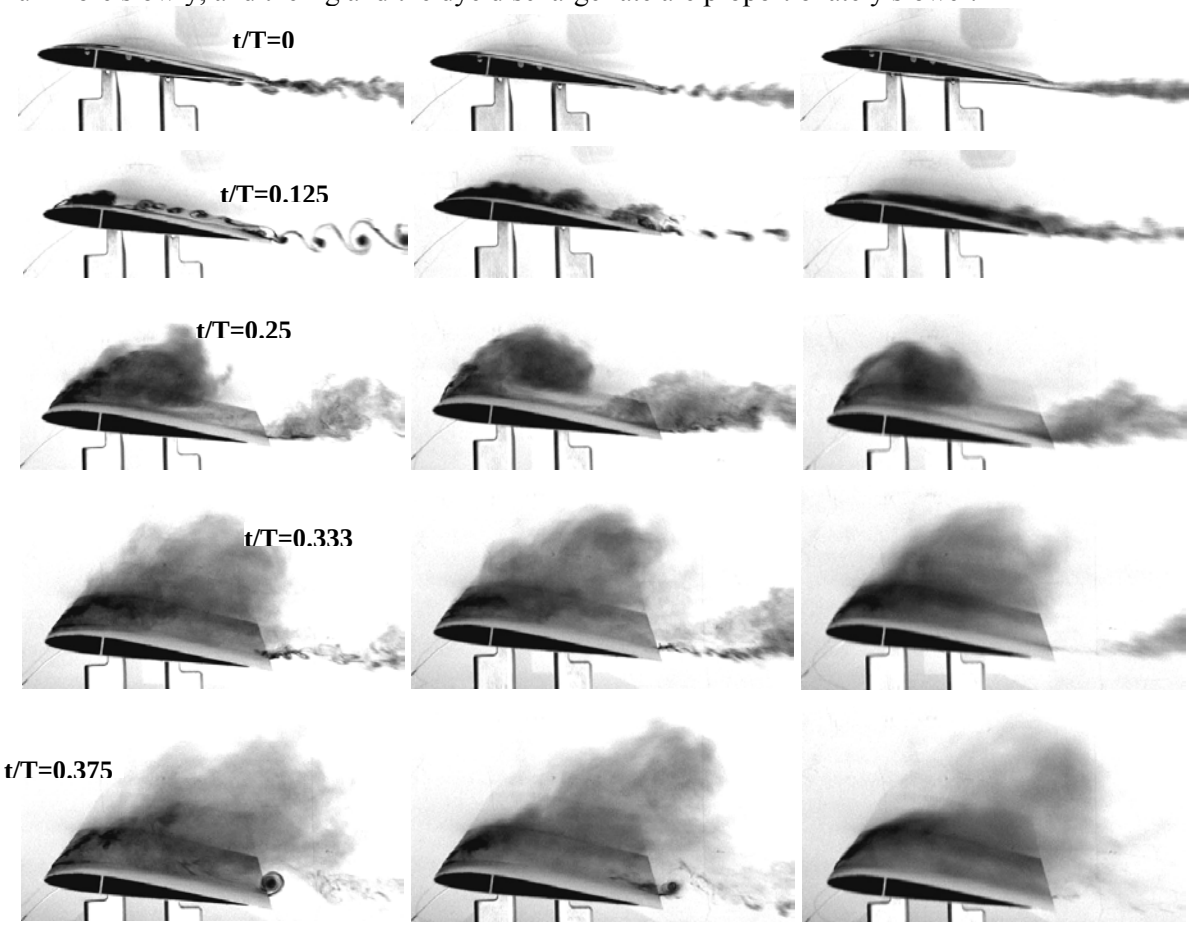

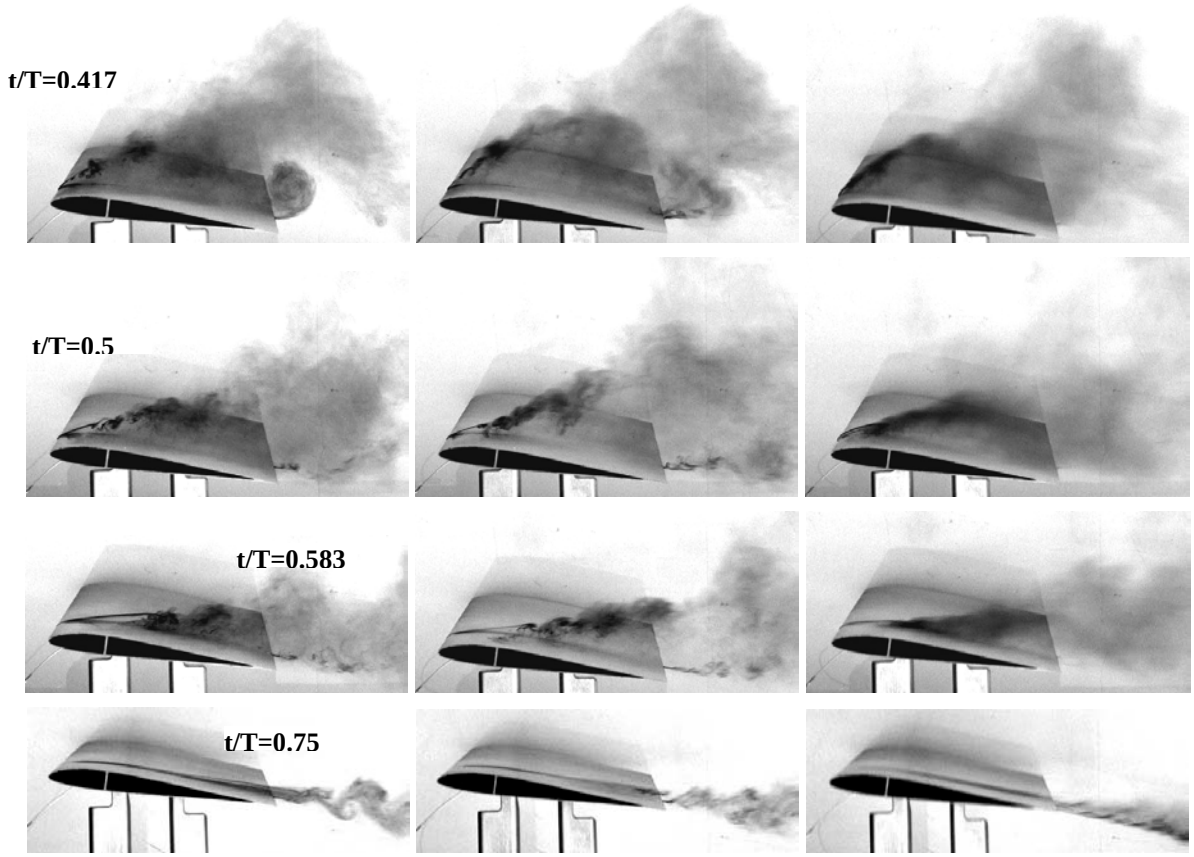

Figure 63. AFRL water tunnel Dye injection for pure-plunge, Re = 20K (left column), 30K (middle column) and 60K (right).

At the trailing edge, at Re = 30K and especially at Re = 20K there is a discernable trailing edge vortex at t/T = 0.375-0.417, with a region of reverse flow just ahead of the trailing edge. At Re = 60K, no TEV is clearly visible in the dye injection, but it was strongly apparent at t/T = 0.417 in the PIV. The near-wake at the top of the plunge stroke also shows a discernable Re-effect, with coherent vortices seen for Re = 20K. In going from t/T = 0 to 0.125 to 0.25, the suction-side dye concentrations splits, as it were, into a leading-edge and trailing-edge portion, the former coagulating into the LEV at t/T = 0.25. Towards the bottom of the plunge stroke, the pocket of dye lacuna just aft of the leading edge is smaller for higher Re, further suggesting that this region can be thought of as a laminar separation bubble.

6.4.4. Aerodynamic Force Coefficients

For practical MAV applications we are more interested in aerodynamic force coefficients than necessarily in the details of the flowfield; but we must know the flowfield well enough to predict force coefficients accurately and on a sound physical basis, rather than from heuristics or curve fits. In this section, experimental measurements of lift coefficient in the water tunnel are compared with theory and with a large set of computations from the PI's various collaborators. These include Large Eddy Simulations from elsewhere in AFRL/RB and from the Canadian National Research Council; Reynolds-averaged Navier Stokes from the University of Michigan, Middle East Technical University, Technical University of Darmstadt; and semi-empirical methods from University of Toronto. HFWT force measurements use the FBG balance.

The most basic quantity of interest is lift coefficient, and indeed one hopes to obtain reasonably correct lift coefficient time history at Re = 60K across the full range of analytical and computational methods, including the lower-order methods. Figure 64 shows computational and measured lift coefficient time history at Re = 60K. The encouraging result is that all curves qualitatively follow the same trend. Also interesting is that the lift time history is essentially sinusoidal, despite the obvious presence of an LEV and its putative dynamic-stall effects on lift, which ought to manifest itself as a large hysteresis for lift plotted vs. angle of attack. Qualitatively the behaviour is surprisingly not far from the inviscid $2\pi\alpha$, despite the fact that peak effective angle of attack is more than *twice* that of static stall.

The present experiment and AFRL 3D LES are very close, as would be expected from a high-fidelity computation. NRC 2D LES essentially splits the difference between AFRL LES and RANS, as is to be expected from the resolution of the NRC computation. But the most remarkable fact is that Theodorsen's formula (dashed black curve in Figure 64) also follows very closely with the 3D LES computations, slightly underpredicting dynamic lift at the max effective angle of attack (t/T = 0.25) and in turn overpredicting lift on the first half of the upstroke (t/T = 0.5 to 0.75). Thus the two extremes of calculation fidelity appear to perform comparably well! RANS computations are also in reasonable agreement, though they tend to overpredict loss of lift at the plunge downstroke (t/T = 0.5), and in general show a slightly stronger dynamic stall than does the LES; in other words, a fuller hysteresis loop. The vortex particle method, on the other hand, overpredicts retention of lift during the upstroke. Curiously, the large difference in velocity/vorticity contour plots between the AFRL 2D and 3D LES and between AFRL and NRC LES does not correspond to much difference in the lift time history.

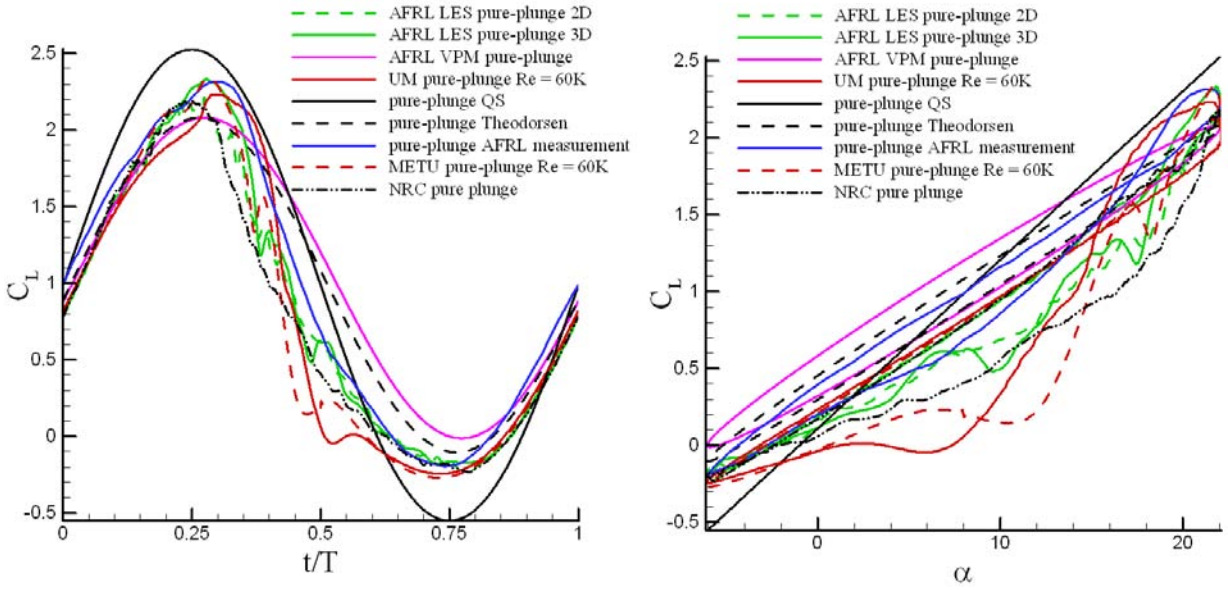

Figure 64. Lift coefficient time history, SD7003 pure-plunge, Re = 60K; plotted vs. motion phase (left) and effective angle of attack (right).

It is of course possible that period-to-period variations in the experiment are smeared in the ensemble average, in the sense that dynamic-stall peaks and troughs in the lift coefficient time history in any one period are attenuated in the average because they vary randomly from period to period. This is disappointing from the viewpoint of fundamental fluid mechanics, but from the viewpoint of applied engineering one concludes that dynamic stall effects are uncorrelated and therefore unimportant, and the lift time history is quite sinusoidal, with small phase lag.

We next turn to the pitch-plunge problem, where angles of attack are lower, and laminar to turbulent transition matters significantly more.

6.5. Low-Frequency Pitch-Plunge and the Role of Transition for Shallow Stall Problems

6.5.1. Introduction and Problem Definition

Here we generalize the motion from the previous section to consider a combination of pitch and plunge. In the context of Figure 59, this is the blue angle of attack curve. Whereas the pure-plunge motion was motivated by the desire to observe a dynamic-stall case and a strong LEV, the pitch-plunge case is motivate by considerations of efficient flapping-wing propulsion. Thus, the effective angle of attack should never venture into too deep of a stall.

6.5.2. Re = 60,000 Results

Particle image velocimetry results for mean streamwise velocity component and out-of-plane vorticity component are shown for three successive data sets, in Figure 65, Figure 66, and Figure 67, respectively. The motivation for three data sets was again the desire to better compare with other labs' experiments. But another reason was the strange disparities in dye injection results, sometimes from adjacent runs. Why would in one run the separation even towards the bottom of the downstroke be well aft of the leading edge, while in a run taken literally minutes later, the separation would commence almost at the leading edge? To be sure, in no cases is there a LEV. All results are topologically identical. But in the context of boundary-layer-type measurements, where one is interested in precise data and regions of large flowfield gradients are thin and close to the model wall, the evinced differences in suction-side separation were significant.

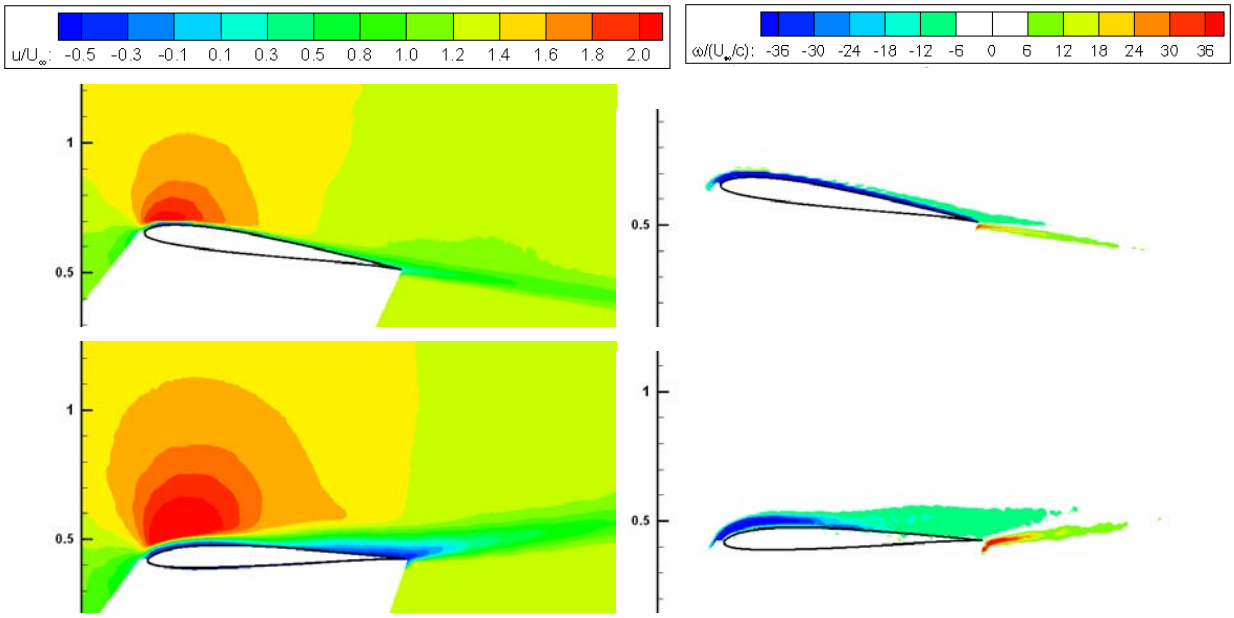

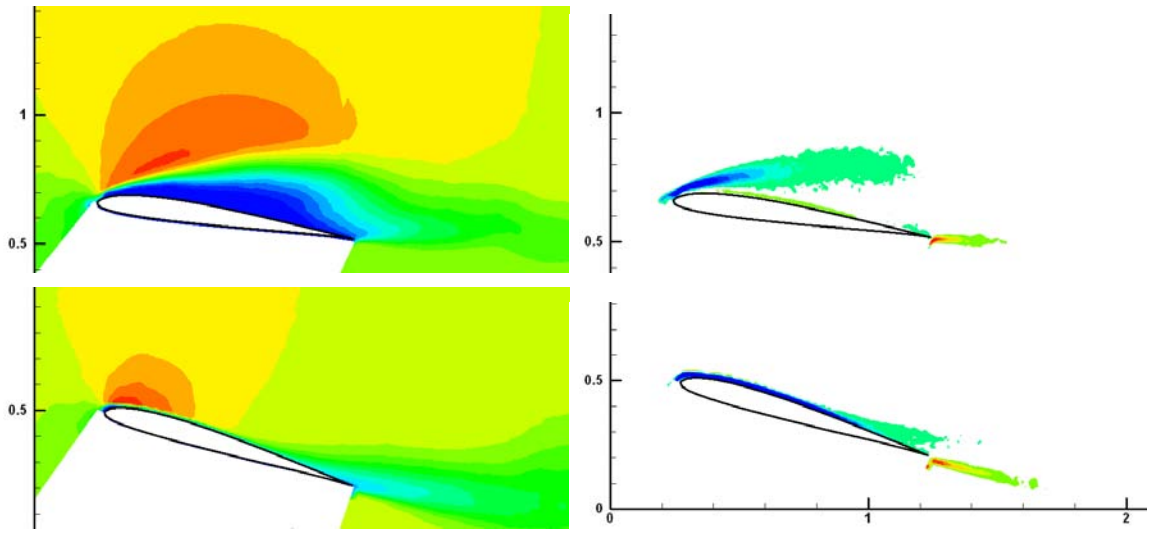

Figure 65. PIV, first data series, phases phi = 0, 90, 180 and 270.

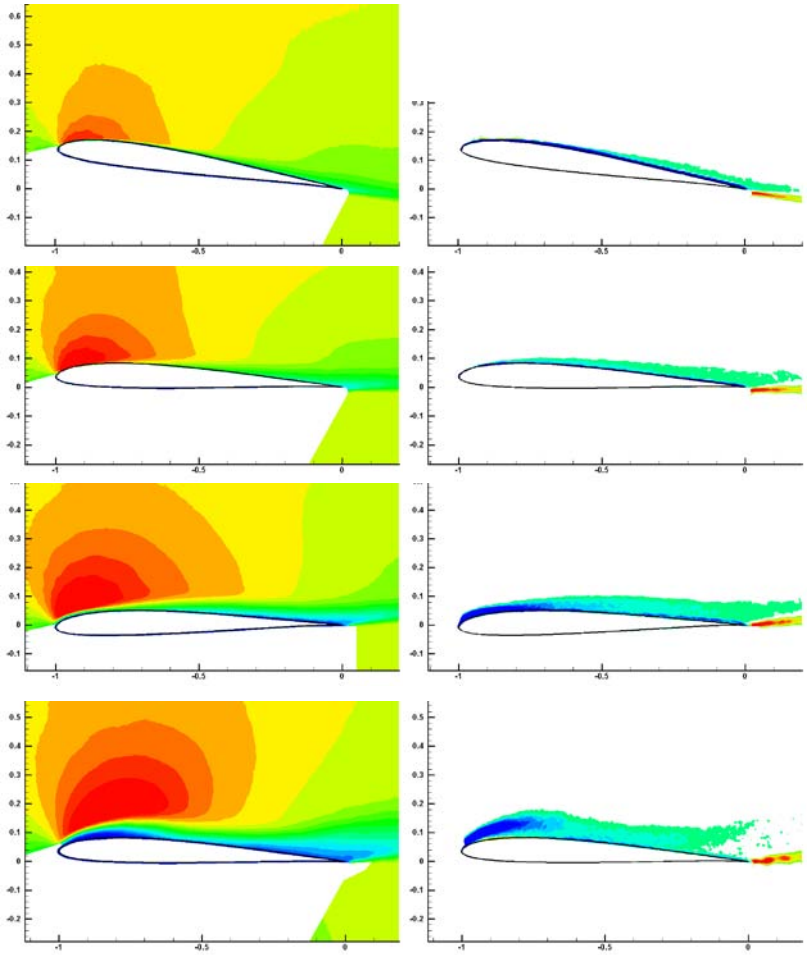

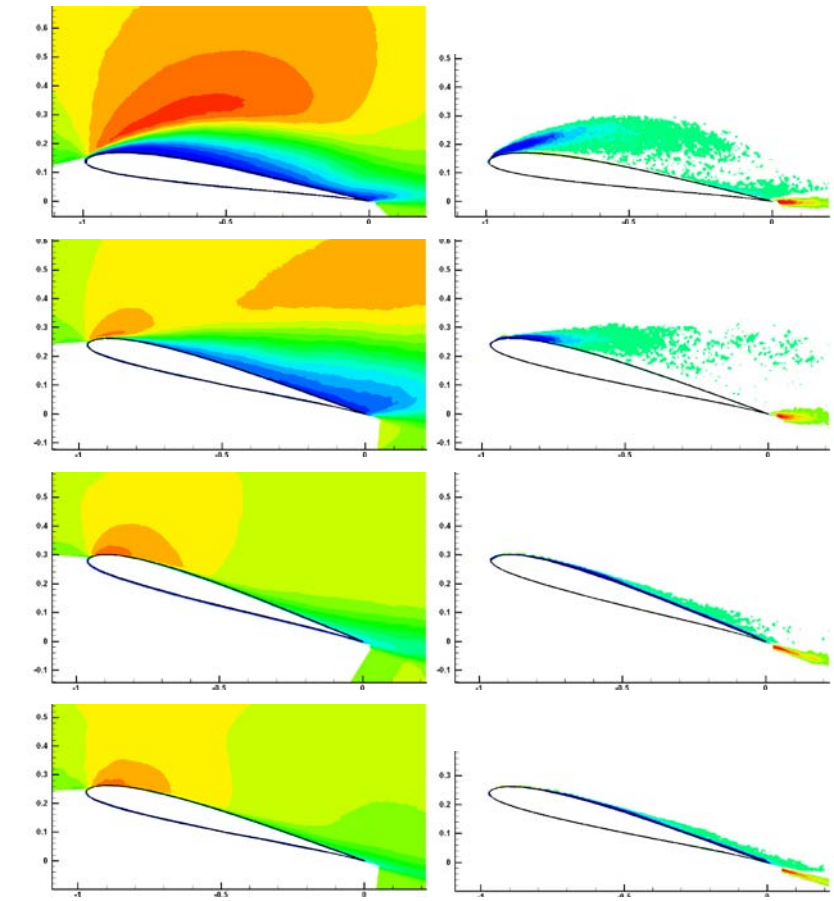

Figure 66. PIV, second data series, phases phi = 0, 45, 90, 135, 180, 225, 270 and 315.

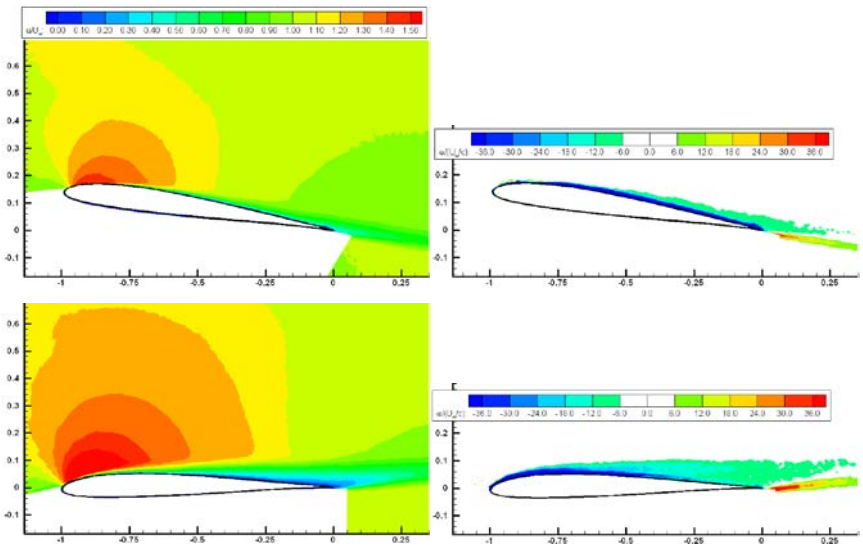

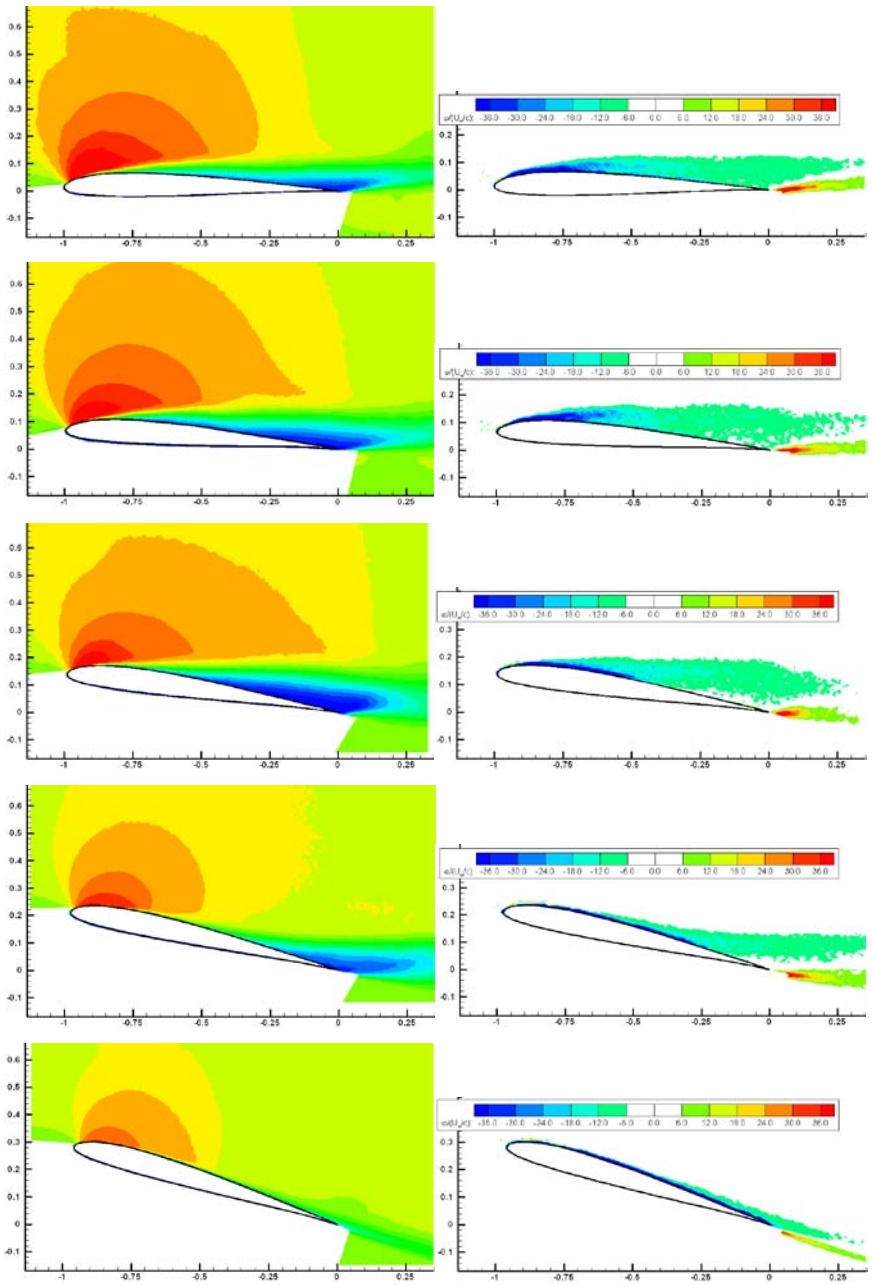

Figure 67. PIV, third data series, phases phi = 0, 90, 120, 150, 180, 210 and 270.

6.5.3. Thoughts on the Role of Transition

Another means of assessing the role of turbulence and transition is to plot turbulent kinetic energy contours. It is reasonable to surmise that for Re ~ 60,000, separation should lead to turbulence. Attached boundary layers may be laminar, but if there is large region of separated flow, it can not remain laminar for long. Indeed, in Figure 68, the comparison of turbulent kinetic energy contours in one realization of the flowfield vs. another – both at t/T – shows significant variation. The one with larger separation shows larger turbulent kinetic energy inside the separated region, but that means that the overall flow is less turbulent, for otherwise the separation would have been smaller. Meanwhile outside of the separated region, turbulent kinetic energy is comparable, and small – so there is not an obvious source of ambient

disturbances in the one case and not in the other, at least not at the amplitude discernable from the contour plot. This does not explain why one realization shows more separation than other, but does show that two identical motions with the same model in the same facility can have large variation, and that such variation is not a fluke.

Unlike in the pure-pitch case, there is good reason to discount the role of spanwise variations. Figure 69 is the analog of Figure 62 shown earlier for pure plunge. For pitch-plunge, there is no LEV and no large spanwise extent of dye spread, until the bottom of the downstroke; and even that only occurs at x/c = 0.5 and further aft. It thus seems reasonable that the apparent spanwise extent of separtion would not depend strongly on spanwise location, and therefore the virous disparities from run to run are unlikley to be due from slight variation of PIV light sheet location.

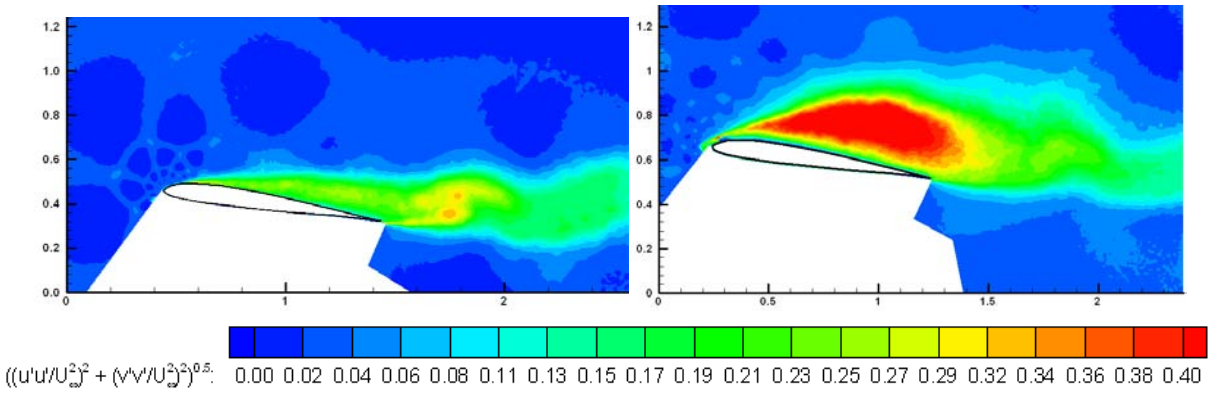

Figure 68. PIV-derived planar turbulent kinetic energy contours, AFRL data sets, phase phi = 180 (bottom of plunge downstroke): "small" separation (left) and "large" separation (right).

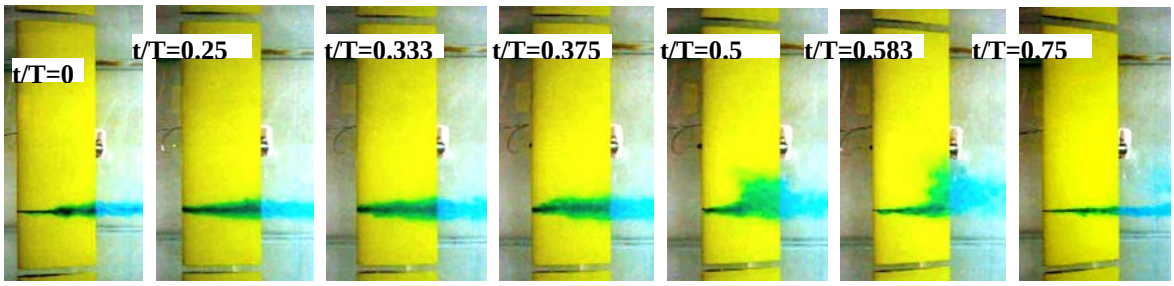

Figure 69. Planform view of dye streaks for pitch-plunge, over one period of motion; dye injected at ¾ span location, near nominal spanwise position of PIV light sheet. Re = 60K.

As a further check on the role of transition vs. other possible causes for explaining the differences in PIV contour plots, we turn to examination of Reynolds number effects.

6.5.4. Reynolds Number Effects

Figure 70 compares dye injection results at Re = 10K, 30K and 60K. Care was taken to select the "small" version of flow separation at Re – 60K. At Re = 30K and below, no run-to-run variation was observed.

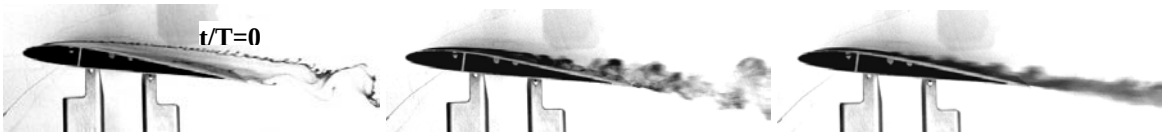

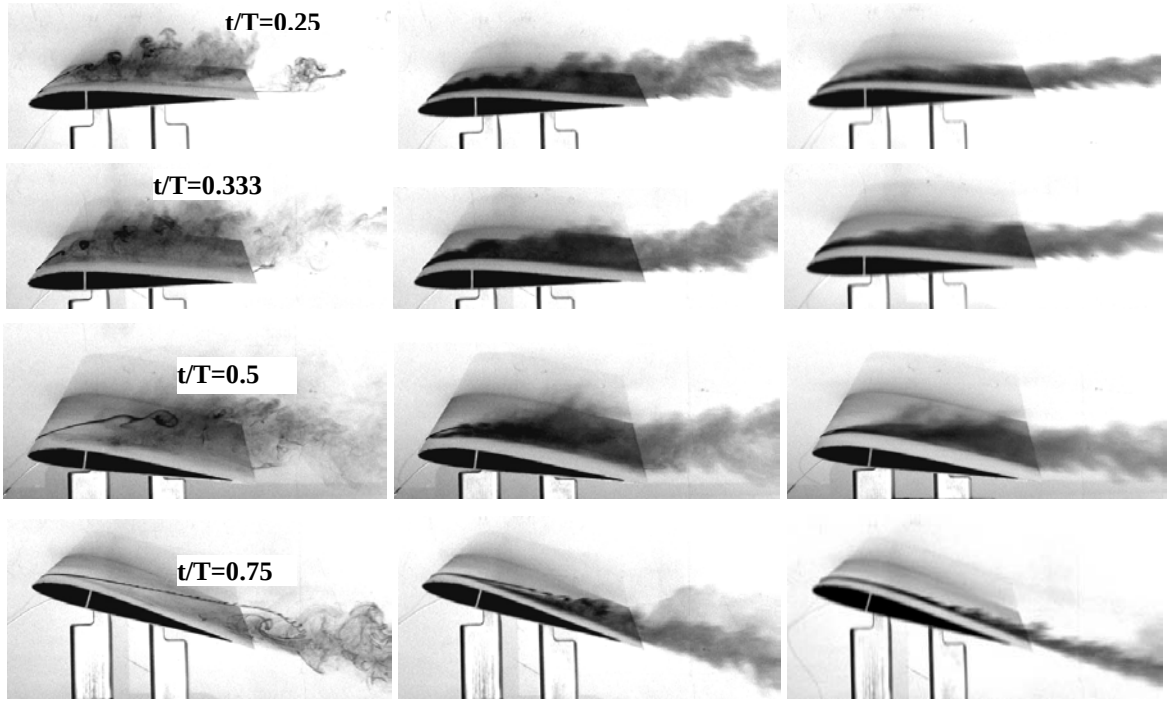

Figure 70. dye injection, Re = 10K (left column), 30K (middle column) and 60K (right column; phases phi = 0, 90, 120, 180 and 270.

At Re = 10K, the flow over the airfoil suction side is never fully attached. Towards the top of the plunge stroke, the dye streakline smoothly bounds an open region of separation, as opposed to a laminar separation bubble; but care is required in interpretation, since the dye is slightly heavier than water, and drift down (down in the lab frame is up in the airfoil frame). By t/T = 0.25, where effective angle of attack is maximum, large disturbances akin to Kelvin-Helmholtz rollers are visible, bounding a broad separated region. By t/T = 0.5 the loss of coherence of such structures suggests shear-layer transition. By t/T = 0.75 a well-organized streakline bounds the separation region all to way to the trailing edge. At Re = 20K (not shown), the suction-side flow separation is thinner and the aforementioned rollers at t/T = 0.25 are no longer discrete, but fully attached flow is still not present at any time. By Re = 30K, the separation at 0.75 < t/T <0 (or 1.0) closes into what might be termed a laminar separation bubble (LSB). The LSB is much smaller but still present at Re = 60K.

The Re = 30K=40K region is a qualitative divide, below which flow separation is largely "open", and above which, the boundary layer varies from attached turbulent to LSB-dominated, to mild separation in the second half of the downstroke. The extent of this separation at Re = 60K is a strong function of transition processes – perhaps ambient turbulence, perhaps some other source. How separation develops in this region depends, in all likelihood, not only on ambient conditions at the time, but on incipient instabilities in the boundary layer earlier in the downstroke. In sum, it is hard to say how imposed dynamics couples with boundary layer physics to affect the flow separation history. Thinking towards MAV applications, the disturbance environment is likely to be stronger than in the water tunnel, because of propwash, flexible surfaces and so forth. So rather than attempting to delve deeper into boundary layer physics, let us turn to estimation of lift coefficient.

6.5.5. Aerodynamic Force Coefficients

Force data (Figure 71) were collected from a broad range of computations – and from HFWT experiments. Lift coefficient time history is compared in Figure 71. The quasi-steady approximation and

Theodorsen's formula are the simplest models, followed by the vortex-particle method, then by the two RANS computations, from the University of Michigan and METU, and finally by the LES computation (NRC). It is here that the argument about sensitivity to transition comes fully to the fore. The METU RANS computation (details not shown) is "laminar" and predicts a large separation; indeed, even an LEV. The UM computation is fully-turbulent. The present measurements, using the FBG balance, fall somewhere in between.

Another important question is the role of classical inviscid predictions. The quasi-steady approximation performs fairly well on the upstroke, but poorly on the downstroke. Theodorsen's formula does better. It overpredicts lift in $t/T < 0.25 < 0.75$, and interestingly enough, it appears to be *worse* for pitch-plunge than for pure-plunge! This is counterintuitive, because pure-plunge has the less planar wake, and much larger separation. The resolution to this dilemma is to realize that LEVs regularize the flow separation and result in behavior more akin to attached flow. But this explanation should not be taken too far, for otherwise the quasi-steady approximation would have performed better on the downstroke.

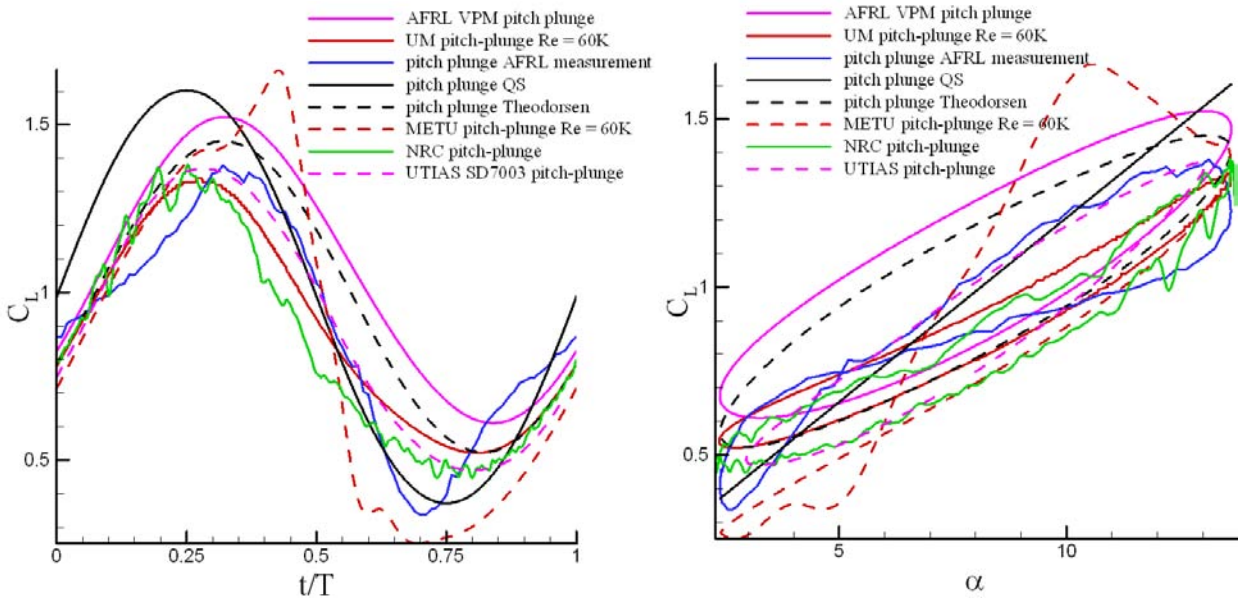

Figure 71. Lift coefficient time history, SD7003 pitch-plunge, Re = 60K; plotted vs. motion phase (left) and effective angle of attack (right).

In sum, the case of moderate dynamic stall, here realized through λ=0.6 pitch-plunge, evinces largely attached flow, but is quite complex because of the coupling with laminar to turbulent transition and the forcing from the motion dynamics. Of course, further work is merited, in parameter studies of different values of λ, frequency and so forth. In particular one needs to assess whether the same effective angle of attack history, produced by different combinations of λ, k and h, produces similar lift history. Preliminary assessment shows that the flowfields are indeed very similar, but have a difference relationship of vortex formation vs. phase of motion.[103]

We next turn to consideration of different sectional geometry – perhaps the more fundamental case of a flat plate, with the same kinematics as from the above two sections.

6.6. Sinusoidal Pitch and Plunge of a Flat Plate

Our second set of low-frequency cases is for flat plates, nominally of 3% thickness and round (semicircular) edges. In some sense the flat plate is a more fundamental problem than the airfoil, because apart from the immediate vicinity of the leading edge, there is no pressure gradient due to the model geometry itself. Plates are also easy to manufacture for experiments, while the round trailing edge somewhat simplifies the computational grid. And plates are a closer analog to membrane-type airfoils and other thin airfoils more likely to be encountered in flight articles in the Re ~ 10K range, but camber As with the airfoil, the plate geometry is nominally 2D, with the model tip gaps of less than 1mm.

The airfoil cases are deeply concerned with understanding the role of boundary layer transition in unsteady aerodynamics, but in many MAV applications transition is perhaps of secondary importance. Wings tend to be thin, with sharp edges; and transition only occurs in the wake, or in the late evolution of large separated structures. For a flat plate with round leading edge (as opposed to say a "super-ellipse"), presumably transition would occur near the leading edge, and would be fixed across a broad range of cases. This indeed turned out to be true.

6.6.1. Pitch-Plunge Case

PIV velocity and vorticity contours at Re = 60K for the pitch-plunge case are shown in Figure 72, while dye injection results for Re = 20K and 60K are in Figure 73.

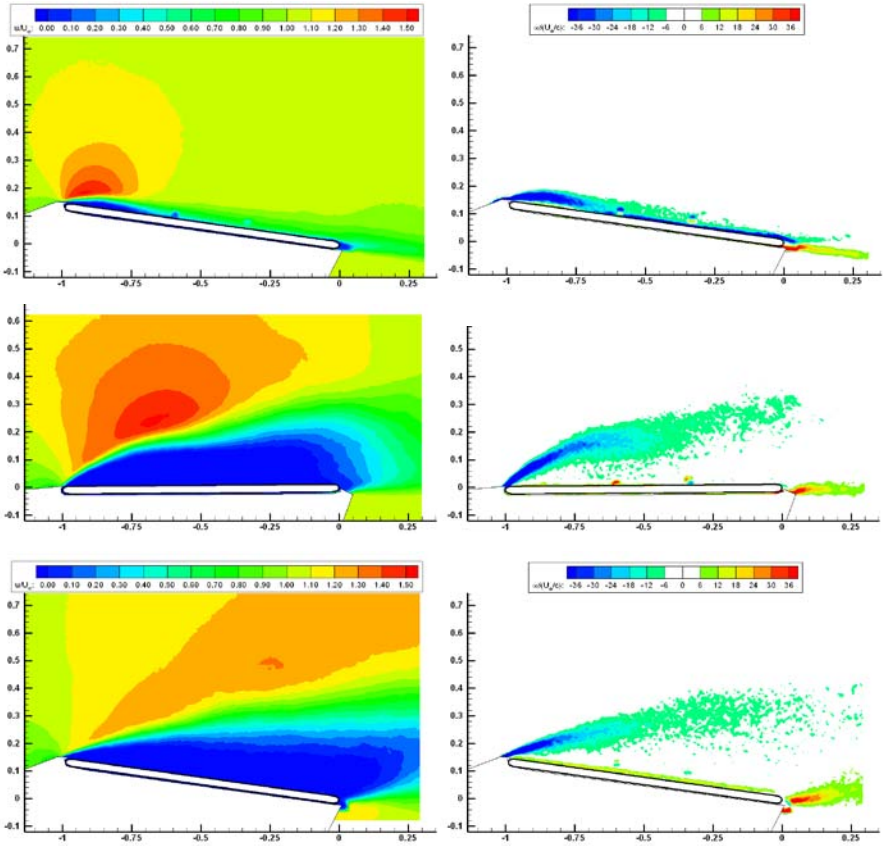

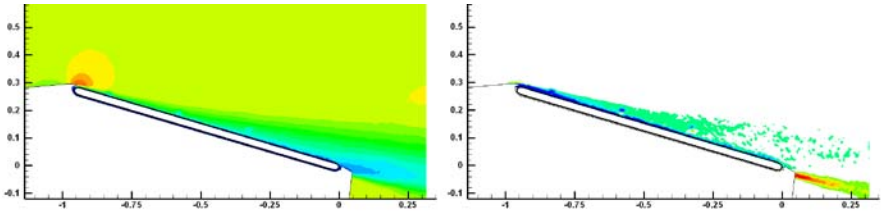

Figure 72. PIV, phases phi = 0, 90, 180 and 270 degrees.

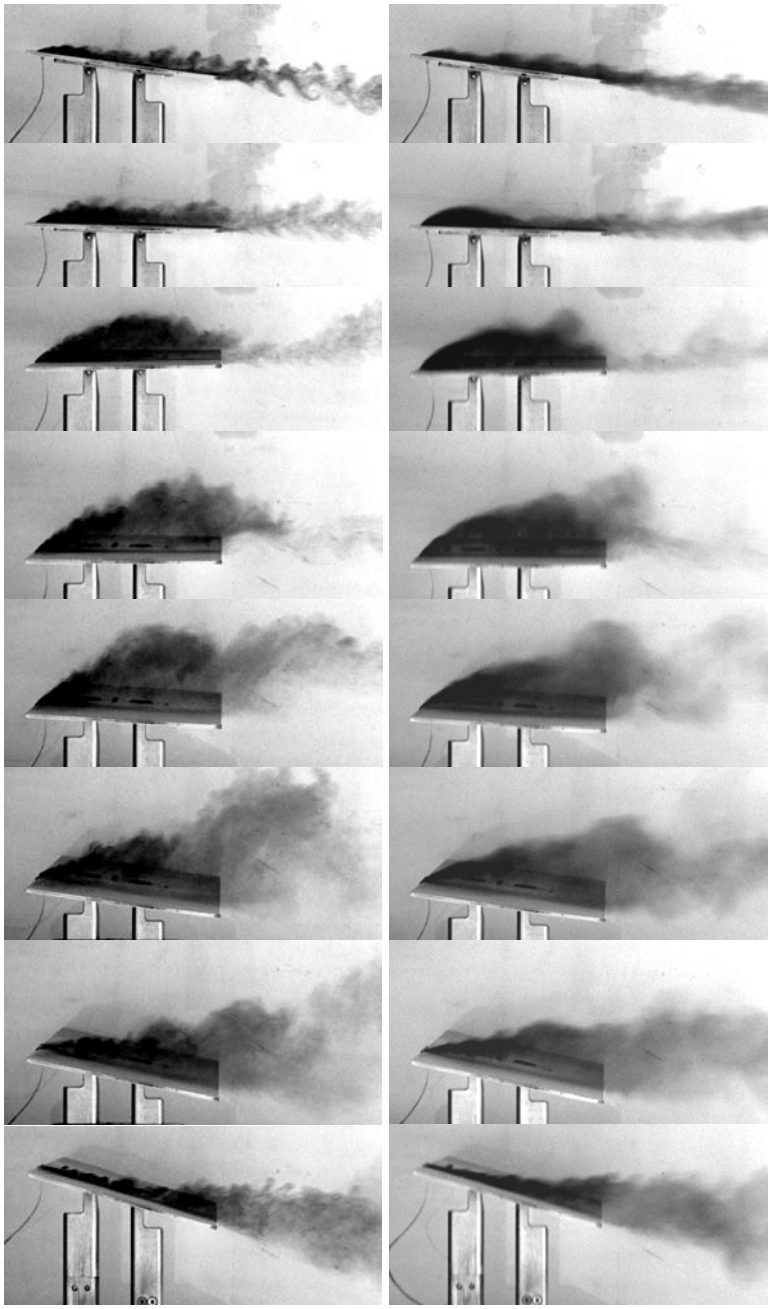

Figure 73. Dye injection for pitching-plunging flat plate, Re = 20K (left column) and Re = 60K (right column); phases phi = 0, 45, 90, 120, 150, 180, 210 and 270.

6.6.2. Pure-Plunge Case

We next turn to the pure-plunge case. Unfortunately only dye injection is available for this case, and it is shown in Figure 74 (Re = 20K and 60K, analogous to Figure 73). As expected, Reynolds number effects are benign. The Re = 20K evinces discrete rollers in the near-wake at t/T = 0.25, whereas in the Re = 60K a continuous mixed wake is apparent. In general the lower-Re case has clearly defined dye streaklines, while the higher-Re case has mixing. It is not entirely clear whether this is partially a figment of the flow visualization technique (diffusivity of dye), or is entirely a statement about turbulent. In any case, there is no discernable effect on the LEV or the overall extent of flow separation.

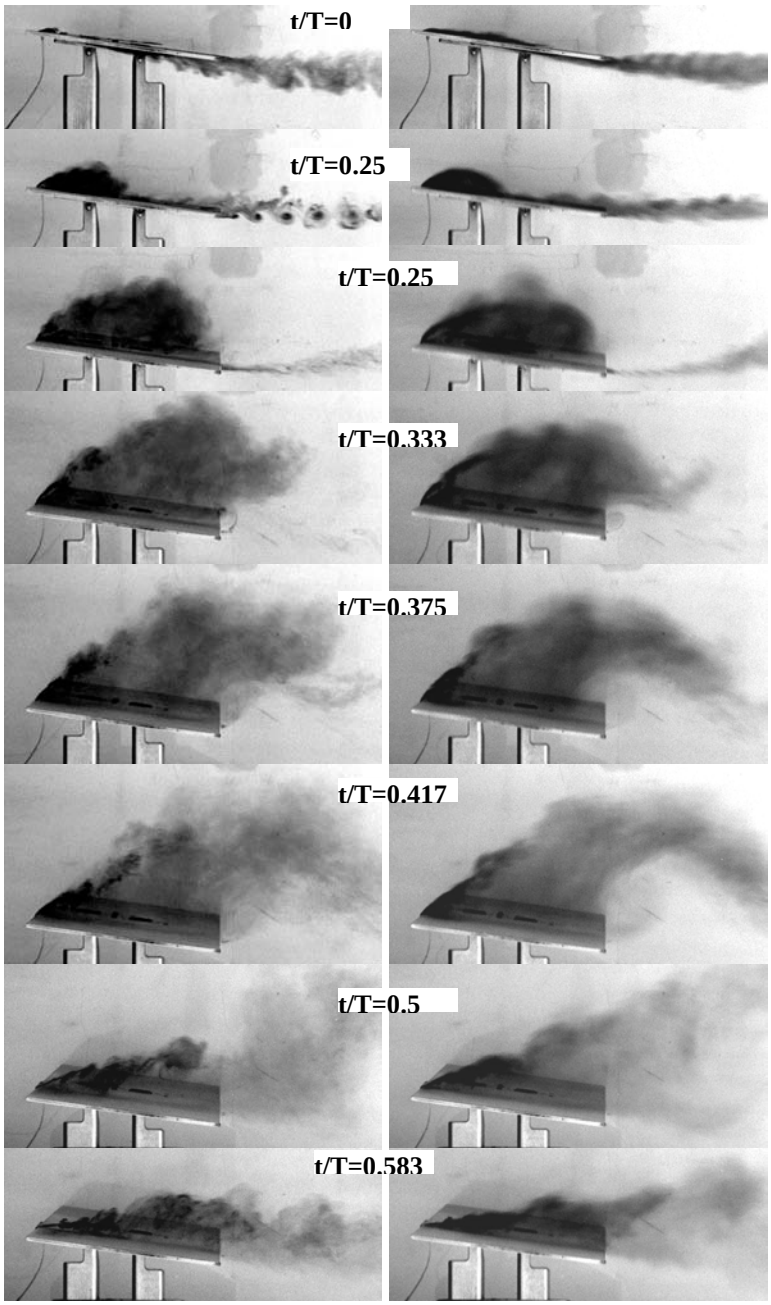

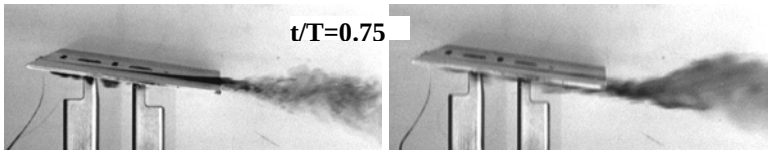

Figure 74. Dye injection, flat plate in pure-plunge, Re = 20K (left column) and 60K (right column. Snapshots from phases of motion as noted.

As compared to the SD7003 airfoil in pure-plunge, the differences are not great; the flat-plate LEV is somewhat larger and more diffuse than for the airfoil, and the low-speed region on the suction side towards the bottom of the downstroke persists less. This may mean (but has not been shown!) that the flat plate has less spanwise variation than the airfoil.

6.6.3. Lift Coefficient Comparison

As with the airfoil, we compare the FBG balance measurements from the HFWT with a wide range of computational results. Unfortunately by the time that these FBG measurements were taken, the balance was no longer behaving within specifications, whence the reported data are to be taken with rather more scepticism than is normally appropriate for such things. The results, such as they are, are in Figure 75. For the pitch-plunge case, the FBG measurement tracks closely with the various RANS computations, but for the pure-plunge case, the FBG measurement has an overshoot. The basic trends are similar to those of the airfoil: sinusoidal lift (even more so than for the airfoil, as expected); unlike for the airfoil, the "laminar" and "turbulent" RANS computations agree closely, suggesting even further that for the flat-plate, Re dependency is absent.

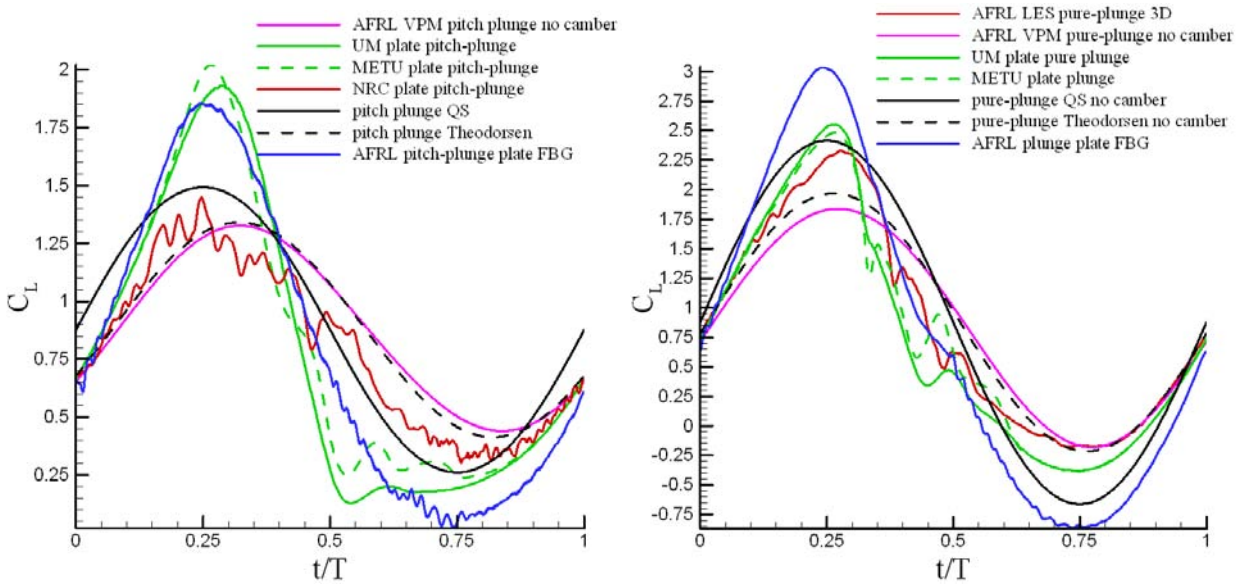

Figure 75. Lift coefficient for pitch-plunge (left) and pure-plunge (right) flat plate, Re = 60K; various computations, and FBG force balance data (blue curve).

6.7. Sinusoidal Pitch and Plunge of an AR=2 Flat Plate

6.7.1. Introduction and Motivations

Perhaps the most natural generalization from wall-to-wall models (in experimental facilities) and spanwise-periodic boundary conditions (in computations) is the finite-wing of high aspect ratio. By systematically reducing aspect ratio from some large but finite value, towards ever smaller values, it is possible to construct a consistent passage into 3D from 2D. This is sensible, for example, in terms of understanding the flapping-flight of large birds (see Chapter 1), which tend to be of high aspect ratio. However, in an experimental facility this introduces the problem of blockage or very low Reynolds number. To avoid blockage, the wingspan needs to be some fraction of the test section width, and at high aspect ratio this severely limits the chord. In turn the Reynolds number, based on chord, becomes very low. But very low Reynolds number problems, besides being inconsistent with the focus of earlier chapters, tend to be of comparatively low aspect ratio, as is the case for most insects. In computation, full resolution of high aspect ratio means a grid much longer in the spanwise than in the streamwise direction, which raises problems of computational size, if we wish to maintain high resolution in the streamwise direction.

The alternative is to consider low aspect ratios. This is more amenable to investigation, but more importantly, it is especially interesting because of the strong interaction expected at low aspect ratio between leading edge vortices and wingtip vortices, where for example the latter might stabilize the former through spanwise pressure gradients. Low aspect ratio wings undergoing various longitudinal-plane manoeuvres are expected to evince a qualitatively different flow structure and loads time history from those of the same sectional geometry, but in 2D. A full treatment of the problem requires detailed 3D velocimetry, which unfortunately is beyond the scope of this study. In keeping with the above-reported results, flowfield data are presented in streamwise-parallel planes, typically at the ¾-span location of the model. The featured configuration is the rectangular-planform flat plate of aspect ratio 2, with round edges on its entire periphery. Both the pure-plunge and the pitch-plunge case are considered. The canonical Reynolds number is now 40,000 rather than the 60,000 for the wall-to-wall cases, as blockage problems are reduced with a smaller model, and thus a smaller chord.

The sectional geometry of a thin flat plate with round edges was selected to deemphasize the role of boundary layer transition and to at least partially solve the problem of how to treat the airfoil section at the wingtips. Such shapes are also easy to manufacture, and in general easy to grid. Looking towards future work, they are amenable to generalization to flexible structures, such as membranes.

6.7.2. Flowfield Results

Pure plunge and pitch-plunge PIV-derived streamwise velocity and vorticity contours for the AR=2 rectangular plate are given in Figure 76 and Figure 77, respectively. PIV data in all cases are at the ¾-span location. The most striking difference between these results and the corresponding motions of the wall-to-wall plate are the absence of a discernable LEV in the pure-plunge case. In general the extent of flow separation for the AR=2 plate is smaller than for the wall-to-wall plate, evidently because of "spanwise relief", or a spanwise pressure gradient. Alternatively, we can revert to thoughts developed for the AR=2 static experiment mentioned above; the effective quasi-steady angle of attack for the AR=2 plate is half of that of the wall-to-wall plate, both according to lifting line and slender body theories. Accordingly, the flow separation for the AR=2 plate should be attenuated. This is basically the case here. As we will see in a subsequent section on higher-rate problems, as the reduced frequency increases, appeal to quasi-steady concepts becomes more tenuous – consistent with intuition.

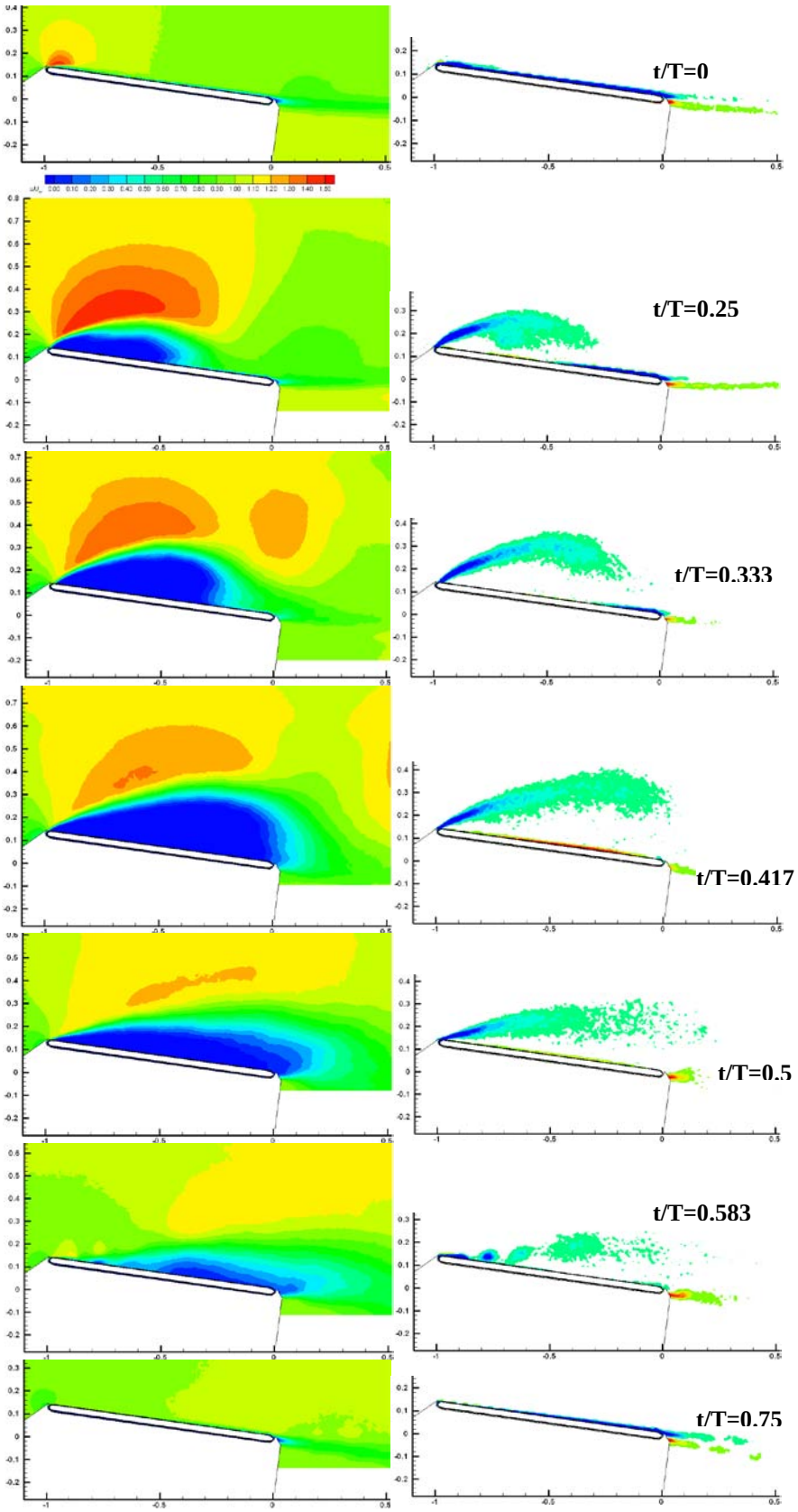

Figure 76. PIV, AR=2 plate in pure plunge, phases phi = 0, 90, 120, 150, 180, 210 and 270.

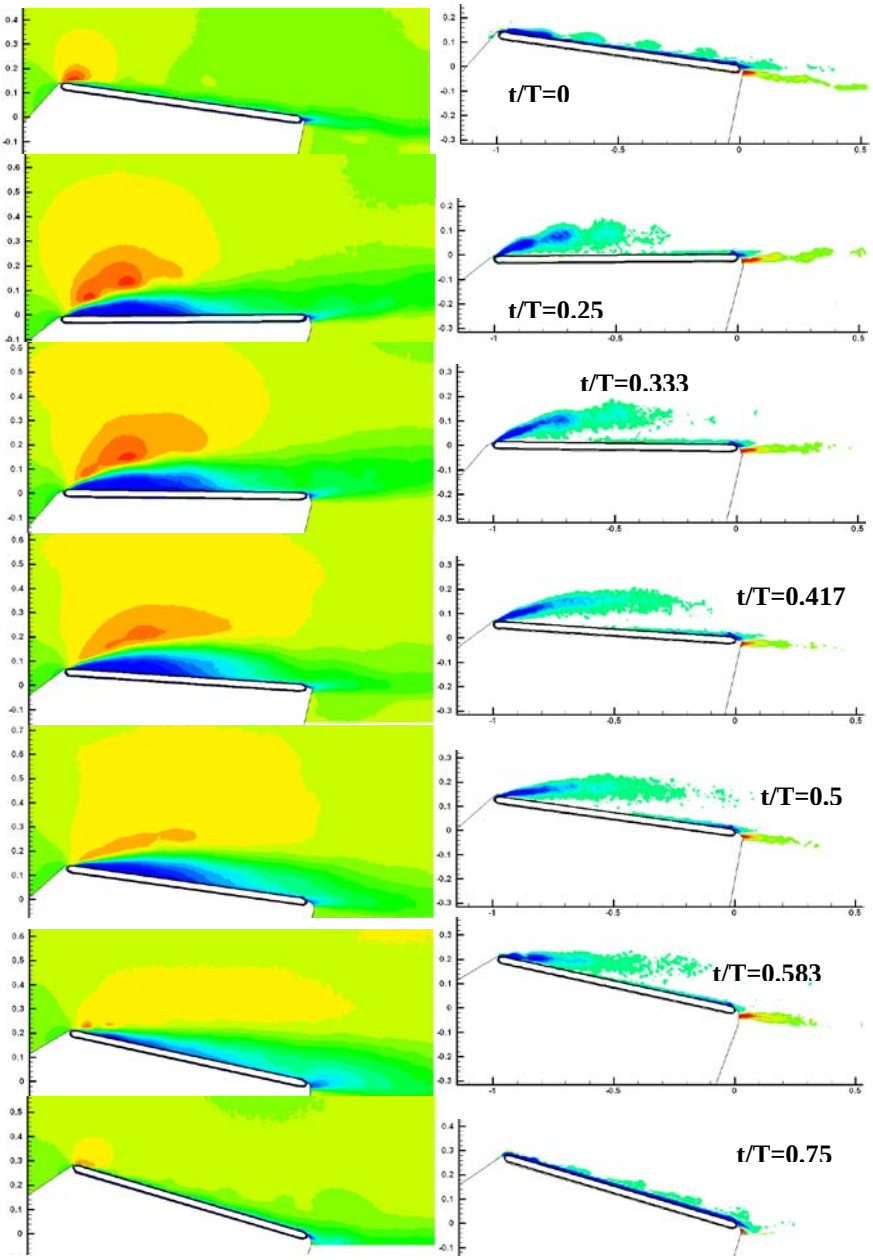

Figure 77. PIV results for AR=2 plate pitch-plunge.

6.8. Mixed-Frequency Problems, where Pitch and Plunge Frequency Differ

6.8.1. Problem Definition

In our final segment on periodic motions, we consider a problem where the frequency of pitch differs from the frequency of plunge by some multiple, while both are sinusoids. Of what relevance is such an exercise? Loosely, it could be a proxy for gust response of flapping-wing vehicles, where the fast frequency models the wing flapping, while the slow frequency models the gust. Sometimes pitch and plunge induced angle of attack are in opposition, resulting in a net low angle; other times, they add constructively, with very large excursions in effective angle of attack. Thus such motions are useful for producing large alpha variations without requiring very aggressive motions.

We consider a pitch amplitude of 15°, plunge amplitude of 0.1, Re = 10,000, mean angle of attack of 4°, and reduced frequency based on plunge of 3.93. As usual, pitch leads plunge by a phase difference of φ=0º. From here, we vary the ratio of pitch to plunge frequency as follows: 0.25, 0.75, 1, 2 and 4. Pitch pivot points at x/c = 0, 0.25, 0.5, 0.75 and 1.0 are considered. The main case of interest has pivot point at the midchord and pitch frequency twice that of plunge frequency. The model was started from rest at φ=0º, and begins motion by pitching nose-down and plunging down. The effective angle of attack, superimposed on the pitch angle, is shown in Figure 78. Commanded and attained values are compared; the latter shows oscillations associated with dynamic startup transients in the linear motors, which presumably respond as a second-order system to a step input in velocity.

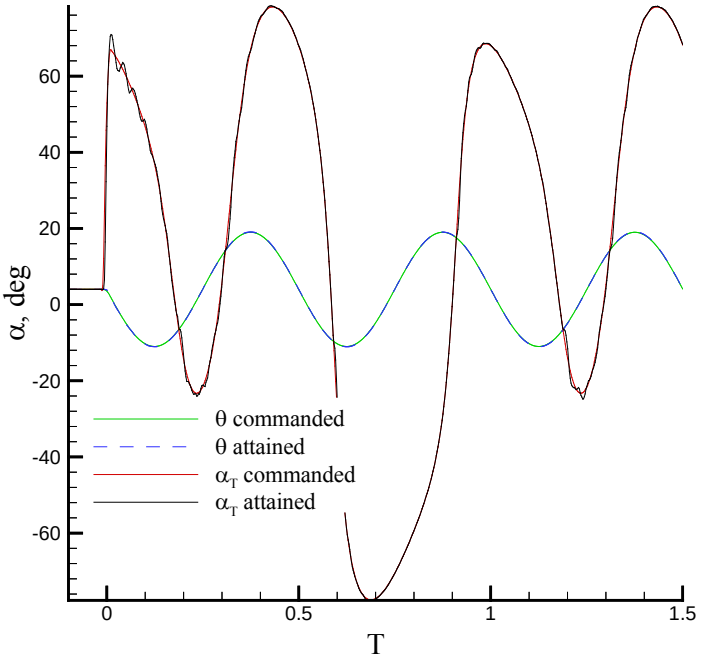

Figure 78. Commanded vs. attained angle of attack history for sinusoidal pitch frequency double that of sinusoidal plunge.

6.8.2. Flowfield Results

Figure 79 is a detailed tracing of the history of flow evolution from PIV and dye injection, at φ = 0º, 45º, 90 º, 135º, 180º, 225º, 270º, 315º, 360º, 405º, 450º, 495º, 540º, 585º, 630º, 675º, 720º, 1080º, and 1440º. φ = 360 completes one period of plunge oscillation after motion onset, 720 º completes two periods, and so forth. PIV resolution was 88 pixels/cm. For 32x32 pixel windows with 16x16 overlap,

this results in 84 velocity vectors per the 152mm chord length. As usual, laser reflections from the model surface limit boundary-layer resolution, and the pressure-side of the airfoil is in the shadow of the PIV light sheet. It would eventually be desirable to have an optically transparent model to acquire PIV data on the suction and pressure sides simultaneously, but even then, parallax would result in a void of data in the immediate model periphery, because the near-edge of the model would block said periphery in the plane of the light sheet. Of course, for more detailed boundary layer physics one can turn to CFD.

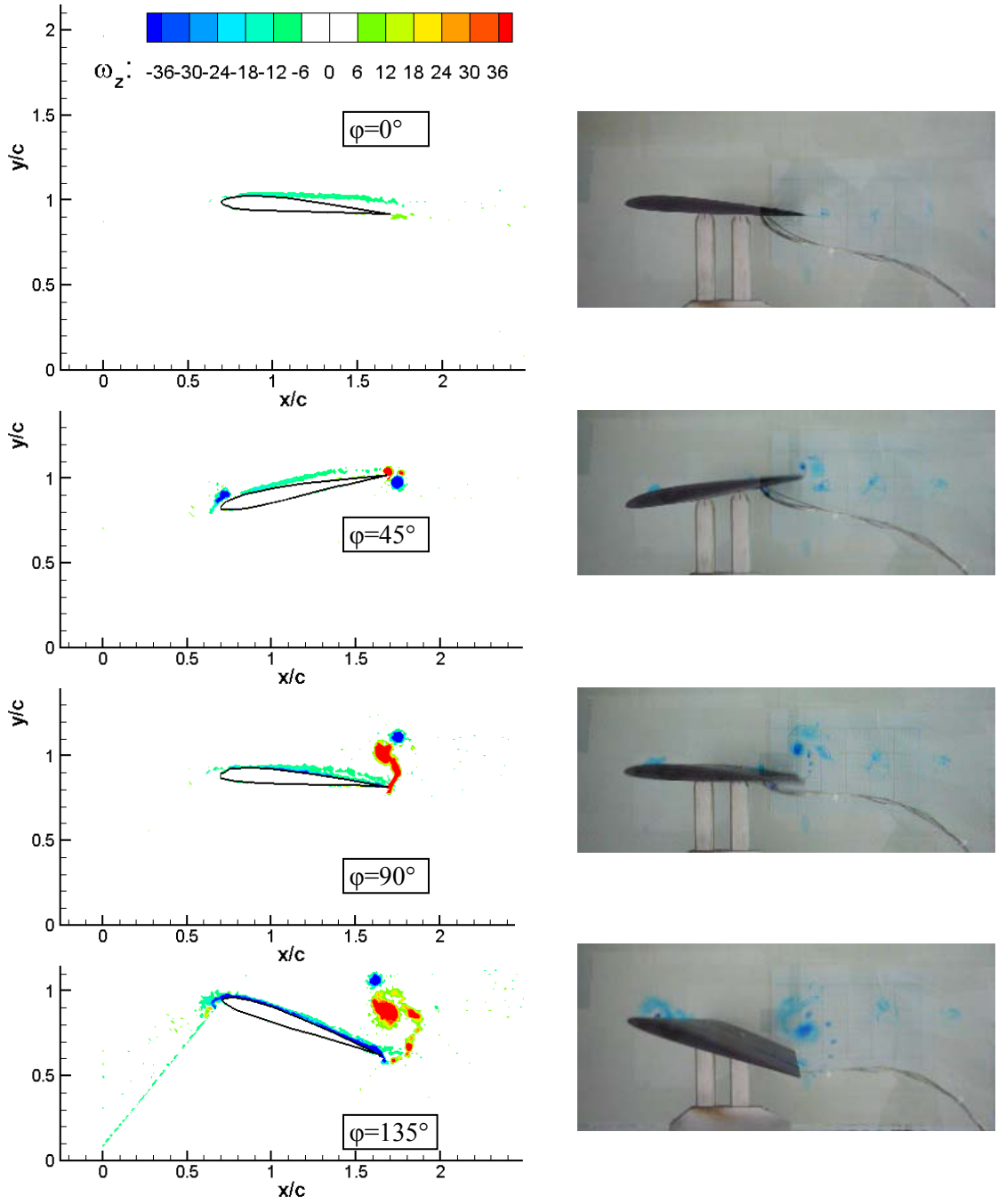

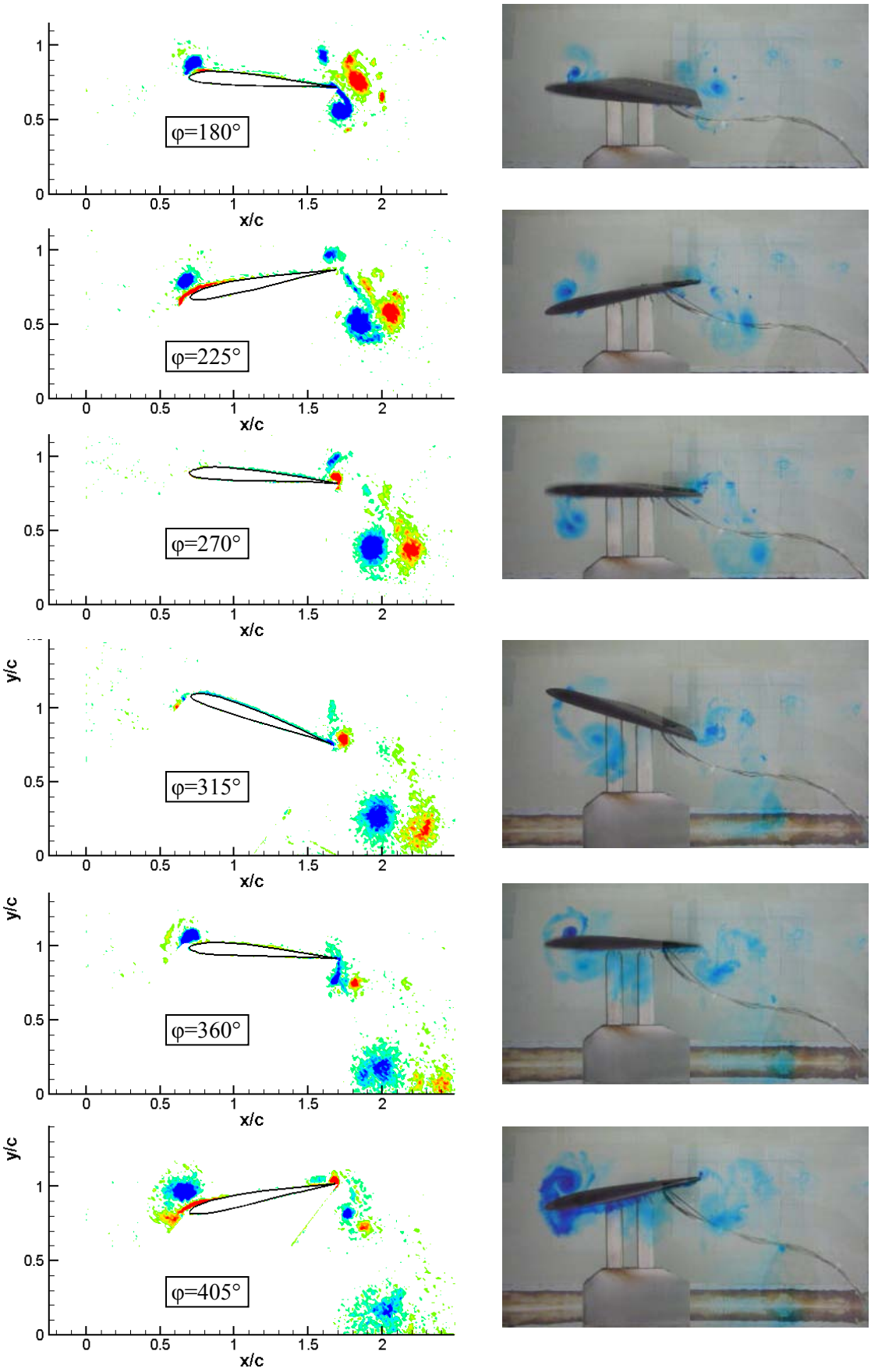
φ=180°
φ=225°
φ=270°
φ=315°
φ=360°
φ=405°
x/c
y/c
0
0.5
1
1.5
2

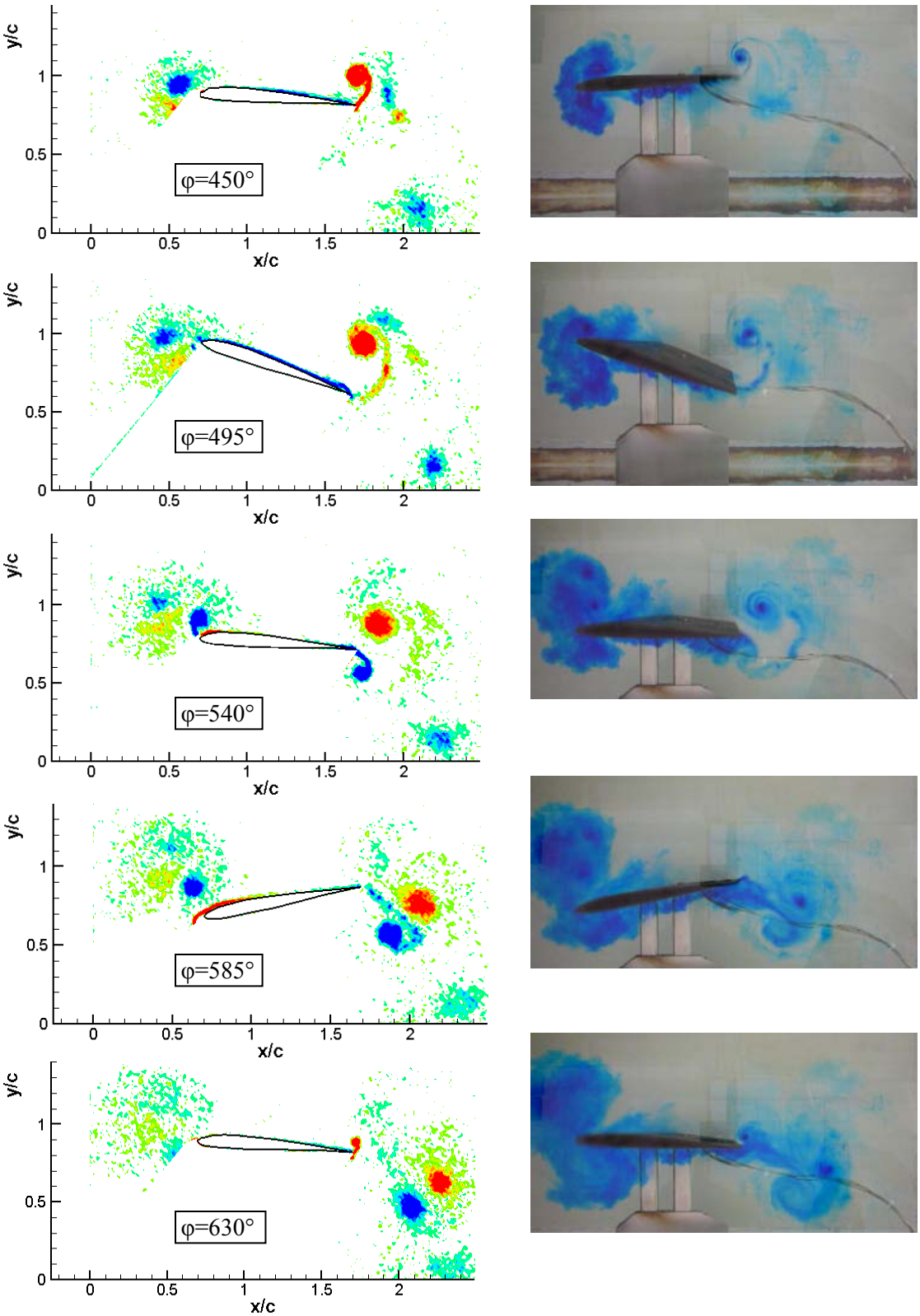
y/c
x/c
φ=450°
φ=495°
φ=540°
φ=585°
φ=630°
0
0.5
1
1.5
2

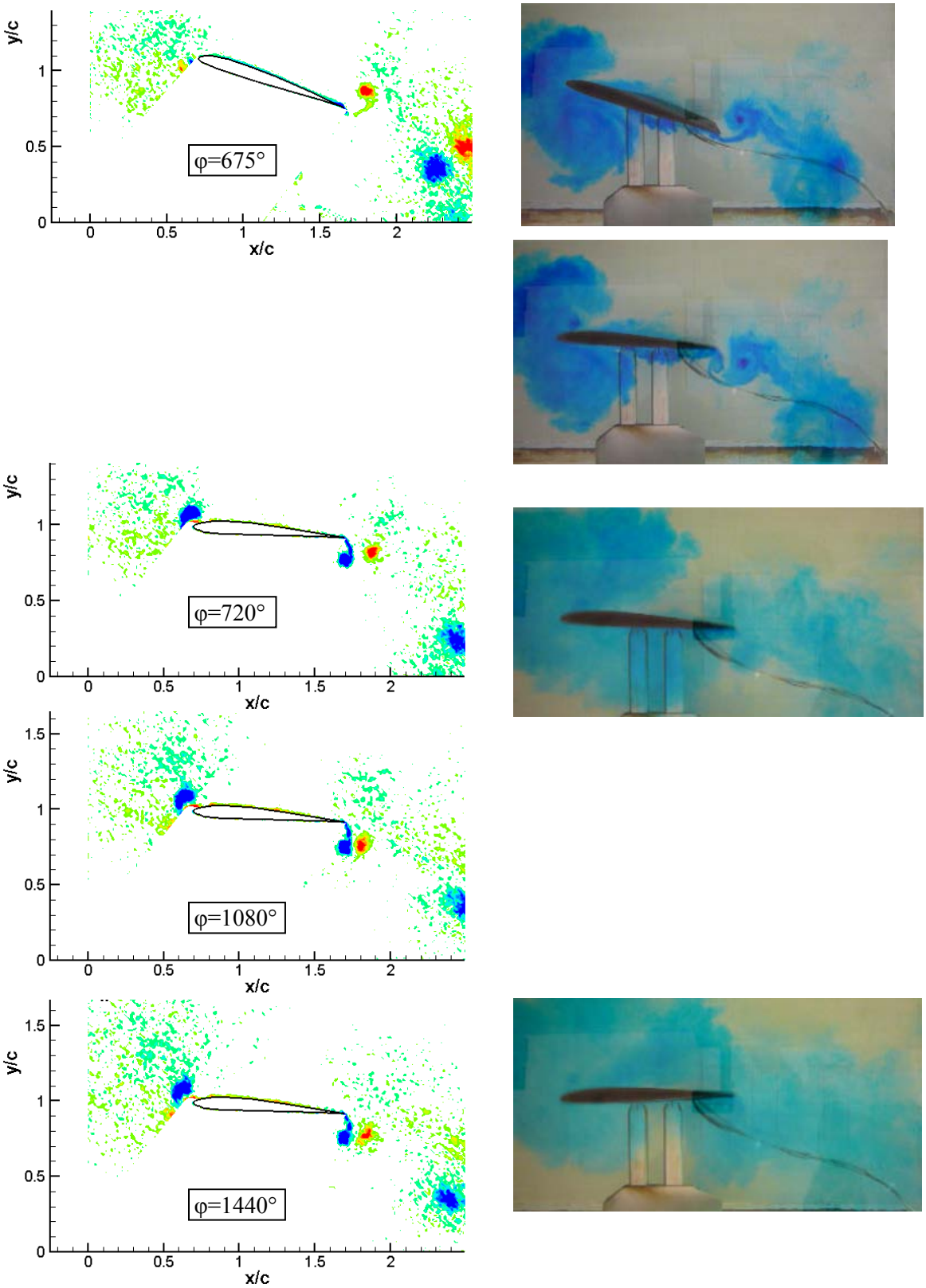

Figure 79. PIV (left), averaged over 10 instantiations per phase, and dye injection (right), Re = 10,000, mixed-frequency pitch-plunge; phases of motion as marked.

The final two frames of Figure 79 illustrate the limitations of dye injection. That is, through the first one and a half periods of motion, agreement between PIV vorticity and intensity of dye concentration is excellent. By two periods of motion, this agreement has declined, as dye is becoming more diffuse. By three periods of motion, agreement is very poor. We can argue towards the general statement that dye flow visualization is an excellent marker for how vortices form and grow, but is less useful for following how vorticity is transported, because the mixing of dye and the stretching/folding of vorticity are different. Of course, this is not a new concept, but it is useful to assess dye vs. more quantitative methods in the general context of low Reynolds number unsteady aerodynamics, as dye visualization is broadly – and unfairly! – denigrated for its crudeness and putative tendency to give dubious results.

Comparing φ = 720º, 1080º and 1440º, the PIV shows strong repeatability. Therefore the flow appears to relax to periodicity – if the ensemble average is to be believed – by two periods of plunge after motion onset. We also see the curious phenomenon of shedding a vortex pair upstream from the leading edge, for example at φ = 450º. The wake behind the trailing edge is not parallel to the free stream but is biased towards the downwash direction. Such wake bias recalls the high-frequency pure-pitch oscillations reported earlier.

We mention only briefly the role of pitch pivot point location, as this will be covered in more detail in the sections on nonperiodic motion, and the effect is much the same as in the periodic cases. Namely, moving the pivot point further aft delays the LEV formation, but results in a stronger LEV when it does eventually form. We also note that the mixed-frequency case is a challenging litmus test for experimental-computational comparison[104], at least for 2D computations, as presumably the same 3D stretching/folding effects that plague dye vs. PIV comparison also affect the computation. That is, in the first 1-1½ periods of motion, computational-experimental agreement is quite good, even across a large mismatch between the two in Reynolds number. But thereafter the agreement decays. This suggests that impulsive or non-periodic problems are more promising, at least in some cases, for experimental-computational agreement. And this is where we turn next.

6.9. Pitch Ramp-and-Return

6.9.1. Introduction

While most of the preceding work related to MAVs was motivated by problems of flapping, here we return to the second major application – perching. Several approaches are possible. One approach is direct perching, where the angle of attack varies from some low to high value, and stays there. An alternative is a motion of pitch ramp, followed by steady hold at high angle of attack, followed by return to the original angle of attack. Here we consider a parameter range similar to that studied by Visbal and Shang[37], and continue to much higher reduced rates. The higher rates were of minimal interest for dynamic-stall applications, prior to the advent of MAVs.

The objectives of this section are to (1) conduct a parameter-study of Reynolds number, pitch pivot point location, reduced frequency and pitch-plunge comparison (the latter to extend sinusoidal pitch-plunge comparisons[105,106] to linear ramps); (2) to mutually-validate a 2D high-resolution computation and a water tunnel experiment, in the sense that the latter is inevitably plagued by tunnel test section wall effects and blockage; and (3) to computationally explore trends in lift coefficient time history for a parameter study of reduced frequency. In departure from most of the above-cited literature, we consider pitch ramp-hold-return, where the plate returns to zero incidence angle, instead of pure pitch ramp-hold. This is motivated by the impression that the return problem has the more complex flowfield transients, and is therefore a richer test case for modeling lift coefficient time histories departing from the simplest abstractions. Subjects (2) and (3) are reported in publications currently in-print, with extramural collaborators; the present report will focus strictly on the in-house research.

6.9.2. Experimental Parameter Study with Dye Injection

The typical motion time history is shown in Figure 80. "Time" is convective time, or number of chords traveled by the free-stream. The baseline case is pitch about x/c = 0.25 at $K = c\dot{\theta}/2U_\infty = 0.70$ and Re = 10K, from an initial incidence of 0º to a final incidence of 40º. The hold at the top of the ramp motion lasts for 0.05c convective time. The "equivalent" plunge, in the sense of h(t) such that $\arctan\left(\frac{\dot{h}(t)}{U_\infty}\right) = \alpha(t)$ matches that of the pitch (ignoring the pitch-rate effect), is shown as the green curve in Figure 80. Plunge time history is parabolic concave-up to compare with linear pitch-up, linear to compare with pitch-hold, and parabolic concave-down to compare with linear pitch-down. Starting and stopping transients are smoothed by cubic splines, set for an upper bound of acceleration of 10 m/s^2. Comparison between commanded and attained plunge rod position shows a maximum deviation of about 0.1mm, corresponding to an angular error of ~0.13º in the plane of the airfoil chord, had the airfoil been a rigid body. However, as mentioned below, the various models suffered from elastic vibrations, resulting in angular excursions at the top and bottom of the pitch stroke, which with present methods cannot be reliably quantified.

In this section, a large but rather superficial survey of flows from various motion parameters is presented, in all cases by dye injection from the plate leading or trailing edge at approximately the ¾-span location. In most cases, snapshots of the flowfield are shown when the model is halfway up to its maximum angle of attack; upon reaching maximum angle of attack; halfway on the downstroke; upon returning back to the zero angle; and one ramp's worth of time after returning to the zero angle. These are denoted with black line segments in Figure 80.

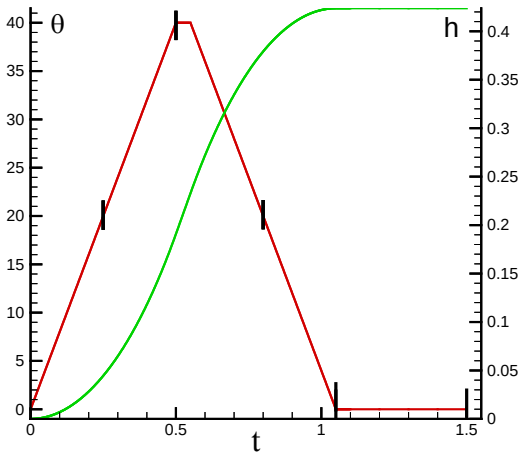

Figure 80. Time-trace of pitch angle and plunge position. Flow visualization frames correspond to position in time denoted by the black line segments; the fifth line segment is one ramp-motion's time after motion cessation.

In Figure 81 the pitch ramp-hold-return is examined across a range of reduced frequency from K = 0.1 through 1.4, keeping the pivot point at x/c = 0.25. All cases show a large leading edge vortex, and all show an interaction between the bluff-body-type Karman vortex street prior to motion onset, with the motion-induced trailing vortex system after motion onset. As K increases, the LEV becomes more compact and is better able to retain its integrity as it eventually convects downstream. Higher K means not only stronger vorticity transport into what becomes the LEV, but also that the LEV has had less time to form, and therefore is less advanced at the same snapshot of model position, relative what happens at lower K. Higher K also results in a pair of vortices in the near-wake, aft and below the plate. This is discussed in more detail in Section 2 below. A small vortex is formed upon return to zero angle of incidence. Finally, the eventual convection of the LEV past the trailing edge results in shedding of a trailing-edge vortex of opposite sign, to observe conservation of circulation, en route to return to the flowfield state seen prior to motion onset. As K increases, the strength of this final TEV also increases. But in all cases, return of the wake to its shape before the motion onset occurs 3-4 convective times after motion completion. This can be seen from Figure 82, which shows the extremes of K = 1.4 and 0.1, with snapshots presented at integer values of convective time after motion cessation. This suggests that the aggregate of flowfield features such as shed vortices convects with the free-stream. Exceptions are vortex-on-vortex interactions, such as in the trailing vortex pair, for the higher reduced frequencies. These may be responsible for transients in lift and especially in pitching moment – a conjecture whose verification is beyond the scope of the present study.

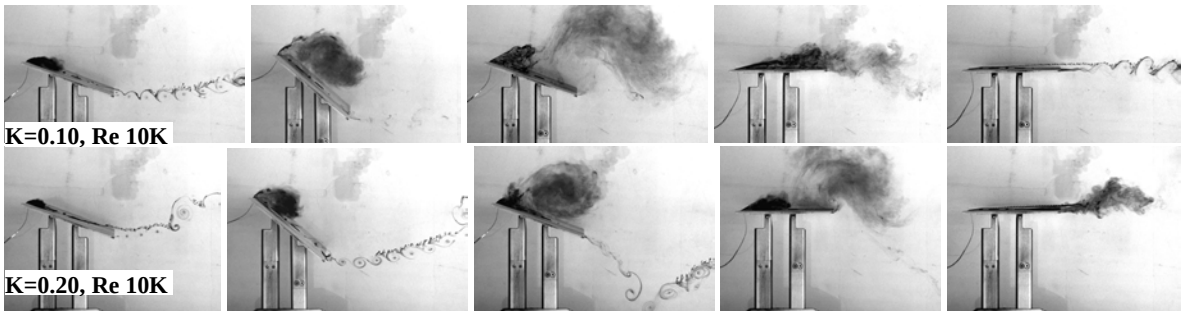

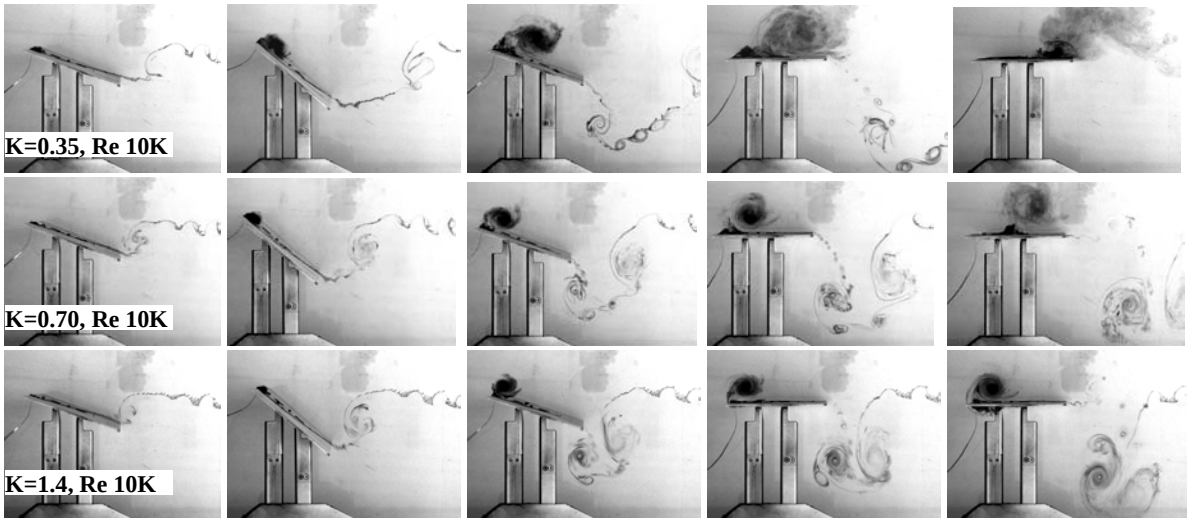

Figure 81. Flat-plate pitch for various reduced frequencies: K = 0.1 (top row), 0.2 (row 2), 0.35 (row 3), 0.70 (row 4), and 1.4 (row 5).

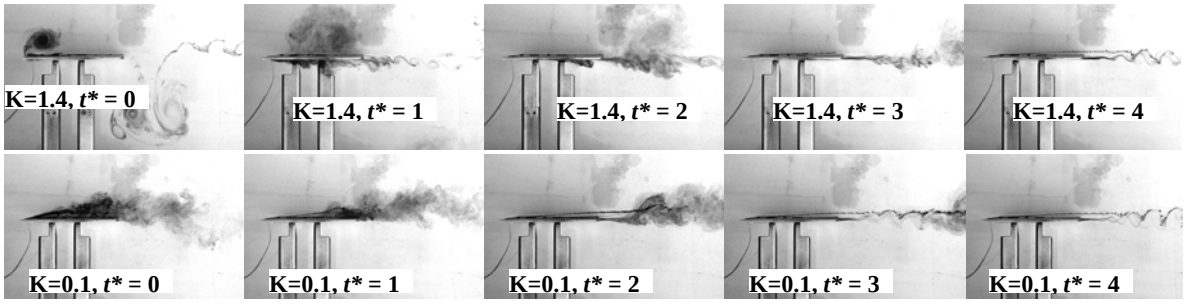

Figure 82. Comparison of highest-rate-motion and lowest-rate-motion flowfield evolution with respect to convective time; *t after motion cessation as marked. K = 1.4 (top row) and 0.1 (bottom row).**

Returning to Figure 81, the flowfields for the SD7003 airfoil and flat plate at K = 0.7 are reasonably similar, suggesting that motion-induced effects dominate those of the model cross-section. With its sharper trailing edge, the airfoil has much stronger dye concentration in the trailing vortex system, especially in the vortex shed during the upstroke, but the shape and convective history of the vortex system are similar to the plate's. The plate's LEV is somewhat stronger, more offset from the model suction-side and more coherent in going downstream. It is not clear whether this is due to the difference in the models' leading edge radii or the camber/thickness distributions.

Figure 83 compares pitch and "equivalent" plunge. Also, pitch and equivalent negative plunge are superimposed in a combined motion, in an effort to discern to what extent the combination, which gives quasi-steady identically zero angle of attack, comes close to producing a vorticity-free flowfield.

Wakes of pitch and plunge are seen to be entirely different, with the latter showing a smooth separation from the trailing edge followed by roll-up into a vortex pair. In the combined pitch-plunge, the flowfield looks similar to that for pure-pitch. Thus pitch-plunge equivalence or cancellation fail completely in regards to the trailing vortex system. On the other hand, the LEV of the plunge is similar in appearance to that of the pitch. And for the combined motion, the LEV is largely vestigial

As with pitch at K = 0.7, plunge for the airfoil vs. the flat-plate have similar flowfields – even more so for plunge than pitch, as in the latter the trialing edge motion is small, and thus the airfoil's sharp trialing edge has less of a role in the overall vorticity production budget. And, as with pitch, in plunge the flat-plate's LEV is somewhat larger than the airfoil's – probably again because of edge radius.

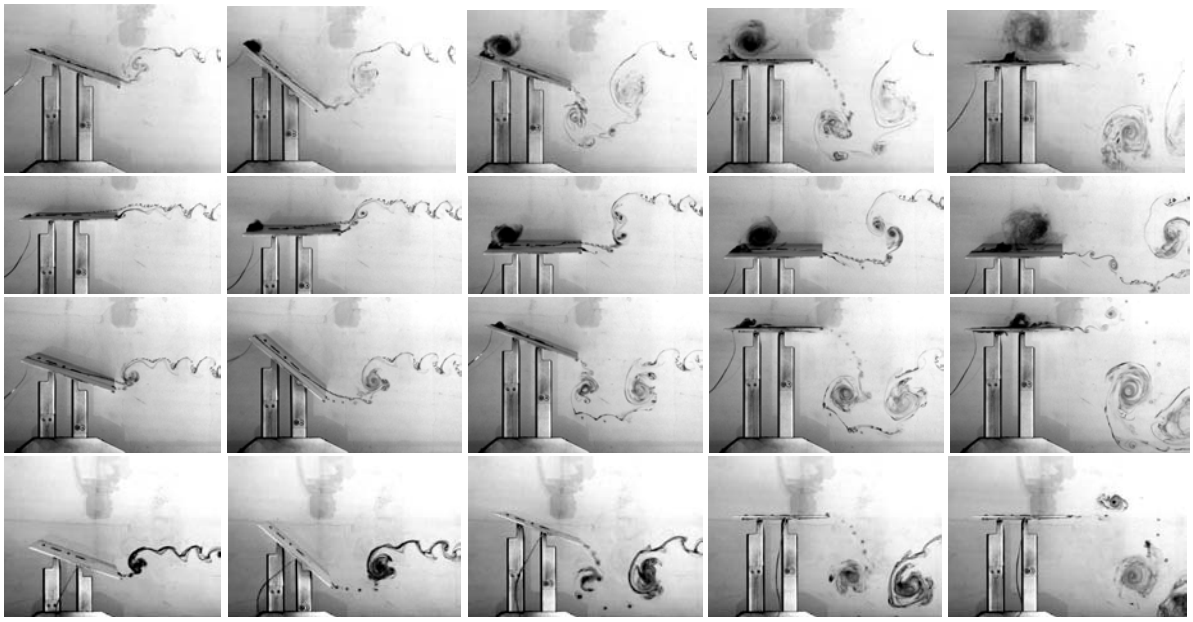

Figure 83. K = 0.70, 0º-40º-0º pitch (top row), "equivalent" pure-plunge (row 2), combined pitch-plunge (row 3); and combined pitch-plunge with trailing edge dye injection (bottom row). Re = 10K.

The above comparison of pitch vs. plunge ignores the effect of pitch-rate, which enters the quasi-steady expression for $C_L(t)$ whenever the pitch pivot point is not x/c = 0.75[87], and which is increasingly important with larger K. While the present work has not extended to linear ramps the pitch-plunge equivalence based on Theodorsen's formula, as considered by McGowan et al[105]., the role of pivot-point changes is considered qualitatively. Figure 84 shows 0-40-0 pitch with pivot point locations x/c = 0, 0.25, 0.5, 0.75 and 1.0. With pivot point further aft, the vertical extent of the near-wake becomes smaller. For pitch about x/c = 1.0, the near-wake begins to resemble that of plunge, from Figure 83. For pivot at x/c = 0.25 and 1.0, dye injection was conducted at both leading and trailing edge, and close agreement between the two implies that the injection method can be deemed to be non-intrusive – or, to be pedantic, equally intrusive. In going towards further-aft pitch pivot point, the LEV on the plate suction-side at peak angle of incidence becomes more concentrated, and during the downstroke the LEV lifts further off of the plate surface. Flow along the vortex axis also becomes stronger, akin to the trailing vortex system reported by Ol for high-frequency sinusoidal pure-plunge[107]. On the plate pressure side, a companion LEV forms for the further-aft pivot point locations. It is subsumed by the suction-side LEV on the downstroke. The larger pressure-side LEV for the further-aft pivot locations stands to reason, as such a motion looks locally to the LE as a pure-plunge, and the "LEV" is the trailing vortex behind a locally plunging plate.

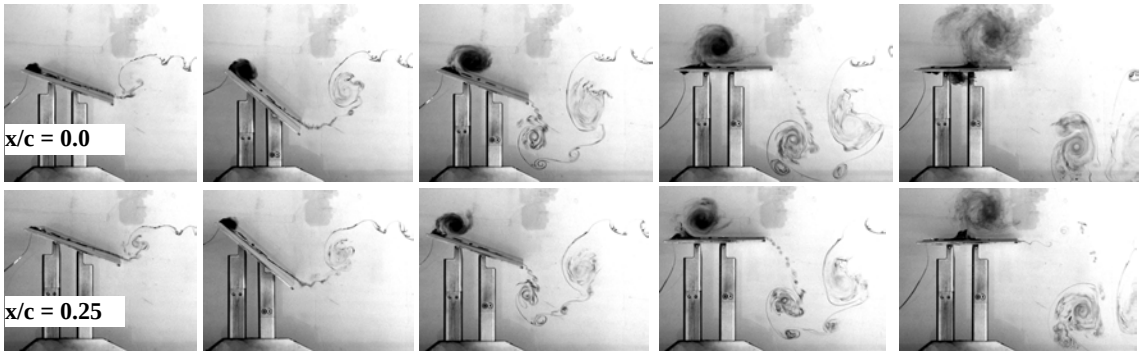

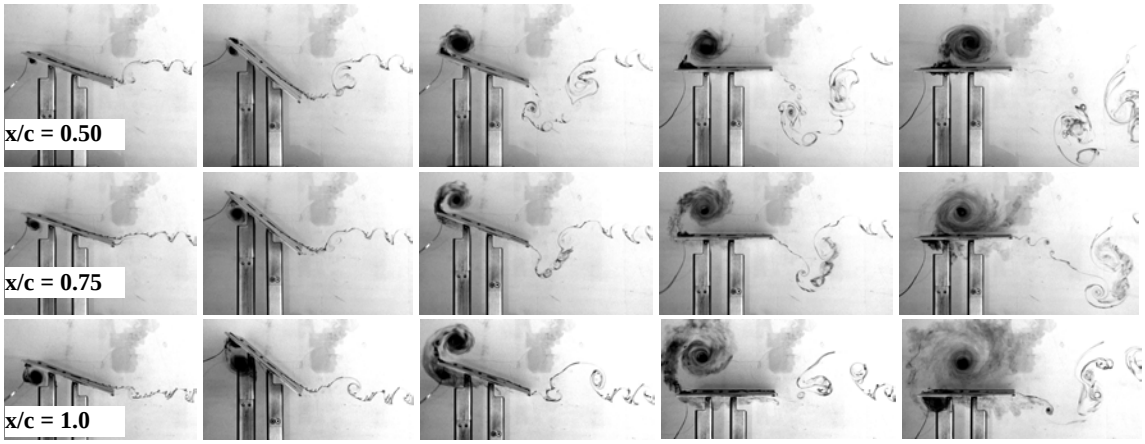

Figure 84. Flat-plate 0º-40º-0º pitch, K = 0.70, Re = 10K; parameter study of role of pitch pivot point. x/c = 0.0 (top row), 0.25, 0.50, 0.75 and 1.0 (bottom row).

6.9.3. Qualitative vs. Quantitative Flow Visualization

PIV and dye injection results from the water tunnel are compared in Figure 85 for K = 0.70, and in Figure 86 for K = 0.20. Figure 85 and Figure 86 also include the computed vorticity field at $\theta = 20º$ and $\theta = 40º$ on the upstroke for K = 0.70 and 0.20, respectively. All results are at Re = 10,000.

To reiterate, the dye injection is "instantaneous", while the PIV is phase-averaged. Because the pre-motion Karman shedding is uncorrelated with the pitch-ramp motion, the Karman vortex street so visible in the dye injection is absent in the PIV vorticity contours. Otherwise, the correspondence between concentrations of dye and peaks of vorticity is quite close, in the sense that high-contrast regions of dye nearly coincide with high-amplitude ensemble-averages of vorticity. PIV data consist of 50 pairs, acquired in a sequence where each ramp-hold-return event was separated from the previous event by ~6 convective times.

The K = 0.7 case has a counter-rotating vortex pair in the near-wake, just downstream of the trailing edge at motion cessation. It consists of a counter-clockwise vortex formed during the upstroke, and a clockwise vortex in the downstroke. Both vortices are connected by feeding sheets, whose constituents themselves roll up into discrete vortices under self-induction. This structure survives the phase-average without smearing. At the leading edge, there is a dynamic stall vortex system akin to what was observed for high-frequency sinusoidal pitch by McGowan et al[105].

The K = 0.2 case, in contrast, has a strongly coherent trail of counter-clockwise discrete vortices shed all the way until the model reaches maximum pitch angle. At the top of the pitch stroke, or shortly after downgoing motion commences, a weak vortex of opposite sign is shed.

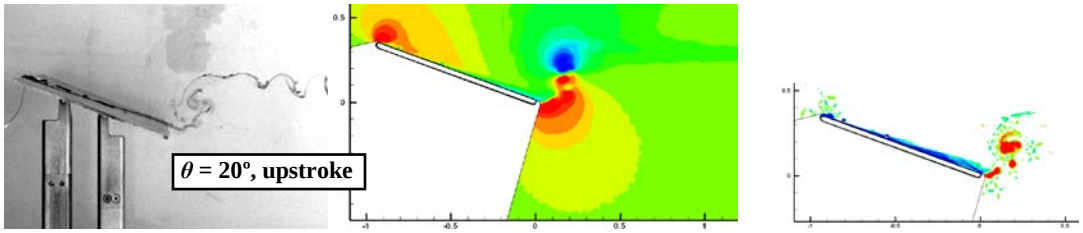

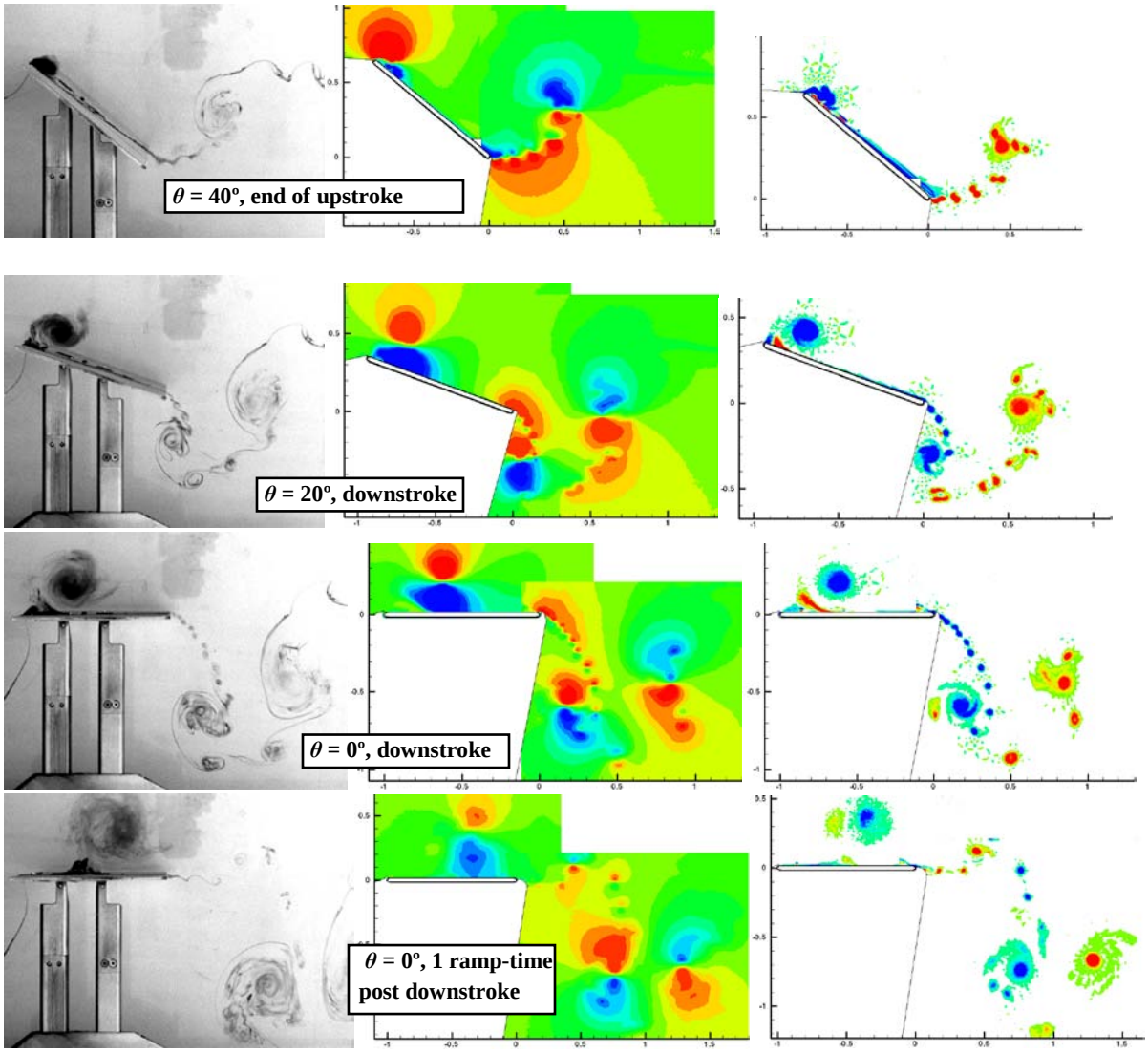

Figure 85. K =0.70, Re =10K; dye injection (left column), phase-averaged velocity (middle column), phase-averaged vorticity (right column) and samples of computed vorticity (also right column).

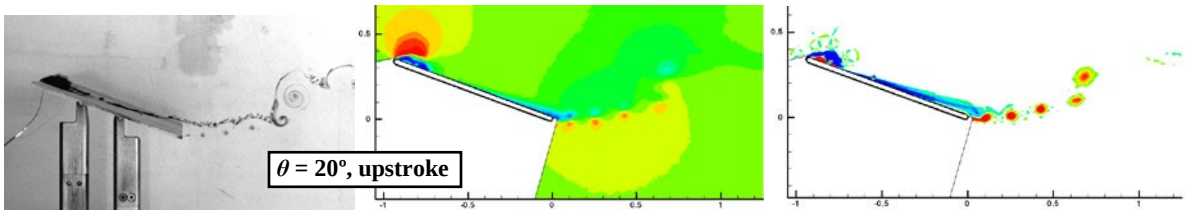

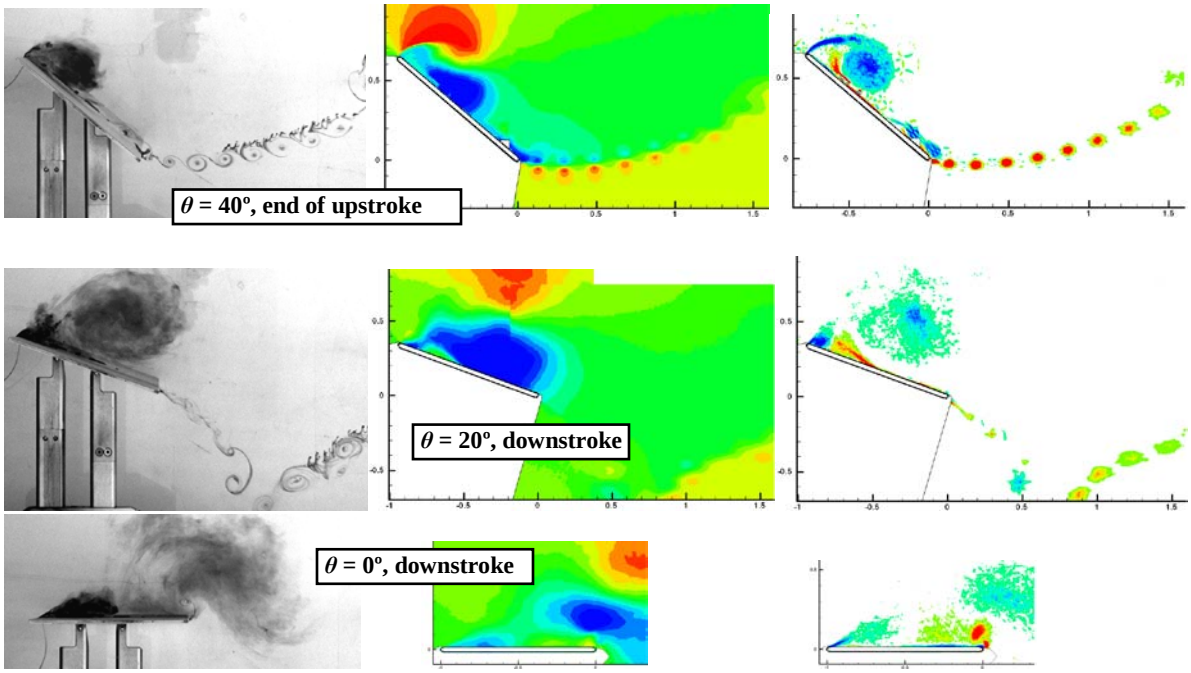

Figure 86. K =0.20, Re =10K; dye injection (left column), phase-averaged velocity (middle column), phase-averaged vorticity (right column) and samples of computed vorticity (also right column).

6.9.4. Removing Parasitic Surge

One of the drawbacks of the original 2-motor installation was an undesired but inevitable fore-aft motion whenever the prescribed pitch pivot point was not coincident with the front lower plunge rod bushing. This is because the front plunge rod was constrained to move up and down, with no provision to swing (otherwise the rig would be flimsy). Having the third linear motor, a fore-aft motion can be programmed to negate the parasitic motion. For example, in the following there is a pitch from 0 to 45 degrees, about the trailing edge of the model. A sequence with no surge correction is compared with a corrected sequence. Because in the former the trailing edge is in undesired motion, the near-wake is different, with stronger trailing edge vortex shedding (Figure 87).

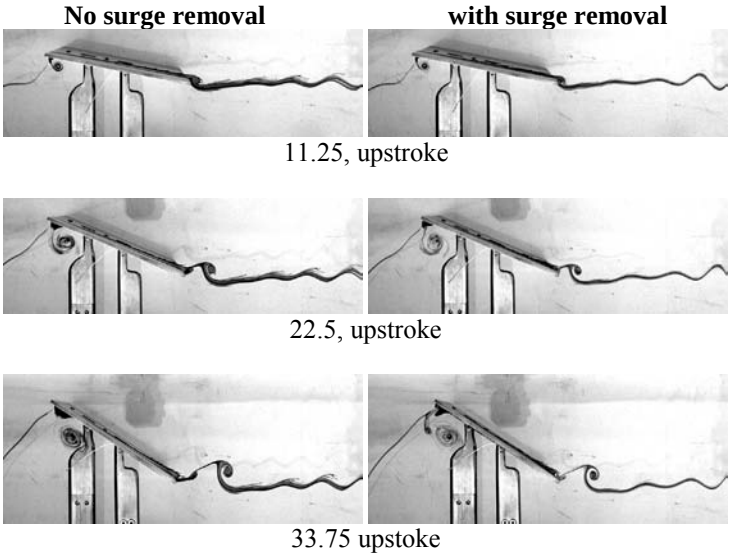

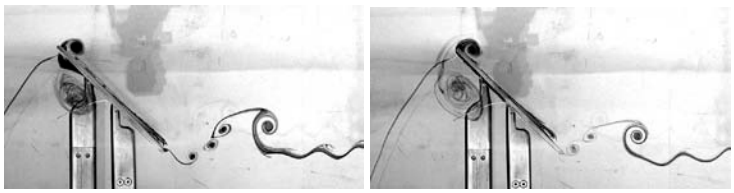

max, no surge

33.75 on downstroke

22.5 on downstroke

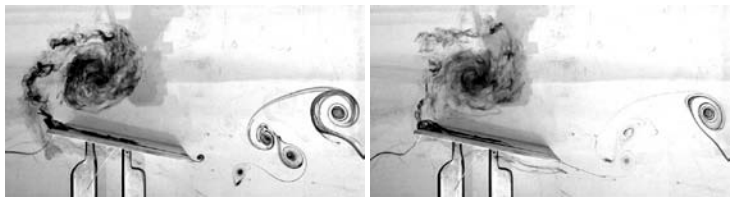

11.25 downstroke

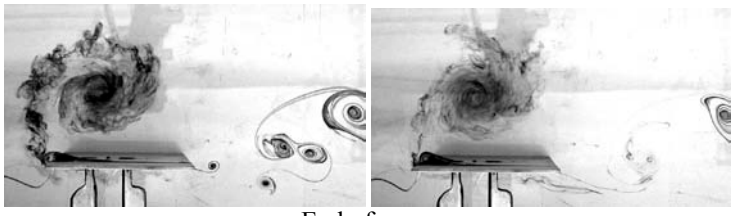

End of ramp

Figure 87. α = 0º-45º linear ramp-hold-return, K = 0.7, pivoting about x/c = 1.0. Without removal of parasitic surge (left) and with removal of parasitic surge using the third linear motor (right).

6.9.5. Pitch Ramp and Return, 2nd Sequence

The previously-described problem is revisited upon gleaning more experience, and was proposed as a "canonical problem". This was the subject of several results reported at the AIAA Aerospace Sciences Meeting in Orlando, FL, January 2010.

6.9.5.1. New Motion Definitions

We define a family of motions with shared angle of attack range and peak angle of attack rate, but in one case with nominally sinusoidal (nearly one-minus-cosine function) angle of attack history, and in

another of trapezoidal history, where accelerations are limited to narrow regions of time, and are zero otherwise. The unsmoothed trapezoidal motion has an upgoing and downgoing linear ramp in angle of attack, defined nondimensionally as $K = c\dot{\theta}/2U_\infty = 0.20$, with pivot about the leading edge.

To avoid model vibration in experiments and numerical instabilities in the computations, and delta-function spikes in calculated noncirculatory force, considerable care is taken to smooth all motions. For a ramp in going from 0 degrees angle of attack to 45 degrees, the first 10% (4.5 degrees) can be replaced with a sinusoid tangent to the baseline ramp, and similarly in approaching the "hold" portion at the peak angle of attack, and again on the downstroke. The result is a piecewise sinusoidal and piecewise linear fit. This unfortunately has discontinuities in the angle of attack second derivative, and was therefore replaced by an alternative C^∞ smoothing function developed by Eldredge[108]. The smoothing function G(t) is defined as:

$$G(t) = \ln\left[\frac{\cosh(aU_\infty(t-t_1)/c)\cosh(aU_\infty(t-t_4)/c)}{\cosh(aU_\infty(t-t_2)/c)\cosh(aU_\infty(t-t_3)/c)}\right]$$

where *a* is a free parameter, c is the chord, and the times t_1 through t_4 are:

t_1 = time from reference 0 until when the sharp corner of the unsmoothed ramp would start
$t_2 = t_1$ + duration of the pitch upstroke, until the sharp corner where the hold would have begun
$t_3 = t_2$ + the unsmoothed hold time at maximum alpha
$t_4 = t_3$ + the unsmoothed pitch downstroke duration

Then, with the pitch amplitude A = 45 deg, the smoothed motion becomes

$$\alpha(t) = A\frac{G(t)}{\max(G(t))}$$

By varying the parameter *a*, G(t) becomes a parametrization of smoothing from true trapezoid all the way to approximate sinusoid. A large value of *a* leads to an abrupt acceleration, presumably with large spikes in noncirculatory lift and pitch (but not drag/thrust, which has no noncirculatory portion).

The relation between linear ramp and sinusoid, in Figure 88, is constrained by matching the amplitude and peak pitch rate between the two. So for a linear ramp with dimensional pitch rate $\dot{\theta}$, the duration of the linear ramp relates to the frequency of the sinusoid as $t_2 - t_1 = 1/2\pi f$, and the length of the linear ramp's hold time becomes $t_3 - t_2 = \frac{1}{2f} - \frac{1}{\pi f}$. Setting a = 2 produces a close fit between the sinusoid, $\theta(t) = A(1-\cos(2\pi f t))$, while a = 11 is in turn a close approximation to the 10% sinusoidal smoothing of an otherwise linear ramp (Figure 89).

Physically, the pitch ramp-hold-return motions in the K range of 0.2-0.7 and Re range of $O(10^4)$ feature the growth of a large leading edge vortex (LEV) that does not pinch off until the pitching motion ends. The hold at maximum angle of attack lasts roughly as long as it would take the LEV to convect from leading to trailing edge at free-stream speed. The downstroke is proposed as a prototypical motion to study flow "memory" effects, where upon returning to zero angle of attack the flow is still recovering from massive separation. We speculated, at this point, that a quasi-steady model with the appropriate tuning can account for lift coefficient time history over the entire upstroke (other than for noncirculatory effects), but will fail on the downstroke. For applications such as insect flapping, there really is no downstroke in the sense of the present case, as the motion essentially starts afresh on every half-stroke. It is perhaps for this reason that quasi-steady models for insect-type flapping are successful[109].

Thus, there are four main cases: two Reynolds numbers and two values of the smoothing parameter *a*, of 2 and 11.

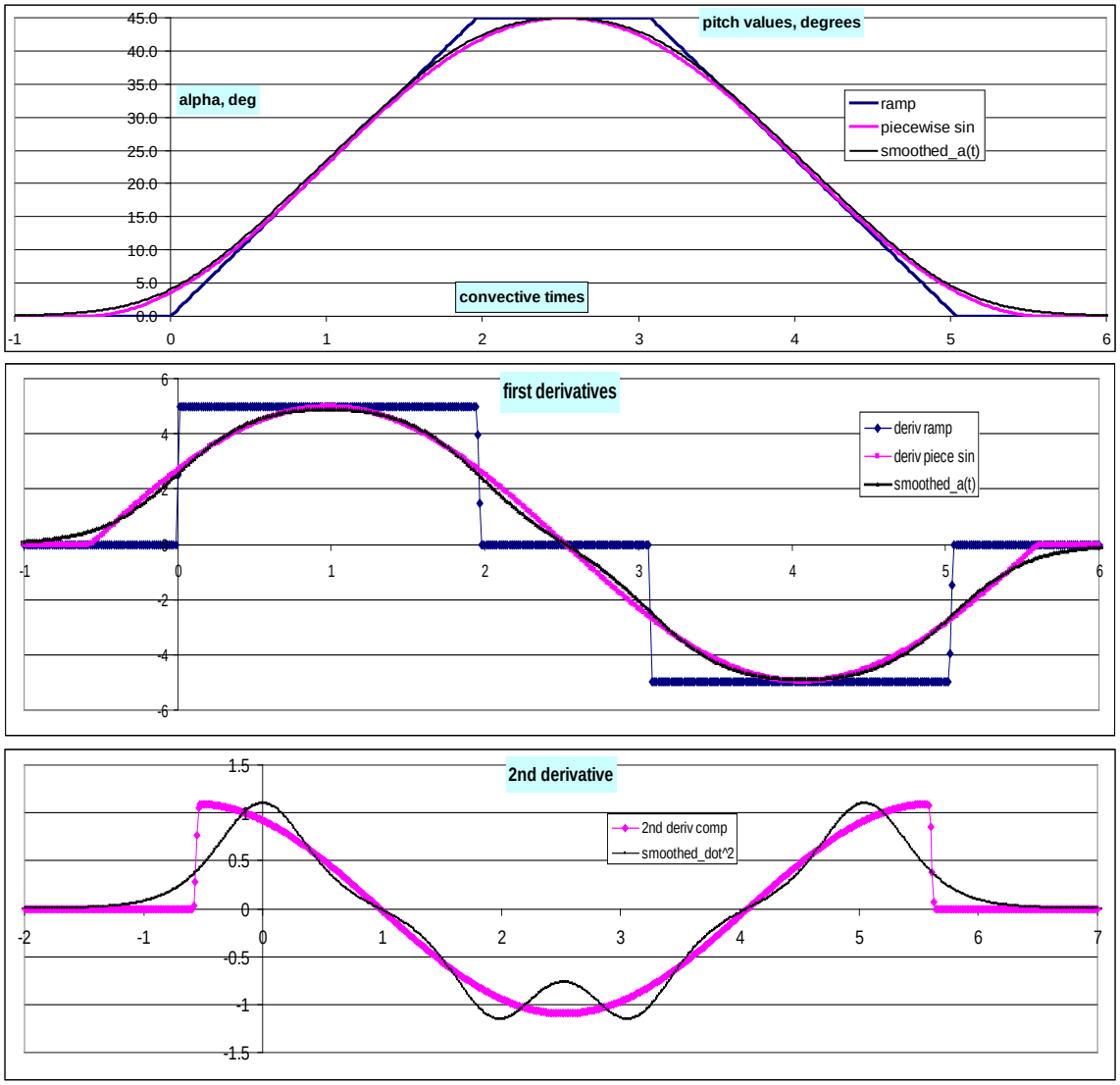

Figure 88. Sinusoidal ramp, angle of attack (top, angle of attack rate (middle) and accelerations (bottom) for pitch-hold-return maneuver.

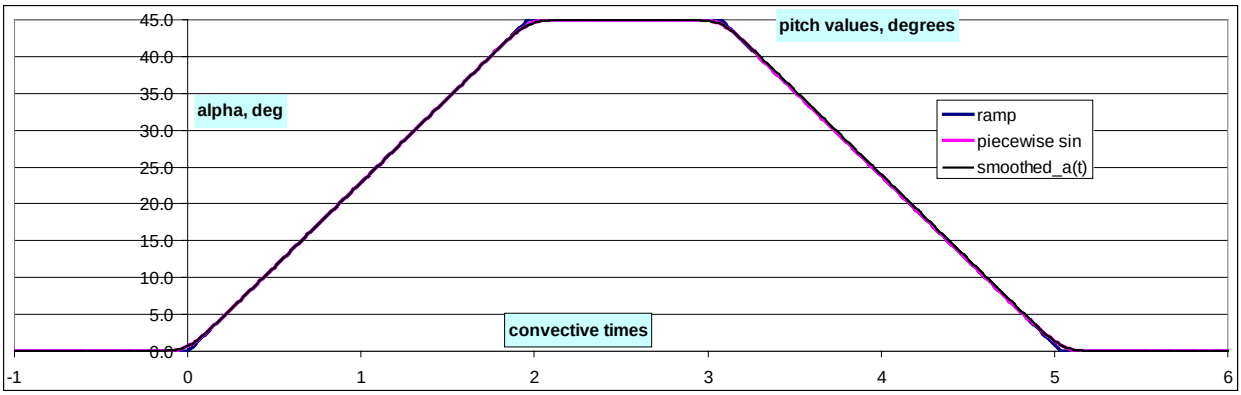

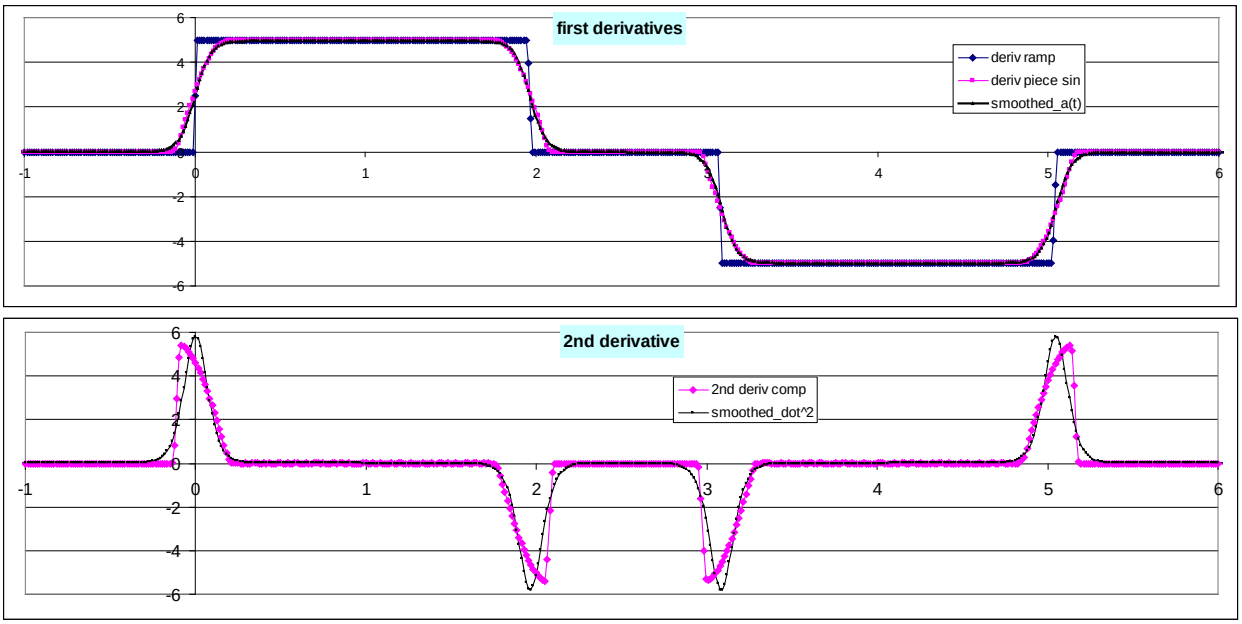

Figure 89. Smoothed linear ramp, angle of attack (top, angle of attack rate (middle) and accelerations (bottom) for pitch-hold-return maneuver.

6.9.5.2. Dye injection results

Dye injection results for Re = 5000 are given in Figure 90. Again there is a parameter study of pitch pivot point location. On the upstroke, growth of the LEV is faster, the closer the pivot point is to the leading edge. The starting vortex from pitch-ramp onset is also weaker. Thus, on the upstroke at least until around α~30º, one can state that the closer to pivot point to the leading edge, the more benign the flow separation overall. But in the subsequent motion history, the role of pivot point diminishes, such that by halfway on the downstroke, LE-pivot and TE-pivot are hard to distinguish.

Sinusoidal vs. ramp motions, both pivoting at the LE, show very little difference on the upstroke, through the hold. The main difference is that the sinusoidal motion, being less abrupt, has a smaller TE starting vortex. Late into the downstoke some differences appear in what remains of the LEV; namely, for the sinusoid there is a longer route towards flow reattachment after returning to zero angle of attack. But overall the sinusoidal and ramp flowfields are similar.

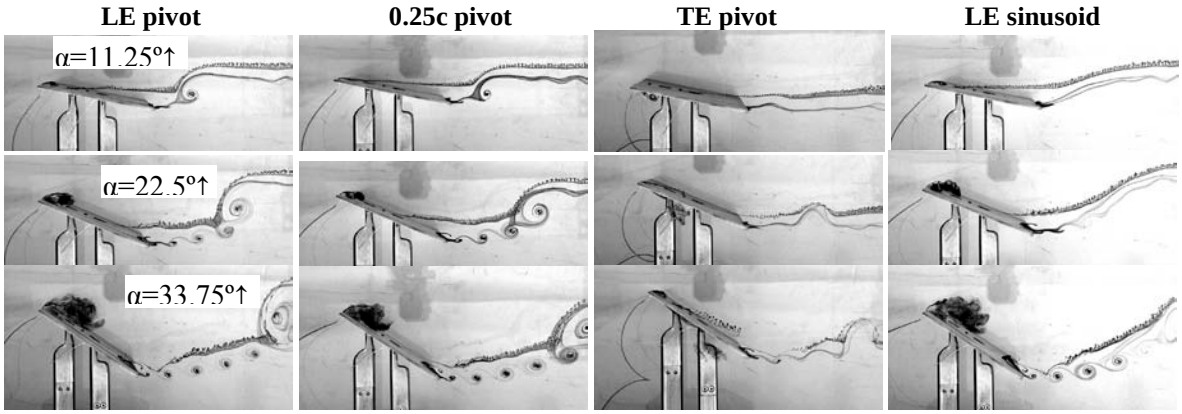

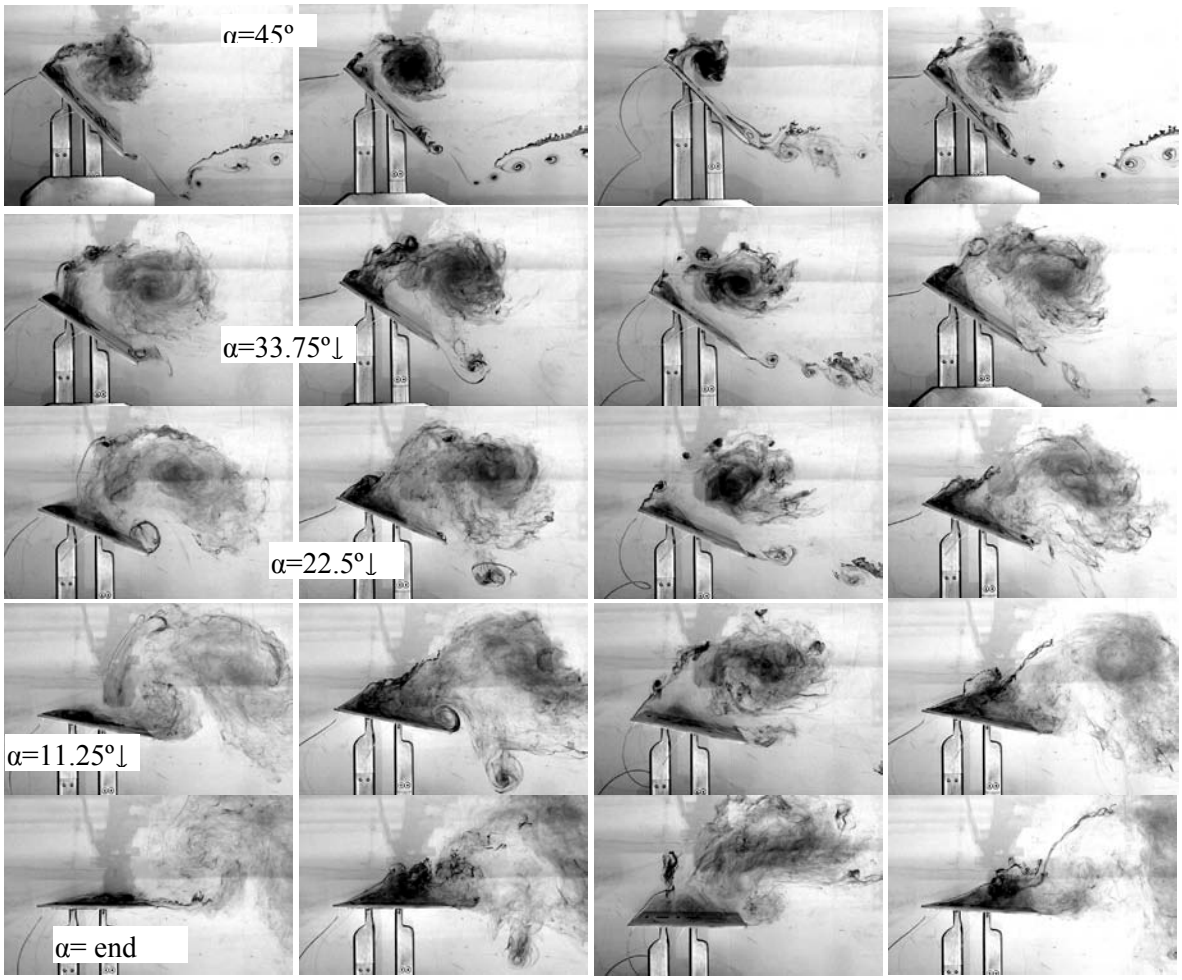

Figure 90. Dye injection results at Re = 5K, smoothed ramp and sinusoid, with pitch pivot location as marked.

6.9.5.4. Lift Coefficient History

Force data using the FBG balance is compared to two computations: implicit Large-Eddy Simulation and Vortex Particle Method (Figure 91). Angle of attack is scaled such that if the lift curve were $2\pi\alpha$, the angle of attack and lift time traces would coincide. To save embarrassment of the experimentalists, the experimental lift coefficient is divided by 1.5. The idea comes from Lian[110], in a computational study of domain size. If one uses a 2D domain with upper and lower bounds corresponding to the ratio of plate chord to the height of the water tunnel test section, then one finds approximately 1.5X increase in peak lift coefficient. In the absence of more sophisticated reasoning or experimental data from other facilities, we will call this scaling of 1.5X a dynamic blockage correction. With this rescaling, the three data sets coincide on the upstroke and hold, and almost coincide on the downstroke. To save computational costs, the numerical results are at the lower of the two canonical Re, while to increase balance signal to noise ratio, the experimental results are at the higher Re.

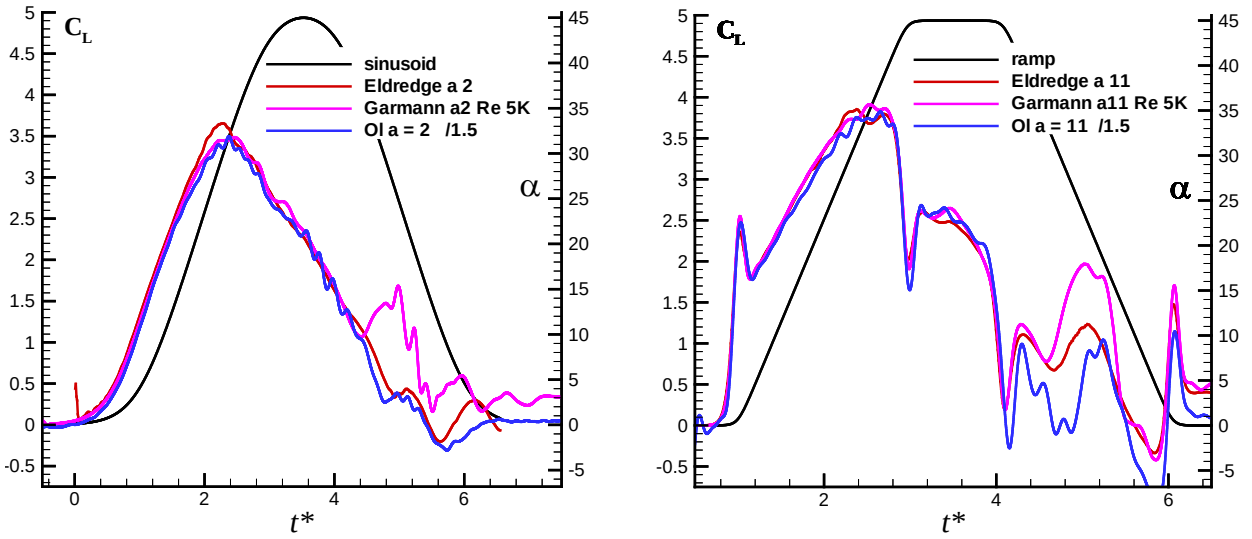

Figure 91. C_L for a = 2 (sinusoidal, left) and a = 11 (smoothed ramp, right), from Garmann and Visbal computation (Re = 5000), Eldredge et al. computation (Re = 5000), and Ol et al. experiment (Re = 40,000).

6.9.5.5. Summary

Both sinusoid and ramp appear to have a phase lead between lift time history and angle of attack time history. How can the aerodynamic force lead the motion? The answer comes from considering the noncirculatory portion of the lift, which is in phase with the pitch acceleration. As seen in Figure 89 for the ramp (the sinusoid is similar), the peak acceleration appears at the very start of the angle of attack ramp, and then quickly drops. The noncirculatory lift therefore has a strong jump at motion onset. When added to the circulatory portion, the combined manifestation is a phase lead and a spike at every "corner" of the ramp motion – thus, four spikes total. For the sinusoid, the noncirculatory lift, when added to the circulatory, does not produce any apparent spikes because the acceleration is smooth; instead the noncirculatory contribution appears as a phase lead in an otherwise sinusoidal response. This behavior is seen in two very different computations and in experiment. All capture the same phase response. And Reynolds number appears to have a very weak influence at most, responsible perhaps for variations in lift oscillation towards the bottom of the downstroke.

We also note the advantage of specific prescription for smoothing the ramp. In the water tunnel experiment of Ol et al., the structural vibration of the model, in spanwise bending, is at approximately 13 Hz, whereas the dominant frequency of the noncirculatory lift spikes is approximately 6 Hz. This separation in frequency allows low-pass filtering to remove structural vibration in lift time history, without significantly attenuating the noncirculatory spikes.

The next challenge is, first, closed-form modeling of the lift (and eventually pitch) response for the entire motion, in its three parts – upstroke, hold, and downstroke; and second, extension of wall-to-wall plate (or nominally 2D) results to finite aspect ratios. Also, it remains to see whether the trends in lift coefficient, such are general independence of Reynolds number, conveys to other quantities, such as pitching moment coefficient. We speculate that aerodynamic force coefficient modeling on the downstroke will be the most challenging, but are sanguine about the reliability of computation and experimental data.

6.10. Perching: an Extension of the Linear Pitch Ramp

Perching was mentioned as one of the core MAV unsteady aerodynamics problems at the start of this report. At a first approximation the maneuver of perching is related to the classical-pitch up problem, where the angle of attack varies fairly quickly over a large amplitude. The key difference between perching and ramp motions in classical unsteady aerodynamics is that in the latter the free-stream velocity is constant during the maneuver, while in perching there is a flight trajectory beginning from a cruise-like condition and terminating in landing. To properly model this in a ground test facility, one needs to reduce the effective free stream by the end of the maneuver to zero – and this is what the surge motor of HIPPO allows.

6.10.1. Motion Definition

All runs are at nominal reduced frequency $K = c\dot{\theta}/2U_\infty = 0.03$. We consider 5 cases, all with linear pitch ramp and sinusoidal smoothing of starting/stopping motion transients:

1. SD7003 airfoil, Re = 50K, constant relative free-stream, angle of attack from 0 through 45 degrees.
2. SD7003 airfoil, Re = 15K, constant relative free-stream, angle of attack from 0 through 85 degrees.
3. Flat plate of ~2% thickness and round edges, Re = 15K, constant relative free-stream, angle of attack from 0 through 85 degrees.
4. Flat plate of ~2% thickness and round edges, nominal Re = 15K based on tunnel free-stream velocity, varying tow speeed, angle of attack from 0 through 85 degrees.
5. SD7003 airfoil, nominal Re = 15K based on tunnel free-stream velocity, varying tow speeed, angle of attack from 0 through 85 degrees.

6.10.2. Dye Injection, PIV and Direct Force Measurement

Dye injection results for all 5 cases are shown in Figure 92, with each case in its respective column. PIV results, presently limited to the first case, are shown in Figure 93. These are instantaneous shots – not phase averages. Data in Figure 93 were taken from motion onset through several convective times after motion completion, and thus reveal the Karman vortex shedding, in the bluff-body sense, of the most-maneuver flowfield.

In all cases in Figure 92, a leading edge vortex (LEV) is formed at an angle of attack of around 20 degrees, and in no case is the LEV long-lived. Indeed, in the lift and drag time trace for the first case, shown in Figure 94, there is no dynamic-stall peak associable with LEV formation. There is, however, a very large peak lift coefficient – which rapidly collapses as the flow degenerates to Karman shedding. Therefore, approximately the first half of the motion time history for all cases is quite similar, but in the second half of the motion time history the effect of decelerating relative free-stream manifests itself.

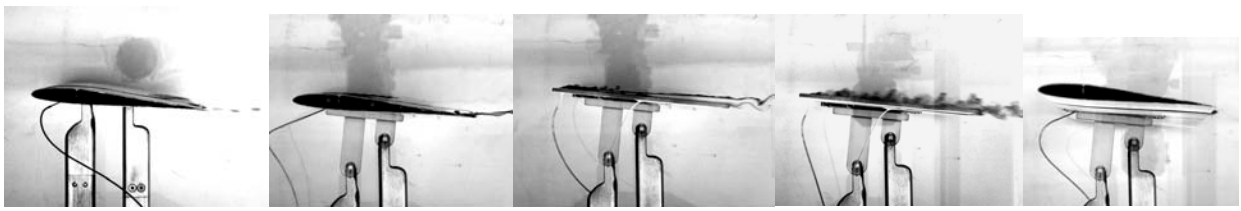

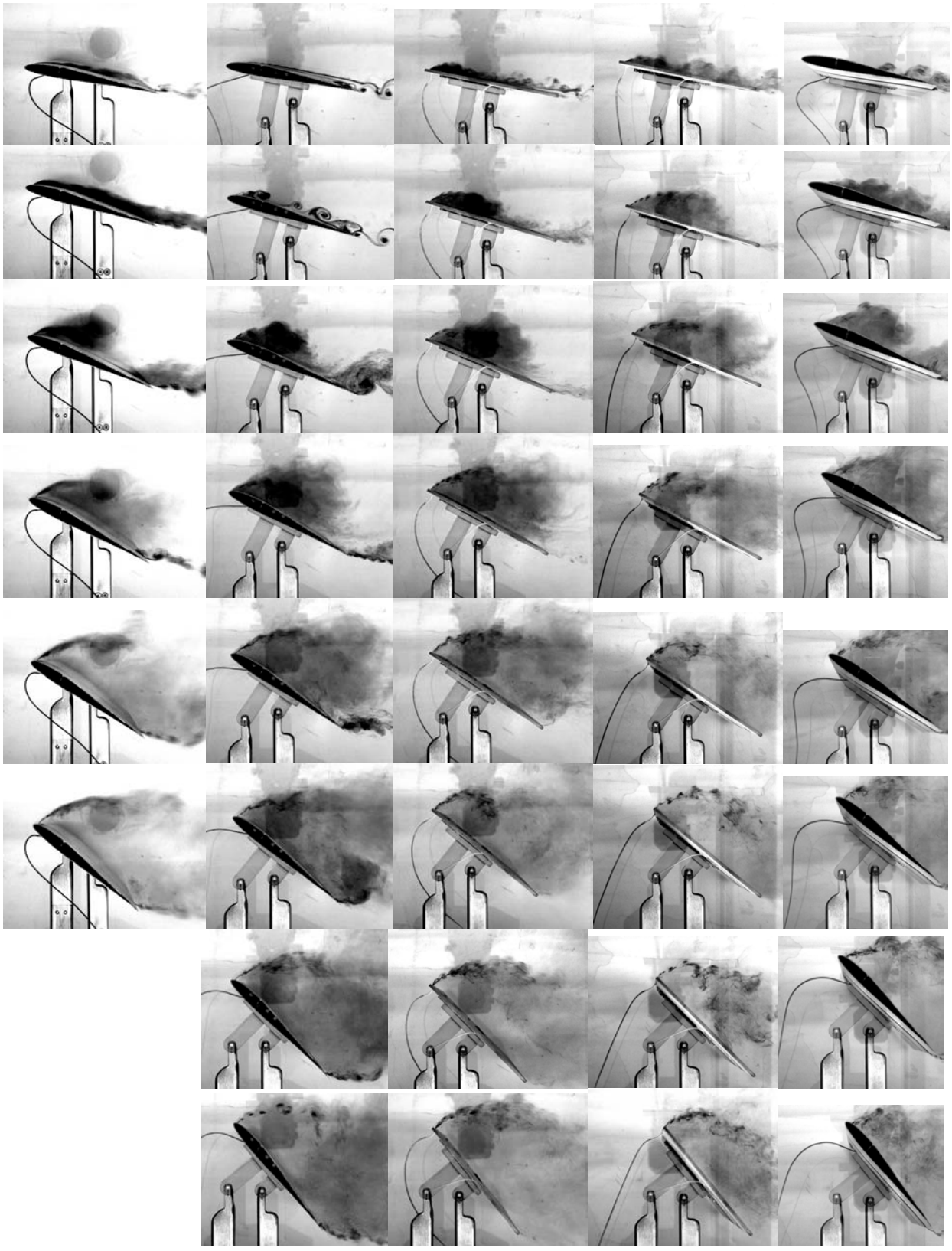

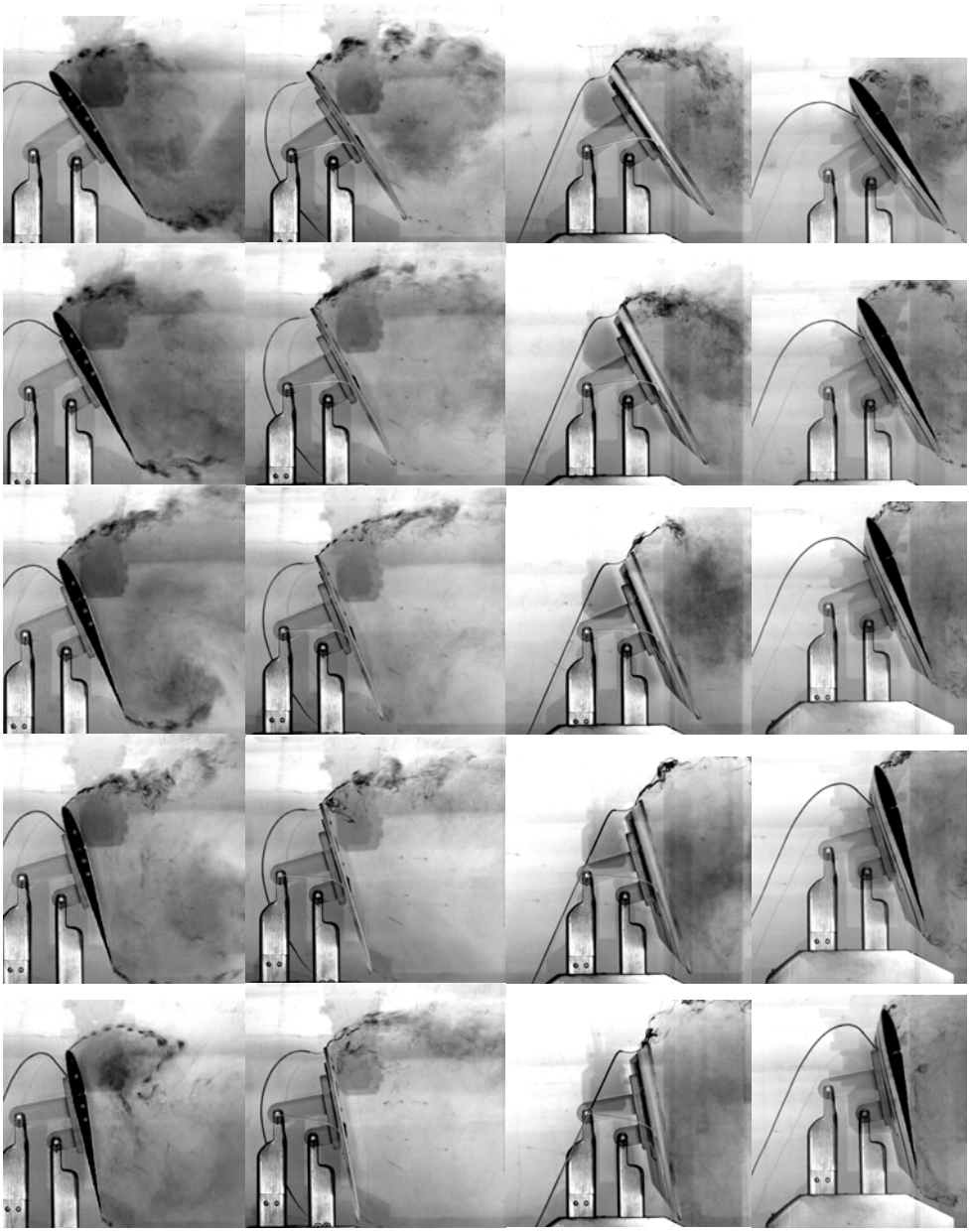

Figure 92. Flow visualization by dye injection of 5 linear pitch ramp-and-hold cases for wall to wall flat plates and airfoils. First column: SD7003 airfoil, 0-45º, constant free-stream, Re = 50K. Second column: SD7003, 0-85º, constant free-stream, Re = 15K. Third column: flat plate, 0-85º, constant free-stream, Re = 15K. Fourth column: flat plate, 0-85º, decelerating, Re = 15K based on tunnel speed. Fifth column: SD7003 airfoil, 0-85º, decelerating, Re = 15K based on tunnel speed. Each row is a sampling at the same angle of attack for all cases: 0.6º, 5.5º, 11.2º, 16.8º, 22.5º, 28.1º, 33.7º, 39.2º, 45.0º, 50.7º, 56.3º, 61.9º, 67.6º, 73.2º, 78.9º, and 84.5º.

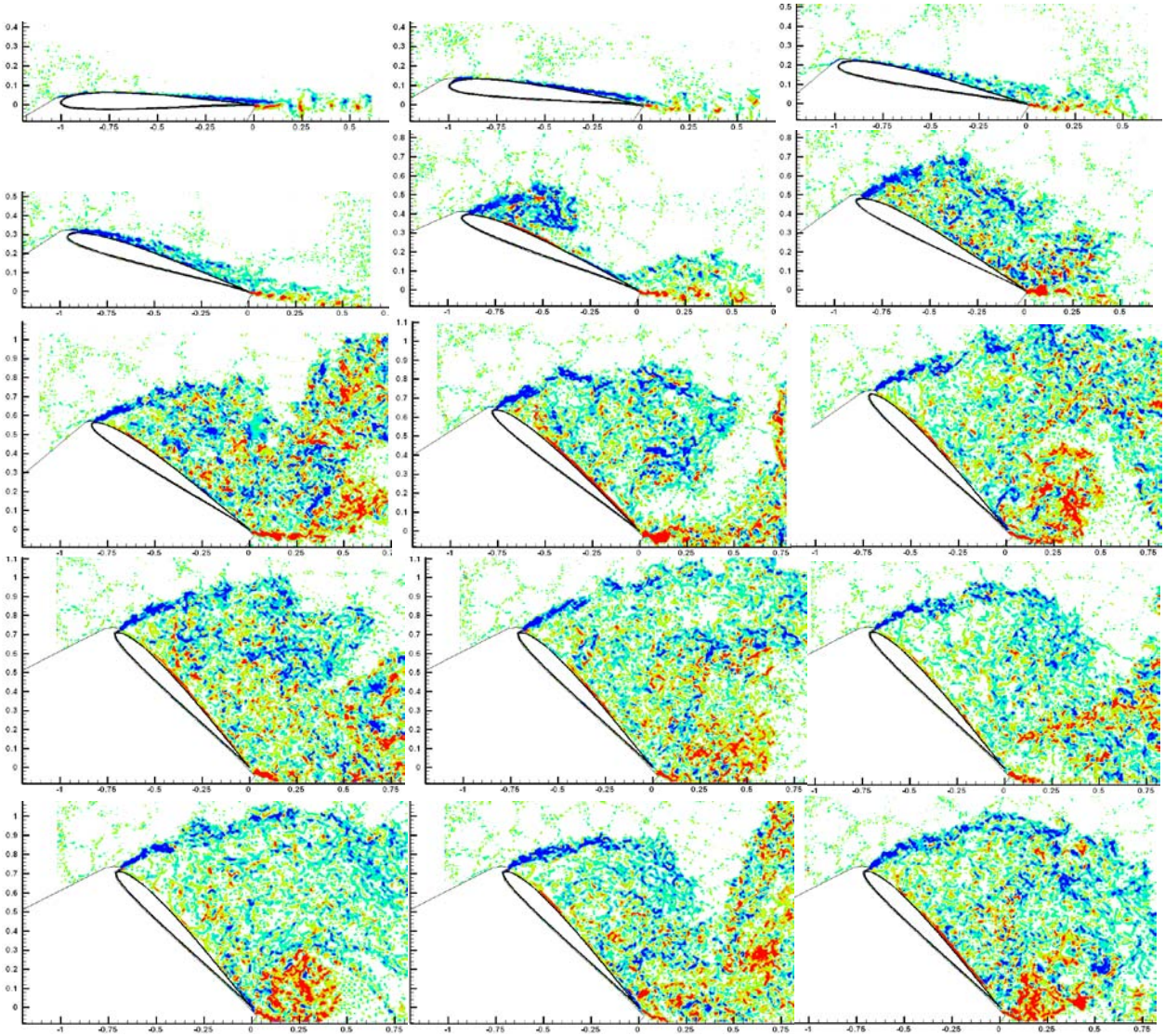

Figure 93. PIV single-shot vorticity contours, SD7003, 0-45º, constant free-stream, Re = 50K. Reading across each row and then down the next column, shots are at α = 0.6º, 5.5º, 11.2º, 16.8º, 22.5º, 28.1º, 33.7º, 39.2º, 44.3º, 45.0º, and thereafter at 45.0º; samples are spaced 1.32 convective times, or 0.76 seconds in physical time.

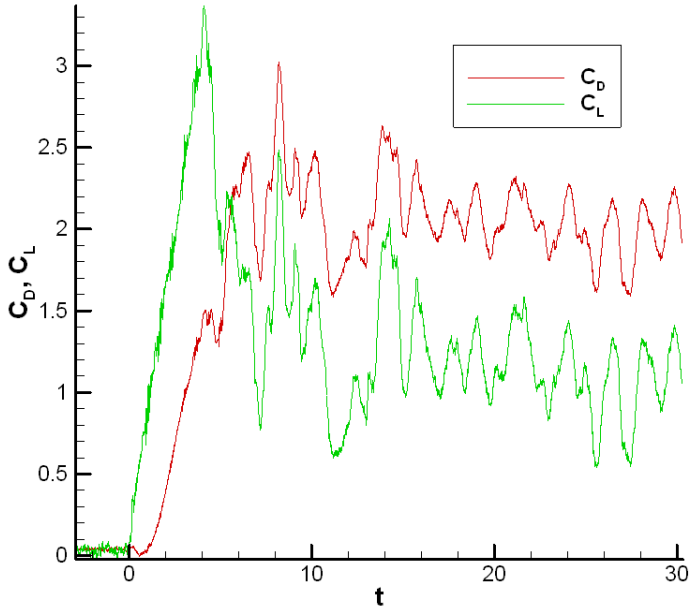

Figure 94. Lift and drag coefficients for the SD7003 airfoil pitching 0-45 degrees angle of attack, plotted vs. physical time in seconds.

As of this writing, work in progress involves selection of "optimal" perching trajectories, which are a combination of elevation change, angle of attack time history and relative forward speed history, chosen for example to minimize energy over the trajectory.

6.10.3. Summary

Perching is a fundamental unsteady motion elucidating the difference between truly quasi-steady aerodynamic response and rate-dependent or acceleration-dependent effects. Follow-on work will focusing on detailed parameter studies of pivot point and pitch rate. So far we can ascertain that the presence of absence of deceleration in the streamwise direction during the perching maneuver has little effect on the flowfield evolution, and that Reynolds number effects appear to be benign in this deep-stall problem – as in most deep-stall problems.

6.11. Flapping

6.11.1. Motivations and Motion Definition

Our final application is flapping in hover. The water tunnel is turned into a tow tank, with the third linear motor as the towing mechanism. Doman et al.[111], proposed a flight control scheme based on the flapping-wing configuration developed by Wood et al.[112], where the wing leading edge is directly actuated in a sinusoidal sweeping motion, but the wing incidence angle is free to float between limiters. The idea is to minimize the number of actuators. The incidence angle is generally right at the limiter throughout the "translation" phase of each half-stroke, with a rapid rotation from one limiter side to the other, at or near the extrema of each half-stroke. Doman et al.[111] assume in their analysis a quasi-steady lift coefficient history throughout the translation stroke, and a non-lifting instantaneous rotation phase. The former assumption is probably justified for conceptual-design purposes based on our earlier results for sinusoidal periodic plunge, where one finds remarkable robustness of the simple $C_L = 2\pi\alpha$ even for large incidence angles. But the latter assumption is only valid if the stroke fraction occupied by the rotation is small, and post-rotation transients dye out quickly. And, since the incidence angle time history during rotation is passively accepted from the combination of body dynamics (wing mass and moment of inertia, hinge dynamics, etc.) and aerodynamic loads (time history of pressure distribution on the wing), the actual incidence angle history is not known a priori. One may find various lags between rotation and translation, and asymmetries between start and end of each stroke endpoint rotation.

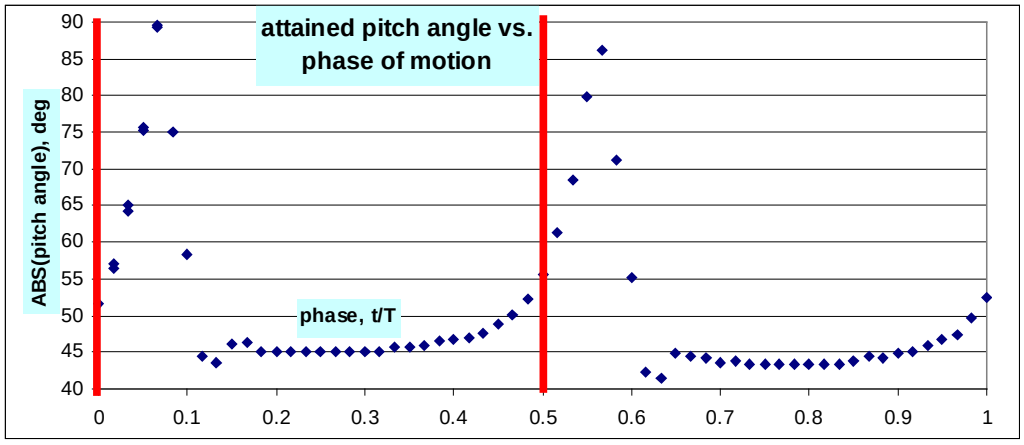

Figure 95. Phase lag between prescribed plunge and passive pitch, "light" plate.

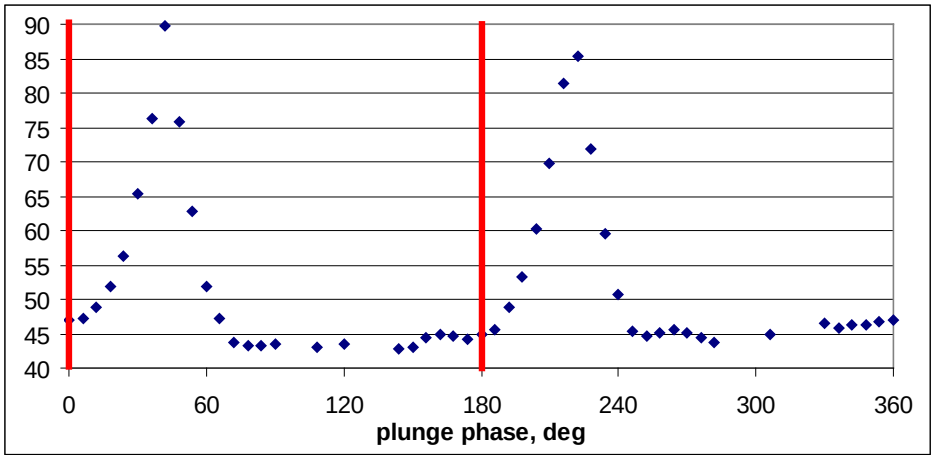

Figure 96. Phase lag between prescribed plunge and passive pitch, "light" plate.

Instead of sweeping motion, which is non rectilinear, we use a rectilinear motion – simple sinusoidal translation. The problem reduced to a form of "normal hover" with imposed translation and rotation history, except that pitch is free to float, instead of being prescribed. The prescribed-pitch problem is very well studied; Milano and Gharib[113], Kurtulus et al.[114], Shyy et al[115]; among others, all considered it, generally with an upper bound of Re < 1000. HFWT data so far are limited to two cases with passive pitch and prescribed sinusoidal plunge of 10cm (=2 chords) amplitude and frequency of 0.5Hz, which corresponds to Re ~ 16,000 and max translation speed of ~31 cm/s.

Figure 95 shows that indeed the angle of attack of the plate settles at nearly 45° on the fore and aft stroke, but that there is an approximately 20 degree phase lag between instantaneous 90° orientation (plates hangs vertically) and the extremum of the fore-aft translation sinusoid. Figure 96 shows that for a heavier plate, the phase lag is essentially double - 40°.

6.11.2. Dye Injection Results

We next turn to dye injection as a preliminary scheme for understanding the flowfield evolution. Figure 97 traces the history of vortex evolution using trailing-edge dye injection, in 30-degree increments of phase of the fore-aft translation, for the plate considered in Figure 96. A strong trailing edge vortex forms shortly after translation stroke reversal, but is quickly shed. On the rotation at the extremum of the opposite stroke, an opposite-sign vortex forms from the plate trailing edge. These form an alternating vortex pair, akin to the reverse vortex street identified by Freymuth[116].

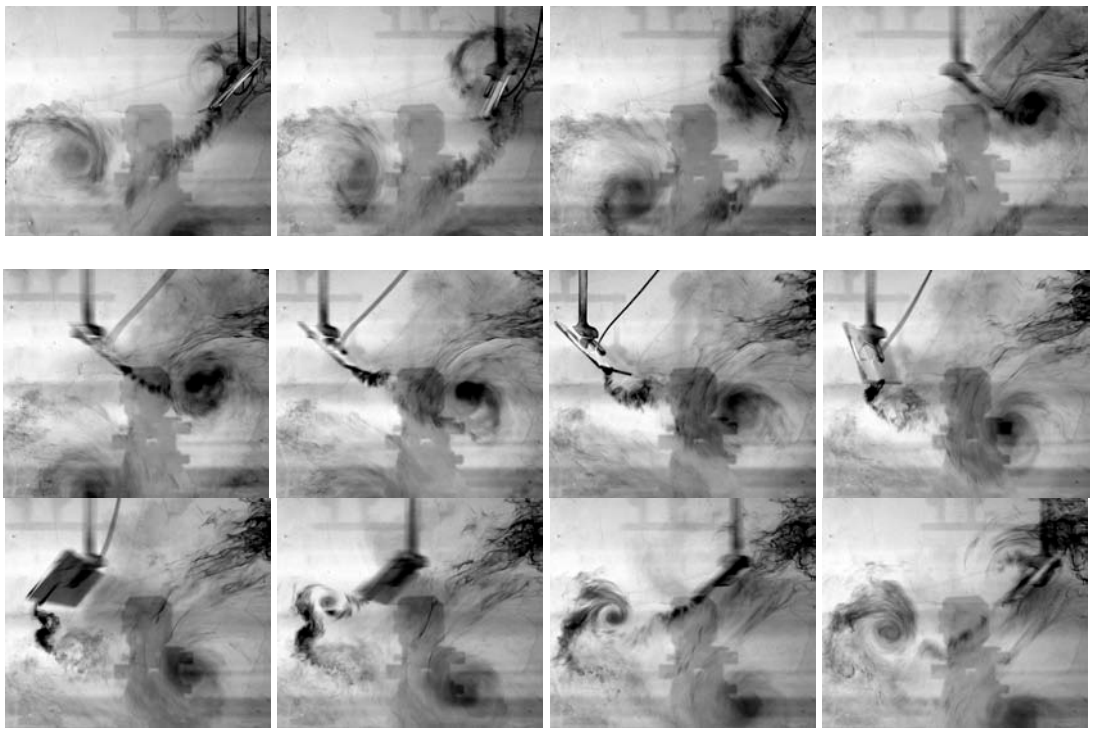

Figure 97. Trailing edge dye injection indicating (in the scalar sense) TEV development. Phases of plunge motion, from top left corner: 0, 30, 60, 90, 120, 150, 180, 210, 240, 270, 300, and 330.

As of this writing (January 2010), we have only begun to study torectilinear free-to-pivot problem. The HIPPO rig can easily handle the nonrectilinear version too, by mounting a desired aspect ratio plate in the with its span along what would be the streamwise direction, and calling the "pitch"

degree of freedom of the HIPPO rig, the sweeping motion. However, this is a task for the follow-on project. Our work here is already good enough for government work.

7. Conclusion

7.1 General Musings

The literature in unsteady aerodynamics at low Reynolds number is vast and growing. University-type of wind tunnels and water tunnels easily lend themselves to low-Re experiments, and low-Re is a natural choice for either resource-limited computations, or high-resolution computations at any resources scale. On the applied aerodynamics side, Micro Air Vehicles are a natural choice for aircraft construction, flight test and experimentation, because of low cost and relative ease of transitioning from the lab to the flight line. Neither is research in low-Reynolds number aerodynamics limited to applications to Micro Air Vehicles or natural flyers; it extends to airfoils in general, for aerodynamic testing of aerospace configurations in small-scale facilities where the Reynolds number happens to be low not by intention but by necessity, for fundamental studies such as oscillating circular cylinders, for flow-control experiments and on and on. The field is breathtakingly broad.

In this humble work, our objectives have been (1) to extend to dynamic problems the recent work on static low Reynolds number airfoils, such as laminar separation bubbles and separations in general; (2) to explore how the Reynolds number, frequency and amplitude range for MAV-relevant problems may differ from those of classical dynamic stall; (3) to consider how classical analytical methods for aerodynamic force prediction, such as Theodorsen's formula, might apply for massively unsteady conditions; (4) to explore the limitations of linear superposition, and the presence of phase lags between force response and motion prescription; (5) to survey conditions for concentrated-vortex formation and shedding, and (6) to build a path from abstract unsteady problems to MAV applications such as perching and flapping. We ignored important problems such as fluid-structure interaction, non-rectilinear motions, very low Re (below 5,000), gust and other unsteady external forcing effects, and on and on.

The aerodynamics of flapping wings is ultimately concerned with the relation between motion kinematics and the time-history of aerodynamic forces and moments. But an important intermediate quantity is the evolution of the flowfield – and in particular of flow separation. Nature's solution to large time-varying pressure gradients, for example those due to aggressive motions, is to form and eventually to shed vortices. We are interested in understanding and exploiting these vortices – for example, in delaying vortex shedding to promote lift in situations where flow separation is in any case inevitable; and in surveying how vortex shedding does or does not lead to non linearities. Once the main trends in aerodynamic force history are understood, we become equipped to run large parameter studies and optimizations, first confined to force/energy/power in aerodynamics, and then in a multi-disciplinary sense, including for example considerations of structure and actuation.

7.2 Resume of Results

Summarizing the findings of research covered by this report, we have:

- As is well known, the flow separation and aerodynamic force history of low-Reynolds number airfoils (Re of ~60,000) depends strongly on laminar to turbulent transition, and therefore on the facility flow quality. In the dynamic case, where the airfoil is pitching/plunging, the role of transition is more subtle. At moderate Reynolds number (10,000 – 60,000) and near-stall peak effective angle of attack, as results from a combined pitch-plunge motion, lift and flow separation are again strongly sensitive to boundary layer transition effects. On the other hand, high effective angle of attack, well beyond stall, means that effects of transition are of secondary importance.
- Flat plates with round edges have much lower sensitivity to either Reynolds number or boundary layer transition effects, whether in static or dynamic conditions.

- For static problems, flat plates of low aspect ratio have lift coefficient behavior in almost exact accordance with predictions of classical slender-wing theory, and wake vorticity measurement gives accurate estimate of lift, relative to direct force measurement with a balance.
- On the other hand, in the dynamic case, small aspect ratio plates (AR = 2) evince flowfield features irreducible to infinite aspect ratio, but the lift and drag history of the AR=2 plate is more quasi-steady and more similar to simple theoretical prediction than what one finds for a wall-to-wall or 2D plate.
- Lift coefficient time history is much more quasi-steady than the evolution of flow separation would purport, suggesting that low-level engineering methods still have good potential for MAV aerodynamics prediction. This is essentially a corollary of the finding that flow separation, especially leading edge vortices, has relatively benign effect on lift coefficient history. It appears that the role of LEVs is more to extend quasi-steady lift curve slopes to post-stall angle of attack, than necessarily to provide "vortex lift".
- Lift production in high-frequency low-amplitude oscillations is dominated by noncirculatory effects, whence classical planar-wake models have good predictive utility despite not resolving the flowfield features even to first order.
- Circulatory and noncirculatory force contributions are additive, in the sense of linear superposition, even for massively nonlinear problems, such as high-rate high angle-of –attack pitch ramps.
- The specific type of motion profile – sinusoidal, linear sawtooth, and so forth – has very much a secondary role in flowfield evolution for high-rate periodic or transient problems.
- Some high-rate high-amplitude (that is, high Strouhal number) motions have nonunique wake states, and the route towards achieving this or that wake flowfield depends on starting conditions.
- No rectilinear motions, whether for low-aspect ratio or wall-to-wall models, was found where the leading edge vortex is retained for any significant amount of dimensionless time; vortex shedding invariably follows vortex formation.

7.3 Toward Future Work

The main emerging theme of this work is the extent to which unsteady, low Reynolds number aerodynamics is really quasi-steady. Unsteadiness comes from viscous effects – separation and so forth; and from unsteadiness, where neither flow state nor aerodynamic forces are reducible to instantaneous position information. We have given many examples of unsteadiness and surprising cases where large unsteadiness is to be expected, but was not evinced; or, for example in the case of high-rate pitch ramps, where circulatory and noncirculatory forces superimpose, although superposition should fail in massively nonlinear problems. The most obvious extension of work conducted so far is more parameter studies. These include:

- Variations of the pitch-plunge parameter λ, plunge amplitude h, plunge frequency h, pitch amplitude, mean incidence angle, and pitch pivot point. One could select various schemes to further study pitch-plunge equivalence, the role of Strouhal number, the breakdown of Theodorsen's lift formula for sufficiently aggressive motions (which must happen eventually!), and the formation of vortex-on-vortex interactions which must, one would think, also occur in fast enough motions – as incipiently happened in the mixed-frequency problems, where LEVs formed into pairs and swam upstream. How do these various flowfield curiosities translate into tangible integrated aerodynamic force effects?
- Impulsive-start problems, where the water tunnel is run as a tow-tank using the streamwise-oriented linear motor. Examples include Wagner-type motions to study indicial response, and more complex motions to compare convolution of indicial response with the motion history, vs.

directly-measured lift. This is yet another test of superposition/linearity, and can be studied at a wide range of geometric conditions (aspect ratio, set angle of incidence, etc.).

In addition, one could study problems more relevant to MAV applications, and more interdisciplinary, beyond strictly aerodynamics. Just a few thoughts include:

- Generalization to flexible plates/wings/airfoils, and the problem of fluid-structure interaction. Does a chordwise-flexible plate bend to orient itself to attenuate separation? Does a spanwise flexible plate, in rectilinear pitch/plunge, have a wingtip deflection history that tends towards producing a spanwise pressure gradient stabilizing a particular kind of flow separation (such as a stable LEV)? And how does structural flexibility couple into the concept of fluid apparent mass?
- How can gusts encountered in flight situations be modeled in a ground test facility? For an accelerating model, there is an noncirculatory force due to acceleration. But in an accelerating flow about a model stationary in the lab-frame, there is pressure gradient necessary to support said acceleration, which also manifests itself as a force on the model. To what extent do these issues matter for gust modeling? And what is the relevant gust spectrum which we ought to be modeling?
- Generalizing to richer kinematics, including both rectilinear and nonrectilinear, how does one begin to search for the "optimum" kinematics of flapping, assuming for the sake of discussion that we have settled on the appropriate definition of "optimal"?
- And finally, to close with a discussion that commenced this report: what really is it about flapping that offers and advantage over rotary flight… especially if both can be adequately modeled by quasi-steady methods, and it turns out that neither really exploits spectacular nonlinearities for lift enhancement?

There are indeed many questions to address. Let us hope that the grant money remains forthcoming!

LIST OF ACRONYMS, ABBREVIATIONS, AND SYMBOLS

ACRONYM/ SYMBOL	DESCRIPTION
MAV	Micro Air Vehicle
LEV	Leading Edge Vortex
TEV	Trailing Edge Vortex
PIV	Particle Image Velocimetry
LSB	Laminar Separation Bubble
RTO	Research and Technology Organization
NATO	North Atlantic Treaty Organization
TTCP	The Technical Cooperation Program
HIPPO	High-Intensity Pitch-Plunge Oscillator Rig
HFWT	Horizontal Free-surface Water Tunnel
CFD	Computational Fluid Dynamics
EFD	Experimental Fluid Dynamics
LES	Large Eddy Simulation
RANS	Reynolds-Averaged Navier Stokes Simulation
FBG	Fiber Bragg Grating Load Cell
ω	Vorticity, out-of-plane component
Γ	Circulation
ν	Kinematic viscosity of water
St	Strouhal Number
k	Reduced Frequency of Sinusoidal Oscillation
C_L	Lift coefficient
C_D	Drag (or thrust) coefficient
C_M	Pitching moment coefficient, about the quarter-chord
U_∞	Free-stream speed, typically cm/s
c	Airfoil, plate or wing reference chord
f	Sinusoidal oscillation frequency of pitch, plunge or surge, in Hz
h	Plunge position as function of time
h_0	Nondimensional plunge amplitude
α_0	Mean angle of attack (the constant pitch angle offset from zero)
t/T	Dimensionless time
λ	Ratio of pitch-amplitude to plunge-induced angle of attack
φ	Phase difference between pitching and plunging; positive → pitch leads
x_p	Pitch pivot point: fraction of chord aft airfoil leading edge
α_e	Total angle of attack from trigonometric combination of pitch and plunge
A	Pitch amplitude (in degrees)
Re	Reynolds number, $Re = c\,U_\infty/\nu$
K	Dimensionless pitch rate in linear pitching motion
°	Degrees (angle of attack, etc.)

Appendix A. The Fiber-Bragg Grating Force Balance

Here we provide a brief summary of the Fiber-Bragg Grating (FBG) custom force balance as used in the above-mentioned experiments. The methodology is not new, but the design of the balance is one-off, in the sense that a conventional balance would not interface with the pitch-plunge oscillation rig, whence a custom solution was necessary.

A.1. FBG Theory of Operation

A FBG sensor is a single-mode optical fiber in which a periodic index-of-refraction modulation along the fiber direction (grating) is introduced in a short section of the fiber. Light propagating along the fiber refracts in the grating resulting in a reflected signal of very narrow wavelength determined by the period of the refractive index modulation. The wavelength of the reflected signal is given by

$$\lambda_B = 2\, n_{eff}\, \Lambda \qquad \text{(Eqn. A1)}$$

where n_{eff} is the effective refractive index of the single-mode optical fiber, and Λ is the period of the refractive index modulation. In typical implementations of the technology, the gratings are 8 to 20 mm long and several can be placed along the same fiber spaced from centimeters to a few meters apart.

FBG sensors measure strain by detecting very small changes in the wavelength of the reflected light. The change in wavelength, $\Delta\lambda_B$ is a function of the strain and the temperature change in the fiber,

$$\frac{\Delta\lambda_B}{\lambda_B} = P_e\, \Delta\varepsilon + \left[P_e\left(\alpha_s - \alpha_f\right) + \varsigma\right]\Delta T \qquad \text{(Eqn. A2)}$$

where P_e is the strain-optic coefficient, $\Delta\varepsilon$ is the strain acting on the fiber, α_s and α_f are the thermal expansion coefficients of the fiber bonding material and the fiber, respectively, and ζ is the thermo-optic coefficient. The normalized constant temperature strain response is,

$$\frac{\Delta\lambda_B}{\lambda_B\, \Delta\varepsilon} = 0.78\times10^{-6}\ 1/\,\text{micro}-\text{strain} \qquad \text{(Eqn. A3)}$$

and the normalized thermal response at constant strain is,

$$\frac{\Delta\lambda_B}{\lambda_B\, \Delta T} = 6.678\times10^{-6}\ (^{\circ}\text{C})^{-1}. \qquad \text{(Eqn. A4)}$$

For typical commercial FBS sensors the wavelength shifts are ~ 1 pm/micro-strain and 10 pm /°C (1 pm = 10^{-12} m).

The second important element of an FBG system is the wavelength reading instrument or optical sensor interrogator. A typical commercial system has the capability to sample multiple channels (4), each having multiple SBG sensors (100s) with resolution as small as 0.1 pm and sampling frequency up to a few kHz. These performance metrics make the technology very attractive for the present application. Key features that are particularly relevant are: 1) the sensing element is optical and should be immune to em-radiation and other noise sources; 2) very small sensors (the size of the optical fiber) that could be easily integrates into the load cell structure. Important challenges for the technology are: 1) high temperature sensitivity that will require temperature compensation, and 2) fiber optic bending radius should be larger 1-inch which may represent a problem for very small systems. These challenges must be adequately addressed in the design of the load cell to achieve the high sensitivity and balance stiffness required for the present application.

A.2. Load Cell Mechanical Design

FBGs measure strain at a specific location in an optical fiber by detecting the spectrum of reflected light. The fiber reflection spectrum has a maximum at a wavelength which is proportional to the local strain at the location of a FBG sensor. As noted above the main advantages of the technology relevant to

the present application are: 1 – It is an optical sensing technique and therefore immune to electronic noise, which is particularly problematic for electronic sensors in water and in proximity to the high current linear motors used to drive the model; 2 – Several FBG strain sensors can be placed in the same fiber at precise locations and, therefore, only a single fiber is needed for a multi component force sensor. For the present research the mounting plate was instrumented with 4 (1st generation) or 5 (2nd generation) FBG sensors to measure the lift, drag and pitching moment acting on the airfoil. The basic geometry of the mounting plate is the same as the original mounting plate. The plunge rods pivot locations, airfoil model attachment points and thickness are the same. The flexures and fiber optic paths are machined to accommodate the FBG sensors. A drawing of the 1st generation instrumented mounting plate is shown in Figure 98. There are two parts in the modified attachment plate, relative to the original design of the HIPPO airfoil installation, which was uninstrumented. The plunge rods are attached to the center part of the plate at the pivot points, while the airfoil model is attached to the outer part of the plate. Thin flexures instrumented with FBG strain sensors join the two parts of the plate. The locations of the FBGs are designed to provide temperature compensation as well as decoupling between the lift, drag and pitching moment component measurements as discussed below.

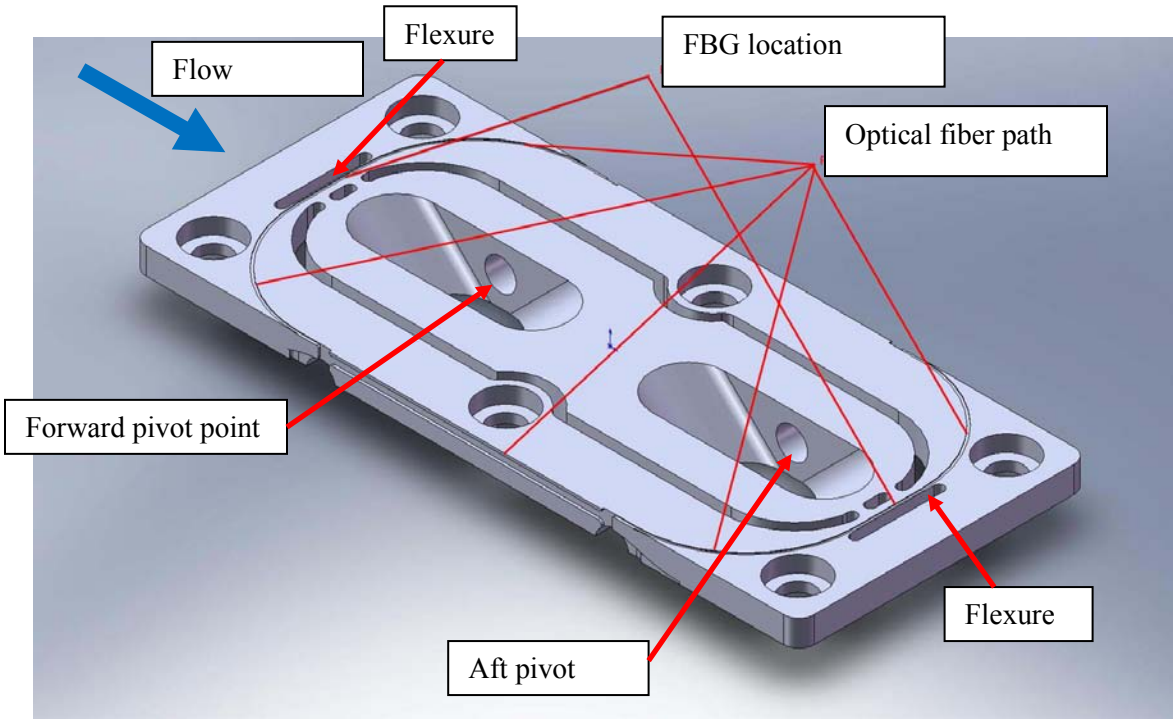

Figure 98. Drawing of the mounting plate showing the optical fiber path and the location of the flexures and FBG sensors on the top surface of the plate. Another two FBG sensors are placed on the bottom side of the flexures.

A commercial CAD package with FEM analysis (SolidWorks, http://www.solidworks.com/) was used to size the flexures and to obtain preliminary estimates of the load cell calibration matrix and stiffness characteristics. The primary design parameters are the flexures length and cross section dimensions; and the spacing between the two attachment points of the load cell center section to the flexures. For the data reported here the flexure lengths are 0.75", the cross sections are 0.033"× 0.140" and the distances between center section attachment points are 0.375". The resonance frequency of the load cell model combination with the SD7003 model mounted was estimated using FEM analysis and is approximately 60 Hz.

A.3. Load Cell Calibration

The load cell is designed to measure the force components normal to the mounting plate, parallel to the plate (that is, the axial force) and the pitching moment. This is achieved with 5 gauges – two are at the front flexure of the load cell, two are at the aft flexure, and the fifth gauge is unstrained, being used as a temperature compensation device. Locations and specifications of the four load-sensing gratings are given in Table A1. During installation the FBG sensors are pre-strained before bonding to the flexures. The resulting shift in wavelength for no load is also given in Table A1.

Table A1. Location and Wavelength of FBG Sensors in Load Cell.

FBG #	Location	Wavelength (nm)	No Load Wavelength (nm)
1	Bottom Aft	1526	1526.833
2	Bottom Forward	1536	1536.765
3	Top Aft	1546	1546.788
4	Top Forward	1556	1556.607

Load cell sensor outputs can be combined to decouple the three force components and a temperature output. A positive normal force (towards the suction side of the airfoil) produces positive strain in the FBGs mounted on the top of the sensor bars and negative strain on the FBGs mounted on the bottom of the sensor bars. Similarly positive axial force (downstream) produces positive strain in the FBG mounted on the forward sensor bar and negative strain in the FBG mounted on the aft sensor bar. A positive pitching moment (forward up) produces positive strain in top forward and bottom aft FBGs and negative strain in the bottom forward and top aft FBGs. And an increase in temperature produces a positive increase of the wavelength of all the FBG sensors. Hence, for the purpose of calibration we define,

$$\begin{aligned}
\Delta\lambda_N &= -\Delta\lambda_1 - \Delta\lambda_2 + \Delta\lambda_3 + \Delta\lambda_4 \\
\Delta\lambda_A &= \Delta\lambda_1 - \Delta\lambda_2 + \Delta\lambda_3 - \Delta\lambda_4 \\
\Delta\lambda_M &= \Delta\lambda_1 - \Delta\lambda_2 - \Delta\lambda_3 + \Delta\lambda_4 \\
\Delta\lambda_T &= \Delta\lambda_1 + \Delta\lambda_2 + \Delta\lambda_3 + \Delta\lambda_4
\end{aligned} \qquad \text{(Eqn. A5)}$$

or in matrix form,

$$\begin{pmatrix} \Delta\lambda_N \\ \Delta\lambda_A \\ \Delta\lambda_M \\ \Delta\lambda_T \end{pmatrix} = \begin{pmatrix} -1 & -1 & 1 & 1 \\ -1 & 1 & -1 & 1 \\ 1 & -1 & -1 & 1 \\ 1 & 1 & 1 & 1 \end{pmatrix} \begin{pmatrix} \Delta\lambda_1 \\ \Delta\lambda_2 \\ \Delta\lambda_3 \\ \Delta\lambda_4 \end{pmatrix} \qquad \text{(Eqn. A6)}$$

Then, in the calibration matrix is

$$\begin{pmatrix} N \\ A \\ M \\ T \end{pmatrix} = \begin{pmatrix} C_{11} & C_{12} & C_{13} & C_{14} \\ C_{21} & C_{22} & C_{23} & C_{24} \\ C_{31} & C_{32} & C_{33} & C_{34} \\ C_{41} & C_{42} & C_{43} & C_{44} \end{pmatrix} \begin{pmatrix} \Delta\lambda_N \\ \Delta\lambda_A \\ \Delta\lambda_M \\ \Delta\lambda_T \end{pmatrix} + \begin{pmatrix} N_o \\ A_o \\ M_o \\ T_o \end{pmatrix} \qquad \text{(Eqn. A7)}$$

The calibration matrix is expected to be almost diagonal, and off-diagonal terms attempt to account for sensor cross-talk. Of course, since compensation and calibration is just successive matrix multiplication, the two can be combined in one step.

Calibrations are in-situ inside the water tunnel, using the water's large thermal inertia to minimize temperature effects. A loading fixture is attached to the load cell, and weights are hung from specific points on the fixture. The pitch/plunge rig is programmed to slowly step through a series of angles of attack in semi-random fashion, typically from -45° to +45°, in 5° increments, in upgoing and downgoing

directions (to control for possibility of hysteresis). Applied loads are from 0 to 5 lbf. The whole process is repeated for at least two nominal values of water temperature, in attempt to build a calibration resulting in load sensing insensitive to temperature. Fresh water introduced into the HFWT is typically at around 57°F, but after 1-2 days the temperature equilibrates to around 68°F. Thus an adequate spread in ambient temperature is achieved by running a loading sequence in water that has been resident for several days, followed by a new sequence after draining and refilling the tunnel.

At each load condition the wavelength shifts $\Delta\lambda_i$, $i = 1-4$ are measured and the values of $\Delta\lambda_N$, $\Delta\lambda_A$, $\Delta\lambda_M$, and $\Delta\lambda_T$ are calculated. A least squares fit to the data gives the calibration matrix, for which a typical value would be

$$\begin{pmatrix} N \\ A \\ M \\ T \end{pmatrix} = \begin{pmatrix} 58.477 & 7.457 & 4.457 & 0 \\ 1.251 & 137.009 & 1.190 & 0 \\ 0.141 & 2.965 & 104.960 & 0 \\ -2.413 & -3.4 & -9.235 & 8.813 \end{pmatrix} \begin{pmatrix} \Delta\lambda_N \\ \Delta\lambda_A \\ \Delta\lambda_M \\ \Delta\lambda_T \end{pmatrix} + \begin{pmatrix} 0.030 \\ 0.011 \\ -0.022 \\ 50.854 \end{pmatrix}. \qquad \text{(Eqn. A8)}$$

where the wavelength shift are expressed in nm, the physical variables (N – normal force, A – axial force, M - pitching moment and T - temperature) are expressed in imperial units.

Standard error for the force and temperature calibration results are given in Table A2. The calibration matrix diagonal elements for the force components are very large compared to the off diagonal elements indicating good decoupling between the measured force components and good temperature compensation. This is also shown by the plots which show excellent correlation between the force applied and component wavelength shift.

Table A2. Load Cell Calibration Standard Error.

	Standard Error
N (lbf)	0.11
A (lbf)	0.15
M (in-lbf)	0.07
T (K)	0.34

A.4. Data Processing

A Micron Optics sm130 4-channel 1000Hz-samping "Optical Sensor Interrogator" was used to record the FBG's wavelength time-history. The instrument recorded the output of all 5 FBG sensors in the fiber, sometimes at the maximum sampling rate, and sometimes subsampled (down to 250 Hz or less) with moving-averages applied. Even 250Hz much higher than necessary for the present experiments where typical motion physical frequency is of the order of 1 Hz or less. The data were smoothed using a recursive low pass filter with a cut-off frequency of 6.5 Hz (-3 dB point), which is well above the airfoil motion frequency and the characteristic flow frequency U/c ~ 2.7 s^{-1}. This filter effectively averages data 50 consecutive data points with weight factors designed to optimize high-frequency roll off and it is implemented with symmetric impulse response to eliminate phase distortion. The frequency cut-off of the filter was determined based on measurements of the power spectra of the FBG outputs. Typical power spectra before and after filtering are plotted in Figure 99. Figure 99(a) shows the power spectra of the output data from a typical unsteady run. At low frequency (i.e. < 5 Hz) there well-defined spectral peaks associated with the airfoil motion. There is also a very strong peak at 25 Hz. It was determine that this spectral peak is associated with the water channel pump rotational speed. Examination of the flow with flow visualization revealed no evidence of flow structure at this frequency. The power spectrum after filtering the data is shown in Figure 99(b), the peak at 25 Hz is still present but the magnitude is significantly reduced, to a value comparable to the noise floor of the present measurements (~ -5 dB/Hz).

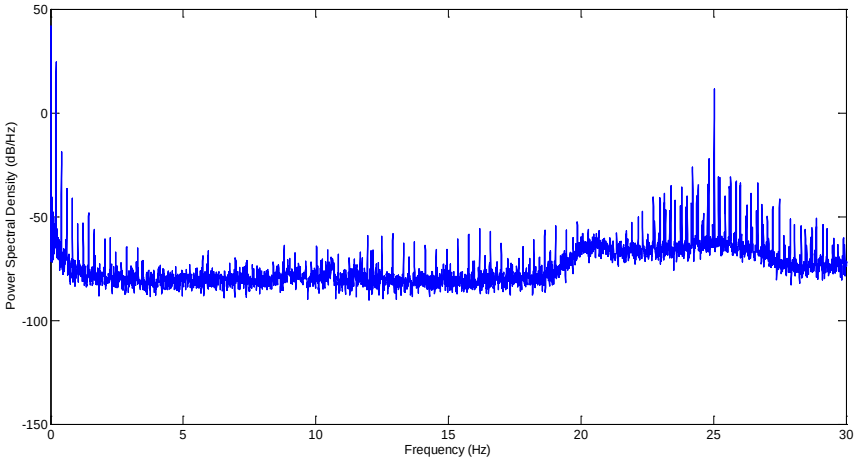

(a)

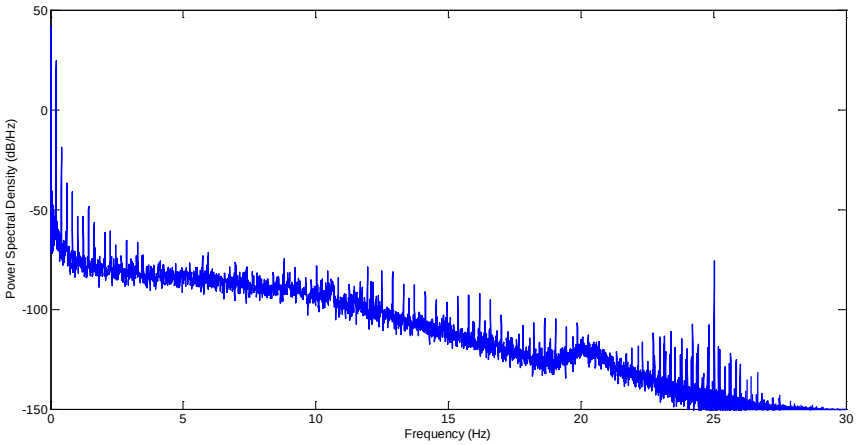

(b)

Figure 99. Typical powers spectra of a FBG sensor output. (a) Spectra of the raw data for a typical run, (b) Spectra after low pass filter.

Critical to successful design of the FBG balance – and for that matter, any balance – is ensuring that the strain in the flexure is much larger than the strain in the non-metric portions of the balance, such as the interior piece connecting to the pitch/plunge rig's plunge rods, and the exterior frame connecting to the model. One attempts to design this using finite-elements, but in practice the geometry of the balance evolves from trial and error, such as episodes where one observes that removing and replacing the model – involving torquing and untorquing bolts connecting the model and the balance – causes drift in the FBG wavelength shifts. Such observations are ongoing, whence evolutions of new iterations of the FBG balance are also ongoing.

Appendix B. Resume of Publications Supporting the Present Work

Self-referentially, this report is based on a series of conference papers and journal articles in 2002-2010, of which the PI was author or co-author. These are listed as follows:

11. OL, M.V. and Gharib, M. "Leading Edge Vortex Structure Of Nonslender Delta Wings At Low Reynolds Number". AIAA Journal, Vol. 41, No.1, pp 16-26. Jan 2003.
12. Biber, K., OL. M.V., and Tilmann, C.P. "Some Examples of Airfoil Design For Future UAV Concepts". AIAA-2004-1050.
13. Khrabrov, A., and OL, M. "Effects of Flow Separation on Aerodynamic Loads in Linearized Thin Airfoil Theory". Journal of Aircraft, Vol. 41, No. 4, pp. 944-949, July-August 2004.
14. OL, M.V., McAuliffe, B. R., Hanff, E. S., Scholz, U., Kaehler, Ch., "Comparison of Laminar Separation Bubble Measurements on a Low Reynolds Number Airfoil in Three Facilities", AIAA 2005-5149.
15. Fonov, S., Goss, L., Jones, G., Crafton, J., Fonov, V., and OL, M.V. "New Method for Surface Pressure Measurements". AIAA-2005-1029.
16. Kaplan, S., Altman, A., and OL, M.V. "Wake Vorticity Measurements for Low Aspect Ratio Wings at Low Reynolds Number". J. Aircraft, Vol. 44, No. 1, pp. 241-251, 2007.
17. OL, M.V. "Water Tunnel Velocimetry Results for the 1303 UCAV Configuration". AIAA-2006-2990.
18. OL, M.V. "Vortical Structures in High Frequency Pitch and Plunge at Low Reynolds Number". AIAA-2007-4233.
19. Lian, Y., OL, M.V., and Shyy, W. "Comparative Study of Pitch-Plunge Airfoil Aerodynamics at Transitional Reynolds Number". AIAA-2008-652, 2008.
20. Dong, H., Webb, C., and OL, M.V. "Effects of Unequal Pitch and Plunge Airfoil Motion Frequency on Aerodynamic Response". AIAA-2008-582, 2008.
21. McGowan, G., Gopalarathnam, A., OL, M.V., and Fredberg, D. "Computation vs. Experiment for High-Frequency Low-Reynolds Number Airfoil Pitch and Plunge". AIAA-2008-653, 2008.
22. OL, M.V., Dong, H., and Webb, C. "Motion Kinematics vs. Angle of Attack Effects in High-Frequency Airfoil Pitch/Plunge". AIAA-2008-3822
23. Abate, G., OL, M.V., and Shyy, W. "Introduction: Biologically Inspired Aerodynamics". AIAA Journal, Vol.46 no.9, pp. 2113-2114, 2008
24. OL, M.V., Parker, G., Abate, G., and Evers, J. "Flight Controls and Performance Challenges for MAVs in Complex Environments". AIAA-2008-6508
25. Chabalko, C., Snyder, S., Beran, P., OL, M.V., and Dong, H. "Study of Deflected Wake Phenomena by 2D Unsteady Vortex Lattice". AIAA-2009-2475
26. McGowan, G., Gopalarathnam, A., OL. M.V., and Edwards, J. "Analytical, Computational, and Experimental Investigations of Equivalence Between Pitch and Plunge Motions for Airfoils at Low Reynolds Numbers". AIAA-2009-535
27. OL, M.V., Bernal, L., Kang, C.-K., and Shyy, W. "Shallow and Deep Dynamic Stall for Flapping Low Reynolds Number Airfoils". Experiments in Fluids, Vol. 46, No. 5, May 2009.
28. Bernal, L.P., OL, M.V., Szczublewski, D., and Cox, C. "Unsteady Force Measurements in Pitching-Plunging Airfoils". AIAA-2009-4031
29. Eldredge, J., Wang, C., and OL, M.V. "A Computational Study of a Canonical Pitch-Up, Pitch-Down Wing Maneuver". AIAA-2009-3687
30. Alam, M., Suzen, Y.D., and OL, M.V. "Numerical Simulations of Pitching Airfoil Flowfields for MAV Applications". AIAA-2009-4029

31. OL, M.V., Reeder, M., Fredberg, D., McGowan, G., Gopalarathnam, A., and Edwards, J. "Computation vs. Experiment for High-Frequency Low-Reynolds Number Airfoil Plunge". International J. of MAVs, Vol. 1, No. 2, 2009.
32. OL, M.V., Eldredge, J.D., and Wang, C. "High-Amplitude Pitch of a Flat Plate: an Abstraction of Perching and Flapping". International J. of MAVs, Vol. 1, No. 3, 2009.
33. Rausch, J., Baik, Y.S., Bernal, L., and Ol, M. "Fluid Dynamics of Rigid and Flexible Lifting Flat Plates in Pitch-Plunge Motion at Low Reynolds Numbers". AIAA-2010-389
34. Baik, Y.S., Rausch, J., Bernal, L., Shyy, W., and Ol, M. "Experimental Study of Governing Parameters in Pitching and Plunging Airfoil at Low Reynolds Number". AIAA-2010-0388
35. OL, M., Altman, A., Eldredge, J., Garmann, D., and Lian, Y. "Summary of Progress on Pitching Plates: Canonical Problems in Low-Re Unsteady Aerodynamics". AIAA-2010-1085
36. Lian, Y., and Ol, M.V. "Computation and Experiment on a Low Aspect Ratio Pitching Flat Plate". AIAA 2010-0385.

Appendix C. Listing of Research Collaborators

The work described in this report would have been impossible to conceive or to execute as sole and individual effort. Cross-pollination of ideas has been invaluable, both amongst experimentalists and with theoreticians and computationalists. In the case of computations, water tunnel experiments have provided validation, and computation has yielded force data where none was available in the experiment. Computation can also reverse-validate experiment, for example to help understand the role of blockage or ambient turbulence intensity. Theory has guided test matrix definition in the water tunnel, and has been a baseline check on experiment and computation alike. And other experiments have lent support to the present results, for example confirming the role of model vibrations in force balance time-traces, or particle image velocimetry resolution in tracking the evolution of Reynolds stresses in laminar separation bubbles. In brief, principal collaborations over the past 7 years have been:

- Prof. Haibo Dong, Wright State University. Computations (immersed boundary methods) on airfoils and flat plates undergoing various motions, including sinusoidal pitch and plunge oscillations and linear ramps.
- Prof. Ashok Gopalarathnam, North Carolina State University. Theory (classical methods) and Reynolds-Averaged Navier Stokes computations on airfoil pitch-plunge equivalence and lift coefficient time history vs. motion time history.
- Prof. Altman, University of Dayton. Adaptation of Rolling Hills Research Company's water force balance in the HFWT, HFWT test campaign on static Aspect Ratio = 2 wings, and experiments on flat-plate plunge in hover.
- Dr. Miguel Visbal, AFRL/RBAC. High-order 2D and 3D computations using Implicit Large Eddy Simulation on a range of airfoil plunge, pitch and "perching" problems, paralleling HFWT experiments.
- Prof. Jeff Eldredge, University of California, Los Angeles. Computations (Immersed Boundary Method) on canonical problem of pitch-hold-return of a flat plate, identifying trends in lift coefficient vs. motion reduced frequency; and theoretical modeling of unsteady loads.
- Prof. Wei Shyy, University of Michigan. Reynolds-Averaged Navier Stokes computations on a range of oscillating airfoil and flat plate cases, comparing computed vortex-formation and time history with HFWT experiments.
- Prof. Luis Bernal, University of Michigan. Water tunnel experiments paralleling experiments in the HFWT, and development of Fiber-Bragg Grating force balance for the HFWT.
- Prof. Holger Babinsky, Cambridge University, United Kingdom. Water tow tank experiments on rectilinear vs. non rectilinear motion of flat plates, to assess role of spanwise flow and stability of the leading edge vortex, paralleling HFWT experiments limited to the rectilinear case.
- Prof. Rolf Radespiel, Technical University of Braunschweig, Germany. Wind tunnel experiments on sinusoidally oscillating airfoils and low aspect ratio flat plates, comparing laminar separation bubble physics vs. facility flow quality, relative to HFWT experiments.
- Prof. Yongsheng Lian, University of Louisville. Reynolds-Averaged Navier-Stokes computations of periodic and aperiodic unsteady problems, compared with water tunnel experiments on the same configuration, with a focus on the role of water tunnel test sectional blockage and other ground-testing corrections.

8. References

[1] McMichael, J. M., Francis, M. S. (1997). Micro Air Vehicles - toward a New Dimension in Flight, www.darpa.mil/tto/MAV/mav_auvsi.html, accessed Sept. 2004.
[2] Pines, D., and Bohorquez, F. "Challenges Facing Future Micro Air Vehicle Development". *Journal of Aircraft*, Vol. 43, No. 2, pp. 290-305, 2006.
[3] Shyy, W., Lian, Y., Tang, J., Viieru, D., and Liu, H. *Aerodynamics of Low Reynolds Number Flyers*. Cambridge University Press, 2008.
[4] Mueller, T.J., "An Overview of Micro Air Vehicle Aerodynamics". Fixed and Flapping Wing Aerodynamics for Micro Air Vehicle Applications. T.J. Mueller, ed., *Progress in Aeronautics and Astronautics*, Volume 195, AIAA, pp.483-500, 2001.
[5] Shyy, W., Lian, Y., Tang, J., Viieru, D., and Liu, H., Aerodynamics of Low Reynolds Number Flyers, Cambridge University Press, New York, 2008.
[6] Pennycuick, C. J., *Bird Flight Performance: A Practical Calculation Manual,* Oxford: Oxford University Press, 1989.
[7] Brown, R.H.J. "The flight of birds". *Biol. Rev*. 38, 460-489, 1963.
[8] Lehmann, F-O., "The Mechanisms of Lift Enhancement in Insect Flight," Naturwissenschaften, Vol. 91, March 2004, pp. 101-122.
[9] Sane, S. P., "The Aerodynamics of Insect Flight," Journal of Experimental Biology, Vol. 206, Dec. 2003, pp. 4191-4208.
[10] Shyy, W., Berg, M., Ljungqvist, D. (1999). "Flapping and Flexible Wings for Biological and Micro Air Vehicles," *Progress in Aerospace Sciences*, Vol. 35, pp. 455.
[11] Ellington, C.P., "Insects versus Birds: The great Divide," AIAA Paper No. 2006-035
[12] Reich, G., and Wojnar, O. "Aerodynamic Performance of a Notional Perching MAV Design". AIAA 2009-0063.
[13] Willis, D.J., Persson, P.-O., Israeli, E.R., Peraire, J., Swartz, S., and Breuer, K.S. "Multifidelity Approaches for the Computational Analysis and Design of Effective Flapping Wing Vehicles". AIAA 2008-0518.
[14] Fry, S.N., Sayaman, R., and Dickinson, M.H. "The Aerodynamics of Free-Flight Maneuvers in Drosophila". *Science*, Vol. 300, No. 495, 2003.
[15] Wood, R.J. "First Takeoff of a Biologically Inspired At-Scale Robotic Insect". *IEEE Transactions on Robotics*, Vol. 24, No. 2, April 2008.
[16] Visbal, M.R. "High-Fidelity Simulation of Transitional Flows Past a Plunging Airfoil". AIAA 2009-0391.
[17] McCroskey, W.J. "The Phenomenon of Dynamic Stall". NASA TM 81264, 1981.
[18] Platzer, M., Jones, K., Young, J., and Lai, J. "Flapping Wing Aerodynamics: Progress and Challenges". AIAA J., Vol. 46, No. 9, pp. 2136-2149, 2008.
[19] Graham, G.M., and Yeow, K.F. "Two Dimensional Post Stall Maneuver of a NACA 0015 Airfoil at High Pitching Rates". AIAA-1990-2810.
[20] Graham, G.M., and Islam, M. "Time-Average Loading on a Two-Dimensional Airfoil in Large Amplitude Motion". *J. Aircraft*, Vol. 29, No. 4, pp. 709-711, 1991.
[21] Strickland, J.H., and Graham, G. "Dynamic Stall Inception Correlation for Airfoils Undergoing Constant Pitch Rate Motions". *AIAA J*., Vol. 24, No. 4, pp. 678-680, 1986.
[22] Chandrasekhara, M.S., Ahmed, S., and Carr, L.W. "Schlieren Studies of Compressibility Effects on Dynamic Stall of Transiently Pitching Airfoils". *J. Aircraft*, Vol. 30, No. 2, pp. 213-220, March-April 1993.
[23] Chandrasekhara, M.S., Carr, L.W., and Wilder, M.C. "Interferometric Investigations of Compressible Dynamic Stall over a Transiently Pitching Airfoil". *AIAA J*., Vol. 32, No. 3, pp. 586-593, March 1994.
[24] Walker, J.M., Helin, H.E., and Strickland, J.H. "An Experimental Investigation of an Airfoil Undergoing Large-Amplitude Pitching Motions". AIAA J., Vol. 23, No. 8, pp. 1141-1142, August 1985.
[25] Stephen, E., Walker, J., Roh, J., Eldred, T., and Beals, M. "Extended Pitch Axis Effects on the Flow about Pitching Airfoils". AlAA 1989-0025
[26] Daley, D.G., and Jumper, E.J. "Experimental Investigation of Dynamic Stall for a Pitching Airfoil". *J. Aircraft*, Vol. 21, No. 10, pp. 831-832, October 1984.
[27] Oshima, H., and Ramaprian, B. R. "Velocity Measurements over a Pitching Airfoil". *AIAA J*., Vol. 35, No. 1, January 1997.

[28] Conger, R. N., and Ramaprian, B.R. "Pressure Measurements on a Pitching Airfoil in a Water Channel". AIAA-1993-0184.
[29] Acharya, M., and Metwally, M.H. "Unsteady Pressure Field and Vorticity Production over a Pitching Airfoil". *AIAA J*., Vol. 30, No. 2, February 1992
[30] Karim, M. A., and Acharya M. "Control of the Dynamic-Stall Vortex over a Pitching Airfoil by Leading-Edge Suction". AIAA 1993-3267.
[31] Koochesfahani, M., and Vanco, S. "Initial Acceleration Effects on Flow Evolution Around Airfoils Pitching to High Angles of Attack", AIAA J., Vol. 30, No. 8, pp 1529-1531, 1993.
[32] Schreck, S.J., Faller, W.E., Robinson, M.C. "Unsteady Separation Processes and Leading Edge Vortex Precursors: Pitch Rate and Reynolds Number Influences". J. Aircraft, Vol. 39, No. 5, September–October 2002
[33] Shih, C., Lourenco, L., Van Dommelen, L., and Krothapalli, A., "Unsteady Flow Past an Airfoil Pitching at a Constant Rate", AIAA J., Vol. 30, No. 5, pp. 1153-1161, 1992.
[34] Crisler, W., Krothapalli, A., and Lourenco, L. "PIV Investigation of High Speed Flow over a Pitching Airfoil". AIAA 1994-0533
[35] Ghosh Choudhuri, P., and Knight, D. "Effects of Compressibility, Pitch Rate, and Reynolds Number on Unsteady Incipient Boundary Layer Separation over a Pitching Airfoil". AIAA 1995-0782.
[36] Okongo'o, N., and Knight, D.D. "Implicit unstructured Navier-Stokes Simulation of Leading Edge Separation over a Pitching Airfoil". AIAA 1997-0657.
[37] Visbal, M.R., and Shang, J.S. "Investigation of the Flow Structure around a Rapidly Pitching Airfoil". *AIAA J*., Vol. 27, No. 8, pp. 1044-1051, 1989.
[38] Visbal, M.R. "Dynamic Stall of a Constant-Rate Pitching Airfoil". *J Aircraft*, Vol. 27, No. 5, pp. 400-407, 1990.
[39] Morgan, P.E., and Visbal, M.R. "Simulation of Unsteady Three-Dimensional Separation on a Pitching Wing". AIAA 2001-2709.
[40] Lentink, D., and Dickinson, M.H. "Rotational Accelerations Stabilize Leading Edge Vortices on Revolving Wings". J. Exp. Bio., Vol. 212, pp. 2705-2719, 2009.
[41] Babinsky, H., and Jones, A.R. "Unsteady Lift Generation on Sliding and Rotating Flat Plate Wings". AIAA 2009-3689.
[42] Ol, M., McAuliffe, B. R., Hanff, E. S., Scholz, U., Kaehler, Ch., "Comparison of Laminar Separation Bubble Measurements on a Low Reynolds Number Airfoil in Three Facilities", AIAA Paper 2005-5149, 2005.
[43] Kaplan, S., Altman, A., and Ol, M. "Wake Vorticity Measurements for Low Aspect Ratio Wings at Low Reynolds Number". *Journal of Aircraft*, Vol.44, No.1, pp. 241-251, 2007.
[44] Willert, C.E., and Gharib, M. "Digital Particle Image Velocimetry," Experiments in Fluids, Vol. 10, No. 4, January, 1991.
[45] Williams, D., Collins, J., Tadmor, G., and Colonius, T. "Control of a Semi-Circular Planform Wing in a "Gusting" Unsteady Freestream Flow: I-Experimental Issues". AIAA-2008-3976, 2008.
[46] Soria, J., New, T.H., Lim, T.T., and Parker, K. "Multigrid CCDPIV Measurements of Accelerating Flow Past an Airfoil at an Angle of Attack of 30º". *Exp. Thermal and Fluid Science*, Vol. 27, pp. 667-676, 2003.
[47] Etkin, B., "*Dynamics of Atmospheric Flight*," Dover Publications, 2005.
[48] Kramer, B. "Experimental Evaluation of Superposition Techniques Applied to Dynamic Aerodynamics". AIAA 2002-0700, 2002.
[49] Bruce, R. J., Mundell, A. R. G., "Low Speed Wind Tunnel Tests on the 1303 UCAV Concept", QinetiQ/FST/TR025502/1.0, QinetiQ, Ltd., Farnborough, UK, March 2003.
[50] Ol, M.V. "Water Tunnel Velocimetry Results for the 1303 UCAV Configuration". AIAA-2006-2990.
[51] Ol, M.V. "The Passage to Stall of Nonslender Delta Wings at Low Reynolds Number". Dissertation, Caltech, 2001.
[52] Rolling Hills Research Corporation. http://www.rollinghillsresearch.com/Water_Tunnels/Brochures/RHRC_Research_Water_Tunnels.pdf
[53] Peter, Deepak C. "Calibration of the Horizontal Free-surface Water Tunnel". M.S.E. project report, Department of Mechanical Engineering, University of Dayton, 2004.
[54] Downs, R. "Flow Quality of the Horizontal Free-surface Water Tunnel." Summer Faculty Report, AFRL Air Vehicles Directorate, 2006.
[55] http://www.measurementsci.com/products_miniLDV.hmtl
[56] Fonov, S., Goss, L., Jones, G., Crafton, J., Fonov, V., and OL, M.V. "New Method for Surface Pressure Measurements". AIAA-2005-1029.
[57] http://www.syringepump.com/NE-1000.htm

[58] Altman, A. "Force Measurements using the Rolling Hills Research Corporation Balance". Summer Faculty Report, AFRL Air Vehicles Directorate, 2005.
[59] Rao, Y.-J. "In-Fibre Bragg Grating Sensors". Meas. Sci. Tech., Vol. 8, No. 4., pp. 355-375, April 1997.
[60] http://www.micronoptics.com/sensing_instruments.php
[61] Tani, I. "Low Speed Flows Involving Bubble Separation," *Progress in Aeronautical Sciences*, Vol. 5, pp. 70-104, 1964.
[62] Watmuff, J. H. "Evolution of a Wave Packet into Vortex Loops in a Laminar Separation Bubble," Journal of Fluid Mechanics, Vol. 397, pp. 119, 1999.
[63] Bao, F., Dallmann, U. C. "Some Physical Aspects of Separation Bubble on a Rounded Backward-Facing Step," Aerospace Science and Technology, Vol. 8, pp. 83, 2004
[64] Arena, A. V., Mueller, T. J. "Laminar Separation, Transition, and Turbulent Reattachment near the Leading Edge of Airfoils," *AIAA Journal*, Vol. 18, pp. 747, 1980
[65] Roberts, W. B. "Calculations of Laminar Separation Bubbles and Their Effect on Airfoil Performance," *AIAA Journal*, Vol. 18, pp. 25-31, 1980
[66] Bastedo, W. G., Jr., Mueller, T. J. "Spanwise Variation of Laminar Separation Bubbles on Wings at Low Reynolds Numbers," Journal of Aircraft, Vol. 23, pp. 687, 1986.
[67] Gopalarathnam, A, Broughton, B.A., McGranaham, B.D., and Selig, M.S. "Design of Low Reynolds Number Airfoils with Trips". *Journal of Aircraft*, Vol. 40, No. 4, July-August 2003.
[68] Biber, K., Ol, M., and Tilmann, C. P. "Some Examples of Airfoil Design for Future UAV Concepts". AIAA 2004-1050.
[69] McAuliffe, B. R., Yaras, M. I. . Separation-Bubble-Transition Measurements on a Low-Re Airfoil Using Particle Image Velocimetry, ASME paper GT2005-68663, 2005.
[70] Drela, M. Xfoil User's Guide, Version 6.94: MIT Aero and Astro Department, 2002.
[71] Selig, M. S. Summary of Low-Speed Airfoil Data - Vol. 1-3: Soartech Publications, 1996-1997; also, http://www.ae.uiuc.edu/m-selig/ads/coord_database.html
[72] Roberts, S. K., Yaras, M. I. (2005). Effects of Surface Roughness Geometry on Separation Bubble Transition, ASME Paper GT2005-68664.
[73] Galbraith, M., and Visbal, M. "Implicit Large Eddy Simulation of Low Reynolds Number Flow Past the SD7003 Airfoil". AIAA 2008-0225.
[74] Gursul, I., Taylor, G. and Wooding, C.L. "Vortex Flows over Fixed-Wing Micro Air Vehicles". AIAA 2002-0698, 2002.
[75] Spedding, G., McArthur, J., M. Rosen, M. "Deducing aerodynamic mechanisms from near- and far-wake measurements of fixed and flapping wings at moderate Reynolds number". AIAA-2006-33
[76] Laitone, E.V., "Wind Tunnel Tests of Wings at Reynolds Numbers Below 70,000," *Experimental Fluids*, Vol. 23, 1997, pp. 405-409.
[77] Cosyn, P., and Vierendeels, J. "Numerical Investigation of Low Aspect Ratio Wings at Low Reynolds Numbers". AIAA 2005-4609.
[78] Polhamus, E. C. "Predictions of Vortex-Lift Characteristics by a Leading-Edge-Suction Analogy", Journal of Aircraft, Vol. 8, No. 4, 1971, pp. 193–199.
[79] Torres, G.E., and Mueller, T.J., "Aerodynamic Characteristics of Low Aspect Ratio Wings at Low Reynolds Numbers", *Fixed And Flapping Wing Aerodynamics For Micro Air Vehicles Applications*. T.J. Mueller, ed., Progress in Aeronautics and Astronautics, Volume 195, AIAA, Chapter 7, pp. 115-139, 2001.
[80] Zuhal, L, and Gharib, M. "Near Field Dynamics of Wing Tip Vortices," *31st AIAA Fluid Dynamics Conference & Exhibit*, AIAA 2001-2710, Anaheim, CA, 2001.
[81] Thwaites, Bryan, *Incompressible Aerodynamics: An Account of the Theory and Observation of the Steady Flow of Incompressible Fluid past Aerofoils, Wings, and Other Bodies*, Dover Publications Inc., New York, 1960, p. 314.
[82] Lamar, J. E.: "Extension of Leading-Edge-Suction Analogy to Wings with Separated Flow Around the Side Edges at Subsonic Speeds", NASA TR R-428, 1974.
[83] Hanff, E.S. et al., "Final Report: RTO AVT-101 Task Group on Low Reynolds Number Aerodynamics," NATO report, 2007.
[84] Parker, K., Soria, J., and von Ellenrieder, K.D. "Characteristics of the Vortex Street behind a Finite Aspect-Ratio Flapping Wing". AIAA 2006-1304, 2006.
[85] Anderson, .J.M., Streitlien, K., Barrett, D.S., and Triantafyllou, M.S. "Oscillating Foils of High Propulsive Efficiency". *J. Fluid Mech.*, Vol. 360, pp. 41-72, 1998.

[86] Kurtulus, D.F., David, L., Farcy, A., and Alemdaroglu, N. "Laser Sheet Visualization for Flapping Motion in Hover". AIAA 2006-0254, 2006.
[87] Leishman, J.G. *Principles of Helicopter Aerodynamics*. Cambridge University Press, 2000.
[88] von Karman, T., and Sears, W. R., "Airfoil Theory for Nonuniform Motion," *Journal of the Aeronautical Sciences*, Vol. 5, No. 10, 1938, pp. 379–390.
[89] McCroskey, W.J. "The Phenomenon of Dynamic Stall". NASA TM 81264, 1981.
[90] Ol, M, Dong, H., and Webb, C. "Motion Kinematics vs. Angle of Attack Effects in High-Frequency Airfoil Pitch/Plunge". AIAA-2008-3822
[91] Mueller, T.J. "Low Reynolds Number Vehicles". AGARDograph No. 288, 1985.
[92] Radespiel, R., Windte, J., and Scholz, U. "Numerical and Experimental Flow Analysis of Moving Airfoils with Laminar Separation Bubbles". AIAA 2006-0501, 2006.
[93] Lai, J.C.S., and Platzer, M.F. "Jet Characteristics of a Plunging Airfoil". *AIAA Journal*, Vol. 37, No. 12, pp. 1529-1537, Dec. 1999.
[94] Jones, K. D., Dohring, C. M., and Platzer, M. F., "Wake Structures Behind Plunging Airfoils: A Comparison of Numerical and Experimental Results," AIAA Paper 96-0078, 1996.
[95] Young, J., and Lai, J.C.S. "Oscillation Frequency and Amplitude Effects on the Wake of a Plunging Airfoil". *AIAA Journal*, Vol. 42, No. 10, 2004. pp. 2042-2052
[96] McAlister, K.W., and Carr, L.W. "Water Tunnel Visualization of Dynamic Stall". *Journal of Fluids Engineering*, Vol. 101, pp. 376-380, Sept. 1978.
[97] Koochesfahani, M.M. "Vortical Patterns in the Wake of an Oscillating Airfoil," AIAA J. Vol. 27, No. 9, pp. 1200-1205, Sept. 1989.
[98] Fukushima, T., and Dadone, L.U. "Comparison of Dynamic Stall Phenomena for Pitching and Vertical Translation Motions". NASA CR-2793, July 1977.
[99] Walker, J.M., Helin, H.E., and Strickland, J.H. "An Experimental Investigation of an Airfoil Undergoing Large-Amplitude Pitching Motions". *AIAA J*., Vol. 23, No. 8, pp. 1141-1142, Aug. 1985.
[100] Ol, M. (Ed.). "NATO RTO AVT-149 Report: Unsteady Aerodynamics for Micro Air Vehicles". [in press]. 2010.
[101]Taylor, G. K., Nudds, R. L., and Thomas, A. L. R. (2003). Flying and swimming animals cruise at a Strouhal number tuned for high power efficiency, *Nature* (London) Vol. 425, pp. 707–11
[102] McCroskey, W. J., Carr, L. W., and McAlister, K. W., "Dynamic Stall Experiments on Oscillating Airfoils," *AIAA J*., Vol. 14, No. 1., pp. 57-63, 1976
[103] Baik, Y.S., Rausch, J., Bernal, L., Shyy, W., and Ol, M. "Experimental Study of Governing Parameters in Pitching and Plunging Airfoil at Low Reynolds Number". AIAA-2010-0388
[104] Dong, H., Webb, C., and OL, M.V. "Effects of Unequal Pitch and Plunge Airfoil Motion Frequency on Aerodynamic Response". AIAA-2008-582, 2008.
[105] McGowan, G., Gopalarathnam, A, Ol, M., and Edwards, J. "Analytical, Computational, and Experimental Investigations of Equivalence Between Pitch and Plunge Motions for Airfoils at Low Reynolds Numbers". AIAA 2008-0535
[106] Ol, M., Dong, H., and Webb, C. "Motion Kinematics vs. Angle of Attack Effects in High-Frequency Airfoil Pitch/Plunge.
[107] Ol, M. "Vortical Structures in High Frequency Pitch and Plunge at Low Reynolds Number". AIAA 2007-4233.
[108] Eldredge, J.D., Wang, C.J., and Ol, M. "A Computational Study of a Canonical Pitch-up, Pitch-down Wing Maneuver". AIAA 2009-3687.
[109] Dickson, W.B., and Dickinson, M.H. "The Effect of Advance Ratio on the Aerodynamics of Revolving Wings". *J. Exp. Bio.*, Vol. 207, pp. 4269-4281, 2007.
[110] Lian, Y., and Ol, M.V. "Experiments and Computation on a Low Aspect Ratio Pitching Flat Plate". AIAA 2010-0385.
[111] Doman, D., Oppenheimer, M., and Sigthorsson, D. "Dynamics and Control of a Minimally Actuated Biomimetic Hypersonic Vehicle: Part 1 – Aerodynamic Model". AIAA 2009-6160.
[112] Wood, R.J. "The First Takeoff of a Biologically Inspired At-Scale Robotic Insect". *IEEE Transactions on Robotics*, Vol. 24, No. 2., pp. 341-347, 2007.
[113] Milano, M., and Gharib, M. "Uncovering the Physics of Flapping Flat Plates with Artificial Evolution". J. Fluid Mech., Vol. 234, pp. 403-409, 2005.

[114] Kurtulus, D.F., David, L., Farcy, A., and Alemdaroglu, N. "A Parametric Study with Laser Sheet Visualization for an Unsteady Flapping Motion". AIAA 2006-3917.
[115] Trizila, P.C., Kang, C.-K., Visbal, M.R., and Shyy, W. "Unsteady Fluid Physics and Surrogate Modeling of Low Reynolds Number, Flapping Airfoils". AIAA 2008-3821.
[116] Freymuth, P. "Thrust Generation by an Airfoil in Hover Modes". *Experiments in Fluids*, Vol. 9, pp. 17-24, 1990.